SYNTHESIS AND CHARACTRIZATION OF WATER SOLUBLE SUGAR-CAPPED METAL SULPHIDE SEMICONDUCTOR NANOPARTICLES AND THEIR TOXICITY

Poslet Morgan Shumbula

(Student number: 335329)

Degree of Doctor of Philosophy in Chemistry

A thesis submitted to the Faculty of Science of the Witwatersrand, Johannesburg, in fulfilment of the requirements for the Degree of Doctor of Philosophy

Academic year 2011

DECLARATION

I declare that the work presented in this thesis was carried out by me under the supervision of Doctor Makwena Justice Moloto. It is being submitted for the degree of Doctor of Philosophy in the University of the Witwatersrand, Johannesburg, and has not been submitted before for any degree or examination at any other university.

_____

Poslet Morgan Shumbula

On this _____ day of _____ 2011

Dedicated to

My beloved wife Ndivhuwo Ramathuba

My mother Sarah Mudzhadzhi Ndou

My father Bethuel Shumbula *My uncle Josias Mbulaheni Shumbula*

My brothers and sisters

and

My pastor Tshimangadzo George Mulima and his late wife Joyce Mulima

"You are truly the best. May the God of heavens bless you all."

ACKNOWLEDGEMENTS

In this world that has lost an attitude of gratitude, I refuse to keep quite and be one of the citizens that are following on those steps. I choose to give credit where it is due. To my supervisor, Doctor Makwena Justice Moloto, I would like to appreciate your effort in seeing that I become one of the counted in this world. Thank you so much for the spirit of confidence you instilled within me. My academic life has really improved in the past three years because of you. You have the ability to groom people to be the best. Your patience with me was amazing. I will always cherish the moment we spent together, when you were my supervisor. You are the best.

To my co-supervisor, Dr Tshinyadzo Robert Tshikhudo, thank you for your help. Your input in shaping my work was valuable.

I would also like to forward my word of gratitude to Mrs Nosipho Moloto (University of Johannesburg), Mr Siyasanga Mpelane (Council for Scientific and Industrial Research) and Mr Benias Nyamuda (Tswane University of Technology) for the XRD analysis and interpretation. I would also like to extend my gratitude to Kailen (National Institute for Occupational Health), the man behind toxicity. Working with you was a privilege. Thank you for contributing in my thesis. You made a huge difference and I will always remember you guys.

To Professor Mike Witcomb, Caroline Lalkhan and Abe Seema, thank you for helping me with the analysis of my samples through transmission electron microscope (TEM). Your patience with me was fantastic.

I also want to thank my colleagues in our research group, the CATOMAT group in the school of chemistry led by Professor Neil Coville and Professor Mike Scurrell. You taught me to be brave and persevere when things were tough. You believed in my ability since my arrival. It was good to be a member of this friendly group. I hope you will continue carrying that spirit. To Prof. Coville, allow me to thank you once more. When my supervisor left to UJ, I never felt lost. You were there when I wanted help. I thank you for everything you have done for me. You are the best.

To the school of chemistry, thank you for allowing me to conduct my research. It was good being part and parcel of the big family. You made me feel loose. I would also want to thank the men downstairs, Mr Elias Baloyi and Mr David Moloto, for helping me with chemicals and other research materials. You guys are the best.

To my beloved wife, Ndivhuwo, may the good God bless you for the unwavering support you gave me throughout my studies. Mostly, I was not there, but you understood. You supported me when I was down and kept me going. You showed interest in my work, and that was enough for me. My gratitude also goes to my family and friends who supported me although they did not understand what I was doing. To my spiritual dad, Pastor Tshimangadzo George Mulima, thank you for the words of encouragement. You believed in me, prayed for me and advised me. I am better because of you. Thank you for caring and may the good God keep you long for us.

I would like to acknowledge the funding I received from MINTEK and NRF. Thank you for helping me to achieve my dream. I am proud of you.

To God be the glory. It was not easy, but it was worthy. I thank Him for guiding me. It was a long and challenging journey, but he was there for me.

Publications and presentations arising from this work

Presentations

- NIC 2008: Oral presentation: 'Synthesis and characterization of sugar-capped metal sulphide (semiconductor) nanoparticles for biological applications'
- SACI 2008: Oral presentation: 'Synthesis and characterization of water soluble sugar capped metal sulphide semiconductor nanoparticles for biological applications'
- SANI 2009: Poster presentation: 'Synthesis and characterization of HDA and sugar-capped metal sulphide semiconductor nanoparticles '
- NIC 2009: Oral presentation: 'The role of the capping agents and their effects on the preparation of hydrophobic and hydrophilic semiconductor nanoparticles/quantum dots'

Publications

- Poslet M. Shumbula, Makwena J. Moloto, Tshinyadzo R. Tshikhudo, Manuel Fernandes, Dichloro (bis[diphenylthiourea]) cadmium complex as a precursor for HDA-capped CdS nanoparticles and their solubility in water, *S. Afr. J. Chem.* **106** (7/8), 1, 2010
- Poslet M. Shumbula, Makwena J. Moloto, Tshinyadzo R. Tshikhudo, Synthesis and characterization of sucrose and glucuronic acid-capped CdS nanoparticles from HDA-capped via ligand exchange, *to be submitted.*

ABSTRACT

Different cadmium, cobalt and zinc complexes of substituted thioureas, dithiocarbamates and thiuram di/monosulfides were synthesized using ethanol or water as solvents. The synthesis of dithiocarbamates complexes were performed at room temperature while the rest were refluxed at 70 ^{o}C. The complexes were easy to synthesize, of low cost and stable in air and were obtained in good yields. The complexes were characterized using various instruments, such as infrared (FT-IR) and proton nuclear magnetic resonance (^{1}H NMR) spectroscopy, elemental analyzer, thermogravimetric analysis (TGA) and X-ray crystallography. The complexes were found to coordinate the ligands through sulphur atom, instead of nitrogen atom. This was concluded after shifts to higher or lower wavenumbers were observed from the infrared spectra of the complexes as compared to their free ligands. The ^{1}H NMR also depicted formation of the complexes, with complexes peaks shifting to downfield as compared to the free ligands. There were also signs of broad NH peaks especially for substituted thiourea complexes. The crystals grown from complex **II** (diphenylthiourea cadmium complex) depicted a tetrahedral geometry, with two sulphur and two chlorine atoms binding to the central atom which is cadmium. The easily synthesized complexes were thermolysed in HDA, TOPO or a mixture of the two to form metal sulphide nanoparticles. The role of the above capping agents or ligands was to control particles growth and prevent them from aggregation. A single source precursor route was employed in synthesizing hydrophobic semiconductor nanoparticles, which are also known as (QDs) quantum dots. Various shapes, which are rods (mono-, bi- and tripods), spheres and hexagonal were revealed through transmission electron microscope (TEM). The sizes of these particles ranged from 1 to 12 nm in diameter. Other instruments used for characterising the as-synthesized semiconductor nanoparticles include X-ray diffractometer (XRD), UV-Visible and Photoluminescence spectroscopy. The optical properties of the particles as determined by the UV-Visible spectroscopy revealed some differences as compared to the bulk materials. All the absorption spectra were blue shifted to the bulk materials signifying finite size of the particles. The XRD peaks observed were broad as compared to the bulk ones, which also signified small particles size. Two phases, which are hexagonal and cubic, were revealed from the XRD.

The hydrophobic semiconductor nanoparticles or quantum dots synthesized were then transferred into water soluble using ligand exchange method. The chloroform and pyridine routes were used to synthesize hydrophilic semiconductor nanoparticles, with pyridine route being preferred. The shape and size of the particles were not influenced by the transfer into water soluble since the experiments were performed at room temperature. This was confirmed by TEM analysis. The capping agents used after displacing water insoluble capping agents were sugars, which were soluble in water. The XRD pattern of the semiconductor nanoparticles/QDs (CdS) capped by sugars after ligand exchange through pyridine yielded multiple peaks which were difficult to assign. The attempt to employ ligand exchange method in transferring hydrophobic Co_xS_y and ZnS nanoparticles to hydrophilic Co_xS_y and ZnS nanoparticles proved unsuccessful. When the materials were centrifuged after the sugars were introduced as capping agents, some solid material settled at the bottom, with some floating on top of the solution. This was an indication that the materials were not miscible.

The hydrophilic CdS, Co_xS_y and ZnS nanoparticles were also synthesized using direct method. In this method, the metal sources and capping (sugars) were dissolved in ethylene glycol at 100 ^oC. The sulphur sources were also dissolved separately in the same solvent. Upon completion, the latter solution was added to the former one. The particles were grown at 160 ^oC for an hour with ethylene glycol as a solvent. The morphology of the particles dominated through this method was spherical-like in shape. The crystallinity of CdS and ZnS nanoparticles depicted hexagonal and cubic phases depending on the complexes used. The XRD indicated the armophous nature of the cobalt sulphide nanoparticles, irrespective of the precursor used.

Due to the toxicity problem of the quantum dots, especially CdS, the water soluble CdS capped by glucuronic acid, glucose and sucrose after ligand exchange were chosen for that study. However, results showed that the CdS used were not toxic. It was measured or deduced by checking the viability which remained above 90%. Add a bit of deductions about toxicity study here, just some of the general trends.

CONTENTS

CHAPTER 6: Water soluble semiconductor nanoparticles/QDs synthesized by direct method

CHAPTER 7: Toxicity studies of CdS nanoparticles/QDs capped by sugars

LIST OF ABBREVIATIONS

a.u	arbitrary units
ATP	adenosine triphosphate
CO_2	carbon dioxide
cm	centimetre
^oC/min	degree celsius per minute
DMSO	dimethylsulfoxide
DNA	deoxyribonucleic acid
E_g	band gap
FBS	fetal bovine serum
FT-IR	fourier transform infrared
g/l	grams per litre
HDA	hexadecylamine
h	hour
LDH	lactate dehydrogenase
μg/ml	microgram per millilitre
μl	microlitre
MTT	(3-(4,5-dimethylthiazol-2yl)-2,5-diphenyl tetrazolium bromide)
nm	nanometre
NMR	nuclear magnetic resonance
PAA	polyacrylic acid
PMA	phorbol-12-myristate-13-acetate
PBS	phosphate buffered saline
PL	photoluminescence
QDs	quantum dots
TEM	transmission electron microscope
TGA	thermogravimetric analysis
TODAB	trioctadecylmethylammonium bromide
TOP	tri-n-octylphosphine
TOPO	tri-n-octylphosphine oxide
eV	electron volts
XRD	X-ray diffraction

LIST OF TABLES

LIST OF FIGURES AND SCHEMES

Chapter 1

Introduction

1.1. Background and rationale

Semiconductor nanoparticles or quantum dots (QDs) whose radii are smaller than the bulk exciton Bohr radius constitute a class of materials intermediate between molecular and bulk forms of matter. The exciton Bohr radius is a concept where excitons have a natural physical separation between the electron and the hole which is dependant on the material. In large semiconductor nanoparticles or QDs, the exciton Borh radius is small compared to the size of the crystal, and the exciton is then relatively free to move around in the crystal. Quantum confinement of both the electron and the hole in all three dimensions leads to an increase in the effective band gap of the material with decreasing crystallite size. Consequently, both the optical absorption and emission of quantum dots shift to higher energies as the size of the dots gets smaller. Although nanocrystallites have not yet completed their evolution into bulk solids, structural studies indicate that they retain the bulk crystal structure and lattice parameter. Recent advances in the synthesis of highly monodisperse nanocrystallites have paved the way for numerous spectroscopic studies assigning the QD electronic states and mapping out their evolution as a function of size. The size and shape of semiconductor nanoparticles control their widely varying electrical and optical properties [1, 2, 3]. One of the most active trends in modern materials chemistry is the development of synthetic routes to size and shape controlled semiconductor nanoparticles. Different routes were developed to synthesize these materials. The discovery of epitaxial growth regimes that favoured the formation of nanometer-sized islands of semiconductor nanoparticles or quantum dots on suitable substrate came into picture. Quantm dots synthesized from these routes are of high quality in terms of size distribution and optical activity. Photoluminescence (PL) from single self-assembled quantum dots is a highly efficient process, characterized by several ultra-narrow emission lines, related to different exciton states in the dots, and is reminiscent of the emission from atoms [4]. However, the main drawback of epitaxial growth methods is that they produce nanoparticles that are attached to a substrate or embedded in a matrix, and therefore limits the range of their applications. A major breakthrough in the synthesis of semiconductor

nanoparticles/QDs was reported by Murray *et al.* [5]. Influenced by the reported work of Stuczynski *et al.* [6], a metal organic route was developed with $Cd(Me)_2$ and elemental Se as the precursors in a matrix of the coordinating ligands tri-octylthosphine (TOP) and tri-octylphosphine oxide (TOPO). This synthetic route was also based upon the classic work of La Mer and Dinegar in 1950 on colloid formation [7]. The injection of precursors above a critical temperature creates a nucleation event and this is followed by rapid cooling to a growth where no further nucleation is favourable. However, this route developed by Murray *et al.* [5] was carried out in harzadous conditions. Trindade and O'Brien then developed single-source precursor route [8]. In this method, a compound containing both elements needed to form semiconductor nanoparticles is used.

One of the difficulties in preparation of 0D (spheres, cubes), 1D (rods, wires) and 2D (discs, prisms, plates) nanopaticles is the control of growth through variation of the reaction parameters [9, 10, 11, 12]. One of the critical parameters used to control the growth of size and morphology of quantum dots is temperature. At high temperatures, the capping agent or surfactant molecules are dynamically adsorbed to the surface of the growing crystal. They are mobile enough to provide access for the addition of monomer units to the growing nanocrystal, while still preventing aggregation of multiple nanocrystals. At low temperatures the capping agents are strongly bound to the surface of the nanocrystals and provide solubility in organic solvents. The significance of the capping agent is stressed by the fact that nanocrystals produced by colloidal routes are generally thought of together with capping agents that coat them. If this coating agent is removed, the nanocrystals loose their solubility, aggregate and some of their size-dependant properties. If they are grown in capping agents that do not passivate the surface of the nanocrystal, then uncontrollable growth of large crystals is observed. This organic coating allows for great synthetic flexibility, in that the capping agents can be exchanged with different organic molecules possessing different functional groups or polarity.

Quantum dots have generated a tremendous amount of interest due to their small size and shape that allows them to be used for diverse applications. The applications range from electrical devices to biological and medical research [13, 14, 15, 16]. High quality colloidal nanocrystals are normally synthesized in organic phase with the presence of strongly coordinating hydrophobic capping agents or organic ligands. However, using nanocrystals in biological system means that these nanomaterials have to be well dispersed and stable in

aqueous solution. To meet the criteria, surface functionalisation is needed to tailor the solubility and biocompatibility of nanocrystals and preserve their desired properties. Quantum dots are known to be toxic. To minimize toxicity, a capping agent that is not or less toxic is needed. That capping agent should possess functional groups such as carboxylic acid, hydroxyl, amine and many more.

1.2. Objectives

The motive behind this project was to synthesize water soluble semiconductor nanoparticles or quantum dots and test some of them for toxicity. The objectives of the research project are then described as follows:

(i) To synthesize and characterize complexes or precursors which are useful for the synthesis of semiconductor nanoparticles or QDs. This involves the use of metal sources such as cadmium chloride, and sulphur sources such as diphenylthiourea. The precursors will be characterized using Fourier transform infrared spectroscopy (FT-IR), nuclear magnetic resonance (NMR) and X-ray crystallography, thermogravimetric analysis (TGA).

(ii) To synthesize and characterize hydrophobic semiconductor nanoparticles capped by hexadecylamine (HDA) and tri-octylphosphine oxide (TOPO) using the above complexes as precursors. The prepared quantum dots will be characterized by ultraviolet-visible (UV-Vis) spectroscopy, photoluminescence (PL) spectroscopy, Fourier transform infrared spectroscopy (FT-IR), transmission electron microscopy (TEM), powder X-ray diffraction (PXRD).

(iii) To synthesize and characterize hydrophilic semiconductor nanoparticles/QDs capped by glucuronic acid, glucose and sucrose. This was achieved by ligand exchange method, converting HDA and TOPO-capped CdS nanoparticles into water soluble. The prepared hydrophilic QDs will be characterized by ultraviolet-visible (UV-Vis) spectroscopy, photoluminescence (PL) spectroscopy, Fourier transform infrared spectroscopy (FT-IR), transmission electron microscopy (TEM), powder X-ray diffraction (PXRD).

(iv) To synthesize and characterize hydrophilic quantum dots capped by glucuronic acid, glucose and sucrose using direct method. This is achieved by mixing metal and sulphur sources, together with the sugars in the presence of the solvent. The prepared QDs will be characterized by ultraviolet-visible (UV-Vis) spectroscopy, photoluminescence (PL) spectroscopy, Fourier transform infrared spectroscopy (FT-IR), transmission electron microscopy (TEM), powder X-ray diffraction (PXRD).

(v) To investigate the toxicity of the selected CdS synthesized through ligand exchange and direct method.

1.3. Thesis outline

This thesis contains 8 chapters. The first part focuses on the general introduction of the semiconductor nanparticles or quantum dots (QDs). Although more work will be covered in literature review (Chapter 2), this work introduces us to some drawbacks and achievements of the work done. The main objectives of the study are also presented in this chapter. Chapter 2 is a general literature review. A description of the sulphur ligands and their complexes will be explored. It will also explore how semiconductor nanoparticles or quantum dots are fabricated, their optical and structural properties. In chapter 3 the synthesis conditions for the synthesis of complexes, hydrophobic and hydrophilic semiconductor nanoparticles are explored. The results of the synthesis of complexes or precursors, and water insoluble quantum dots, capped by HDA, TOPO or a mixture of HDA and TOPO using single source precursors route are discussed in chapter 4. In chapter 5, the capping agent or ligand exchange with different sugars for CdS capped by HDA, TOPO or a mixture will be described. Chapter 6 will discuss the results of sugars-capped semiconductor nanoparticles through direct method. Chapter 7 briefly focuses on the toxicity studies done for selected CdS nanoparticles capped by sugars. Chapter 8 presents a general summary and conclusion of the work presented in this thesis. The chapter highlights the successes of the projects, together with some recommendations.

1.4. References

1. M. Nirma1, D. J. Norris, M. Kuno, M. G. Bawendi, A. L. Fros, M. Rosen, *Phys. Rev. Lett.* **75,** 3728, 1995
2. A. P. Allivisatos, *Scient. Am.* **271,** 933, 1996
3. C. M. Lieber, *Solid State Commun.* **107,** 607, 1998
4. L. Landin, M. S. Miller, M. E. Pistol, C. E. Pryor, L. Samuelson, *Science*, **280,** 262, 1998
5. C. B. Murray, D. J. Norris, M. G. Bawendi, *J. Am. Chem. Soc.* **115,** 8706, 1993
6. S. M. Stuczynski, J. G. Brennan, M. L. Steigerwald, *Inorg. Chem.* **28,** 4431, 1989
7. V. K. La Mer, R. H. Dinegar, *J. Am. Chem. Soc.* **72,** 4847, 1950
8. T. Trindade, P. O'Brien, *Chem. Mater.* **9,** 523, 1997
9. Yu, J. Yang, Y. Qian, M. Yoshimura, *Chem. Phys. Lett.* **361,** 362, 2002
10. J. Yang, J. Zeng, S. Yu, L. Yang, G. Zhou, Y. Qian, *Chem. Mater.* **12,** 3259, 2000
11. J. Zhan, X. Yang, D. Wang, *Adv. Mater.* **12,** 1348, 2000
12. Y. Chen, J. Ding, Y. Guo, L. Kong, H. Li, *Mater. Chem. Phys.* **77,** 734, 2002
13. S. Coe, W-K. Woo, M. G. Bawendi, V. Bulovic, *Nature*, **420,** 800, 2002
14. D. Battaglia, X. Peng, *Nano Lett.* **2,** 1027, 2002
15. S. M. Lee, Y. W. Jun, S. N. Cho, J. Cheon, *J. Am. Chem. Soc.* **124,** 11244, 2002
16. W. C. Chan, S. Nie, *Science*, **281,** 2016, 1998

Chapter 2

Literature review

2.1 Thiourea, dithiocarbamate, thiuram mono/disulfide, thiosemicarbazide complexes and their applications

Thiourea is an organic compound that is composed of carbon, nitrogen, sulphur and hydrogen, with the formula $(NH_2)_2CS$. Mostly, thioureas are commonly prepared from reaction of isothiocynate with amine (Scheme 2.1), but there are also reports on reactions of amine or carbodiimides with several thionating reagents.

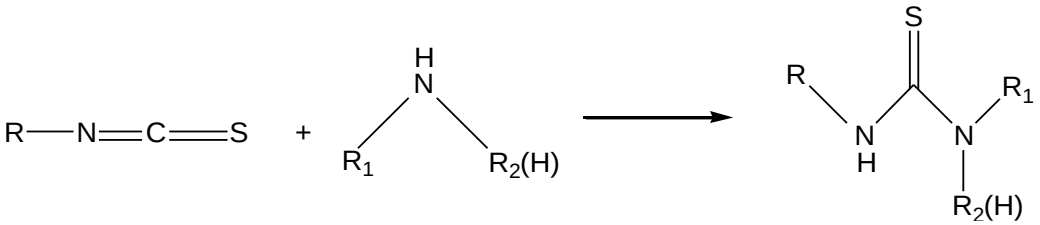

Scheme 2.1: Reaction scheme for the preparation of thiourea.

Besides simple thiourea, substituted thioureas have also been studied for the past decades. Rodriguez-Fernandez *et al.* [1] reported that various substituents in the thiourea ligands are expected to play a huge role in enhancing the solubility (hydrophobic/hydrophilic) of the drug and increasing its potency. Some thioureas afford different heterocyclic derivatives when subjected to dehydration or desulfuration.

Thiourea derivatives can have different conformations where the thioamide hydrogen atom and the thiocarbonyl bond are *cis* or *trans*. For N-alkylthiourea, there are two isomers, *trans* and *cis*, whereas for N, N'-dialkylthiourea, there are three isomers, namely.; *trans-trans*, *cis-cis* and *cis-trans* (Figure 2.1).

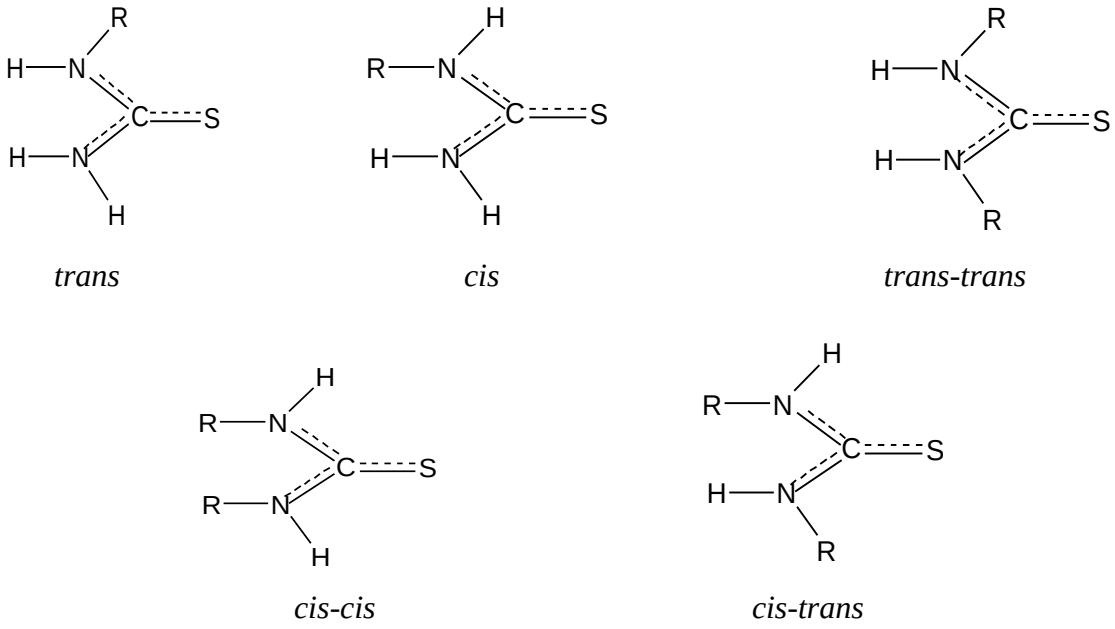

Figure 2.1: Different conformations of N-alkylthiourea and N, N'-dialkylthiourea.

Lane *et al.*[2] studied the infrared spectra of several thiourea derivatives in the solid state, and reported that N, N'-dimethylthiourea and N, N'-diethylthiourea were *trans-trans* isomers, with N, N'-butylthiourea showing both structures *cis* and *trans*. But the authors were not able to determine whether it was the *cis-trans* isomer or a mixture of the *cis-cis* and *trans-trans* compounds. An alylthiourea, that is methylthiourea, was identified as the trans isomer.

N, N'-Disubstituted thioureas bearing double NH groups have previously been prepared and developed as sensors and catalysts because of hydrogen bonding ability. [3]. Tetramethylthiourea (Figure 2.2) is another important substituted thiourea that has been studied before. The dipole moments in thiourea and tetramethylthiourea lie along the C_{2v} axis which also contains the –C=S group. The electronic structures of thiourea or substituted thiourea, in this case tetramethylthiourea, can be depicted by means of conventional resonance structures (Figure 2.3). Such structures show some partial double bond character of the C-N bond due to delocalization of the nitrogen lone-pair electrons to the –C=S group. Support for this suggestion is provided by means of some ^{13}C NMR data for tetramethylthiourea [4], which gave an estimate of about 6 kcal/mol for the C-N rotation barrier. Similarly, for thiourea the barrier is estimated to 14 kcal/mol from a ^{1}H NMR study [5]. The NMR studies will be discussed later in this chapter. The structure of tetramethylthiourea is non-planar due to steric hindrance. It has a shallow pyramidal

configuration at the nitrogen atom, as shown by electron diffraction measurements in the gas phase, and X-ray data for the solid state. In contrast, thiourea is planar in the solid phase but microwave measurements reveal it to be non-planar in the gas phase [6]

Aliphatic and aromatic thiourea compounds have demonstrated to be antimicrobial agents able to control different microorganisms. Previous reports show thioureas having strong antifungal activities comparable to the activity observed for the common antifungal antibiotic ketoconazole [7] and their antimicrobial and insecticidal properties have been documented for more than fifty years [8]. Thioureas can be used not only in the control of plant pathogenic fungi [9] but also they have been shown to possess antitubercular, antithyroid, anthelmintic, antibacterial, insecticidal and rodenticidal properties [10]

Thiourea and its derivatives, which are important precursors for the preparation of metal sulphide nanoparticles, have found extensive applications in the fields of agriculture, medicine and analytical chemistry. They are also widely used for the preparation of biologically relevant heterocycles. Besides focusing on the applications of these ligands, special attention has been placed on their coordination chemistry to different metal atoms. This is due to various potential donor sites that these ligands possess [11]. Thioureas are potentially capable of forming co-ordinate bonds through sulphur and nitrogen although the extremely low basicity of the ligands militates against the formation of nitrogen-metal bonds. Both these possibilities were reflected by various authors through the infrared spectra of complexes.

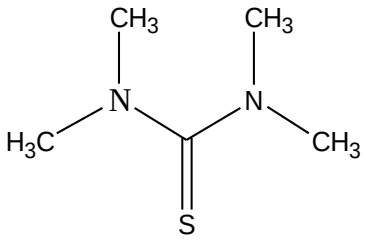

Figure 2.2: Structures of tetramethylthiourea

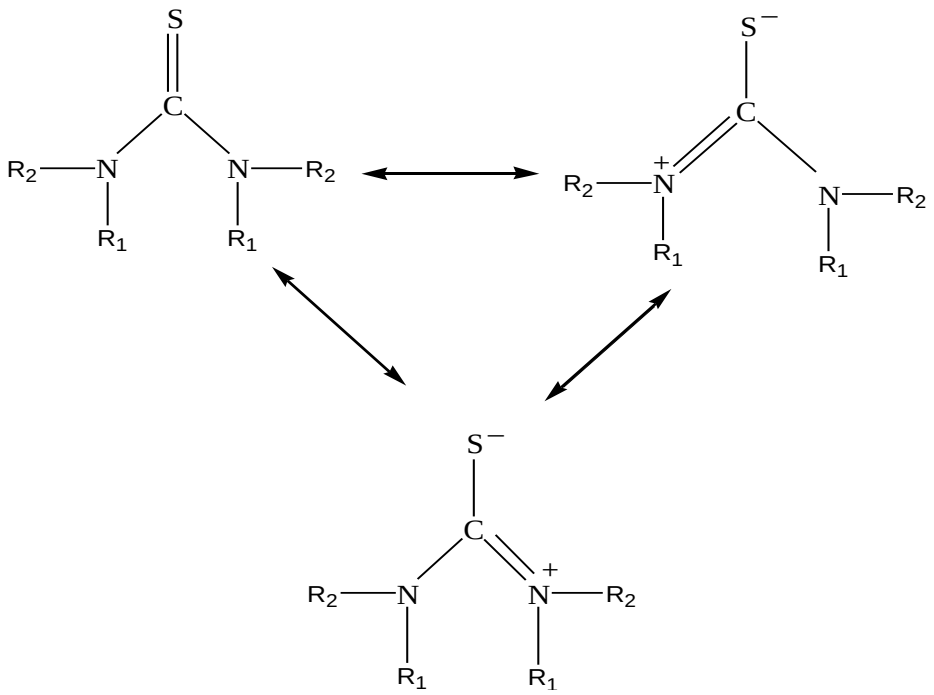

Figure 2.3: Resonance structures of a conventional representation of the electronic structure of thiourea systems

Substituted thioureas have a long history as ligands in coordination chemistry being able to coordinate to a metal through either sulphur or nitrogen. Various complexes were synthesized from different metals with substituted thioureas. Rosenheim and Meyer [12] reported the complexation of Fe(II) with thiourea giving the formulas $Fe(thiourea)_3(SCN)_2$ and $Fe(thiourea)_4Cl_2$, and concluded that the coordination is through the sulphur atom. They have used infrared spectroscopy and X-ray diffractions to determine the coordination. In addition, complexes prepared using the alkyl thiourea such as methylthiourea gave evidence using infrared spectroscopy that coordination is through sulphur [13]. Ni(II) complexes of thiourea type of ligands have been reported before, exhibiting a variety of formulas and stereochemistries e.g. octahedral, tetrahedral, planar and tetragonal [14] . Coordination was confirmed to be through the sulphur atom of the ligand. However, there are some Ni(II) complexes especially with the analogous urea ligands, that have been synthesized and coordination was reported to be through oxygen using X-ray analysis [15, 16] or infrared spectroscopy [17].

Kukushkin *et al.* [18] reported thiourea and its derivatives as important ligands for transition metals, especially platinum. The high *trans*-effect caused by thiourea is a useful help in the study of substitution reactions in square planar complexes. However, a large

number of platinum complexes with thiourea and its derivatives have been synthesized and their chemistries studied. Schafer and Curran [19] mentioned that the lowering of the ν(C=S) value by 25 cm^{-1} in comparison to the free ligand, in the infrared spectrum of the complex $[PtCl_2.L]$, where L was the tetramethylthiourea, was good evidence for monodentate ligation through sulphur and concluded by reporting that the complex should therefore have a dimeric structures. There are also instances where transition metals were reacted with thiourea and coordination found to be through nitrogen. Dunina [20] studied the complexes $[PdCl_2.L]$, where L was mono-, di-, and trisubstituted thioureas using spectrophotometry and conluded that the above ligands are monodentate and coordinate to the metal through nitrogen rather than sulphur. Although not always unambiguous in its results, the infrared spectroscopy technique has been applied frequently in the study of the coordination of thioureas and was found to be one of the paramount and useful approaches.

Dithiocarbamates and their derivatives are extremely versatile substances which have been used, for example, in the treatment of alcoholism [21], sarcoma cells [22], as possible protection against the lethal effects of X-rays [23]. A number of bis metal derivatives of dithiocarbamates have been studied in recent years in which the central metal ion is either fourfold coordinated or is pentacoordinated because of dimerization [24]. Thiuram sulfides (Figures 2.4 and 2.5), which are also known as bis(*N*,*N*-dialkylthiocarbamoyl)sulfides, $R_2NC(S)SnC(S)NR_2$ have been reported to have the ability of binding to different atoms through sulphur. These thiuram sulfides are the thiocarbamoyl esters of dialkyldithiocarbamic acids. The disulfides (n = 2) R_4tds are known on account of their biological activity, which leads to applications as fungicides, rubber vulcanization accelerators, agents of alcoholism therapy [25, 26], and quite recently, as arrestors of Human Immunodeficiency Virus infections such as AIDS [27]. This wide diversity of examples of biological activity has been attributed to a combination of at least two factors [28], that is, (i) the capability to fit into a receptor site and (ii) the ability to undergo reversible redox reactions at suitable potentials. From this point of view, the equilibrium relating thiuram disulfides and dithiocarbamates is very relevant to the chemistry of the disulfides.

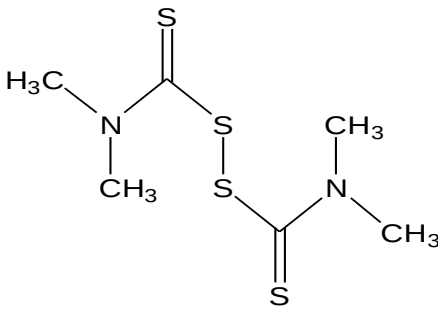

Figure 2.4: Structure of tetramethylthiuram disulfide.

A peculiarity of metal dithiocarbamate chemistry is the recognized ability of the ligands to stabilize unusually high oxidation states in transition metals, a property which has been attributed to the ligand ability to delocalize positive charge from the metal towards the periphery of the complex [29].

Thiuram disulfides are unique among thiolato-type ligands, in that reductive scission of the S-S bond leads to chelating systems (dithiocarbamate anions), which are particularly well suited to stabilize high oxidation states under the premise outlined above. The monosulfides (n = 1) R_4tms, perhaps because they lack the wide breadth of applications known for the disulfides in agriculture and experimental medicine, have been much less extensively studied and where such studies deal with the subject of interaction of monosulfides and metal species, the field remains virtually unexplored. Fan *et al*. [30] reported the synthesis of bis(dialkyldithio-/diseleno-carbamato)cadmium(II) or bis(dialkyldithio-/diseleno-carbamato)zinc(II) complexes.

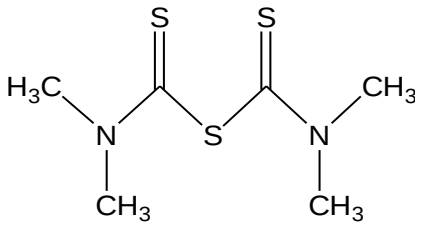

Figure 2.5: Structure of tetramethylthiuram monosulfide.

The above complexes were prepared by reacting CS_2 or CSe_2 with excess alkylamine and a base at low temperatures, followed by the addition of cadmium chloride or zinc chloride. The complexes were reported in high yields. Some of the precursors that have been

explored are those with symmetric alkyl groups (R = R' = Me, Et, Pr) or asymmetric R groups such as R = Me or Et, R' = ^{n}Hex, ^{n}Bu. The priority of the synthesizing the above complexes was to prepare metal sulphide or selenide nanoparticles since the cadmium or zinc metals were known to bind through the sulphur.

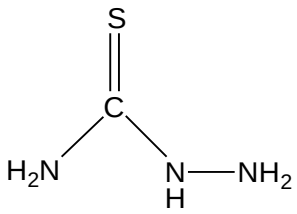

Figure 2.6: Structure of thiosemicarbazide.

Another ligand of interest which possesses potential donor sites, such as sulphur and nitrogen atoms, includes thiosemicarbazide (Figure 2.6). Burrows *et al.* [31] employed substituted thiosemicarbazides such as 4-methylthiosemicarbazide, 4-ethylthiosemicarbazide, 4-phenylthiosermicarbazide and 1,1,4-trimethylthiosemicarbazide in the synthesis of platinum complexes. The reported results demonstrated that thiosermicarbazides are very versatile ligands in platinum coordination chemistry as they are able to bind to the metal atom in a number of different modes. They can be monodentate, bound solely through sulphur atom, they can be bidentate, bound through the sulphur atom and nitrogens, or they can be monodentate but chelating through an intramolecular N-H…Cl hydrogen bond.

Like thiourea and its derivatives, thiosemicarbazide and its derivatives were also used as sulphur source by some researchers. In order to obtain acceptable results, complexes prepared from these ligands must be stable for long time, easy to synthesize, inexpensive and yield good quality crystalline particles.

(a) Infrared spectral analysis

As mentioned above, the infrared spectroscopy is one of the best tools mostly employed for the analysis of thiourea and its derivatives, dithiocarbamates and many more ligands used for the preparation of precursors for metal sulphide nanoparticles. When preparing the complexes, peaks of the ligands and their prepared complexes were compared where some shifts were obtained. Infrared spectroscopy has shown that in thiourea there are almost

equal contributions from the canonical forms 1, 2 and 3 (Figure 2.7).

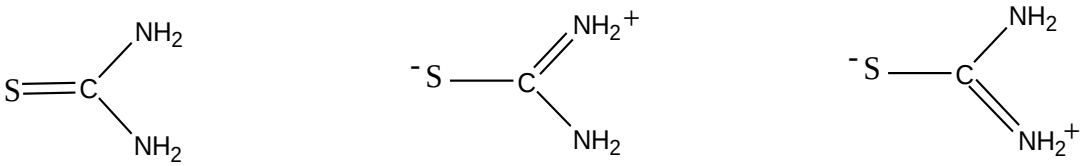

1 2 3

Figure 2.7: Canonical forms of thiourea.

Bonding through sulphur will increase the contributions from the canonical forms 2 and 3, thus decreasing the bond order of the carbon-sulphur link towards the value for a single bond whilst that of the carbon-nitrogen bond approaches the value for a double bond. Hence, in such complexes, the C-S stretching frequency should decrease and that of the C-N should increase. If on the contrary, a nitrogen-metal bond is formed, the opposite effect is to be expected. Furthermore, the N-H frequency should decrease if the metal is coordinated through nitrogen, while increases or remain substantially unaffected if the bonding is through sulphur.

(b) NMR spectral analysis

Beside infrared spectroscopy which was employed to determine the mode of ligand binding to metal, another instrument of interest which was also used for that determination is nuclear magnetic resonance (NMR). Various thiourea and its derivatives complexes (e.g., Nickel, Platinum, Cobalt, etc) were synthesized and studied through this instrument. It is also imperative to mention that temperature and solvents are some of the vital features that influence the shift or splitting of proton resonances when NMR is employed. In their studies of thiourea and its derivatives, Eaton and Zaw [32] reported that each spectrum show one N-H resonance at room temperature, while two resonances were observed at low temperature. The CH_3 behave in a parallel resonance. Methylthiourea, dimethylthiourea and diethylthourea all showed doubling of the alkyl resonances at low temperatures, tetramethylthiourea showing a singlet at all temperatures while 1-(1-naphthyl)-2-thiourea showed a doublet at all temperatures. The doubling of both CH_3 and N-H resonances at low temperatures was also echoed by Tompa *et al.* [33] who studied the behaviour of N-methylthiourea in a few nonpolar and polar solvents at various temperatures by NMR

technique. This study was done to determine whether hindered rotation was present in those molecules and whether any solvent interactions existed. The two NH resonances of thiourea were observed to be of the same intensity since only one resonance was present. However, in the case of methylthiourea, the two NH and two CH_3 resonances were reported to be unequal indicating that the *cis* and *trans* isomer were not equally populated. The difference becomes more marked for dimethylthiourea and still more for diethylthiourea. A model indicates that "inside" alkyl groups are likely to cause steric hindrance and that the *cis* isomer of methylthiourea would therefore be considered. For dimethylthiourea, the *cis-cis* isomer is likely to be the most stable followed by the *cis-trans*. The resonances are assigned on this basis and a similar argument applies to diethylthiourea. The situation of tetramethylthiourea showing one CH_3 resonance as stated above seemed to be analogous to the one found for the tetramethyl allyl radical [34].

In the preparation of platinum complexes from $Pt(NH_3)_2$ and substituted thioureas (methylthiourea, dimethylthiourea or tetramethylthiourea) by Rochon *et al.* [35], it was reported that all protons of methyl group shifted towards lower field (downfield) upon coordination, with the amine being more affected than thioureas. In the case of dimethylamine platinum complexion, that is synthesis from $Pt[NH_3(CH_3)_2]$ and substituted thioureas, the splitting of the peaks which was caused by steric hindrance of four bulky groups were observed. The splitting prevented the free rotation around the Pt-N and Pt-S bonds. The same reasoning was supplied for the explanation of the splitting of dimethylthiourea signals into two peaks in all complexes. Since no coupling was deduced between Pt and the methyl protons of the used thioureas, therefore the binding site of thioureas was concluded not to be through N atom, but through S atom.

(c) X-ray structural analysis

Crystallographic studies on the structures of the biological compounds have provided valuable information which has led to a better understanding of the properties of the compounds as well as to their function in life processes. These studies result in complete intramolecular and intermolecular stereochemical information. This includes configuration, conformation, bond lengths, valence angles and the system of hydrogen bond. The data required for the crystal structure can be obtained by X-ray, neutron or electron diffraction methods. To an increase extent, the structure determinations of a series of related

compounds have been planned and completed. The results of these studies are much more meaningful than an isolated crystal structure investigation, and enable us to predict the conformation of structures which have not yet been studied. For thiourea and its derivatives, an appreciable number of compounds have been studied, either as the free molecule [36, 37, 38], or as components of more complex molecules [39].

In their work, Ramnathan *et al.* [40] reported the crystal structure determinations of 1,3-diethylthiourea, 1,3-diisopropylthiourea and 1,3-diphenylthiourea. These compounds have been used before as rubber accelerators, intermediates in dye preparation and for the preparation of unsymmetrical thioureas, which are very useful agrochemical intermediates [41]. Their interest was in the molecular conformations and the details of the N–H…S hydrogen bond formation of these ligands in the solid state. They found that the N-H…S hydrogen bonds link the molecules into two dimensional networks in the case of diethylthiourea and diisopropylthiourea suitable for X-ray diffraction studies. In short, the conclusion of their studies was that a *trans-cis* configuration of the substituents leads to the formation of two dimensional layers of thiourea derivatives, while a *cis-cis* configuration leads to one dimensional chain through N-H…S hydrogen bonds. The hydrogen atoms were geometrically fixed in the case of diethylthiourea and located from different maps for diisopropylthiourea and diphenylthiourea. The large R factors for diethylthiourea and diphenylthiourea result from the partly disordered structure and/or large displacement factors [40].

Different metal atoms have been employed in the preparation of thiourea and its derivatives complexes. Dithio-alkyl compounds are widely used as collecting reagents in the flotation of the sulphide minerals. In order to shed light on the understanding of the flotation mechanism on an atomic scale, the crystal structures of alkylxanthates and diethyldithiophosphates of lead, zinc or iron have been studied. The natures of the metal metal-sulphur bonds peculiar to these systems have thus been elucidated. Following these lines, the structure analysis of diethyldithiocarbamate [$M(S_2CNEt_2)_2$], where M is commonly sodium or potassium, was undertaken in order to obtain more information on the type of coordination between the sulphur atoms and a metal atom [42].

Dithiocarbamate ligand was popularly used to prepare different complexes which were analysed through X-ray crystallography. The structure and chemistry of nickel(II)

dithiocarbamates continue to be of interest. Selvaraju *et al.*[43] reported the crystal structure of the α form of *bis*-(N,N-diethyldithiocarbamato)nickel(II). The structure has been redetermined at 290 K by single crystal X-ray method. Their report confirms that the metal, which is nickel, assumes a four coordinate square planar geometry with two isobidentate dithiocarbamate groups. Their main priority of redetermination using diffractometric data collected with Mo $K\alpha$ radiation was to obtain more accurate bond parameters. The same ligand was used by Fabiani *et al.* [44] to prepare Tellurium(II) *bis*-(diethyldithiocarbamate), $[Te(S_2CNEt_2)_2]$. Red monoclinic crystals, with four formula units in the unit cell were fromed. Their report shows the four sulphur atoms in the compound bound to tellurium with two short bonds and two long ones, while the fifth sulphur atom belonging to the centrosymmetrically related compound approaches tellurium at a distance of 3.579 (5) Å.

2.2 Nanotechnology

Nanotechnology is a big word which refers to small things. It can be seen as a recent offshoot of the semiconductor microelectronic revolution, which earlier spawned the development of microelectromechanical systems. The word nano derives from the Greek word “nanos”, which means dwarf or extremely small. This word can be used as a prefix for any unit like a second or a liter to mean a billionth of that unit [45]. The commercial needs of electronics manufactures have generated the necessity to create, understand, and control objects on even smaller scales thus giving an impetus to researchers to come up with other novel ideas. A nanometer is one billionth of meter (10^{-9} m), about one hundred thousand times smaller than the diameter of a human hair, a thousand times smaller than a red blood cell, or about half the size of the diameter of DNA. The scale of objects in the nanometer is represented by Figure 2.8.

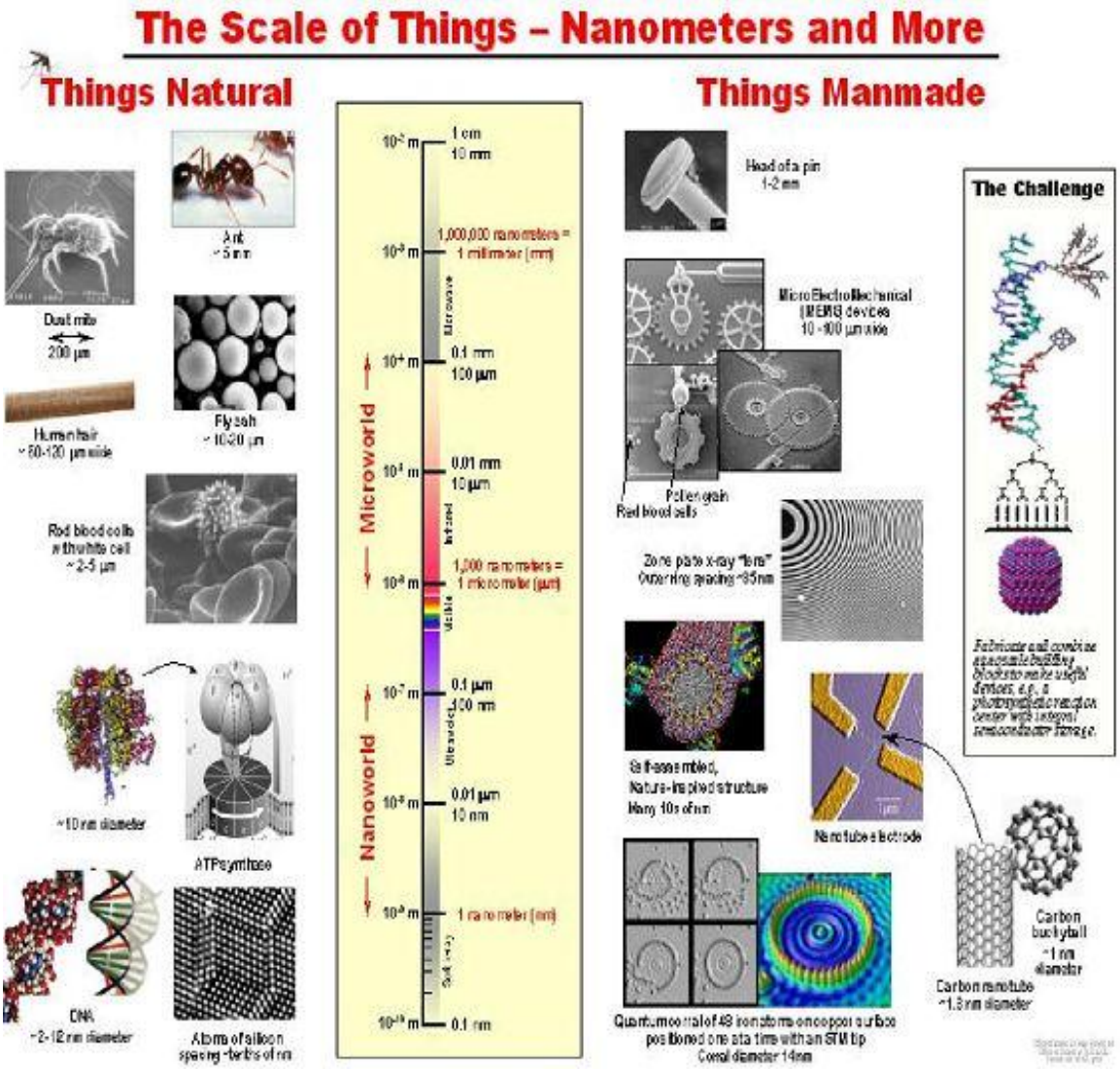

Figure 2.8: Diagram indicating relative scale of nanosized objects.

The essence of nanotechnology is the creation and utilization of materials and devices at the level of atoms, molecules, clusters and supramolecular structures, and the exploitation of unique properties and phenomena of matter at 1 to 100 nanometers. Even though nanoscopic materials have been known since several decades, e.g., colloidal particles, it is only recently that scientists have begun to comprehend the underlying principles for the assembly of macromolecules at the molecular level. To fully benefit from the advantages offered by nanotechnology it is important to understand how to build, analyze and predict the properties of nanoscopic entities [46]. In short, nanotechnology is a multidisciplinary task, bringing together chemists, physicists and biologists as well as engineers to investigate these unique opportunities.

2.3 Semiconductor nanoparticles/quantum dots

Nanoparticles are generally defined as small clusters of atoms about 1 to 100 nanometers long, while quantum dots are semiconductor nanoparticles with a diameter ranging between 1 and 10 nm range, coincident with their respective excitonic Bohr radius. Excitons have a natural physical separation between the electron and the hole which is dependant on the material. In large semiconductor crystals, the exciton Bohr radius is small compared to the size of the crystal, and the exciton is then relatively free to move around in the crystal. However, in quantum dots, quantum confinement occurs that serves to restrict the motion of electrons, holes, and excitons in 1, 2, or 3 dimensions, respectively [47]. Quantum dots of semiconductors will be useful materials for the implementation of new technologies in the 21st century. These quantum dots are formed by atoms of, e.g., group II (alkyl metals) and group VI (S, Se, and Te), They are usually synthesized using hexadecylamine (HDA), trioctadecylmethylammonium bromide (TODAB), trioctylphosphine oxide (TOPO) and trioctylphosphine (TOP) as ligands, which make them soluble in organic solvents such as toluene and chloroform [48, 49]

Quantum dots were also prepared from elements of group III-V (InP, GaAs) and VI (Si). However, group II-VI, which are more ionic compared to III-V, has been dominating in the past decades. These compounds of group II-VI have been successfully synthesized at low temperatures, whereas III-V semiconductors have not. Although materials of group III-V were reported to be stable than materials of group II-VI, not much was done because they were found to be more difficult to synthesize [50]. Investigated of quantum dots over the past few years has been motivated by a desire to reach a fundamental understanding of several of their specific optic, electronic, catalytic properties and by the wealth of potential applications involving the use of these materials, ranging from electronic devices to in vivo cellular imaging [51]. These properties emerge from the high-surface-to-volume ratio present in nanoparticles. Quantum dots can be made to emit fluorescent light in the ultraviolet to infrared spectrum just by varying their size. The wavelength of fluorescence of the quantum dots depends on its energy gap (i.e. the difference between the excited and the ground state) which is determined by the size of the QD [52]. By judiciously controlling the growth conditions, the size, and even the shape of II–VI, nanocrystals can be easily tailored. The ability to control these parameters has a profound impact in material science since it can be harnessed for engineering assemblies of nanometer scale units with novel

characteristics [53, 54]. The shape of nanocrystals plays a crucial parameter in the determination of their properties. The shape of nanocrystals can be simply classified by their dimensionality. Different morphologies of the nanocrystals have been reported before. Figure 2.9 illustrates the basic geometrical motifs of inorganic nanocrystals: Zero dimensional (OD) isotropic spheres, cubes, and polyhedrons; 1D rods and wires; and 2D discs, prisms, and plates [55, 56].

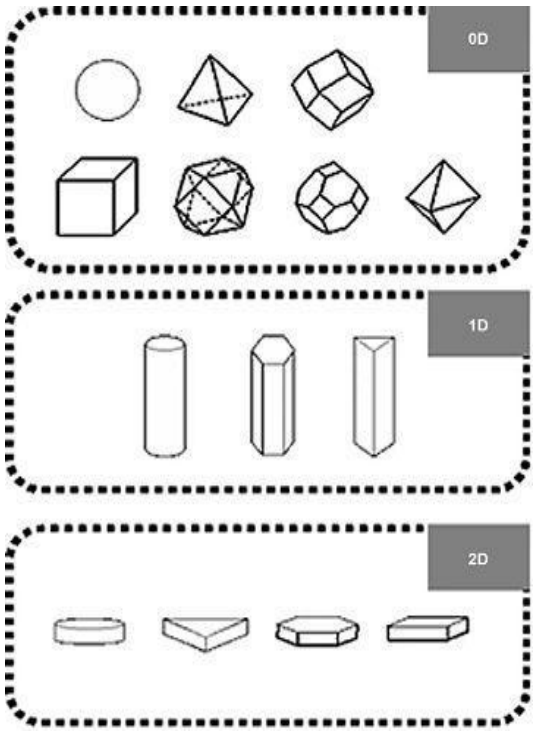

Figure 2.9: Basic motifs of inorganic nanocrystals: 0D spheres, cubes, and polyhedrons; 1D rods and wires; 2D discs, prisms, and plates.

In the past decades, as stated above, much work on semiconductor nanoparticles using different metals e.g., Cd, Zn, Co and chalcogenides e.g., S, Se, Te has been reported. Below is an exploration of some examples of semiconductor nanoparticles (CdS, CdSe, CdTe, ZnS, CoS) used before:

(i) CdS, CdSe, CdTe and ZnS nanoparticles

As stated above, the most popular quantum dots are materials of group II-VI elements such as CdS, CdSe, CdTe and ZnS which recently can be synthesized in an astonishing variety of shapes and sizes for a wide range of applications [57, 58]. However, the preparation of

CdTe quantum dots is more complicated than CdS and CdSe because Te is very sensitive to oxygen [59]. The band gaps of bulk CdS, CdSe and CdTe materials are 515 nm (2.41 eV), 712 nm (1.74 eV) and 861 nm (1.44 eV), respectively. There are differences between the above nanocrystals as compared to their bulk materials as stated above. Bulk inorganic crystals possess their own characteristics and innate properties, such as color and melting point, while at the nanometer scale these properties can be tailored as desired. For example, CdSe semiconductor crystals have characteristic red luminescence, however, on the sub 10 nm scale their luminescence can be tuned continuously from red to blue [60, 61, 62].

One of the unique properties of the semiconductor nanocrystals is their band gap increase with decreasing particle size due to carrier confinement effects, which was first reported by Ekimov and Onushchenko in 1982 when they observed sharp and discrete absorption peaks in CuCl nanocrystal embedded in a transparent insulating matrix [63]. ZnS is among the oldest and probably the most important material with a relatively high direct band gap (3.68 eV) [64, 65], strong fluorescence, and resistance to high electric field [66] and therefore has potential applications in areas such as solar cell and infrared windows, laser and displays [67]. ZnS has also been used as a pigment, in water purification, electroluminescence and non-linear optical devices. ZnS nanocrystals can also be used as effective catalysts for photocalytic evolution of H_2 and photoreduction of toxic ions under visible-light irradiation [68]. However, an important application of ZnS is as a photocatalyst in environmental protection through the removal of organic pollutants and toxic water pollutants. They have also been used for the photocatalytic degradation of organic pollutants such as dyes, p-nitrophenol, and halogenated benzene derivatives in wastewater treatment [69]. Nevertheless, the applications of ZnS NCs in photocatalysis are limited to a considerable degree because of the high cost of their large-scale production, coupled with the tremendous difficulties in separation, recovery, and recycling in industrial applications.

More work on ZnS quantum dots focused on challenges in exploring the preparation route capable of stabilizing such small crystallite sizes and which also maintain a narrow size distribution. Hence, much effort has been devoted to the development of methods for the synthesis of small ZnS particles of various controllable sizes, while overcoming the challenge of preventing their rapid self-aggregation. Successful routes include synthesis in capping agents and many more [70, 71]. Diameters were achieved which, with increasing the size up to the bulk material, exhibit a monotonic red-shift of the absorption band in the

near UV from 230 to 340 nm. The low exciton Bohr radius (2.5 nm) of ZnS also makes its nanoparticles interesting as small biomolecular probes for fluorescence and laser scanning microscopy [72]. Photophysical properties of ZnS nanoclusters have been studied by Kumbhojkar *et. al.*[65], where the quantum size effect has been clearly observed. They reported a significant effect of capping agents on optical properties demonstrated through variations of the emission peak energies of ZnS nanoclusters with different capping agent. It was also found that uncapped ZnS nanoclusters have their excitonic peak located at higher wavelengths. Moreover, the capping agents further stabilize the nanocrystals. This is because at higher temperatures, the surfactant molecules are dynamically adsorbed to the surface of the growing crystal where they provide access sites for the addition of monomer units to the growing nanocrystal and at the same time preventing their aggregation. At low temperatures the surfactant are strongly bound to the surface of the nanocrystals where they provide solubility in organic solvents [73]. The effect of the capping agents or surfactants on quantum dots will be explained in detail in this chapter.

(ii) CoS nanoparticles

Cobalt sulfide is material that is composed of elements of group VIII and VI. This material has been reported to be of interest because of their magnetic properties, especially in the fabrication of diluted magnetic semiconductors. It is also one of the most complicated metal sulfides, which has a number of phases and chemical compositions [74]. However, besides its complication, it is a material known to be of importance especially because their chemical bonds Co-S have several forces and binding mechanisms that can form ionic bonds, covalent bonds and metallic bonds which are bound in a molecule. As stated above, diverse cobalt sulfide material exists in several phases, such as Co_4S_2, Co_9S_8, CoS, $Co_{1-x}S$, Co_3S_4, Co_2S_3, and CoS_2, which have attracted great attraction in virtue of their excellent properties and potential application for hydrodesulfurization catalysts, magnetic devices and hydrodearomitization in many industrial fields [75, 76]. Cobalt sulfide compounds have been employed in serving as a low-cost replacement for the state-of-the-art EC material RuO_2 in electrochemical capacitors and as a negative electrode material for rechargeable lithium batteries [77]. Pyrite CoS_2 is metallic solid material which displays ferromagnetic properties, with a Currie temperature of 120 K and has fundamental physics in spintronics and potential applications in spin-electronic devices due to their open bands containing electrons with a single spin state [78, 79, 80, 81]. Although the shape control studies are

actively being pursued on the semiconductor and metal nanoparticles, only a little work has been reported on cobalt sulfides. The challenges for shape-controlled synthesis of cobalt sulfides can be caused by the stoichiometry of cobalt sulfides, which is much more complicated than that of cobalt oxides because of the coexistences of strongly reducible cobalt ion and oxidizable sulphide ion. In addition, cobalt ion has a very strong affinity to oxygen. It is not easy to exclude cobalt oxide or cobalt hydroxide impurities from the resultant materials. Another but not the last challenge is that the reaction temperature needs to be well-controlled because of the complicated phase diagram of cobalt sulfides. Recently, synthesized CoS and CoS_2 nanoparticles [82, 83], Co_3S_4 nanotubes [84], and hollow structured Co_9S_8 [85] have been reported. However, few of them have well-defined morphology.

2.3.1 Advantages of semiconductor nanoparticles/quantum dots

Semiconductor quantum dots (QDs) with superior optical properties are a promising alternative to organic dyes for fluorescence-based bioapplications. For the effective use in such applications, nanoparticles have to be uniform in size, shape and crystallinity [86]. QDs have been shown to be more stable than a number of organic dyes [87], including Alexa488, reported to be the most stable organic dye [88]. Although organic dyes have been widely used as fluorophores in biomedical imaging and detection, they are known to have a number of drawbacks, that is, they are vulnerable to the physiological environment, quickly photobleached under normal imaging conditions (e.g., rhodamine B underwent photobleaching in 10 minutes, compared with 4 hours for CdSe quantum dots), and also found not to be good for multicolor imaging because of two inherent properties, i.e., (i) organic dyes have relatively broad emission spectra (Figure 2.10), meaning the spectra of different dyes may overlap to a large extent; and (ii) one organic dye can only suitably excited by the lights within a certain narrow wavelength range and it thus needs nearly the same number of excitation light sources as the dyes used [89]. Use of organic dyes has proven to be difficult. It is difficult to label proteins with organic dye fluorophores because sufficient technical expertise and experience is required to inject the biolabels at the microscopic level with minimal damage to the object of the tag. Targeting specific proteins in vivo is also difficult with organic dyes. Biological materials can also be highly fluorescent and when organic dyes are attached, there is difficulty in resolving them from background fluorescence. Most organic dyes are not chemically stable, and this result in

decay of fluorescent properties. Therefore, organic dyes are usually stored in the dark at refrigerator temperatures (ca. 4 ^{o}C). Since large amounts of chemical dyes are often required, poisoning of the cell may result.

Such disadvantages have widely prompted scientists to use quantum dots in order to find solutions. Unlike organic dye molecules, quantum dots are very attractive as biological labels, because of their small size and emission tunability. Quantum dots can be excited by any wavelength above its band gap with built-in tunability and they have a high number of photons and can give high luminescence intensities [90].

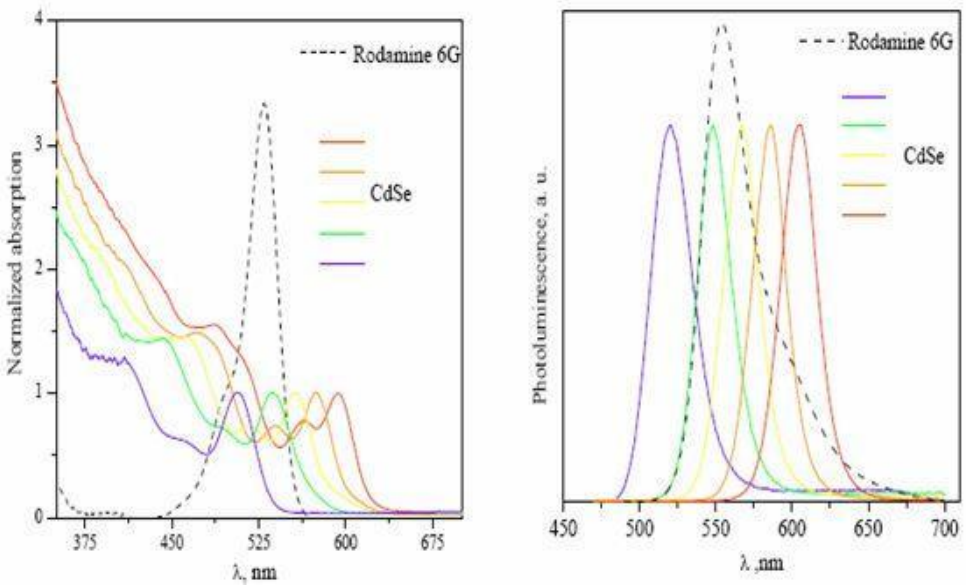

Figure 2.10: Comparison of the absorption and emission characteristics of CdSe nanoparticles of different size and the organic dye Rodamine-6 G.

They are also less sensitive to environmental changes and have lower rates of photodegradation, allowing long term experiments. Quantum dots have a longer photoluminescence lifetime (20-50 ns) compared to conventional organic fluorophores and thus make it easier to trace the drug delivered in living organisms [91, 92]. Narrow and symmetric emission spectra, which can be controlled in a relatively simple manner by variation of core size and composition, variation of surface coating and broad absorption spectra for quantum dots are further advantages of nanoparticles (Figure 2.10).

2.3.2 Manipulation of size and shape of nanoparticles

Considerable progress has been made on determining factors that influence the size of the nanoparticles [93]. In relation to these studies, there has also been a drive to synthesize nanoparticles of various shapes. The morphology of the particles, for example, whether they are spherical-, rod-, tetrapod-, or hexagonal-shaped will have an effect on their electronic, magnetic, catalytic and electrical properties and also influence the self-assembly process [94]. It is anticipated that nanocrystals with unique shape-dependent properties will be important for development of new materials for the biomedical and electronic applications [95].

More extensive reports have been published in the past few years [96] demonstrating that by changing the reaction conditions, that is, the concentration of the starting materials, the nature of the solvents, and the suitable capping/stabilizing agents, it is possible to synthesize a variety of nanocrystallites with different sizes. In most of these synthetic methods, one uses a capping agent which covalently binds to the surface atoms of the nanocrystallite and, thus, prevents them from forming a microscopic bulk material. This stabilizes the nanocrystallites, making it possible to extract them as free-standing powders. The ability to extract such particles in a powder form which is stable under atmospheric conditions and the solubility of these nanocrystallite powders in suitable solvents for the purpose of making thin films without disrupting the integrity of the nanocrystals are two important factors for any real technological application of these nanocrystallites [97].

2.3.3 Synthetic techniques for semiconductor nanoparticles

The synthesis and properties of semiconductor quantum dots have been reviewed by several authors [98, 99]. Chemical synthesis allows the manipulation of matter at the molecular level. Due to its versatility in synthesizing nanoparticles and the feasibility in controlling the particle size, shape, and size distribution, many methods have been developed for the synthesis of II-VI semiconductor nanoparticles [100, 101, 102]. Importantly, it is imperative to emphasize that an ideal method should result in pure, monodisperse, crystalline particles which are reasonably stable to preserve their properties.

(a) Colloidal method

The colloidal route was the first reported method used to synthesize small particles and involves controlled precipitation reaction in a homogenous solution. Colloidal semiconductor nanocrystals are synthesized from precursor compounds dissolved in solutions, much like the traditional chemical processes. The synthesis of colloidal semiconductor nanocrystals is based on a three-component system composed of (i) precursors, (ii) organic surfactants, and (iii) solvents. When heating a reaction medium to a sufficiently high temperature, the precursors chemically transform into monomers. Once the monomers reach a high enough supersaturation level, the crystal growth starts with nucleation process. The temperature during growth process is one of the critical factors in determining optimal conditions for the nanocrystal growth. It must be high enough to allow for rearrangement and annealing of atoms during synthesis process while being low enough to promote crystal growth. Another critical factor that has to be stringently controlled during nanocrystal growth is the monomer concentration. The growth process of nanocrystals can occur in two different regimes, "focusing and defocusing". At high monomer concentrations, the critical size (the size where nanocrystals neither grow nor shrink) is relatively small, resulting in growth of nearly all particles. In this regime, smaller particles grow faster than large ones (since larger crystals need more atoms to grow than small crystals) resulting in "focusing" of the size distribution to yield nearly monnodisperse particles. The size focusing is optimal when the monomer concentration is kept such that average nanocrystal size present is always slightly larger than the critical size. When the monomer concentration is depleted during growth, the critical size becomes larger than the average size present, and the distribution "defocuses".

Summing up this route, Johnson and LaMer [103] proposed that if seeds (nuclei) could be made to grow into larger particles in a controlled manner, monodisperse particles could be formed. It must be understood that the particles were typically micrometric by that time. Further, if nucleation and growth are properly controlled, particles with dimensions of the order of nanometers can be reproducibly synthesized. Nanocrystals, which are less stable, dissolve and then recrystallize on larger ones that are more stable. This process is known as Ostwald ripening [102]. The above stages will be discussed in detail later under sub-heading "General growth mechanism of nanocrystals". The colloidal route is one of the good methods used for the preparation of nanosized semiconductor particles. Advantages of

employing this method is that large batches of quantum dots may be synthesized and it is acknowledged as one of the least toxic route for the synthesis of quantum dots. However, some shortcomings of this method is that it cannot be employed to easily synthesize some types of semiconductors like CdSe, GaAs, InP, and InAs and the instability of colloids at high temperatures makes annealing of the particles difficult, which leads to poor crystalline materials being formed 104].

(b) Growth-in-confined matrices

This is a popular method that was employed for nanodimensional particles. It requires the use of confined matrices such as zeolites [105], layered solids [106], molecular sieves [107], micelles [108], gels [109], polymers [110] and glasses [111]. However, although this method is popular, it carries its own disadvantages. Degradation of the host upon nanoparticle formation and particle size restriction due to the host structure are some of the problems associated with this method of synthesis [104].

(c) Single-source precursor method

Considering that the ideal method should give pure, monodisperse, crystalline particles that are stabilized from the surrounding chemical environment by a capping agent, Murray *et al.* [62] described the precursor method which became popular for the preparation of high quality, crystalline and monodisperse nanoparticles. This method helped in overcoming the problems that were encountered by the use of colloidal route by making use of organometallic and/or metal organic compounds under anaerobic conditions. Some of the examples of the high quality, monodisperse crystalline nanoparticles that were prepared by this route include CdSe, CdS and CdTe.

The preparation of CdSe was achieved by using a harzadous metal alkyl (dimethylcadmium) and a chalcogen source TOPSe (tri-n-octylphosphine selenide oxide), which is a polar coordinating lewis base solvent. Injection of the solution into hot TOPO in the temperature range of 120 ^{o}C to 300 ^{o}C yielded highly dispersed (± 5 %, Figure 2.11) TOPO capped nanocrystallites of CdSe. One of the most important features in the control of the particles size distribution is the temperature at which the synthesis is undertaken, with

larger particles being obtained at high temperatures, while lower temperatures yielded smaller particles.

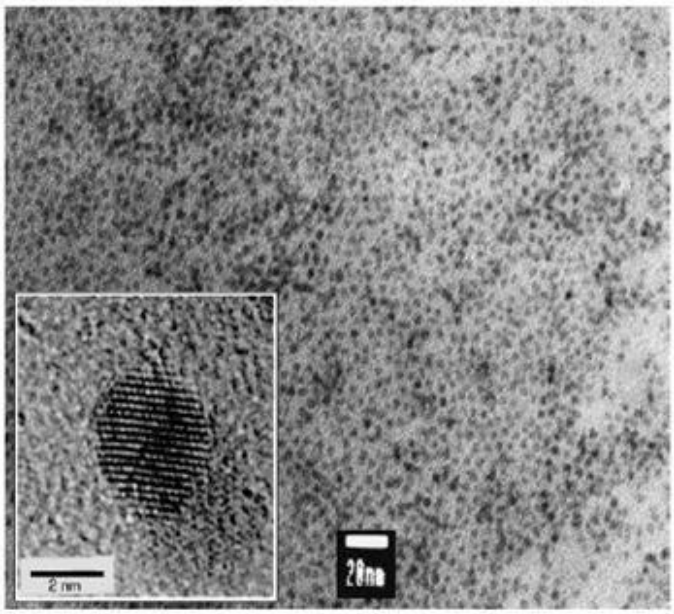

Figure 2.11: TEM image of TOPO capped CdSe nanoparticles; inset, HRTEM image.

Although this method was found to produce highly monodispersed particles, which is one of the requirements of semiconductor quantum dots, the use of dimethylcadmium still posed some danger because of its hazardous status. To avoid this problem, a method similar to those used to produce thin films by MOCVD was used. This method, which is known as single source precursors, i.e., a single compound containing all elements required within the nanocrystallite, is useful. It was used to synthesize TOPO capped semiconductor nanoparticles like CdSe, CdS, ZnS and many more. In short, there are a number of potential advantages of using single-source/molecular precursors over other existing routes, such as (i) Low temperature deposition routes are possible, (ii) Single source routes avoid the need for volatile, sometimes toxic and/or pyrophoric precursors, (iii) Some II-VI and III-V nanoparticles are air sensitive. All precursor synthesis is carried out under anaerobic conditions, with the resulting precursors being air and moisture stable, (iv) One involatile precursor is involved, purification of which is easier than that of two or more volatile precursors, and hence there is less chance of the incorporation of impurities into the nanoparticles, (v) although there are theoretical models predicting the optical properties of semiconductor nanoparticles, the properties of nanoparticles obtained by new synthetic

routes are sometimes hard to anticipate and may lead to particles with and unanticipated, but useful, properties [86, 112, 113].

2.3.4 General growth mechanism of nanocrystals

The mechanism for growing nanocrystals is divided into parts, that is; (i) nucleation, where nanocrystals spontaneously form through an assembly of freely dispersed atoms and (ii) the actual growth process.

(a) Nucleation

Nucleation is the first step in the growth of any sort of nanocrystals. Though a density fluctuation of the medium several atoms assemble to a small crystal that is thermodynamically stable, and thus does not decay to free atoms or ions. In that sense the nucleation can be understood as the overcoming of a barrier.

The nucleation in a solution at constant temperature and pressure is driven by the difference in the free energy between two phases. In simple terms the driving forces in the nucleation event can be reduced to two, that is, the gain in the chemical potential and the increase of the total surface energy. The gain in the chemical potential can be understood as the energy freed by the formation of the bonds in the growing crystal. The surface term takes into account the correction for the incomplete saturation of the surface bonds. Upon formation of a spherical nucleus consisting of number of atoms (n), the total free energy of the system changes by the value

$$\Delta G = n(\mu_c - \mu_s) + 4\pi r^2\sigma \quad \text{(eq. 2.1)}$$

where μ_c and μ_s are the chemical potentials of the nanocrystalline phase and the solution, respectively, r is the radius of the nanocrystal or nucleus while σ is the surface tension. In the above equation, the surface term constitutes the main difference between nanomaterials and bulk crystals. Bulk material is dominated by volume effects and thus the surface energy term (eq. 2.1) can be neglected whereas in nanocrystals a non-negligible portion of atoms might be situated on the surface and thus this term is of importance. The surface tension in the above equation is assumed to be constant for any size and morphology of the crystal,

which is a very rough approximation. This uniformity of the surface tension refers to the model of the nucleation. In a more detailed discussion one would have to take into account an effect related to the small size of the defined crystalline surface. One can gain a qualitative understanding of the size effect, when considering the surface tension as a result of the interaction between the surface atoms and the bulk of the crystal. It is evident that this interaction is actually weaker for smaller crystallites as there are no long range interactions. It has been calculated that under the assumption of Lennard-Jones interaction between the atoms the total surface energy of a cluster of 13 atoms is reduced by 15 % with respect to the total surface energy of a flat surface [114]. In nanocrystals, the effect of the presence of facets on the total surface energy is related to the precise arrangement of the atoms on the individual facets. Between different facets the densities of atoms vary and also the arrangements of the dangling bonds. One can assume that in general those facets which exhibit a closer packing of the atoms and a smaller number of unsaturated bonds are more stable, and thus have a lower tension. In case where a spherical shape for the nanocrystals is assumed while neglecting any variation of the surface tension, the number of atoms in the first term of eq. (2.1) is expressed by the radius of the nanocrystals, taking into account the density dm of atoms in the nanocrystals. Then the equation reads:

$$\Delta G = 4\pi\, dm/3\ r^3(\mu_c - \mu_s) + 4\pi r^2\sigma \quad \text{(eq. 2.2)}$$

In case where the chemical potential of an atom in the solution is smaller compared to that of an atom within the crystal, the minimum of the free energy is given when all atoms are unbound, and so no stable crystals are formed. In this part the interest is in the opposite case with the chemical potential atoms in solution being larger that that of bound atoms. In that case the first term becomes negative, and thus the free energy reaches a maximum for a certain radius r_c, termed initial size, at which a nucleation barrier is imposed (eq. 2.2). For small nuclei the surface energy term dominates the free energy, whereas only for a much larger r_c the growth is driven by the gain in chemical potential and in principle the crystal can grow to an infinite size. The amplitude of the nucleation barrier controls the rate at which crystals nucleate [115].

(b) Growth

The actual process of the deposition of monomers onto the growing nanocrystal can be split into two steps. Firstly, the monomers have to be transported towards the surface of the nanocrystal and secondly, the monomers have to react with the nanocrystal. Generally, the first process is accomplished through diffusion and thus at a rate dominated by the diffusion constant (D), whereas the speed of the second process is given by the rate of reaction between free monomers and the crystal surface. The discussion of the dynamics of the growth process begins from a mechanistic view of the growth in which the growth rate $\dot{r} = dr/dt$ of a crystal. This latter rate is simply the time derivative of the number of monomers in the crystal and it describes the number of monomers that go through the two processes mentioned above (diffusion and reaction) during a unit of time. The growth rate ($\dot{r}$) can be written as

$$dr/dt = \dot{n}/4\pi r^2 d_m \quad \text{(eq. 2.3)}$$

In the above equation d_m denotes the density of monomers in the crustal, thus the increase of the volume occupied by one monomer. The last equation is the time derivative $\dot{n} = dn/dt$ of the number of monomers in the crystal solved for the growth rate. Following is the discussion of how the deposition rate of monomers ($\dot{n}$) behaves:

In atypical synthesis, an excess of free monomers is injected to initiate the growth process. Under these conditions the effect of the diffusion process can be virtually neglected due to the high concentration of monomers. Monomers are available whenever there is a free site for their incorporation into a growing crystal. In this case the incorporation rate depends only on the rate of the reaction monomer crystal. This rate is proportional to the surface area of the crystal. Therefore the growth rate in eq. 2.3 is independent of the radius of the crystal. This growth regime is called reaction controlled growth and it is vital only at very high concentrations of monomers. In this regime the width of the size distribution (Δr) does not vary with time. Only the relative width decreases with time. After a while the reservoir of monomer is partially depleted and the growth rate is dictated by the rate at which monomers reach the surface of the crystal [116].

The Gibbs-Thompson effect simply introduces a competing effect to the growth [115]. Crystals or particles in general, have a higher vapour pressure the smaller they are, and thus monomers evaporate into solution more easily from smaller particles than from larger ones. Due to the increased surface curvature, the surface atoms are more exposed to the surrounding while experiencing a weaker binding strength to the smaller particle core. Experimentally, the Gibbs-Thompson effect is observed in the lower melting temperature of smaller nanocrystals [99, 117]. The vapour pressure of a crystal of radius can be obtained by calculation by employing the Gibbs-Thompson equation (eq. 2.4),

$$S_r = S_b \exp(2\sigma V_m / rRT) \quad \text{(eq. 2.4)}$$

Where S_r and S_b are the solubility of the nanocrystal and the corresponding bulk solid, Vm is the molar volume of the material, R is the gas constant and T is the temperature.

The employment of gas equation leads to vapour pressure being expressed as the concentrations of monomers in the vicinity of the surface (eq. 2.5),

$$C_i = C_\infty \; 2\sigma / e^{rdmkBT} \approx C_\infty \; (1 + 2\sigma / rdm^k B^T) \quad \text{(eq. 2.5)}$$

where, C_∞ is the vapour pressure of a flat surface, σ is the surface tension. Formally, the same reasoning is applied to the concentration C_b. The radius of a crystal in equilibrium with the concentration of monomers in the bulk is introduced as the critical size r* of the growth process

$$C_b = C_\infty \; 2\sigma / e^{r^*dmkBT} \approx C_\infty \; (1 + 2\sigma / r^*dm^k B^T) \quad \text{(eq. 2.6)}$$

Combining the above two equations, growth rate can be calculated as

$$dr/dt = 2\sigma D C_\infty / d^2_m k B^T \; 1/r \; (1/r^* - 1/r) \quad \text{(eq. 2.7)}$$

The critical size r* is characterized by a zero growth rate, as a crystal of the size is in equilibrium with the solution. Nanocrystals smaller than a critical size have negative growth rates (dissolve), while larger ones grow at rates dependent strongly on size. It thus

becomes evident that the quantity r* is actually equal to the critical size r_c that characterizes the position of the energy barrier in the nucleation event.

The general dependence of the growth rate on the radius of the crystal is illustrated in Figure 2.12. It is interesting to note the presence of a maximum at a radius of 2r*. If all crystals present in the solution have a radius larger that this value, the smallest crystal grow fastest, and therefore the size distribution becomes narrower over time. The value of r* depends mainly on the overall concentration of free monomers, but also on the reaction temperature and on the surface tension.

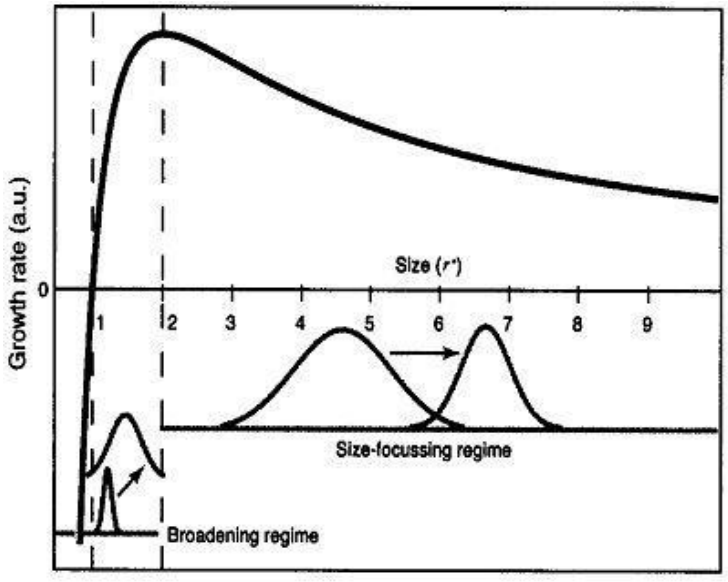

Figure 2.12: Sketch of growth rate of nanocrystal versus critical size, according to model of Sugimoto [116].

During the reaction the concentration of monomers decreases and the critical size shifts to higher values. If the critical size is sufficiently small the system is said to be in the narrowing or size focussing regime. During the run of the synthesis the critical size increases and as soon as the size of maximal growth rate, that is 2r*, has reached a value situated in the lower end of the size distribution of the nanocrystal, the system enters in the broadening regime. Finally, when r* is larger than the radius of smallest nanocrystals present, the system enters into the Ostwald ripening regime, which is characterized by a large broadening of the size distribution and, more importantly, by a decrease of the total concentration of the nanocrystals. The smallest nanocrystals melt to free monomers that are incorporated into the large nanocrystals. In an experiment the effect of the size focussing is limited by the broadness of the initial size distribution. In other words, the nucleation event

has a strong influence in the size distribution of the final sample. Ideally, the nucleation event should be finished well before the system enters into diffusion controlled growth regime. The sharpness (in terms of time duration) of this event is therefore of great importance [118]. If on the contrary the nucleation event spans a considerable amount of time, those nanocrystals that nucleated first have grown already too far, resulting in a broad size distribution. In that case the effect of size focussing might not be sufficient to obtain a reasonably narrow distribution at the desired average size of the nanocrystals. The limiting factor in this case is that the size focussing is always accompanied with an overall growth of all nanocrystals.

In the case of fluorescent nanocrystals, the width of the fluorescence spectrum is a good indicator for quality of size distribution. In some synthesis schemes it is inevitable to consume the reservoir of monomers and thus obtain a broadening of the fluorescence band. In these cases the system can be maintained in focussing by repeated injections of fresh monomers [62, 119]. Experimentally it is not always possible to obtain a perfect size distribution. In some cases the distribution is broadened or shows several distinct peaks. A possible, but somewhat laborious way to improve size distribution is to perform a size-selective precipitation after the synthesis is completed. In order to do so, a non-solvent is added slowly in a controlled way. As an example the addition of the polar solvent methanol to nanocrystals dissolved in a non-polar solvent such as chloroform or toluene promotes the precipitation of the nanocrystals. The large particles become unstable in the solution at lower concentrations of the non-solvent than the smaller particles, and thus they precipitate first [120]. This process has been successfully applied in the synthesis of CdTe [121] and CdSe [62].

2.3.5 Properties of nanoparticles

Nanoparticles are of great scientific interest as they are effectively a bridge between bulk materials and atomic or molecular structures. The physical and chemical properties of semiconductor quantum dots differ from bulk semiconductors. A bulk material should have constant physical properties regardless of its size, but at the nano-scale this is often not the case. Size-dependent properties are observed such as quantum confinement in semiconductor particles, surface plasmon resonance in some metal particles and supermagnetism in magnetic materials. The following section gives a description of the

properties of nanoparticles such as optical, electronic and photoluminescence.

(a) Optical properties

An important parameter of a semiconductor material is the width of the energy gap that separates the conduction from the valence energy bands (Figure 2.13a). In semiconductors of macroscopic sizes, the width of this gap is a fixed parameter, which is determined by the material's identity. However, the situation changes in the case of nanoscale semiconductor particles with sizes smaller than ~10 nm (Figure 2.13b). This size range corresponds to the regime of quantum confinement for which electronic excitations "feel" the presence of the particle boundaries and responds to changes in the particle size by adjusting their energy spectra. This phenomenon is termed quantum size effect, whereas nanoscale particles that exhibit it are often referred to as quantum dots. Quantum size effects have been observed experimentally for many nanocrystalline semiconductors [122, 123]. In addition to quantum size effects, coating nanoparticles with different materials is a preferred way of controlling the dimensions of the bandgap of nanoparticle quantum dots [124]. The optical absorption spectrum of a nanocrystallite semiconductor provides an accessible and straightforward method for the evaluation of quantum size effects. The absorption of a photon, leading to excitation of an electron from a valence band to the conduction band, is associated with the band gap energy (Eg). The absorption of photons with energy similar to that of the band gap, $h\upsilon = Eg$, leads to an optical transition producing an electron in the conduction band of the semiconductor along with a hole in the valence band. Absorption of photons with energy much greater than Eg leads to excitations above the conduction-less processes. The absorption (A) of light by a semiconductor material with thickness l can be expressed by an expression analogous to the Beer law (eq. 2.8), where α represents the absorption coefficient of the solid and is a function of the radiation frequency.

$$A = \alpha l \quad \text{(eq. 2.8)}$$

All electronic transitions are subject to selection rules: for semiconductors the requirements (beside $h\upsilon = Eg$) are that the wave vector, K, should be conserved. K_{photon} is small when compared with the wave vectors of the electron before (K_e) and after excitation (K'_e) (eq. 2.9).

$$K_e + K_{photon} = K'_e \quad \text{(eq. 2.9)}$$
$$K_e = K'_e$$

The absorption coefficients for a photon of a given energy (eq. 2.10) is proportional to the probability (P_{if}), the density of states in the initial state (n_i), and the density of available final state (n_f). This process must be summed for all possible transitions between states separated by an energy difference equal to the energy of the incident photon.

$$\alpha(h\upsilon) \propto \Sigma P_{if} n_i n_f \quad \text{(eq. 2.10)}$$

Semiconductors in which there is conversion of the wave vector for optical transitions are referred to as direct band gap semiconductors and have large absorption coefficients. A useful expression relating the absorption coefficient and the photon energy of a direct transition near the threshold is given by eq. 2.11 [125]. Semiconductors where lowest electronic transition, between the valence band and the conducting band, is formally forbidden are said to have an indirect band gap and normally have small absorption coefficients.

$$\alpha(h\upsilon) \propto (Eg - h\upsilon)^{1/2} \quad \text{(eq. 2.11)}$$

The energy gap of a quantum dot depends on the size of the dot. The larger the size is, the lower is its absorption and fluorescence energy (red shift). The smaller the dot is, the higher is its absorption and fluorescence energy (blue shift). There are two ways that can be used to determine the band gap energy (eV) of the prepared nanocrystalline semiconductor. One easy way is to experimentally estimate it from the spectrum, with the second one being achieved by calculation. Both methods agree that a shift to lower wavelength of the prepared semiconductor nanoparticles, as compared to the bulk materials gives a measure of the finite size of the particle [47].

There are special phenomena that are used to define nanoparticles of certain sizes. Some of those properties are higher stability and larger gap. These properties are very important since they play a crucial role in differentiating semiconductor nanoparticles from bulk semiconductors. The correlation between band gap size and particle stability was explained

by simple bonding descriptions in which the highest occupied molecular orbital and lowest unoccupied molecular orbital gap give a measure of the orbital overlap. However, the above mentioned statement was found to be true only for nanoparticles prepared from group II-IV [126]. In their work, Brus *et al*. [127] differentiated small particles from bulk semiconductor particles by stating that the band gap of small particles is greater than that of the bulk semiconductors. Band gap of the nanoparticles can simply calculated from eq. 2.12,

$$E = hc/\lambda \qquad \text{(eq. 2.12)}$$

where E is the band gap energy, h is the planck's constant, c is the velocity of light and λ is the absorption edge in reflectance spectra [128].

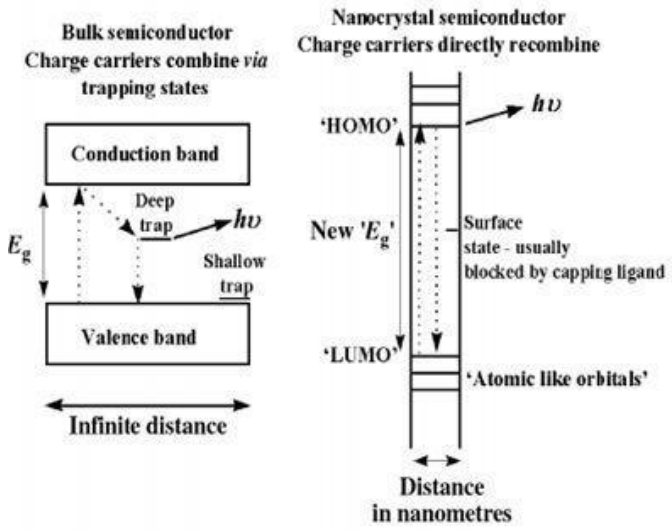

Figure 2.13: Spatial electronic state diagram for bulk semiconductor (a) and nanoparticles (b), after report by Brus and coworkers [127].

In summary, quantum size effect, which is also confinement effect, can be described using a simple "quantum box" model. In addition to the increasing energy gap, quantum confinement leads to a collapse known as quantum of the continuous energy bands of the bulk material into discrete, "atomic" energy levels.

(i) Absorption and emission properties of semiconductor nanoparticles

The luminescence spectra of nanocrystalline semiconductors are known to shift to lower energy or higher wavelength in emission as compared to the corresponding absorption spectra as seen in Figure 2.14. However, the ideas that have been used to understand these phenomena illustrate an interesting relationship between experiment and theory. Two models were used to explain the origin of this effect. Brus [127] explained, on the basis of theoretical and experimental studies, the features expected in the luminescence spectra of quantum confinement semiconductors and finally anticipated the results of many subsequent experiments. The second model attributed the red-shifted band-edge emission observed in luminescence studies on surface-passivated CdSe quantum dots to the existence of a 'dark exciton' [129]. Photoluminescence spectra play an integral part in complimenting the absorption spectra in semiconductor nanoparticles. It is interesting to know that it can be successfully used in the determination of the size dependent electronic structure [65].

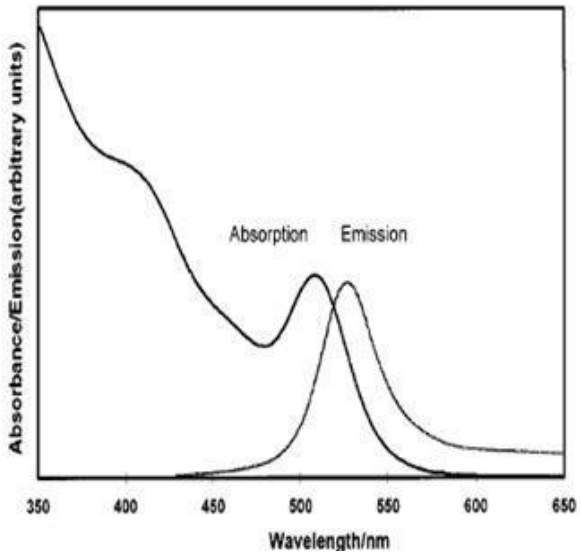

Figure 2.14: Electronic and photoluminescence spectra of TOPO-capped CdSe nanoparticles.

2.3.6 Role of the capping agents on semiconductor nanoparticles

There is a difference between quantum dots that are coated or passivated with organic or inorganic materials and those that are not coated. Their difference can be determined from their absorption spectra, emission spectra and also with the confirmation of the sizes of

their particles through transmission electron microscopy, and etc. It is therefore imperative that quantum dots be coated for stabilization. A poorly capped surface of a quantum dot, characterized by the presence of electron and/or hole traps, plays a significant role in the luminescence properties. It is therefore essential to carefully control the surface defects along with the size of a dot in order to obtain the desired radiative properties.

These capping agents are important in the synthesis of quantum dots in that

(a) they control the growth of quantum dots
(b) they coat dangling bonds at the quantum dot surface
(c) they protect the quantum dots from aggregation
(d) they determine solubility

Following is a brief explanation of what is meant in (a), (b), (c) and (d)

(a) Coating agents are known to have chemical group with an affinity for either cation or the anion. Under the growth conditions of the semiconductor nanocrystals the compexing properties of the coordinating molecules play a vital role. The nanocrystal grows within a shell of capping agents. The final particle size is determined by the growth kinetics. If bonding with the surface atoms of the quantum dot is too weak there will be uncontrolled growth of the semiconductor beyond the quantum size regime. If the bonding is too strong the particle growth is prohibited. However, to get quantum dots of the desired nm size the growth conditions have to be chosen such that the binding of the capping agents is neither too strong nor too weak. The growth rate, and thus the particle size, is determined by the nature and concentration of the capping agents, the growth temperatures and precursor concentrations.

(b) Since quantum dots are extremely small crystallites, the surface to volume ratio is large. At the crystal surface the periodicity of the crystal breaks down which may result in state within the band gap. These surface states act as recombination centers for the excitons by first trapping one of the charge carriers followed by radiative or non-recombination with the other charge carrier. In the case of radiative recombination an emission band is observed on the long wavelength side of the

excitonic emission band. This emission is referred to as defect emission or trap emission. Due to the large lattice relaxation involved in the trapping and recombination process, often the presence of surface states leads to non-recombination. The non-radiative losses lower the luminescence quantum efficiency and are undesirable in applications which rely on efficiently luminescing quantum dots.

(c) Semiconductor quantum dots are not a thermodynamically stable phase. There will be a thermodynamically driven tendency for aggregation of quantum dots. Capping agents play a significant part in preventing aggregation from taking place. In non-polar solvents the quantum dots are sterically stabilized by the long non-polar alkyl chains of the capping agents. In polar solvents the stabilization can also occur through charges on the capping agents.

(d) Quantum dots are soluble in different solvents. The type of solvent that can be used is determined by the capping agent used to coat the quantum dots. For example, quantum dots coated by tri-*n*-octylphosphine oxide are soluble in toluene or chloroform. This capping agent does not permit solubility in solvent like water. There are capping agents that will not permit solubility in either toluene or chloroform, for example, starch and glucose. These capping agents are known to assist quantum dots to be soluble in water.

2.3.7 Toxicity of semiconductor nanoparticles/quantum dots

Discussions of quantum dots toxicity can be confusing due to the differences QDs are being synthesized. In order to clarify or simplify this topic, it should be emphasized that not all QDs are alike. Each individual type of quantum dot possesses its own unique physiocochemical properties, which in turn determines its potential toxicity or lack thereof. In general, there are discrepancies in the current literature regarding the toxicity of QDs that can be attributed to several factors. Quantum dots contain toxic components, such as cadmium (from cadmium chalcogenide-based quantum dots) or lead (from lead chalcogenide-based dots). Cd^{2+} and Pb^{2+} could be released from quantum dots and then kill the cells [130]. The extent of cytotoxicity has been found to be dependent upon a number of factors including size, coating agents, colour, dose of quantum dots, mechanical stability,

photolytic, oxidative, surface chemistry, coating bioactivity and processing parameters [131, 132]. For example, some quantum dots have been found to be cytotoxic only after oxidative and/or photolytic degradation of their core coatings. However, it must be stated that studies that are specifically designed for toxicologic assessment are still immature or very few. At this stage, a direct method that has been applied to avoid possible toxicity of quantum dots is to make them well coated to become biological inert. The coating materials can be low or nontoxic organic molecules or polymers (e.g. PEG) or inorganic layers (e.g. ZnS and silica). A few studies show direct, extracellular cytotoxicity of water-soluble CdSe and CdSe/ZnS quantum dots, because Cd^{2+} is released from the nanoparticles which are highly due to poor purifications and/ or simple surface cappings/coatings [133].

2.3.8 Water soluble semiconductor nanoparticles/quantum dots

An immediate application of semiconductor nanoparticles is in biology. This includes using these materials as fluorescent labels, drug and or gene delivery systems, MRI contrast enhancers, for phagokinetic studies, probing of DNA structures etc. The fact that nanoparticles exist in the same size domain as the biomolecules such as proteins makes them ideal indispensable tools for biological applications. Solubilisation of QDs is essential for many biological applications, but presents a significant challenge. Non-water-soluble QDs can be grown easily in hydrophobic inorganic solvents, but solubilisation requires sophisticated surface chemistry alteration [134].

Since biological processes are typically situated in an aqueous environment, a hydrophilic nanocrystal surface is desired for reactions with biological molecules [135]. In short, quantum dots should first be attached to a hydrophilic surfactant or ligand that will render them water soluble and provide a site for covalent coupling to various biomolecules such as peptides, proteins, sugars and many more. It is known that quantum dots from inorganic solvents are insoluble in water and thus presents a challenge of finding a solution in converting them into water soluble materials. Various methods have been used to transfer quantum dots that are soluble in inorganic solvents to water soluble. Below is the description of the methods used:

(a) Solubilization by ligand exchange

This method involves the displacement of hydrophobic ligands with hydrophilic moieties that coordinate with surface atoms in the outermost layer. The hydrophilic ligands should possess functionality reactive toward the surface atoms of the nanoparticles at one end and a water compatible functionality on the other end of molecule (Scheme 2.2). Ligand exchange methods do not change the whole particle size much and are suitable for large-scale production. In the first described ligand exchange experiment [91], the ligand used was mercaptoacetic acid, which possesses an SH binding group and a carboxylic group, which provides water solubility through the repulsive electrostatic interactions of the charged COO^- groups [136]. Other methods beside ligand exchange were also employed to convert hydrophobic nanoparticles to hydrophilic nanoparticles. Those methods are hydrophobic interaction and silica encapsulation as seen below in Scheme 2.2. However, silica encapsulation has been reported by Yu *et al.,* [137] as complicated. Although the latter method has the ability to produce stable quantum dots, the disadvantage is that the particles are large.

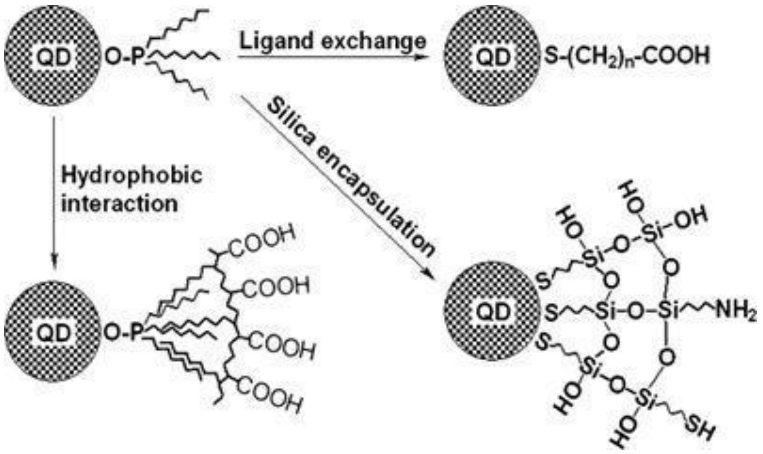

Scheme 2.2: Schematic representation of the strategies employed to synthesize water soluble nanoparticles.

(b) Solubilization by hydrophobic interaction

Hydrophobic interaction can be achieved by using surfactants such as phospholipids such as 1,2-dipalmitoyl-*sn*-glycero-3-phosphoethanolamine-*N*-[methoxy(polyethylene glycol)] or 1,2-dipalmitoyl-*sn*-glycero-3-phosphocholine. These surfactants normally coat quantum

dots in the core by forming oil-in-water micelles through hydrophobic interaction between their hydrophobic ends and the surface ligands of the quantum dots and provide water-solubility via hydrophilic exterior ends [138]. Long chain-length amphiphilic polymers are excellent surfactants for the formation of micelle-like structures for the conversion of water insoluble quantum dots into water. There are instances where poly(acrylic acid) was partially grafted with octylamine through EDC-coupling (EDC = *N*-(3-dimethylaminopropyl)-*N'*-ethylcarbodiimide hydrochloride] to become amphiphillic and then formed micelle-like structures where hydrophobic quantum dots were encapsulated in the core and –COOH faced outward (Scheme 2.2) [139].

Stability and highly water soluble structures can be achieved by introducing a carboxylic acid groups (-COOH) and graft them by amino-terminated poly(ethylene glycol) (PEG-NH_2) molecules through EDC-coupling. Nie and coworkers reported the synthesis of water soluble quantum dots using a two-step EDC-coupling [140]. Poly(maleic anhydride-alt-1-tetradecene) was used to convert hydrophobic quantum dots into water in the presence of bis(6-aminohexyl)amine which played a role in increasing the stability by cross-linking the polymers[141].

The use of amphiphilic polymers gives this technique advantage over ligand exchange in the sense that, (a) the method does not allow interaction between the quantum dots and the hydrophilic surfactants, (b) the polymer's large number of hydrophobic side chains strengthens the hydrophobic interaction to form more steady structures and consequently more stable water-soluble quantum dots, and (c) some of the polymers used inexpensive as compared to other molecules such as peptides and phospholipids in large-scale preparation.

(c) Silica encapsulation

Another method of preparing water soluble quantum dots is coating the quantum dot through layer of silica (Scheme 2.2) [142]. This requires the involvement of organosilicone molecules with $–NH_2$ or –SH, which provide surface functionalities for biomedical applications [143]. Just like the ligand exchange technique, this method lead in quantum efficiency decrease [144]. Some shortcomings that can be experienced if this method has to be used are that (a) the procedures are complicated, and (b) large quantum production is not possible, due to dilute conditions that are used [143]. To avoid the above shortcomings,

Ying and her coworkers reported a simple way of coating quantum dots with silica through reverse microemulsion [145].

In summary, the key to develop quantum dots as a tool in biological system is to achieve water solubility, biocompatibililty and photostability, and, importantly, to provide flexible quantum dots surface chemistry/functionality that will enable efficient coupling of targeting and/or sensing ongoing biological processes.

2.3.9 Applications of Quantum Dots

Quantum dots are particularly significant for optical applications due to their theoretically high quantum yield. In electronic applications they have been proven to operate like a single electron transistor and show the Coulomb blockade effect. They have also been suggested as implementations of qubits for quantum information processing. The ability to manipulate size of quantum dots is advantageous for many applications. For example, larger quantum dots show greater spectrum shift towards red compared to smaller dots, and exhibit less pronounced quantum properties. Conversely, the smaller particles allow one to take advantage of more subtle quantum effects.

Quantum dots have also been reported to have a wide array of potential biomedical applications, especially when combined with antigen-specific coatings or functional groups on their surfaces. The therapeutic and diagnostic usefulness of inorganic nanoparticles depend on their size and physical properties in addition to their chemical composition. They must be small enough to circulate through the bloodstream and tissues without becoming lodged in capillaries or other microanatomies. However, they have to be larger than atomic size in order to lend enhancement to images or separation techniques [146, 147]. The benefits of quantum dots materials, which are large two-photon cross sections, broad excitation wavelength ranges, sharp emission line-widths, high quantum yields, and high photostability, and etc., have been mentioned above in comparison to organic dyes. Coating QDs with hydrophilic ligands provide water soluble, biocompatible semiconductor nanoparticles, which allow the attachment of biomolecules to enhance the function of semiconductor nanoparticles [148, 149]. Biological molecules add chemical selectivity to the properties of the nanomaterial [150]. Typically, the biomolecular-induced changes in semiconductor nanomaterial properties which are observed by fluorescence-induced

changes in photoconductivity are less commonly reported, but have also been observed. The key to integrating biomolecular function into nanomaterial properties is to use enzymatically generated compounds or a biomolecule-attached reporter compound [151, 152]. Below are some of the reported applications of quantum dots:

(a) Light emitting devices

There are several inquiries into employing quantum dots as light emitting diodes to make displays and other light sources, such as quantum dot-light emitting diodes displays, and quantum dot-white light emitting diodes. Few years ago, Quantum dot Vision announced technical success in making proof of concept quantum dot display and show a bright emission in the visible and near infrared region of the spectrum. Quantum dots are valued for displays, because they emit light in very specific Gaussian distributions. This can result in a display that more accurately renders the colours of the human eye can perceive. Quantum dots also require very little power since they are not colour filtered. Additionally, since the discovery of white-light emitting quntum dot, general solid-state lighting applications appear closer than ever. A colour liquid crystal display (LCD), for example, is powered by a single fluorescent lamp that is colour filtered to produce red, green and blue pixels. Displays that intrinsically produce monochromatic light can be more efficient, since more of the produced reaches the eye.

(b) Photovoltaic devices

Quantum dots may be able to increase the efficiency and reduce the cost of today's typical silicon photovoltaic cells. According to an experimental proof, quantum dots of lead selenide can produce as many as seven excitons from one high energy photon of sunlight (7.8 times the band gap energy). This compares favourably to today's photovoltaic cells which can only manage one exciton per high energy photon, with high kinetic energy carriers losing their energy as heat. This would not result in a 7-fold increase in final output however, but could boost the maximum theoretical efficiency from 31% to 42%. Quantum dot photovoltaics would theoretical be cheaper to manufacture, as they can be made using simple chemical reactions. The generation of more than one exciton by a single photon is called multiple exciton generation (MEG) or carrier multiplication.

(c) Computing

Quantum dot technology is one of the most promising candidates for use in solid-state quantum computation. By applying small voltages to the leads, the flow of electrons through the quantum dot can be controlled and thereby precise measurements of the spin and other properties therein can be made. With several entangled quantum dots, or qubits, plus a way of performing operations, quantum calculations and computers that would perform them might be possible.

(d) Diagnostics tools

Investigation of nanoparticles for diagnostic purposes is currently the most advanced and well studied in the field of oncology [153, 154, 155]. Cancer is presently the leading cause of death in North America and the number of new cases in the United States is expected to be over 1.5 million in 2008. Current cancer therapies are lacking due to inadequate understanding of the multimodality disease, particularly failing to detect tumor formation with early diagnosis and accurate prognosis, and in turn impending the effectiveness of anticancer drugs. Existing diagnostic approaches are mostly limited to the detection of relatively large, solid tumors, which often involve invasive techniques such as tissue biopsies [156]. In most cases, this detectable tumor is at a late stage, at which the cancer has metastatized to other tissues, resulting in a greater challenge for both tumor detection and proper therapeautics. In addition, tissue biopsies are difficult to obtain from deep tissues, bioanalytical assays from urine and blood samples are often not providing reliable results, and imaging with contrast agents are limiting as current dyes cannot distinguish between the highly invasive and benign types of tumor [157]. It would therefore be useful to have diagnostic tools which could allow for simultaneous detection of multiple proteins with sufficient sensitivity. Quantum dots, among other nanotechnological products, could become versatile tools for screening cancer markers in biological fluids and tissue biopsies, as well as high resolution contrast agents for medical imaging of metastatic tumor [158]. The rationale for employing quantum dots as diagnostics in cancer are the following, (i) they are highly fluorescent and can be used for deep tissue imaging in vivo, (ii) they can serve as sensitive probes for multiple cell types because of their multiplexing abilities and wide range of tunable emissions [159], and (iii) utilization of functionalized quantum dots to target tumors in experimental animals shows promising results for future developments

and eventual applications in humans.

(e) Cell labeling

One of the most important uses of fluorescent probes in biology is the labeling of cellular structures. Naturally, the earliest demonstrated uses of QDs in biology were to label cells with a new class of bright and stable fluorophores. Multicolor labeling of cells is a powerful technique for visualizing many of these structures simultaneously, such as cytoskeletal proteins or organelles, and to elucidate intracellular processes. Although cell labeling with organic has been commonplace for decades, using multiple labels simultaneously remains a cumbersome procedure due to the narrow absorption profiles of most dyes. Effective multicolor labeling requires an assortment of filters to properly excite and collect fluorescence from specific dye molecules. Moreover, if laser excitation is used, multiple sources are typically required to excite all of the dyes labeling the cell which can be expensive and requires a complex microscopy arrangement specific to the experiment. The continuous excitation of dyes inevitably results in significant photobleaching that quenches the luminescence over short time scales. This severely limits the practical observation time for sample, even with the addition of various anti-bleaching chemical agents [160].

By contrast, QDs are excellent fluorescent probes for long-term multicolor cell labeling. They have been widely used as luminescent cell makers that identify molecular structures. However, overcoming the challenge of creating stable, water soluble materials that could be delivered within cells was formidable. Two strategies were developed to achieve a similar goal. Brunchez *et al.* [92] used phalloidin to specifically target actin filaments, followed by exposure to streptavidin and biotinylated QDs to form a sandwich structure. Electrostatically-charged QDs bearing trimethoxysilylpropyl urea and acetate groups were shown to label the nucleus. Chan and Nie [62] demonstrated transferring-mediated endocytic uptake of QDs within HeLa cells which resulted in efficient and preferential delivery of transferring-labeled QDs versus unlabeled QDs. These studies showed that QDs could perform similar duties to organic dye fluorophores within cells and provided initial guidance regarding successful strategies for efficient cell delivery. With the availability of commercial labeling kits, the prevalence of QDs in cell labeling applications has increased dramatically. Despite their popularity and success, commercial materials currently have somewhat limited potential due to the use of specific proprietary coatings and surface

ligands to passivate and stabilize the nanoparticles.

(f) Biosensing and energy transfer

The fact that QDS have unique physical and optical properties, scientist managed to employ them in developing new methods of biosensing. By attaching biomolecules to the QD surface, it is possible to generate complex bioconjugates that merge biological specificity and function with the desirable optical characteristics of QDs. In many cases the nanometer size of QDs allows the nanocrystal to become a central structural component that can accommodate numerous copies of a particular biomolecule or several different biomolecules simultaneously. As a result, these bioconjugates are sometimes referred to as "nanosensors." As robust fluorophores, QDs are compatible with conventional biosensing techniques that implement fluorescence to produce a large measurable signal. Fluorescent resonance energy transfer (FRET) in particular has been a popular method of signal transduction due to its sensitivity to molecular scale interactions [161, 162]. An early FRET-based technique was demonstrated by Patolsky *et al.* [163] for the study of telomerization and DNA replication dynamics. Thiolated DNA was attached to the surface of water soluble CdSe-ZnS QDs. In the presence of appropriate enzymes and dye-labeled nucleotides, the emission spectra showed a time dependent red-shift indicating efficient energy transfer from QD to dye specifically due to telomerization or replication, respectively. The telomerization results were corroborated with AFM images showing growth of DNA extending from the QD surface. The same group later looked at QD-based FRET for detecting DNA hybridization and cleavage [164]. In their results, they noted that full recovery of the fluorescence emission following the addition of enzyme was not possible due to nonspecific interactions between the dyes and nanoparticles. A related approach for developing a prototype FRET-based QD biosensor capable of detecting the nutrient sugar maltose in solution was employed by Medintz *et al.* [165]. Maltose binding protein (MBP), pre-bound to an analog sugar-dye complex, was conjugated to water soluble QDs resulting in many MBP attached to each QD. In the initial state, fluorescence from the QD was significantly quenched by the non-emissive dye. As maltose is added to solution, the analog sugar-dye complex is progressively displaced resulting in a substantial increase in fluorescence signal with increasing concentration. A reagentless implementation of a maltose biosensor was also demonstrated where the QD transfers energy to a Cy3 dye covalently attached near the binding pocket of MBP [166].

(g) In vivo imaging

The ability to visualize native processes occurring in living organisms is invaluable for clinical diagnostic applications, yet remains elusive in practice due to conventional imaging limitations and the availability of suitable fluorescence markers. Regarding the latter, many organic dyes have very short lifetimes (~1 ns), are susceptible to photodegradation, and show inadequate fluorescence brightness [159]. Additional, tissue autofluorescence can exhibit similar spectroscopic characteristics making it difficult to resolve the desired signal from unwanted background. Due to their unique photophysical properties, quantum dots are promising fluorophores for *in vivo* fluorescence imaging and can overcome many of the usual limitations of dyes. An early study by Akerman *et al.* [167] examined targeted delivery of quantum dots to specific locations within live mice, however fluorescence imaging was performed after the animal was sacrificed and the tissue sectioned. Non-invasive, real-time *in vivo* fluorescence imaging requires exciting fluorophores and detecting their emission through tissue which is invariably hindered by scattering and absorption of both the excitation and emission wavelengths.

In vivo fluorescence imaging has undoubtedly benefited from the development of quantum dot fluorophores where their unique properties allow more flexible imaging strategies. For example, the expanded use of multi-photon microscopy can provide a more efficient method of exciting quantum dots *in vivo*. This is due to the exceptional multi-photon absorption cross-section of semiconductor nanocrystals [168]. In certain cases, the effective brightness of quantum dot fluorophores is two or more orders of magnitude higher than organic dyes using multi-photon excitation. By preferentially exciting fluorophores very near the highly focused excitation beam, high-resolution fluorescence images can be generated while eliminating out-of-focus and autofluorescence contributions. This method has yet to be fully realized, however. Other *in vivo* imaging modalities such as magnetic resonance imaging (MRI) and positron emission tomography (PET) could benefit from quantum dots [169].

(h) Drug delivery

Unfortunately, poor diagnosis and prognosis are only small parts of the overall cancer problem, as this inevitably leads to inadequate development of treatments. Current

chemotherapeutic agents are highly cytotoxic, however, most are lacking in specificity to cancerous cells and resulting in systemic toxicity and adverse side effects [170]. Nanoparticles, such as quantum dots, may not only improve tumor targeting, but may also act as new drug delivery tool, and even as direct therapeutics against tumor cells [171]. There is a growing trend for the development of multifunctional nanoparticles to image, diagnose and deliver treatment to cancer cells. The major struggle underlying the design of drug delivery system is the same problem encountered in developing tools for imaging and diagnosis, and that is, target specificity. Encapsulating drugs in nanosized micelles was a big step forward in the research and development of drug delivery systems, as these nanoparticles can be easily surface conjugated with ligands for targeted delivery, but more importantly, the release of drugs can be localized at the targeted region, reducing side effects due to non-specific drug action [172]. However, the current trend in the design of nano-delivery systems is focused on yet another level, which is monitoring of drug action. Quantum dots, among the array of nanomaterials, may be the optimal tool for all these purposes [173]. Bagalkot *et al.* [174] recently proposed in their study the design of cancer imaging, therapy, and sensor system based on functionalized CdSe/ZnS QDs. Quantum dots were first surface conjugated with A10 RNA aptamers, which target the PSMA specific on prostate tumors, and subsequently, a fluorescent anticancer agent, doxorubicin, was intercalated with aptamer to yield the QD-Apt(Dox) probe. Based on the concept of a bi-fluorescence resonance energy transfer, QD dot and Dox fluorescence are quenched by their close proximity with each other in the intact QD-Apt (Dox) probe. Upon the PSMA-mediated internalization of the nanosystem into the tumor cell, there is a release of the drug from the QD, thereby unquenching the fluorescence of both. The group reported that this nanosystem is indeed functional and specific to PSMA cells in vitro, and showed that the fluorescence can be unmistakably distinguished.

2.4 References

1. E. Rodríguez-Fernández, E. García, M. R. Hermosa, A. Jiménez-Sánchez, M. Mar Sánchez, E. Monte, J. J. Criado, *J. Inorg. Biochem.,* **75**, 181, 1999.
2. T. J. Lane, A. Yamaguchi, J. V. Guagliano, J. A. Ryan, S. Mizushima, *J. Am. Chem. Soc.,* **81,** 3824, 1959.
3. M. Koketsu, H. Ishihara, *Curr. Org. Synth.,* **3**, 439, 2006.
4. F. A. L. Anet, M. Ghiaci, *J. Am. Chem. Soc.,* **101**, 6857, 1979.

5. K. A. Haushalter, J. Lau, J. D. Roberts, *J. Am. Chem. Soc.*, **118**, 8891, 1996.
6. L. Fernholt, S. Samdal, R. Seip, *J. Mol. Struct.*, **72**, 217, 1981.
7. T. Phuong, T. Khac-Minh, N. T. Van Hal, H. T. Phuong, *Bioorg. Med. Chem. Lett.*, **14**, 653, 2004.
8. O. F. Huebhr, J. L. Marsh, R. H. Mizzoni, R. P. Mull, D. C. Schroeder, H. A. Troxell, C. R. Scholz, *J. Am. Chem. Soc.*, **75**, 2274, 1953.
9. K Ramadas, G. Suresh, N. Janarthanan, S. Masilamani, *Pestic. Sci.*, **52**, 145, 1998.
10. V. K. Madan, A. D. Taneja, *J. Indian Chem. Soc.*, **68**, 471, 1991.
11. M. J. Moloto, N. Revaprasadu, P. O'Brien, M. A. Malik, *J. Mat. Sci.-Mater. Electron.*, **15**(5), 313, 2004.
12. A. Rosenheim, V. J. Meyer, *Z. Anorg. Chem.*, **49**, 13, 1906.
13. R. A. Bailey, T. R. Peterson, *Can. J. Chem.*, **45**(10), 1135, 1967.
14. S. L. Holt Jr, R. L. Carlin, *J. Am. Chem. Soc.*, **86**, 3017, 1964.
15. M. Nardelli, L. Coghi, *Ric. Sci.*, **29**, 134, 1959.
16. M. B. Cingi, L. Coghi, C. Guastini, *Hazz. Chim. Ital.*, **95**, 368, 1965.
17. B. C. Stonestreet, W. E. Bull, R. J. Williams, *J. Inorg. Nuc. Chem.*, **28**, 1895, 1966.
18. Yu. N. Kukushkin, V. V. Sibirskaya, T. K. Mikhal'chenko, L. V. Konovalov, *Zh. Obshch. Khim.*, **45**, 1584, 1975.
19. M. Schafer, C. Curran, *Inorg. Chem.*, **5**, 265, 1966.
20. V. V. Dunina, *Ph.D. Dissertation, University of Moscow*, 1969.
21. J. Hald, E. Jacobsen, V. Larsen, *Acta Pharmacl. Toxicol.*, **4,** 285, 1984.
22. A. K. Powell, *Brit. J. Cancer*, **8,** 529, 1954.
23. J. A. Cohen, O. Vos, D. W. Bekkum, "*Advances in Radiobiology," G. C. Hevesy, Ed., Oliver & Boyd Ltd., Edinburg*, 134, 1957.
24. A. Domenicano, L. Torelli, A. Vaciago, L. Zambonelli, *J. Chem. Soc. A.*, 1351, 1968.
25. T. Kitson, *Education in Chemistry*, 43, 1985.
26. G. D. Thorn, R. Ludwig, *The Dithiocarbamates and Related Compounds, Elsevier, Amsterdam*, 1981.
27. P. K. Gessner, T. Gessner, *Disulfiram and its Metabolite, Diethyldithiocarbamate, Chapman and Hall, London*, 1992.
28. R. G. Compton, J. C. Eklund, A. Hallik, S. Kumbhat, L, Nei, A. M. Boond, R. Colton, Y. A. Mah, *J. Chem. Soc. Dalton*, 1917, 1995.
29. J. J. Steggerda, J. A. Cras, J. Willemse, *Rec. Trav. Chim.*, **100**, 41, 1981.

30. D. Fan, M. Afzaal, M. A. Mallik, C. Q. Nguyen, P. O'Brien, P. J. Thomas, *Coord. Chem. Rev.,* **251**, 1878, 2007.
31. A. D. Burrows, M. D/ Coleman, M. F. Mahon, *Polyhedron,* **18,** 2665, 1999.
32. D. R. Eaton, K. Zaw, *J. Inorg. Nucl. Chem.,* **38,** 1007, 1976.
33. A. S. Tompa, R. D. Barefoot, E. Price, *J. Phys. Chem.,* 73, 435, 1969.
34. J. K. Kochi, P. J. Krusic, D. R. Eaton, *J. Am. Chem. Soc.,* 91, 1879, 1969.
35. F. D. Rochon, J. Bariyanga, P. C. Kong, *Can. J. Chem.,* **63,** 2425, 1985.
36. N. R. Kunchur, M. R. Truter, *J. Chem. Soc.,* **517,** 2551, 1958.
37. J. Goldsmith, J. G. White, *J. Chem. Phys.,* **31,** 1175, 1959.
38. M. M. Elcombe, J. C. Taylor, *Acta Cryst.,* **A24,** 410, 1968.
39. M. S. Ferrari, G. G. Fava, C. Pelizzi, *Acta Cryst.,* **B32,** 901, 1976.
40. A. Ramnathan, K. Sivakumar, K. Subramanian, *Actra Cryst.,* **C51,** 2446, 1955.
41. K. Ramadas, N.Srinivassan, N. Janarthanan, *Tetrahedron Lett.,* **34,** 6447, 1993.
42. H. Iwasaki, H. Hagihara, *Acta Cryst.,* **B28,** 507, 1972.
43. R. Selvaraju, K. Panchanatheswaran, A. Thiruvalluvar, V. Parthasarathi, *Acta Cryst.,* **C51,** 606, 1995.
44. C. Fabiani, R. Spagna, A. Vaciao, L. Zambonelli, *Acta Cryst.,* **B27,** 1499, 1971.
45. K. Martinac, Ž. Metelko, *Diabetologia Croatica,* **34**(4), 105, 2005.
46. H. Warad, A. Suhane, Y. Boontongkong, C. Thanachayanont, J. Dutta, *The third Thailand Materials Science and Technology Conference (MSAT III), Bangkok*, 16, 2004.
47. M. L. Steigerwald, L. E. Brus, *Acc. Chem. Res*., **23**, 183, 1990.
48. C. Burda, X. Chen, R. Narayanan, M. A. El-Sayed, *Chem. Rev.,* **105,** 1025, 2005.
49. K. Sato, Y. Tachibana, S. Hattori, T. Chiba, S. Kuwabata, *J. Colloid. Inter. Sci.,* **324,** 257, 2008.
50. S. V. Kershaw, M. Harrison, A. L. Rogach, A. J. Kornowski, *Select. Topics Quantum Electron.,* **6,** 534, 2000.
51. C. M. Niemeyer, *Angew. Chem., Int. Ed.,* **40,** 4128, 2000.
52. T. Kippeny, L.A. Swafford, S.J. Rosenthal, *J. Chem Educ.,* **79,** 1094, 2002.
53. W. Huyhn, X. Peng, A. P. Allivisatos, *Adv. Mater.,* **11**, 923, 1999.
54. Y. A. Vlasov, N. Yao, D. J. Norris, *Adv. Mater.,* **11,** 165, 1999.
55. L. –S. Li, J. Hu, W. Yang, A. P. Alivisatos, *Nano Lett.,* **1,** 349, 2001.
56. S. V. Gaponenko *in Optical Properties of Semiconductor Nanocrystals, Cambridge University, New York,* 23, 1998.

57. I. Robel, V. Subramanian, M. Kuuno, P. V. Kmat, *J. Am. Chem. Soc.*, **128**, 2385, 2006.
58. Y. Zhang, S. Gao, J. Y. Ying, *Adv. Mater.*, **19**, 376, 2007.
59. M. L. Steigerwald, L. E. Brus, *Annu. Rev. Mater. Sci.*, **19**, 471, 1989.
60. V. F. Puntes, K. M. Krishnan, A. P. Alivisatos, *Science*, **291,** 2115, 2001.
61. G. Markovich, C. P. Collier, S. E. Henrichs, F. Remacle, R. D. Levine, J. R. *Heath, Acc. Chem. Re*s., **32,** 415, 1999.
62. C. B. Murray, D. J. Norris, M. G. Bawendi, *J. Am. Chem. Soc.*, **115,** 8706, 1993.
63. A.I. Ekimov, A. A. Onushchenko, *Sov Phys Semicond.*, **16,** 772, 1982.
64. R. Chen, D. J. Lockwood, *J. Electrochem. Soc.*, **149,** s69, 2002.
65. N. Kumbhojkar, V. V. Nikesh, A. Kshirsagar, S. Nahamuni, *J. Appl. Phys.*, **88,** 6260, 2000.
66. H. –Y. Lu, S. –Y. Chu, S. –S. Tan, *J. Cryst. Growth,* **269,** 385, 2004.
67. W. Tang, D. C. Cameron, *Thin Solid Films,* **280,** 221, 1996.
68. A. Kudo, M. Sekizawa, *Chem. Commun.,* 1371, 2000.
69. J. Dai, Z. Jiang, W. Li, G. Bian, Q. Zhu, *Mater. Lett.,* **55,** 383, 2002.
70. Y. Nayaoka, Y. Nosaka, *Langmuir*, **23**, 708, 1997.
71. N. Herron, Y. Wang, H. Echert, *J. Am. Chem. Soc.,* **112**, 1322, 1990.
72. A. Thakur, C. Fradin, *Can. Undergraduate Phys. J.*, **3**, 7, 2005.
73. E. Scher, L. Manna, A. P. Alivisatos, *Phil. Trans. Lond. A.*, **361,** 241, 2003.
74. X. Y. Chen, Z. J. Zhang, Z. G. Qiu, C. W. Shi, X. L. Li, *J. Colloid. Interface Sci.*, **308,** 271, 2007.
75. D. M. Pasquariello, R. Kershaw, J. D. Passaretti, K. Dwight, A. Wold, *Inorg. Chem.*, **23,** 872, 1984.
76. A. Wold, K. Dwight, *J. Solid State Chem.*, **96,** 53, 1992.
77. J. L. Gomez-Camer, F. Martin, J. Morales, L. Sanchez, *J. Electrochem. Soc.*, **115,** A189, 2008.
78. K. Ramesha, R. Seshadri, C. Ederer, T. He, M. A. Subramaniani, *Phys. Rev.,* **B70,** 214409, 2004.
79. L. Wang, K. Umemoto, R. M. Wentzovitch, T. Y. Chen, C. L. Chien, J. G. Checkelsky, J. C. Eckert, E. D. Dahlberg, C. Leighton, *Phys. Rev. Lett.*, **94,** 056602-1, 2005.
80. L. Wang, T. Y. Chen, C. Leighton, *Phys. Rev.*, **B69,** 094412-1, 2004.
81. B. Morris, V. Johnson, A. Wold, *J. Phys. Chem. Solids,* **28,** 1565, 1967.

82. D. Chen, K. B. Tang, G. Z. Shen, J. Sheng, Z. Fang, X. M. Liu, H. G. Zheng, Y. T. Qian, *Mater. Chem. Phys.*, **82,** 206, 2003.

83. X. F. Qian, X. M. Zhang, C. Wang, K. B. Tang, Y. Xie, Y. T. Qian, *J. Alloys Comp.*, **278,** 110, 1998.

84. X. Y. Chen, Z. J. Zhang, Z. G. Qiu, C. W. Shi, X. L. Li, *J. Colloid. Interface Sci.*, **308,** 271, 2007.

85. Y. D. Yin, C. K. Erdonmez, A. Cabot, S. Hughes, A. P. Allivisatos, *Adv. Func. Mater.*, **16,** 1389, 2006.

86. P. O'Brien, N. L. Pickett, *Chem. Mater.*, **13**, 3483, 2001.

87. X. Y. Wu, H. J. Liu, J. Q. Liu, K. N. Haley, J. A. Treadway, J. P. Larson, *Nat. Biotechnol.*, **21,** 41, 2003.

88. N. Panchuk-Voloshina, R. P. Haugland, J. Bishop-Stewart, M. K. Bhalgat, P. J. Millard, F. Mao, *J. Histochem. Cytochem.*, **47,** 1179, 1999.

89. J. Aldana, Y. A. Wang, X. Peng, *J. Am. Chem. Soc.*, **123**, 8844, 2001.

90. W. Chan, D. Maxwell, X. Gao, R. Bailey, M. Han, S. Nie, *Current Opinion Biotechnol.*, **13,** 40, 2002.

91. W. C. W. Chan, S. Nie, *Science*, **281,** 2016, 1988.

92. Jr., M. Bruchez, M. Moronne, P. Weiss, A. P. Alivisatos, *Science*, **281**, 2013, 1988.

93. H. Weller, *Adv. Mater.*, **5,** 88, 1993.

94. X. G. Peng, L. Manna, W. D. Yang, J. Wickham, E. Scher, A. Kandavich, A. P. Allivisatos, *Nature*, **404**, 59, 2000.

95. Y-W. Jun, J-S. Choi, J. Cheon, *Angew. Chem. Int. Ed.*, **45**, 3414, 2006.

96. T. Vossmeyer, L. Katsikas, M. Giersig, I. G. Popovic, K. Diesner, A. Chemseddine, A. Eychmuller, H. Weller, *J. Phys. Chem.*, **98**, 7665, 1994.

97. J. Nanda, S. Sapra, D. D. Sarma, *Chem. Mater.*, **12**, 1018, 2000.

98. K. Rajeshwar, N. R. Tacconi, C. R. Chenthamarakshan, *Chem. Mater.*, **13,** 2765, 2001.

99. A. P. Alivisatos, *J. Phys. Chem.*, **100,** 13226, 1996.

100. J. K. Furdyna, *J. Appl. Phys.*, **64,** R29, 1988.

101. R. N. Bhargava, D. Gallagher, X. Hong, A Nurmikko, *Phys. Rev. Lett.*, **72,** 416, 1996.

102. M. Green, P. O'Brien, *Chem. Commun.*, 2235, 1999.

103. T. Johnson, V. K. La Mer, *J. Am. Chem. Soc.*, **69**, 1184, 1947.

104. M. A. Malik, P. O'Brien, N. Revaprasadu, *Phosphorus, Sulfur, and Silicon*, **180**,

689, 2005.

105. Y. Wang, N. Herron, *J. Phys. Chem.,* **91**, 257, 1987.

106. T. Cassagneau, G. B. Hix, D. J. Jones, P. Maireles-Torres, M. Rhomari, J. Roziere, *J. Mater. Chem.*, **4**, 189, 1994.

107. T. Abe, Y. Tachibana, T. Uematsu, M. Iwamoto, *J. Chem. Soc. Chem. Commun.,* 1617, 19995.

108. H. J. Wazke, J. H. Fendler, *J. Phys. Chem.*, **91**, 854, 1987.

109. K. M. Choi, K. J. Shea, *J. Phys. Chem.,* **98**, 3207, 1994.

110. Y. Wang, A. Suna, W. Mahler, R. Kasowski, *J. Chem. Phys.,* **87**, 7315, 1987.

111. H. Shinojima, J. Yumoto, S. Omi, Y. Asahara, *Appl. Phys. Lett.,* **55**, 1519, 1989.

112. M. A. Malik, P. O'Brien, N. Revaprasadu, *S. A. J. Science*, **96**, 55, 2000.

113. N. L. Pickett, P. O'Brien, *The Chemical Record,* **1,** 467, 2001.

114. G. C. Benson, R. Shuttleworth, The surface energy of small nuclei, *J. Chem. Phys.,* **19**(1), 130, 1951.

115. I. V. Markov, *Crystal Growth for beginners, 2nd ed., Singapore: World Scientific,* 546, 2003.

116. T. Sugimoto, *Adv. Colloid. Interf. Sci.,* **28,** 65, 1987.

117. P. Buffat, J. –P. Borel, *Phys. Rev. A.,* **13**(6), 2287, 1976.

118. V. K. Lamer, R. H. Dinegar, *J. Am. Chem. Soc.,* **72**(11), 4847, 1950.

119. X. Peng, J. Wickham, A. P. Allivisatos, *J. Am. Chem. Soc.,* **120**(21), 5343, 1998

120. P. S. Shah, J. D. Holmes, K. P. Johnston, B. A. Korgel, *J. Phys. Chem. B.,* **106**(10), 2545, 2002.

121. V. Talapin, S. Haubold, A. L. Rogach, A. Kornowski, M. Haase, H. Weller, *J. Phys. Chem. B.,* **105**(12), 2260, 2001.

122. A. Henglein, *Chem. Rev.*, **89**, 1861, 1989.

123. A. Henglein, M. Gratzel, *Chem. Rev.*, **95**, 49, 1995.

124. X. Ma, W. Shi, B. Li, *Semicond. Sci. Technol.,* **21,** 713, 2006.

125. J. L. Pankove, *Optical Process in Semiconductors, Dover Publications Inc.: New York,* 1970.

126. M. F. Jarrold, *Science*, **252**, 1085, 1991.

127. L. E. Brus, N. Chestoy, T. D. Harris, R. Hull, *J. Phys. Chem.* **90**, 3393, 1986.

128. M. Sharma, S. Kumar, O. P. Pandey, *Digest Nanomaterials and Biostructures,* **3**(4), 189, 2008.

129. A. L. Efros, M. Rosen, M. Kuno, M. Nirmal, D. J. Norris, M. G. Bawendi, *Phys.*

Rev., **B54**, 4843, 1996.

130. C. Boudene, M. damerval, *Toxicol. Eur. Res.*, **4**,143, 1982.
131. A. Shiohara, A. Hoshino, K. Hanaki, K. Suzuki, *Microbiol. Immunol.*, **48**, 669, 2004.
132. R. A. Hardman, *Environ. Health Perspect.*, **114**, 165, 2006.
133. A. M. derfus, W. C. W. Chan, S. N. Bhatia, *Nano Lett.*, **4**, 11, 2004.
134. T. Jamieson, R. Bakhshi, D. Petrova, R. Pocock, M. Imani, A. M. Seifalian, *Biomat.*, **28,** 4717, 2007
135. O. V. Salata, *J. Nanobiotechnol.*, **2,** 1, 2004.
136. A. M. Derfus, W. C. W. Chan, S. N. Bhatia, *Adv. Mater.*, **16,** 961, 2004.
137. W. W. Yu, E. Chang, R. Drezek, V. L. Colvin, *Biochem. Biophys. Res. Commun.*, **348,** 781, 2006.
138. B. Bubertret, P. Skourides, D. J. Norris, V. Noireaux, A. H. Brivanlou, A. Libchaber, *Sciences*, **298**, 1759, 2002.
139. X. Wu, H. Liu, K. N. Haley, J. A. Treadway, J. P. Larson, N. Ge, F. Peale, M. P. Bruchez, *Nat. Biotechnol.*, **21**, 41, 2003.
140. X. Gao, Y. Cui, R. M. Levenson, L. W. K. Chung, S. Nie, *Nat. Biotechnol.*, **22**, 969, 2004.
141. T. Pellegrino, L. Manna, S. Kudera, T. Liedl, D. Koktysh, A. L. Rogach, S. Keller, J. Raedler, G. Natile, W. J. Parak, *Nano Lett.*, **4**, 703, 2004.
142. M. Bruchez Jr., M. Moronne, P. Gin, S. Weiss, A. P. Alivisatos, *Science*, **281**, 2013, 1998.
143. D. Gerion, F. Pinaud, S. C. Williams, W. J. Parak, D. Zanchet, S. Weiss, A. P. Alivisatos, *J. Phys. Chem. B.*, **105**, 8861, 2001.
144. A. L. Rogach, D. Nagesha, J. W. Ostrander, M. Giersig, N. A. Kotov, *Chem. Mater.*, **12**, 2676, 2000.
145. S. T. Selvan, T. T. Tan, J. Y. Ying, *Adv. Mater. (Weinheim, Germany)*, **17**, 1620, 2005.
146. J. K. Jaiswal, S. M. Simon, *Nat. Chem. Biol.*, **3,** 92, 2007.
147. T. Thurn, E. M. B. Brown, A. Wu, B. Lai, J. Maser, T. Paunesku, G. E. Woloschak, *Nanoscale Res. Lett.*, **2,** 430, 2007.
148. M. Zhou, I. Ghosh, *Biopolymers*, **88,** 325, 2007.
149. K. E. Sapsford, T. Pons, I. L. Medintz, H. Mattoussi, *Sensors*, **6,** 925, 2007.
150. R. C. Somers, M. G. Bawendi, D. G. Nocera, *Chem. Soc. Rev.*, **36,** 579, 2007.

151. R. Gill, F. Patolsky, E. Katz, I. Willner, *Angew. Chemie, Int. Ed.*, **44,** 4554, 2005.
152. D. E. Benson, *In Nanomaterials for Biosensor* (Kumar, C. S. S. R., Ed.), Wiley-VCH, Weinheim, 337, 2006.
153. M. Stroh, J. P. Zimmer, D. G. Duda, *Nat. Med.*, **11,** 678, 2005.
154. Matsumura, H. Maeda, *Cancer Res.*, **46,** 6378, 1986.
155. Gao, Y. Gui, R. M. Levenson, L. W. Chung, S. Nie, *Nat. Biotechnol.*, **22,** 969, 2004.
156. N. L. Henry, D. F. Hayes, *Oncologist*, **11,** 541, 2006.
157. R. Heath, M. E. Davis, *Annu. Rev. Med.*, **59,** 251, 2008.
158. E. B. Voura, J. K. Jaiswal, H. Mattoussi, S. M. Simon, *Nat. Med.*, **10,** 993, 2004.
159. A. P. Allivisatos, W. Gu, C. Larabell, *Annu. Rev. Biomed. Eng.*, **7,** 55, 2005.
160. J. R. Lakowics, *Principles of Fluorescence Spectroscopy, Second edition, Kluwer Academic/Plenum Publishers*, 1999.
161. A. R. Clapp, I. L. Medintz, J. M. Mauro, *J. Am. Chem. Soc.*, **126,** 301, 2004.
162. I. L. Medintz, J. H. Konnert, A. R. Clapp, *Proc. Natl. Acad. Sci.*, **101,** 9612, 2004.
163. F. Patolsky, R. Gill, Y. Weizmann, *J. Am. Chem. Soc.*, **125,** 13918, 2003.
164. R. Gill, I. Willner, I. Shweky, *J. Phys. Chem. B.*, **109,** 23715, 2005.
165. I. L. Medintz, A. R. Clapp, H. Mattoussi, *Nature Mater.*, **2,** 630, 2003.
166. I. L. Medintz, A. R. Clapp, J. S. Melinger, *Adv. Mater.*, **17,** 2450, 2005.
167. M. E. Akerman, W. C. W. Chan, P. Laakkonen, *Proc. Natl. Acad. Sci.*, **99,** 12617, 2002.
168. D. R. Larson, W. R. Zipfel, R. M. Williams, *Science*, **300,** 1434, 2003.
169. X. Michalet, F. F. Pinaud, L. A. Bentolila, *Science*, **307,** 538, 2005.
170. S. Nie, Y. Xing, G. J. Kim, J. W. Simons, *Annu. Rev. Biomed. Eng.*, **9,** 257, 2007.
171. M. J. Vicent, R. Duncan, *Trends Biotechnol.*, **24,** 39, 2006.
172. R. Duncan, *Nat. Rev. Cancer*, **6,** 688, 2006.
173. N. G. Portney, M. Ozkan, *Anal. Bioanal. Chem.*, **384,** 620, 2006.
174. Bagalkot, L. Zhang, E. Levy-Nissenbaum, *Nano Lett.*, **7,** 3065, 2007.

Chapter 3

Experimental

3.1. Materials

Cadmium chloride, cobalt chloride, zinc chloride, diphenylthiourea, tetramethylthiuram monosulfide, tetramethylthiuram disulfide, N,N'-dimethylthiourea, sodium diethyldithiocarbamate trihydrate, 1-methyl-2-thiourea, ethylene glycol, ethanol and methanol were used as purchased from Aldrich. HDA (hexadecylamine), TOPO (*tri-n-octylphosphine oxide*), TOP (tri-*n*-octylphosphine), pyridine, ethyl acetate, chloroform, toluene and diethyl ether were also purchased from Aldrich and used without further purification. Glucose, sucrose and glucuronic acid which were obtained from Aldrich were used as capping agents for the synthesis of water soluble semiconductor quantum dots.

3.2. Instrumentation

(a) Microanalysis

Purity of the complexes was performed on a CARLO ERBA elemental analyzer for C, H, N, S.

(b) FT-IR and NMR spectroscopy

Infrared spectra were recorded on Bruker Optics Tensor 27. Spectra were collected over the range from 400 to 4000 cm^{-1}. NMR spectra were recorded on a varian Associates Inova spectrometer (400 and 300 MHz)

(c) Thermogravimetry

Thermogravimetric analysis was performed from 20 ^{o}C to 900 ^{o}C on a Perkin Elmer Pyris 1 TGA with nitrogen flow and heating rate of 5 ^{o}C/min.

(d) X-ray crystallography

Intensity data were collected on a Bruker APEX II CCD area detector diffractometer with graphite monochromated Mo K_α radiation (50kV, 30mA) using the APEX 2 [1] data collection software. The collection method involved ω-scans of width 0.5° and 512x512 bit data frames. Data reduction was carried out using the program *SAINT+* [2] (Bruker, 2005b) and absorption corrections carried out using *SADABS* [2]. The crystal structure was solved by direct methods using *SHELXTL* [3]. Non-hydrogen atoms were first refined isotropically followed by anisotropic refinement by full matrix least-squares calculations based on F^2 using *SHELXTL*. Hydrogen atoms were first located in the difference map then positioned geometrically and allowed to ride on their respective parent atoms. Diagrams and publication material were generated using SHELXTL, PLATON [4] and ORTEP-3 [5].

(e) Optical characterization

Optical absorption measurements were carried out using an Analytikjena SPECORD 50 UV-visible spectrophotometer, and the samples were placed in quartz cuvettes (1-cm path length), using toluene and dimethylsulfoxide as reference solvents. Emission spectra of the particles were recorded on a Perkin Elmer LS 45 photoluminescence (PL) spectrometer with a xenon lamp at room temperature. The samples were placed in glass cuvettes (1 cm).

(f) Electron microscopy

The particles size and shape were determined by Tecnai G^2 Spirit electron microscope operating at 120 kV. Samples were prepared by spreading a drop of dilute dispersion of the as-prepared products on copper grids and then dried in air.

(g) X-ray diffraction analysis

X-ray diffraction (XRD) patterns on powdered samples were carried out in the 2θ on a D 8 diffractometer. Samples were placed in a glass holder. Measurements were taken using a glancing angle of incidence detector at an angle of 2^o, for 2θ values over $20^o - 60^o$ in steps of 0.05^o with a scan speed of 0.01 $^o2\theta.s^{-1}$.

3.3. Synthesis of complexes

The following compounds, $[CdCl_2\{(CH_3)_4(N_2C_2S_3)\}_2]$ **I,** $[CdCl_2\{CS(NHC_6H_5)_2\}_2]$ **II**, $[CdCl_2\{CS(NHCH_3)_2\}_2]$ **III**, $[CdCl_2\{CSNH_2(NHCH_3)\}_2]$ **IV**, $[CdCl_2\{(C_2H_5)_2NCS_2\}_2]$ **V**, $[CoCl_2\{(CH_3)_4(N_2C_2S_3)\}_2]$ **VI**, $[CoCl_2\{CS(NHCH_3)_2\}_2]$ **VII**, $[CoCl_2\{CSNH_2(NHCH_3)\}_2]$ **VIII**, $[CoCl_2\{(C_2H_5)_2NCS_2\}_2]$ **IX**, $[ZnCl_2\{(CH_3)_4(N_2C_2S_3)\}_2]$ **X**, $[ZnCl_2\{CS(NHC_6H_5)_2\}_2]$ **XI**, $[ZnCl_2\{CS(NHCH_3)_2\}_2]$ **XII**, $[ZnCl_2\{CSNH_2(NHCH_3)\}_2]$ **VIII**, $[ZnCl_2\{(C_2H_5)_2NCS_2\}_2]$ **XIV** were synthesized as outlined below. The complexes were refluxed in ethanol to give white and yellow powder, with the exception of complexes **V**, **IX** and **XIV** which were prepared in water at room temperature by mixing metal salt and diethyldithiocarbamate ligand. The single crystals of complex **II** were grown in ethanol. The solution was left in the refrigerator at -4 ^oC overnight. Attempts to grow crystals for other complexes yielded no crystals, hence the products obtained were mostly in powder form.

(a) $[CdCl_2\{(CH_3)_4(N_2C_2S_3)\}_2]$ (I)

In a typical hot solution of of tetramethylthiuram monosulfide (9.1 g, 43.6 mmol) in ethanol (20 ml) was added to a heated solution of cadmium chloride (4.0 g, 21.8 mmol). The mixture was stirred and refluxed for 2 h. The mixture was then filtered, washed with ethanol and left to dry overnight. Yield: 72%. Anal. Calcd.: C, 18.40; H, 3.09; N, 7.15; S, 24.56. Found: C, 18.48; H, 3.23; N, 7.02; S, 25.90. FT-IR (cm^{-1}): 3165(w), 2912(w), 1516(vs), 1377(s), 1229(s), 1138(s), 1039(w), 962(s), 848(w), 814(w). ^1H NMR (δ, CD_3COCD_3) ppm: 2.81 (s, CH_3)

(b) $[CdCl_2\{CS(NHC_6H_5)_2\}_2]$ (II)

Cadmium chloride (4.0 g, 21.8 mmol) was dissolved in ethanol (20 ml), followed by the addition of a solution of diphenylthiourea (9.9 g , 43.6 mmol) in ethanol (20 ml) while stirring. The solution was refluxed for 2 h, and then filtered to remove unreacted material. The filtrate was stored in a refrigerator at -4 ^oC. The yellow crystals were formed from the solution and filtered. Yield: 55%. Anal. Calcd.: C, 48.80; H, 3.78; N, 8.76; S, 10.02. Found: C, 48.74; H, 3.56; N, 8.89; S, 9.91. FT-IR (cm^{-1}): 3328(m), 3227(w), 3179(w), 1594(m), 1535(s), 1504(s), 1450(m), 1369(m), 1284(s), 1070(m), 1025(w), 940(m),

904(w), 755(m), 689(m), 628(w). ^{1}H NMR (δ, CD_3SOCD_3) ppm: 9.74 (s, br, 4H, NH), 7.24-7.43 (m, 20H, C_6H_5)

(c) $[CdCl_2\{CS(NHCH_3)_2\}_2]$ (III)

The complex was prepared in a similar manner to complex **I**. Yield: 78%. Anal. Calc.: C, 18.40; H, 4.12; N, 14.31; S, 16.37. Found: C, 18.57; H, 3.94; N, 14.02; S, 15.75. FT-IR (cm^{-1}): 3275 (vs), 3040(w), 1591(vs), 1539(s), 1437(m), 1373(w), 1300(m), 1186(w), 1144(w), 1032(m), 725(m), 664(m), 547(m). ^{1}H NMR (δ, CD_3SOCD_3) ppm: 7.52 (br, s, 4H, NH), 2.80 (s, 12H, CH_3)

(d) $[CdCl_2\{CSNH_2(NHCH_3)\}_2]$ (IV)

The complex was prepared in a similar manner to complex **I**. Yield: 78%. Anal. Calc.: C, 13.21; H, 3.33; N, 15.41; S, 17.64. Found: C, 13.96; H, 3.11; N, 15.68; S, 17.71. FT-IR (cm^{-1}): 3173(w), 2912(w), 1516(vs), 1383(vs), 1240(s), 1140(s), 1039(w), 950(s), 850(w). ^{1}H NMR (δ, CD_3COCD_3) ppm: 8.31, 7.86 and 7.58 (br, NH and NH_2), 2.94 (s, CH_3)

(e) $[CdCl_2\{(C_2H_5)_2NCS_2\}_2]$ (V)

In a typical experiment a solution of sodium diethyldithiocarbamate trihydrate (4.9 g, 21.8 mmol) in water was added into a beaker containing a solution of cadmium chloride (2.0 g, 10.9 mmol) in water. White precipitates formed immediately. The mixture was stirred for 2 h at room temperature, and then filtered through suction. The white powder was washed several times with water and then left to dry overnight at room temperature. Yield: 92%. Anal. Calc.: C, 29.37; H, 4.93; N, 6.85; S, 31.36. Found: C, 31.11; H, 5.02; N, 7.09; S, 31.71. FT-IR (cm^{-1}): 2962(m), 2925(w), 1506(vs), 1419(vs), 1346(m), 1271(vs), 1201(vs), 1144(s), 1064(vs), 979(vs), 906(vs), 833(s), 777(s), 606(w), 554(s). ^{1}H NMR (δ, CD_3COCD_3) ppm: 3.92 (s, 8H, CH_2), 2.76 (s, 12H, CH_3)

(f) $[CoCl_2\{(CH_3)_4(N_2C_2S_3)\}_2]$ (VI)

The preparation was similar to cadmium complexes, where cobalt chloride and tetramethylthiuram monosulfide were refluxed in a 1 : 2 mole ratio. Yield: 54%. Anal.

Calc.: C, 26.37; H, 4.43; N, 10.25; S, 35.20. Found: C, 26.18; H, 4.49; N, 10.37; S, 35.37. FT-IR (cm^{-1}): 1514(s), 1349(s), 1244(m), 1130(s), 978 (m). ^1H NMR (δ, CD_3COCD_3) ppm: 3.12 (s, CH_3)

(g) $[CoCl_2\{CS(NHCH_3)_2\}_2]$ (VII)

The complex was prepared in a similar manner to complex **III**, with cobalt chloride used instead of cadmium chloride. Yield: 83%. Anal. Calc.: C, 21.31; H, 4.77; N, 16.58; S, 18.92. Found: C, 21.28; H, 4.68; N, 16.55; S, 18.86. FT-IR (cm^{-1}): 3292(s), 3047(w), 2947(w), 1533(s), 1443(m), 1375(m), 1299(m), 1193(m), 1141(m), 1031(s), 712(m), 661(m). ^1H NMR (δ, CD_3COCD_3) ppm: 10.19 (br, s, 4H, NH), 3.13 (s, 12H, CH_3)

(h) $[CoCl_2\{CSNH_2(NHCH_3)\}_2]$ (VIII)

The complex was prepared in a similar manner to complex **IV**, with cobalt chloride used instead of cadmium chloride. Yield: 61%. Anal. Calcd.: C, 15.49; H, 3.90; N,18.07; S, 20.63. Found: C, 15.13; H, 3.85; N, 18.12; S, 20.59. FT-IR (cm^{-1}): 3400(m), 3296(s), 3211(m), 1620(s), 1568(s), 1494(w), 1450(w), 1404(w), 1292(m), 1109(w), 760(m), 696(m). ^1H NMR (δ, CD_3COCD_3) ppm: 11.50, 7.78 and 5.94 (br, NH and NH_2), 4.39 and 3.05 (s, CH_3)

(i) $[CoCl_2\{(C_2H_5)_2NCS_2\}_2]$ (IX)

The complex was prepared in a similar manner to complex **V**, with cobalt chloride used instead of cadmium chloride. Yield: 72%. Anal. Calcd.: C, 33.78; H, 5.67; N,7.88; S, 36.08. Found: C, 33.75; H, 5.59; N, 7.87; S, 35.89. FT-IR (cm^{-1}): 1487(s), 1443(s), 1362(w), 1265(s), 1209(s), 1136(s), 1070(m), 997(m), 912(m), 844(m), 781(m). ^1H NMR (δ, CD_3COCD_3) ppm: 3.68 (s, 8H, CH_2), 2.78 (s, 12H, CH_3)

(j) $[ZnCl_2\{(CH_3)_4(N_2C_2S_3)\}_2]$ (X)

The complex was prepared in a similar manner to complex **I**, with $ZnCl_2$ used instead of $CdCl_2$. Yield = 57%. Anal. Calcd.: C, 26.07; H, 4.38; N,10.14; S, 34.73. Found: C, 26.11; H, 4.39; N, 10.11; S, 34.77. FT-IR (cm^{-1}): 1504(s), 1435(w), 1369(s), 1234(s), 1139(s),

1047(m), 954(s), 860(s). ^{1}H NMR (δ, CD_3COCD_3) ppm: 3.41(s, CH_3)

(k) $[ZnCl_2\{CS(NHC_6H_5)_2\}_2]$ (XI)

The complex was prepared in a similar manner to complex **II**, with $ZnCl_2$ used instead of $CdCl_2$. However, no crystals were grown in this case. White powder precipitated from the reaction. Yield = 63%. Anal. Calcd.: C, 52.66; H, 4.08; N,9.45; S, 10.79. Found: C, 52.65; H, 4.08; N, 9.47; S, 10.82. FT-IR (cm^{-1}): 3195(m), 3032(m), 15919m), 1524(s), 1444(m), 1338(m), 1277(m), 1065(m), 1012(m), 930(m), 758(s), 688(s), 634(m). ^{1}H NMR (δ, CD_3COCD_3) ppm: 8.97 (s, 4H, NH), 7.48-7.09 (m, 20H, C_6H_5)

(l) $[ZnCl_2\{CS(NHCH_3)_2\}_2]$ (XII)

The complex was prepared in a similar manner to complex **III**, with $ZnCl_2$ used instead of $CdCl_2$. Yield = 88%. Anal. Calcd.: C, 20.91; H, 4.68; N, 16.26; S, 18.75. Found: C, 20.95; H, 4.67; N, 16.28; S, 18.71. FT-IR (cm^{-1}): 3287(s), 3031(m), 2949(w), 1589(s), 1537(s), 1442(m), 1375(m), 1303(m), 1190(w), 1142(w), 1032(s), 716(m), 663(m). ^{1}H NMR (δ, CD_3COCD_3) ppm: 8.41 (br, s, 4H, NH), 2.44 (s, 12H, CH_3)

(m) $[ZnCl_2\{CSNH_2(NHCH_3)\}_2]$ (VIII)

The complex was prepared in a similar manner to complex **IV**, with $ZnCl_2$ used instead of $CdCl_2$. Yield = 71%. Anal. Calcd.: C, 15.17; H, 3.82; N, 17.70; S, 20.21. Found: C, 15.21; H, 3.84; N, 17.69; S, 20.23. FT-IR (cm^{-1}): 3394(m), 3296(s), 3207(m), 1624(s), 1573(s), 1502(m), 1450(m), 1406(m), 1298(s), 1157(w), 1118(w), 764(m), 700(m), 607(m). ^{1}H NMR (δ, CD_3COCD_3) ppm: 8.22, 7.73 and 7.53 (br, NH and NH_2), 3.78 and 2.93 (s, CH_3)

(n) $[ZnCl_2\{(C_2H_5)_2NCS_2\}_2]$ XIV

The complex was prepared in a similar manner to complex **V**, with zinc chloride used instead of cadmium chloride. Yield = 93%. Anal. Calcd.: C, 33.18; H, 5.56; N,7.74; S, 35.43. Found: C, 33.15; H, 5.52; N, 7.72; S, 35.41. FT-IR (cm^{-1}): 2972(w), 2829(w), 1500(s), 1429(s), 1348(m), 1269(s), 1201(s), 11439s), 1070(s), 989(s), 910(s), 841(m), 777(m). ^{1}H NMR (δ, CD_3COCD_3) ppm: 3.14 (s, 8H, CH_2), 2.11 (s, 12H, CH_3).

3.4 Preparation of nanoparticles

3.4.1 Preparation of hydrphobic semiconductor nanoparticles

In a typical experiment, hexadecylamine (HDA) (4.0 g) was loaded into a reaction three-necked flask and then heated to a specified temperature under a nitrogen flow. About 1.0 g of the precursor was dispersed in 5 ml of tri-n-octylphosphine (TOP), and then the solution was swiftly added into the hot HDA solution under stirring, which makes the temperature of the reaction mixture, drop by 15 to 20 ^{o}C. Heating was continued to recover the temperature (120 ^{o}C, 160 ^{o}C or 180 ^{o}C), and then the reaction was maintained for 1 h. The solution was then cooled to about 70 ^{o}C and an excess amount of methanol was added. The flocculants formed was centrifuged and the supernatant decanted and then the isolated solid was dispersed in toluene. The above centrifugation and isolation procedure was then repeated three times for the purification of the prepared CdS nanocrystals.

3.4.2 Preparation of hydrophilic semiconductor nanoparticles

(a) Ligand exchange with chloroform

To a three-necked flask, 0.5 g of HDA-capped CdS was dissolved in chloroform (10 ml). A mixture of glucose (5 g) or sucrose (5 g) and methanol (10 ml) was added while vigorously stirring. Addition of the above mixture resulted in the formation of an oil-in-water. Stirring was continued for 24 h at room temperature. Chloroform was then evaporated through heating and a small yellowish sticky solid which is partially soluble in water was obtained.

(b) Ligand exchange with pyridine

To a three-necked flask, 1.0 g of HDA-capped CdS or ZnS nanoparticles in 5 ml of pyridine was added. The mixture was heated to 40 ^{o}C and stirred while vigorously stirring for 1 h. After cooling to room temperature, hexane was added to precipitate the nanoparticles, followed by centrifugation, and finally the supernatant was decanted. A mixture of either glucose or glucuronic acid and methanol was added to a three-necked flask followed by the transfer of the nanoparticles. The mixture was heated for an hour at 40 ^{o}C and then overnight at room temperature. Chloroform and ethyl acetate were added to

precipitate the nanoparticles, followed by the addition of diethyl ether for the removal of excess pyridine. Nanoparticles were then centrifuged and the supernatant decanted. A small amount of the as-prepared particles was dispersed in a dimethylformamide for analysis through UV-Visible and fluorescence spectroscopy.

(c) Direct Chemical Method

The zinc chloride (2.50 g, 18.30 mmol) and glucuronic acid (6.00 g) were dissolved into 30 ml of ethylene glycol and heated to 100 ^{o}C. Tetramethylthiuram monosulfide (3.82 g, 18.30 mmol) was separately dissolved into another 30 ml ethylene glycol and heated up to 100 ^{o}C. The two solutions were then mixed in a three necked flask and heated to 160 ^{o}C while vigorously stirring. The pH of the solution was adjusted to 9 by adding a solution of sodium hydroxide. Upon completion of the reaction, the solution was allowed to cool, followed by the addition of acetone to precipitate particles. The particles were separated by a centrifuge. The supernatant was discarded.

3.5 Protocol for toxicity

3.5.4 Culture conditions of cell line

Monocyte-derived macrophages U937 cells were maintained *in vitro* in suspension culture under standard conditions in RPMI (Roswell Park Memorial Institute)-1640 10% media supplemented with heat-inactivated FBS (Fetal Bovine Serum), penicillin and Streptomycin. They were maintained in a fully humidified atmosphere containing 5% CO_2 (carbon dioxide) at 37^{o}C until the cells reach 90% confluency. Cells were stimulated with PMA (phorbol-12-myristate-13-acetate) for 3 days. Viability of macrophages was assessed by trypan blue dye exclusion for 80-90% viability.

3.5.1 Protocol for sub-culturing U937cells

The cell suspension was transferred to a 50 ml falcon tube, and centrifuged for four minutes at 500 x *g*. The supernatant was discarded. The pellet was resuspended in 5 ml media (RPMI with 10% FBS). The cells were counted using hemocytometer. Cells were then

diluted to appropriately to a concentration of 1 x 10^6 cells per ml with media and then transferred into a flask. The flask was placed, lying down, in an incubator.

3.5.2 Determining cell count and viability using a hemocytometer

In an eppendorf, 90 µl of trypan blue solution was added, followed by the addition of 10 µl of the resuspended cell suspension and then mixed by pipetting. To a clean hemocytometer, 10 µl of the above solution was added, while avoiding air bubbles. The cells in the four corner squares were counted to determine the viability, where clear cells are alive and blue cells dead.

3.5.3 Differentiation of U937 cells

For performing the experiments, differentiated cells were required. All steps including the dilution of cells were performed on the day of sub-culturing. A 15 ml of cells was added to a flask, followed by the addition of 9.5 µl of a 50 µM PMA solution in DMSO (dimethyl sulfoxide). The flask was placed, lying down in an incubator for three days, followed by the performance of the experiments.

3.5.5 Treatments

For the glucose dehydrogenase assay as well as the cytotoxicity and genotoxicity assays, cultured U937 cells were incubated with the semiconductor nanocrystals or QDs at various concentrations, and then incubated for 1, 3, 24 and 48 hours at 37°C

3.5.6 Quantification of ATP level and LDH release (cell viability and cytotoxicity)

The cell viability was determined using the CellTiter-Glo luminescent assay (Promega). The cell viability assay determines mitochondrial activity in cells by quantifying the level of ATP present which is proportional to the luminescent signal, in so determining the number of viable cells. The assay was performed according to the manufacturer's instructions. Briefly, following the treatment of cells on a 96-well plate, the CellTiter-Glo reagent was added to lyse the cells, for the release of the ATP. The plate was incubated at

room temperature, with shaking, to stabilize the luminescence which was then recorded on a FLx 800 fluorometer.

3.5.7 Comet Assay (DNA damage)

The alkaline version of the Comet assay has ability to detect single-strand DNA breaks, double-strand DNA breaks, oxidative induced base damages, alkali-labile sites, and sites undergoing DNA repair. The Comet assay was performed according to the method used by Collins *et al.* [6], with minor modifications. Briefly, following the treatments, cells were washed with PBS and embedded onto pre-coated microscope slides with agarose. Embedded cells were then lysed and rinsed with PBS followed by the unwinding of the DNA, using an alkaline treatment. Electrophoresis was performed on the slide at 25 V and 300 mA for 1 hour. Slides were neutralized and left overnight to dry. Ethidium bromide was used to stain the DNA on the slide and was visualized on a fluorescent microscope where 50 images were captured and analyzed by specialized image analysis software (Komet 5.5) using the percentage Tail DNA parameter to express the results.

3.6 References

1. Bruker (2005a). APEX2. Version 2.0-1. Bruker AXS Inc., Madison, Wisconsin, USA.
2. Bruker (2005b). SAINT+. Version 6.0. (includes XPREP and SADABS) Bruker AXS Inc., Madison, Wisconsin, USA.
3. Bruker (1999). SHELXTL. Version 5.1. (includes XS, XL, XP, XSHELL) Bruker AXS Inc., Madison, Wisconsin, USA.
4. A. L. Spek, *J. Appl. Cryst.* **36,** 7, 2003.
5. L. J. Farrugia, *J. Appl. Cryst.*, **30,** 565, 1997.
6. A. R. Collins, M. Dušinská, C. M. Gedik, R. Štětina, *Environment. Health Pespect.*, **104,** 465, 1996.

Chapter 4

Hydrophobic semiconductor nanoparticles synthesized from cadmium, zinc and cobalt complexes as precursors and their characterization

4.1 Introduction

The most widely utilized quantum dots to date are II-VI semiconductor nanocrystals. Preparation methods for the synthesis of high quality and nearly monodisperse semiconductor nanoparticles of quantum dots have typically utilized tri-n-octylphosphine oxide (TOPO), hexadecylamine (HDA) and trioctylphosphine (TOP) as these compounds provide the most controlled growth conditions. Prior to the use of TOPO, CdSe nanocrystals were prepared by using organometallic reagents in inverse micellar solution [1]. Bawendi and co-workers showed that injection of the metal-organic precursors into a hot reaction pot with TOPO and TOP as solvent resulted in a short burst of homogeneous nucleation and a narrow size distribution covered by TOPO ligands [2]. Size control is primarily achieved by varying reaction conditions. Talapin *et al.* [3] showed that incorporation of alkylamines such as HDA into the synthesis led to much improved quantum yields. HDA ligands with high boiling points are superior agents as growth solvents for high temperature chemical synthesis methods. Recently, high fluorescent colloidal quantum dots with a narrow size distribution were synthesized in the presence of HDA agents [4]. TOPO and HDA, which serve as the primary surface ligands, are completely soluble in hydrophobic solvents such as toluene, chloroform and hexanes

Different complexes have been reported in the praparation of semiconductor nanoparticles. Ligands such as thiuram disulfides, dithiocarbamates, substituted thioureas, ethylxantates and many more were used for the praparation of cadmium, zinc, copper, cobalt complexes, which were employed as precursors for semiconductor nanoparticles. Memon *et al.* [5] used dialkyldithiocarbamate cadmium complex [$Cd(S_2CNHC_{12}H_{25})_2$] as a precursor for thermolysis of CdS nanoparticles capped by HDA. TEM results showed multipods, along with some single rods which were grown at 200 ^oC for 2.5 h. The use of tetramethylthiuram disulfide cobalt complex as a precursor for CoS nanoparticles was reported to give spherical shape by Moloto *et al.* [6]. In another reported work, Moloto *et al.* [7]

thermolysed tetramethylthiuram disulfide cadmium complex to yield CdS nanoparticles capped by HDA. The rod-shaped particles were obtained as the precursor concentration was increased. However, when the same precursor was thermolysed in TOPO, under the same conditions, spherical particles were obtained. The use of metal alkylthiourea complexes as precursors for the synthesis of CdS nanoparticles have been previously reported [8]. The N,N-diisopropylthiourea and N,N-dicylclohexylthiourea zinc(II) complexes were synthesized and then thermolysed in HDA to give ZnS. The synthesized ZnS nanoparticles resulted in a mixture of elongated and spherical particles. When the cadmium complexes of the same ligands (N,N-diisopropylthiourea and N,N-dicylclohexylthiourea) were synthesized under the same conditions, only rods particles were obtained [9, 10].

Recently, there has been work reported on the deposition of II/VI materials in quantum dot form [11]. Semiconductor thin films have been synthesized by a wide range of routes including spray pyrolysis [12], metal organic chemical vapor deposition [13], chemical bath deposition [14] and sputtering [15]. Chemical bath deposition is an alternative route which is simple, convenient and cheap. Thin films of CdS and ZnS by the use of cadmium diethyldithiocarbamate and zinc diethyldithiocarbamate as cadmium and zinc sources and Na_2S as sulfide source have been successfully deposited at the interface of toluene and water. Different parameters such as temperature, time and precursors concentration were studied, with the temperature having a paramount effect. The temperature has been reported to affect both crystal size and morphology, while time and precursors concentration influenced the thickness of the films [16]. Ortega-Borges and Lincot [17], utilized ethylenediamine/thiourea/cadmium acetate system to deposit polycrystalline films of CdS of good quality. The supersaturation of the solution with respect to hydroxy complexes of cadmium appeared to be a key factor controlling the quality of the films deposited. The mechanism of deposition of the films must incorporate both hydrolysis of thiourea to generate sulfide ions and their subsequent reaction with cadmium.

In this work, the synthesis of the metal sulfide or semiconductor nanoparticles was achieved by employing the single source precursor method. This method was initially reported by Trindade and O'Brien [18]. The properties of these semiconductor nanoparticles were thoroughly studied and reported. Since semiconductor nanoparticles or quantum dots have become an interesting subject all over the world because of their unique size and shape, the use of TEM for their studies or analysis was found to be very

significant. The IR spectra of the synthesized semiconductor nanoparticles/QDs showed similarity based on the capping agents used. All particles (CdS, Co_xS_y and ZnS) capped by HDA did not show significant differences when analysed through FT-IR spectroscopy. This was also the same in the case of particles capped by TOPO irrespective of the complex used. Therefore, this prompted us to record IR results for CdS nanoparticles capped by HDA, TOPO and HDA-TOPO synthesized from complex **5**. The nanoparticles prepared are known to be different to their bulk materials in terms of colour, sizes, phases. There are a lot of parameters that influences the size and shape of quantum dots. Temperature, reaction time, ratio of the capping agent and precursors employed have an effect on the size and shape of the particles. For example, higher temperatures normally lead to bigger sizes of the particles.

4.2 Results and discussion

4.2.1 Synthesis of metal complexes and their characterization

All complexes **(I-XIV)** used in this work are easily synthesized, air stable and can be synthesized under atmospheric bench-top conditions, which meets the goal of environmentally friendly synthesis and low cost. Interest in the ligands used, i.e., alkylthioureas, alkyldithiocarbamate and alkylthiuram monosulfide, mounted due to their ability to donate or provide sulphur ion to the heavy metals which are cadmium, cobalt and zinc. The prepared complexes were further used as single source precursors for CdS, Co_xS_y and ZnS nanoparticles. Complexes were refluxed for 2 h while stirring in 1:2 ratio (metal salt: ligand) with ethanol or methanol as solvents (Scheme 3.1). This is with the exception of diethyldithiocarbamates metal complexes which were prepared in water and stirred for two hours at room temperature. The complexes were characterized using elemental analysis (EA), Fourier transform infrared (FT-IR) spectroscopy, nuclear magnetic resonance (NMR) spectroscopy and thermal gravimetric analysis (TGA).

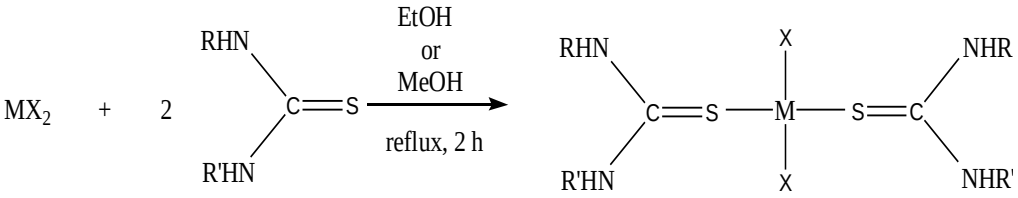

A

Alkylthiourea

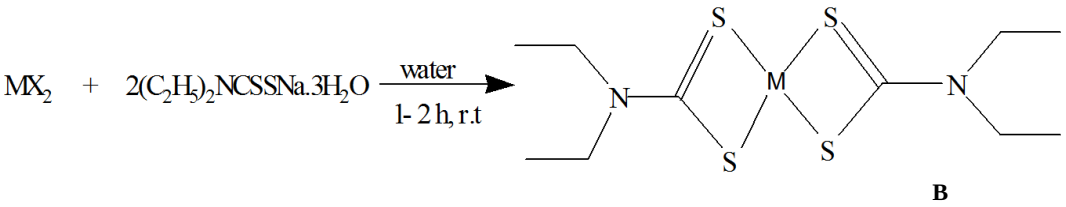

B

Alkyldithiocarbamate

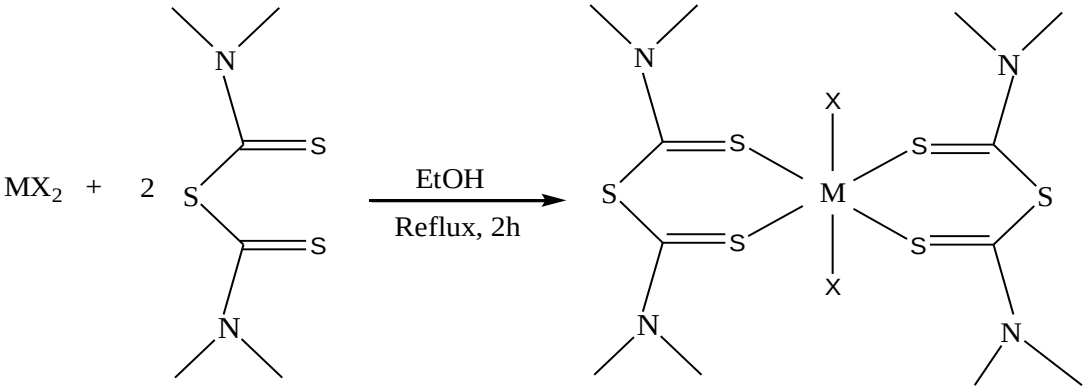

C

Alkylthiuram monosulfide

M= Cd, Zn, Co R = R' = CH_3, C_6H_5 R = H, R' = CH_3 X = Cl

r.t. = room temperature.

Scheme 4.1: Preparation of Cd, Zn or Co complexes from alkyl or aryl substituted thiourea, diethyldithiocarbamate or tetramethylthiuram monosulfide ligands

4.2.1.1 Spectroscopic studies

(a) Infrared spectra

Infrared spectroscopy is a relevant technique in determining the binding mode of the ligand to the metal. More studies on infrared absorption spectra were reported for some metal

thiourea complexes. Thiourea and its derivatives are well known to have the ability of binding to the metal atoms through different atoms such as the sulphur atom of the C=S group, and the nitrogen atoms of the NH_2 or NHR groups. Yamaguchi *et al.* [19, 20] established that the ν(NCN) and the ν(CS) frequencies are respectively increased and lowered on sulphur coordination while the opposite occurs on nitrogen coodination. In the platinum complexes they prepared, they reported that the higher frequency N-H absorption bands in the spectrum of thiourea were not shifted to lower frequencies on the formation of the metal-thiourea complexes, which indicate that the nitrogen to metal bonds are not present and that therefore the bonding in these complexes must be between the sulfur and metal atoms. To further elucidate the report above, Belluco *et al.*[21] studied the infrared spectra of several platinum complexes with thiourea derivatives $[PtT_4]Cl_2$ where T=N, N'–dimethylthiourea, methylthiourea, and tetramethylthiourea. They observed a decrease of the frequency of ν(NH) and therefore suggested that the coordination is through the nitrogen atom. In another observation which supports the coordination of the metal to sulphur, Macrotrigiano *et al.*[22] studied ethylthiourea complex and reported that the ν(NH) frequencies at 3340, 3240 and 3160 cm^{-1} for the free ligand increase in the complexes. Also the $\delta(NH_2)$ band observed in the ligand at 1681 cm^{-1} was shifted to higher frequencies. The strong band at 1542 with a shoulder at 1560 cm^{-1} was assigned mainly to $\nu(NCN)_{asym.}$ with some contributions of ν(CS) and NH_2 deformation. In all their complexes, this band increased in energy on coordination, indicating an increased double bond character of the CN bond. The ν(CS) frequency in the ligand was assigned to 738 cm^{-1}. In the complexes this band was split into two bands, one or both shifted to lower frequencies in agreement with a decreased double bond character of the CS bond resulting from a sulphur coordination of the ligand to the metal. Table 3.1 shows the infrared spectral values of selected bands of interest of all complexes synthesized. The complexes revealed some differences in terms of the bands shift as compared to their respective ligands.

Figure 4.1 shows the infrared spectra of dimethylthiourea ligand (a) and its cadmium complex (b). The band observed at 3277 cm^{-1} is undoubtedly assigned to the N-H stretching frequency for the complex. It is interesting to notice that the higher frequency N-H absorption band was not shifted to lower frequency on the formation of the metal-dimethylthiourea complex. This simply indicates that the nitrogen to metal bonds are not present and therefore the bonding in this complex is between the sulfur and the cadmium. The bonding of sulphur to metal ion is expected to increase the contribution of the highly

polar structure to the dimethylthiourea molecule, resulting in a greater double bond character for the nitrogen to carbon bond and a greater single bond character for the carbon to sulfur bond. The free ligand bands observed at 1553 and 1352 cm^{-1}, with contribution of *v*(NCN) stretching, have shifted to higher frequencies by 24 and 23 cm^{-1}, respectively, in the complex. The free ligand band observed at 719 cm^{-1}, which is due to a contribution of *v*(CS) stretching, has shifted to lower frequency by 2 cm^{-1} in the complex. This behaviour signify a decrease in the double bond character of the C=S bond which confirms the the sulphur coordination of dimethylthiourea to the cadmium metal, as stated above.

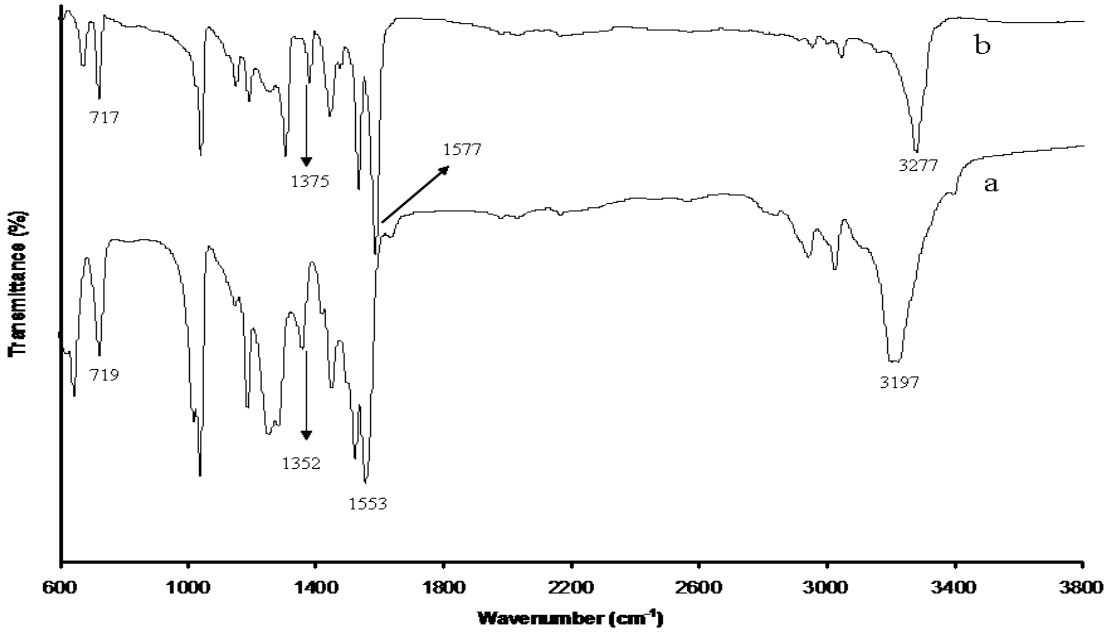

Figure 4.1: Infrared spectra of dimethylthiourea (a) and its cadmium complex (b)

Figures 4.2 depicts the infrared spectra of sodium diethyldithiocarbamate trihydrate ligand (a), its cobalt complex (b), and its cadmium complex (c), while the infrared spectra of tetramethylthiuram disulfide ligand (a) and its zinc complex are shown in Figure 4.3. Both thiuram monosulfide and dithiocarbamate complexes present the same absorption bands in the infrared region. They both have the C=N stretching band, C-N stretching (from CH_3-N), C=S and C-S bands. However, there are two differences that could be deduced, that is (i) the positions of these bands, and (ii) in the tetraalkyl thiuram disulfides a S-S stretching mode is also present, although the corresponding band is very weak and only possible to observe in some special compounds. The four vital bands of thiuram monosulfide zinc complex appear in the region of 800-1510 cm^{-1}; (i) a strong band at about 1504 cm^{-1} called

"the thioureide (C-N) band", (ii) a band positioned at 1234 cm^{-1} due to the C-N vibration of the alkyl group, (iii) a band at 957 cm^{-1} which corresponds to the C=S stretching mode, and (iv) a band at 858 cm^{-1} which is due to the C-S stretching mode. The band correspoding to the S-S stretching mode is not observed in Figure 4.3. This vibration is normally observed as a very weak band in the 400-500 cm^{-1} region, and is identified only as a very strong Raman line. In the case of diethyldithiocarbamate cobalt and cadmium complexes (Figure 4.2), the four vital bands are positioned almost at the same region, that is 1496 cm^{-1} (C=N), 1267 cm^{-1} (CH_3-N), 987 cm^{-1} (C=S) and 839 cm^{-1} (C-S). However, comparison of complexes and their ligands bsnds showed some shift. The bands due to all complexes had shifted to higher wavenumbers which signify formation of complexes.

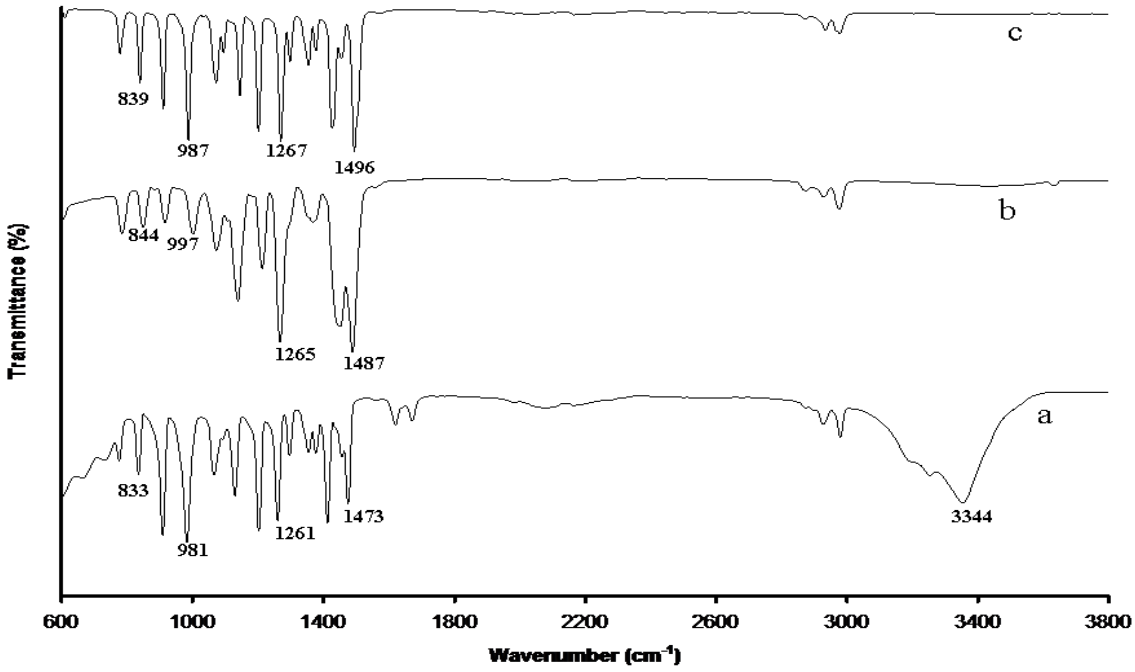

Figure 4.2: FT-IR spectra of sodium diethyldithiocarbamate trihydrate (a), its cobalt complex (b) and its cadmium complex (c)

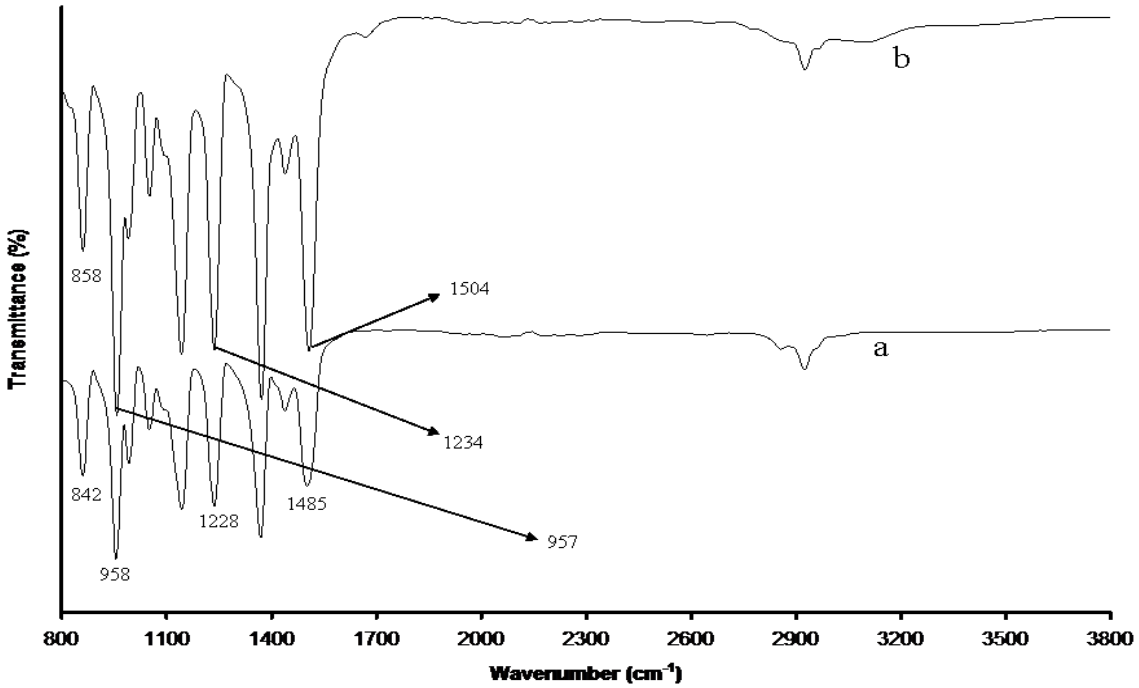

Figure 4.3: FT-IR spectra of tetramethylthiuram monosulfide ligand (a) and its zinc complex (b)

Table 4.1: IR spectral data for complexes (**I - XIV**)

Complex	**Selected i.r. bands (cm^{-1})**			
	υ (N-H)	υ (C=S)	υ (C-N)	υ (C-S)
$[CdCl_2\{(CH_3)_4(N_2C_2S_3)\}_2]$ **(I)**	-	956	1236,1374, 1502,1589	852
$[CdCl_2\{CS(NHC_6H_5)_2\}_2]$ **(II)**	3231,3323	688,759	1446,1533, 1589	-
$[CdCl_2\{CS(NHCH_3)_2\}_2]$ **(III)**	3277	717	1375,1577	-
$[CdCl_2\{CSNH_2(NHCH_3)\}_2]$ **(IV)**	3186,3283, 3335	613,711	1294,1409, 1485,1560	-
$[CdCl_2\{(C_2H_5)_2NCS_2)\}_2]$ **(V)**	-	987	1267,1496	839
$[CoCl_2\{(CH_3)_4(N_2C_2S_3)\}_2]$ **(VI)**	-	978	1244,1385	877
$[CoCl_2\{CS(NHCH_3)_2\}_2]$ **(VII)**	3045,3292	661,713	1300,1375, 1442,1431, 1589	-
$[CoCl_2\{CSNH_2(NHCH_3)\}_2]$ **(VIII)**	3211,3294, 3398	698,759	1292,1404, 1497,1566	-
$[CoCl_2\{(C_2H_5)_2NCS_2)\}_2]$ **(IX)**	-	997	1265,1444, 1487	844
$[ZnCl_2\{(CH_3)_4(N_2C_2S_3)\}_2]$ **(X)**	-	957	1234,1504	858
$[ZnCl_2\{CS(NHC_6H_5)_2\}_2]$ **(XI)**	3032,3198	692,756	1277,1338, 1524,1591	-
$[ZnCl_2\{CS(NHCH_3)_2\}_2]$ **(XII)**	3053,3287	663,715	1304,1443, 1537,1589	-
$[ZnCl_2\{CSNH_2(NHCH_3)\}_2]$ **(XIII)**	3207,3296, 3395	607,700	1298,1406, 1574	-
$[ZnCl_2\{(C_2H_5)_2NCS_2)\}_2]$ **(XIV)**	-	989	1267,1354, 1429,1502	841

(b) NMR spectroscopy

^{1}H NMR spectroscopy has been used to characterize the conformations in the ligands of the –NH–CS–NH– group in a series of di- and tri-substituted thioureas. In the studies done by Galabov *et al.* [23] for the conformational isomerism in a series of N,N'-diarylthioureas, it was shown that compounds participate in a complex equilibrium between several forms. Various conformational forms are detected resulting from the possibility of *cis* and *trans* arrangements of the –CS–NH– groups. The *trans* –CS–NH– form occurs when there is no steric hindrance whereas with bulkier aliphatic or aromatic substituents a proportion of *cis* structures is found. Some ambiguity exists in the interpretation of the experimental data of cases where *cis* and *trans* –CS–NH–forms are found simultaneously in that no definite conclusion can be reached as to whether the two forms appear in equilibrium or as a stabilized *cis-trans* structure.

The ^{1}H NMR spectra of the selected complexes (**II**, **III, V** and **X**) were recorded at room temperature in deuterated acetone (CD_3COCD_3) or deuterated dimethylsulfoxide (CD_3SOCD_3) in a standard 5 mm tube at 300 MHz. The ^{1}H NMR data for selected complexes are listed in Table 4.2. There is a collapse in the multiplicity of the signals of protons associated with the nitrogen atoms, either neighbouring or directly bonded to them. This observation is consistent with studies of these compounds by variable temperature NMR [24]. The ^{1}H NMR spectrum of complex **II** (Figure 4.4), recorded in deuterated dimethylsulfoxide, depicts a downfiled broad peak at 9.74 ppm that is assigned to the NH protons. The multiplet peaks appearing from 7.24-7.43 ppm are due to the phenyl rings protons. The ^{1}H NMR spectrum of complex **III** (Figure 4.5), which was recorded in deuterated dimethylsulfoxide, also shows a downfield broad singlet peak, appearing at 7.52 ppm which is assigned to the NH protons. A broad singlet peak at 2.80 ppm was also observed, and that peak is due to the methyl protons. The peak appearing at 3.32 is due to the solvent used, which is dimethylsulfoxide. Figure 4.6 shows the ^{1}H NMR spectrum of complex **V** recorded in deuterated acetone. As expected, methyl and methylene protons of complex **V** resonate at high field strength . The peak appearing at 3.91 ppm is due to the methylene protons, whilst methyl protons are represented by a peak at 2.77 ppm. The ^{1}H NMR spectrum of complex **X** recorded in deuterated acetone (Figure 4.7), depicts single resonance appearing low field at 3.43 ppm. The singlet peak is due to the presence of methyl protons. Comparison between ^{1}H NMR spectra of complexes and their respective

ligands (not shown) revealed significant differences. The proton peaks of the complexes were found to have shifted downfield as compared to their respective ligands proton peaks. This was interesting since it revealed formation of the complexes. The metals used, withdraw electrons from the ligands forcing the peaks to shift.

Table 4.2: ^{1}H NMR data for selected complexes

Complex (compound)	**δ values (ppm) assignments**
$[CdCl_2\{(CH_3)_4(N_2C_2S_3)\}_2]$ **(I)**	2.81 (s, CH_3)
$[CdCl_2\{CS(NHC_6H_5)_2\}_2]$ **(II)**	9.74 (br, s, NH), 7.43 – 7.24 (m, C_6H_5)
$[CdCl_2\{CS(NHCH_3)_2\}_2]$ **(III)**	7.52 (br, s, NH), 2.80 (br, s, CH_3)
$[CdCl_2\{CSNH_2(NHCH_3)\}_2]$ **(IV)**	8.31, 7.86 and 7.58 (br, NH and NH_2), 2.94 (s, CH_3)
$[CdCl_2\{(C_2H_5)_2NCS_2)\}_2]$ **(V)**	3.92 (s, CH_2), 2.76 (s, CH_3)
$[CoCl_2\{(CH_3)_4(N_2C_2S_3)\}_2]$ **(VI)**	3.12 (s, CH_3)
$[CoCl_2\{CS(NHCH_3)_2\}_2]$ **(VII)**	10.19 (br, s, NH), 3.13 (s, CH_3)
$[CoCl_2\{CSNH_2(NHCH_3)\}_2]$ **(VIII)**	11.50, 7.78 and 5.94 (br, NH and NH_2), 4.39 and 3.05 (s, CH_3)
$[CoCl_2\{(C_2H_5)_2NCS_2)\}_2]$ **(IX)**	3.68 (s, 8H, CH_2), 2.78 (s, 12H, CH_3)
$[ZnCl_2\{(CH_3)_4(N_2C_2S_3)\}_2]$ **(X)**	3.41 (s, CH_3)
$[ZnCl_2\{CS(NHC_6H_5)_2\}_2]$ **(XI)**	8.97 (s, 4H, NH), 7.48-7.09 (m, 20H, C_6H_5)
$[ZnCl_2\{CS(NHCH_3)_2\}_2]$ **(XII)**	8.41 (br, s, 4H, NH), 2.44 (s, 12H, CH_3)
$[ZnCl_2\{CSNH_2(NHCH_3)\}_2]$ **(XIII)**	8.22, 7.73 and 7.53 (br, NH and NH_2), 3.78 and 2.93 (s, CH_3)
$[ZnCl_2\{(C_2H_5)_2NCS_2)\}_2]$ **(XIV)**	3.14 (s, 8H, CH2), 2.11 (s, 12H, CH_3)

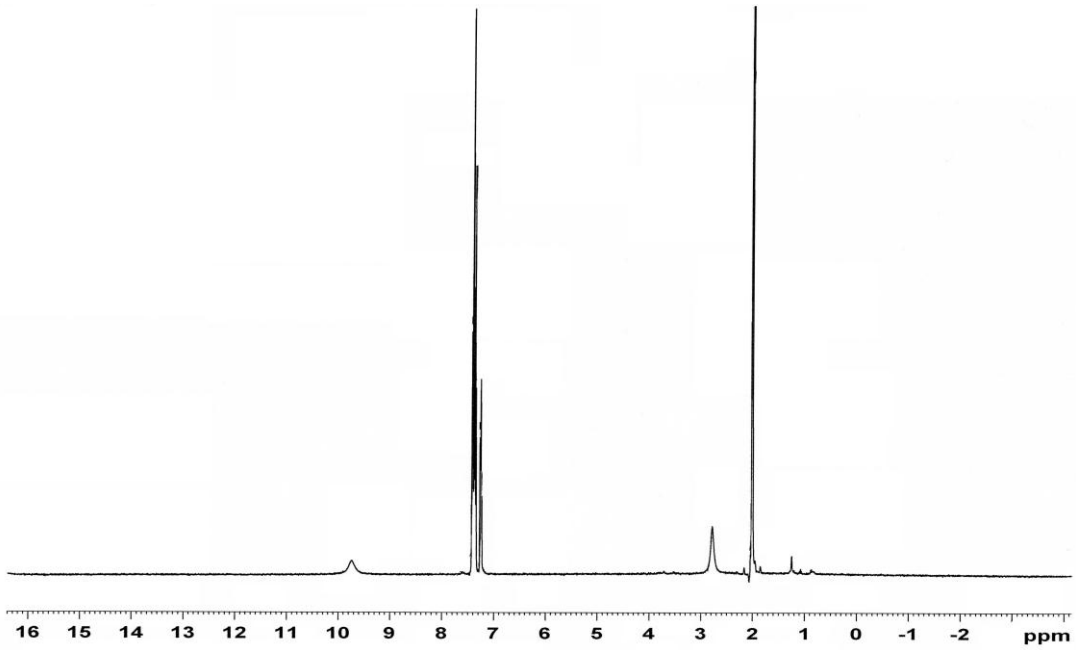

Figure 4.4: ^{1}H NMR spectrum of $[CdCl_2\{CS(NHC_6H_5)_2\}_2]$ **II** recorded in CD_3SOCD_3

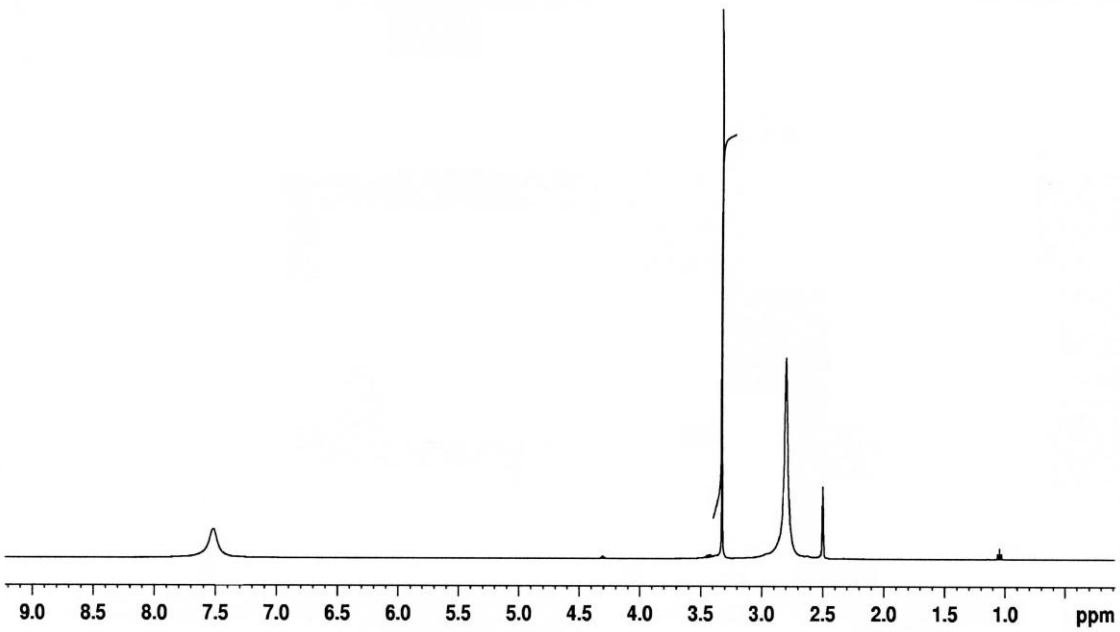

Figure 4.5: ^{1}H NMR spectrum of $[CdCl_2\{CS(NHCH_3)_2\}_2]$ **III** recorded in CD_3SOCD_3

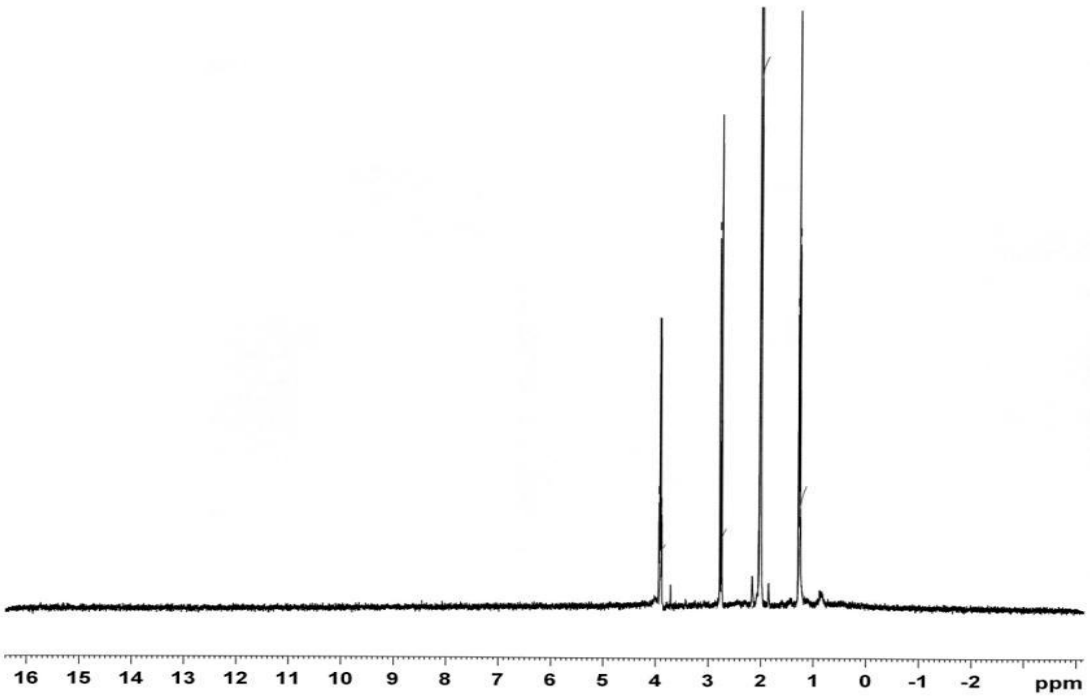

Figure 4.6: ^{1}H NMR spectrum of $[CdCl_2\{(C_2H_5)_2NCS_2)\}_2]$ **V** recorded in CD_3COCD_3.

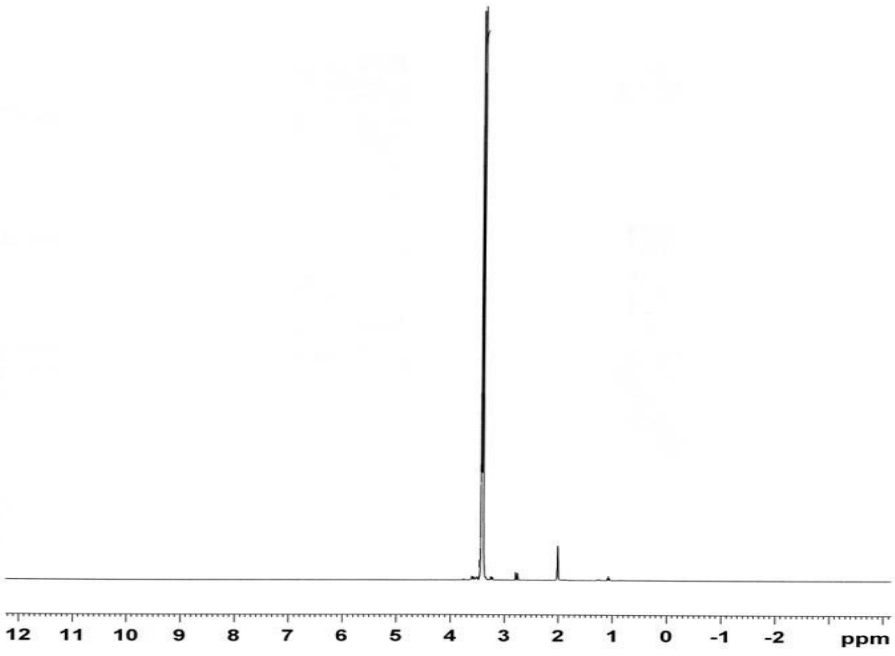

Figure 4.7: ^{1}H NMR spectrum of $[ZnCl_2\{(CH_3)_4(N_2C_2S_3)\}_2]$ **X** recorded in CD_3COCD_3.

(c) Thermogravimetric analysis

Synthetic studies on chemical and physical changes provided by heating in chemical compounds brings information on the mechanisms and steps of their decomposition, and therefore permit determination of the kinetic parameters of the reactions [25] [26]. The metal compounds of thioureas comprise an extensive series of sulphur-bonded complexes. Thermal decomposition studies of some nickel (II) thiourea compounds [27], and acetylthiourea complexes of molybdenum [28] and cadmium (II) [29] have been done. Thermal decompsition of alkylthiourea metal complexes of copper, zinc, cadmium and tin in static air led to the formation of metal sulphide in a main degradation step between 200 ^{o}C and 300 ^{o}C.

The thermogravimetric analyses (TGA) were conducted to evaluate the physical behaviour of cadmium, cobalt and zinc complexes of substituted thiourea, diethyldithiocarbamato and tetramethylthiuram monosulfide. The thermal decomposition of the complexes reported in this work was studied by using thermogravimetric analysis method under inert atmosphere. The TGA curves are shown in Figures 4.8, 4.9, and 4.10. The TGA curves for the cadmium complexes (**I**, **II**, **IV** and **V**), which undergo multistage decomposition, are shown in Figure 4.8.

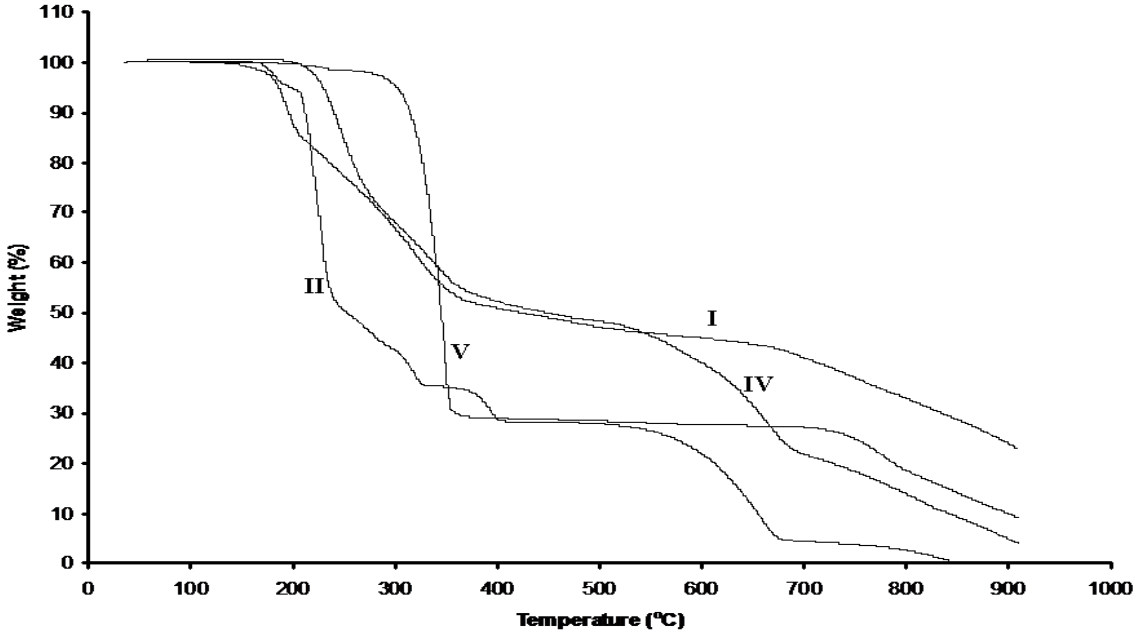

Figure 4.8: TGA (under nitrogen) curves for cadmium complexes **I, II, IV** and **V**

The TGA curves indicate that the loss of weight of cadmium complexes started at around 200 ^{o}C and continued to about 400 ^{o}C, signifying loss of most of the organic part of the molecule and the chloride. A period of slow loss of weight led to the formation of the metal sulphide, which was completed at about 800 ^{o}C. The TGA curves for cobalt complexes, which also displayed the beginning of weight or mass loss at 200 ^{o}C and continued to 400 ^{o}C, are shown in Figure 4.9. Complexes **VII** and **VIII** reveal a multiple stage decomposition. Contrary to complexes **I**, **II**, **IV**, **V**, **VII** and **VIII**, that decompose in more than one stage, complexes **VI** and **IX** show predominantly single stage decomposition. Figure 4.10 shows the TGA curves of zinc complexes (**X**, **XI**, **XII**, **XIII** and **XIV**) studied under nitrogen. The zinc complexes show multistage decomposition with the exception of complex **XIV**, which shows a single step decomposition.

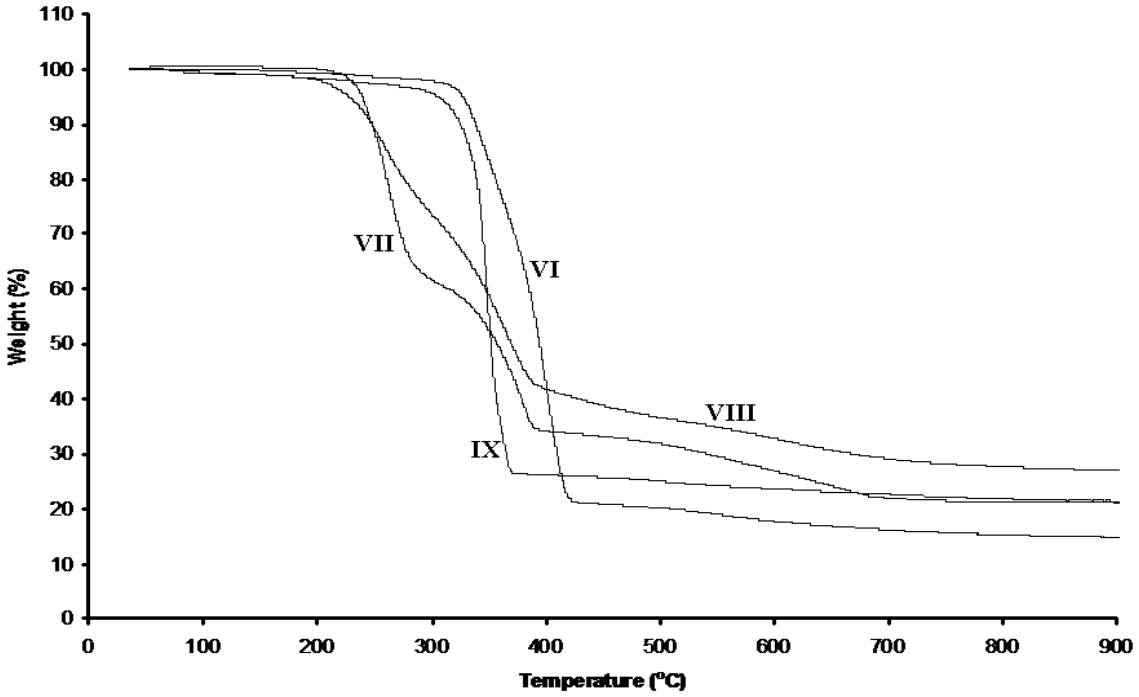

Figure 4.9: TGA (under nitrogen) curves for cobalt complexes **VI, VII, VIII,** and **IX**

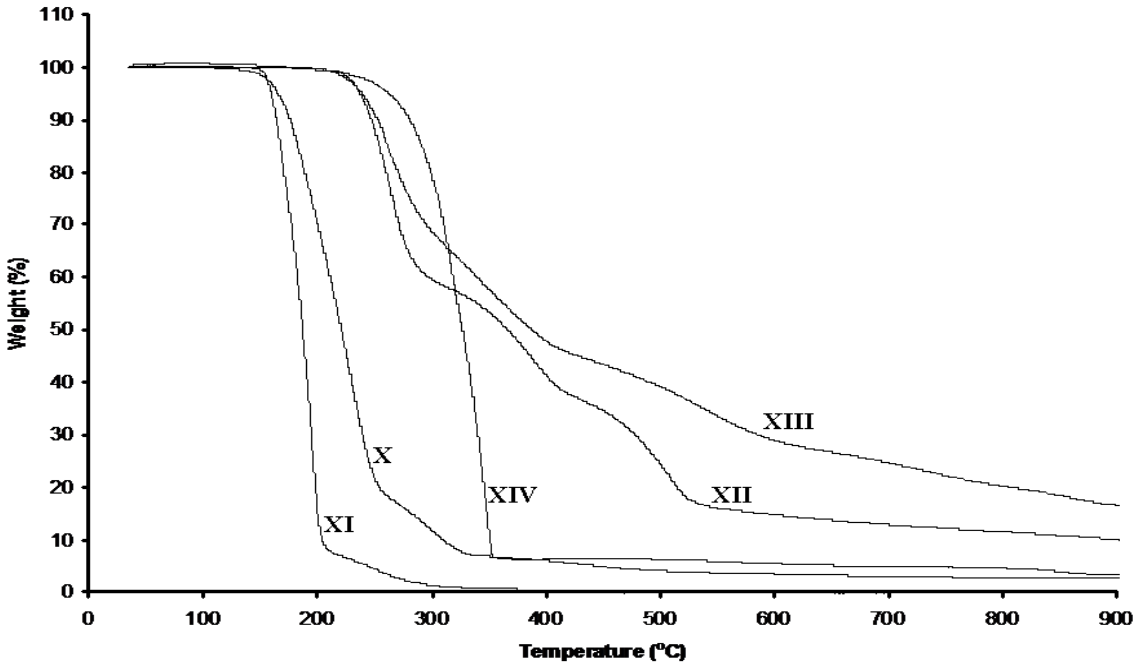

Figure 4.10: TGA (under nitrogen) curves for zinc complexes **X, XI, XII, XIII,** and **XIV**

(d) X-ray structural analysis

The synthesis of complex **II** is similar to the other substituted thiourea compounds and their complexes reported by Moloto *et al* [20]. The reaction was performed by reacting $CdCl_2$ with $(C_6H_5NH)_2CS$ in a 1:2 ratio (metal salt : ligand). Absolute ethanol was used as a solvent and the reaction was refluxed for 2 h. A clear yellow solution was observed after 20 minutes. The purity of the compound was confirmed by using elemental analyser that corresponded well with the calculated percentages of the elements carbon, hydrogen, nitrogen and sulphur. The crystals formed were air stable and obtained in low yield (37 %)

Single crystals of **II** suitable for X-ray analysis were obtained from recrystallization of the respective compound from ethanol at -15 ^{o}C. Crystallographic data of **II** is represented in Table 4.4, while selected bond lengths and bond angles are shown in Table 4.5. The molecular drawing of **II** is given in Figure 4.11.

Complex **II** crystallizes in the triclinic crystal system with a centre of symmetry and it is monomeric in nature. The cadmium complex **(II)** contains the central atom in distorted square planar geometry, whose edges are shared by two sulphur atoms of the thiourea and

two chlorine atoms of the metal source. The two thiourea units are *trans* to each other. The Cd1-Cl1, Cd1-Cl2, Cd1-S1 and Cd1-S2 bond distances are 2.4438(4), 2.4233(4), 2.5511(4) and 2.5588(4), respectively. Both thiourea groups are tilted to different side resulting in different degrees, displaying Cl1-Cd1-S1-C1 and Cl1-Cd1-S2-C14 torsion angles of 69.74(6) and -177.41(6), respectively. The bite angle of the diphenylthiourea ligand is 108.522(15). The Cd-S bonds, 2.5511(4) and 2.5588(4) are longer than in the N-ethylthiourea complex reported by Moloto *et al.*,[30] which suggest that the δ-bond character of this bond is weak. The C-S, 1.7142(16) and C-N, 1.3322(6) bonds in diphenylthiourea ligands show intermediate character between a single and a double bond length. These bond distances/lengths are in good agreement with those on the thiourea molecules reported in the Cambridge Structural database (CSD) by Allen *et al*.[31] i.e., 1.726 Å (C-S) and 1.322 Å (C-N).

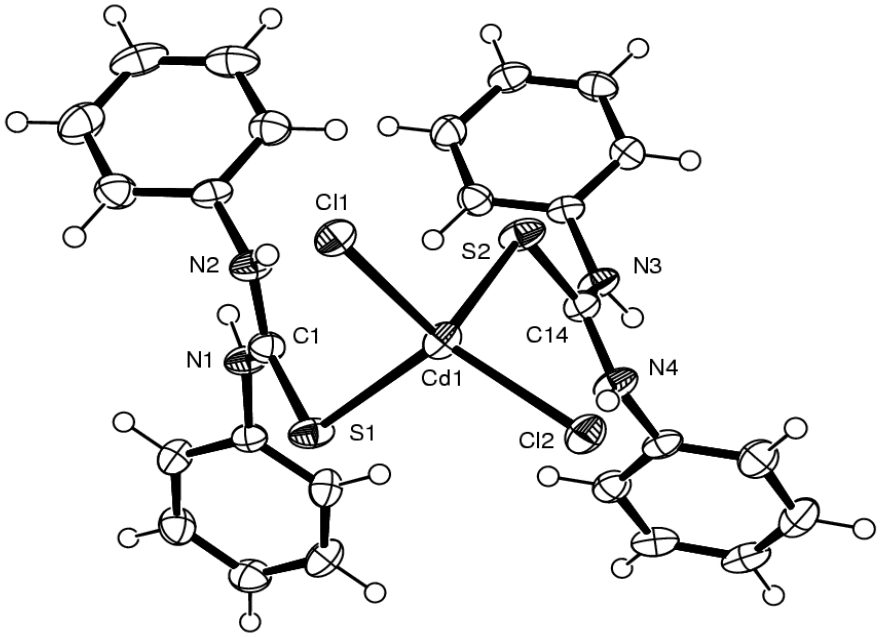

Figure 4.11: Molecular structure of **II**. Thermal ellipsoids are drawn at the 50 % probability level.

Table 4.3: Crystal data and structure refinement for complex **II**

	Complex **II**	
Empirical formula	$C_{26}\ H_{24}\ Cd\ Cl_2\ N_4\ S_2$	
Formula weight	639.91	
Temperature	173(2) K	
Wavelength	0.71073 Å	
Crystal system	Triclinic	
Space group	P-1	
Unit cell dimensions	a = 7.7236(2) Å	α = 100.3210(10)°
	b = 11.5115(3) Å	β = 95.5730(10)°
	c = 15.5004(3) Å	γ = 94.9430(10)°
Volume	1341.87(6) $Å^3$	
Z	2	
Density (calculated)	1.584 Mg/m^3	
Absorption coefficient	1.191 mm^{-1}	
F(000)	644	
Crystal size	0.40 x 0.26 x 0.12 mm^3	
Absorption correction	Semi-empirical from equivalents	
Max. and min. transmission	0.8703 and 0.6472	
Goodness-of-fit on F^2	1.072	
Final R indices [I>2sigma(I)]	R1 = 0.0214, wR2 = 0.0534	
R indices (all data)	R1 = 0.0238, wR2 = 0.0546	

Table 4.4: Bond lengths [Å] and angles [°] for complex **II**

Complex **II**	[Å] lengths
Cd(1)-Cl(2)	2.4233(4)
Cd(1)-Cl(1)	2.4438(4)
Cd(1)-S(1)	2.5511(4)
Cd(1)-S(2)	2.5588(4)
C(14)-S(2)	1.7098(16)
C(1)-S(1)	1.7187(15)
C(1)-N(1)	1.3299(19)
C(1)-N(2)	1.333(2)
C(14)-N(3)	1.329(2)
C(14)-N(4)	1.337(2)
	[°] angles
Cl(2)-Cd(1)-Cl(1)	122.087(14)
Cl(2)-Cd(1)-S(1)	114.813(14)
Cl(1)-Cd(1)-S(1)	101.268(14)
Cl(2)-Cd(1)-S(2)	103.162(14)
Cl(1)-Cd(1)-S(2)	106.330(14)
S(1)-Cd(1)-S(2)	108.522(15)
C(1)-S(1)-Cd(1)	98.66(5)
C(14)-S(2)-Cd(1)	104.12(5)

4.3 Synthesis of CdS, ZnS and Co_xS_y nanoparticles capped by HDA or/ and TOPO and their characterization

Table 4.6 outlines the detailed experimental conditions, band edges, emission maxima and sizes for the synthesis of semiconductor nanoparticles capped by HDA and TOPO.

Table 4.5: Summary of synthetic conditions, band edges, emission maxima and size of CdS, Co_xS_y and ZnS prepared

Complex	Time (h)	Temp. (^oC)	Surfactants	Band edge (nm)	Emission maxima (nm)	Average particles size (nm)
I	1	120	HDA	465	467	2.6
		180		497	499	4.8
III	1	120	HDA	450	452	4.7
IV	1	120	HDA	447	451	2.5
V	1	120	HDA	485	488	4.5
		180		502	510	5.6
		180	TOPO	444	441	2.6
		120	HDA/TOPO	504	506	6.5
VI	1	120	HDA	514	518	11.3
VII	1	120	HDA	443	518	7.5
VIII	1	120	HDA	516	532	1.7
IX	1	180	HDA	505	507	5.7
			TOPO	513	519	3.8
X	1	120	HDA	325	368	3.1
XI	1	120	HDA	312	351	4.4
XII	1	120	HDA	310	349	3.1
XIII	1	120	HDA	342	350	4.6
XIV	1	180	HDA	321	334	1.6
			TOPO	314	348	1.6

4.3.1 Synthesis of CdS, Co_3S_4 and ZnS semiconductor nanoparticles from $[CdCl_2\{(CH_3)_4(N_2C_2S_3)\}_2]$ I, $[CoCl_2\{(CH_3)_4(N_2C_2S_3)\}_2]$ VI, and $[ZnCl_2\{(CH_3)_4(N_2C_2S_3)\}_2]$ X

Thiuram monosulfide is a well known compound in the application of medicine [32, 33]. Due to the presence of sulphur atoms, which could be used as a sulphur source for the synthesis of metal sulfide nanoparticles, this compound has been receiving attention in the

field of quantum dots.

(a) Optical properties

One of the major factors that influences the growth of the particles is temperature. The temperature of the reaction has an effect on the particle size with higher temperatures favouring larger particles size. The reaction temperature also affects the shape of the nanoparticles due to the competition between the kinetic and thermodynamic growth regime. The absorption spectra of CdS nanoparticles capped by HDA synthesized from complex **I** are shown in Figure 4.12. The reactions were run for a maximum of 1 h at 120 ^{o}C (a) and 180 ^{o}C (b). The absorption spectra of the nanocrystallite samples were recorded by dispersing the particles in toluene. The as-prepared CdS absorption spectra are blue shift with respect to the bulk CdS (515 nm, 2.41 eV), which signifies a finite size of the nanoparticles. The size of the nanoparticles decreases as the energy increases, that is, lower wavelength. The absorption band edge of HDA-capped CdS nanoparticles synthesized at 120 ^{o}C is 465 nm which corresponds to 2.67 eV. Employing the same precursor at a slightly higher temperature (180 ^{o}C) caused a shift of the absorption spectrum to higher wavelength. This obvious change signified the growth of CdS QDs with the reaction temperature. However, it must be emphasized that the spectrum remained blue shift as compared to the bulk CdS material, confirming the small sizes of the particles. The band edge which was located at approximately 497 nm (2.49 eV), had a blue shift of approximately 18 nm with respect to the band gap of 515 nm (2.41 eV) for bulk CdS. The blue shift was caused by the strong quantum size effect. Comparison between the absorption spectra of the two samples revealed some distinct differences. It was clear that HDA-capped CdS nanoparticles synthesized at 120 ^{o}C depicted sharp excitonic peak while the one synthesized at 180 ^{o}C looses sharpness. The sharpness of the excitonic peak symbolizes small size of the particles and monodispersity, whilst an increase in temperature caused tailing of the spectrum, with size distribution widening. This agrees well with work reported by Moloto *et al.* [34].

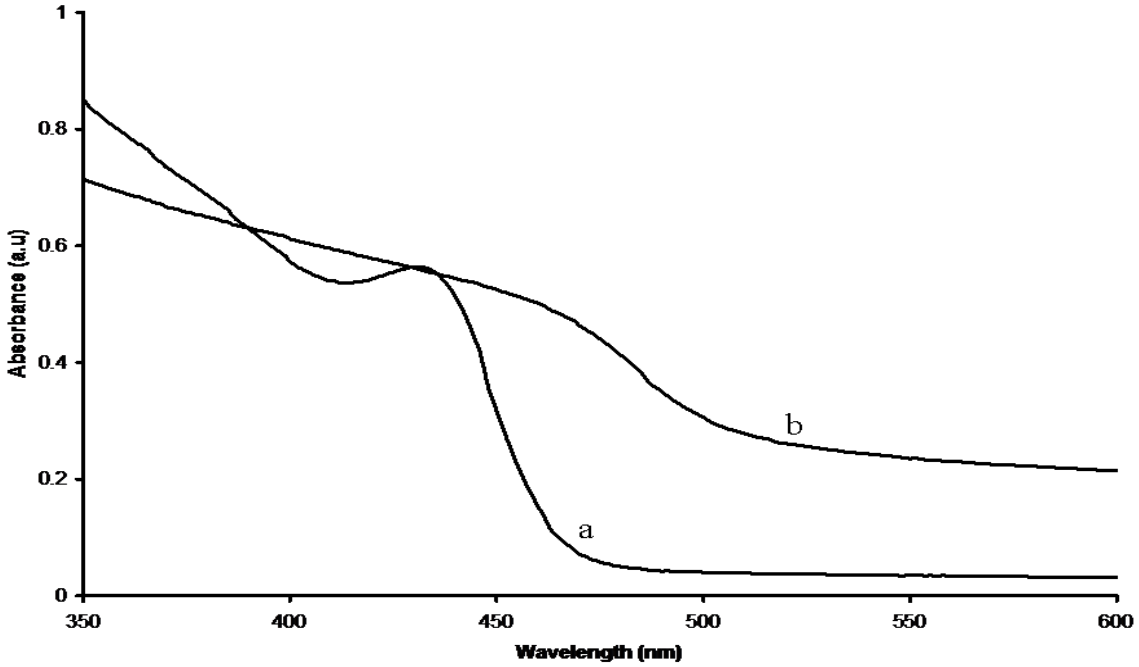

Figure 4.12: Absorption spectra of CdS nanoparticles capped by HDA synthesized from complex **I** at 120 ^{o}C (a) and 180 ^{o}C (b).

Figure 4.13 shows the photoluminescence spectra of CdS nanoparticles capped by HDA synthesized from complex **I** for a maximum of 1 h at 120 ^{o}C (a) and 180 ^{o}C (b). The same samples dispersed in toluene, used for absorption spectra analysis, were also used for photoluminescence analysis. The quality differences between the samples were further substantiated by their photoluminescence spectra. The photoluminescence spectra depicted narrow (HDA-capped CdS at 120 ^{o}C) and broader (HDA-capped CdS at 180 ^{o}C) emissions due to the wide distribution of particle sizes, with emission maxima very close to the band edges. Any defect-related emission was hardly seen in the emission spectra. The maximum emission peaks for CdS capped by HDA synthesized at 120 ^{o}C and 180 ^{o}C appeared at 467 nm (2.66 eV) and 499 nm (2.48 eV), respectively. The difference was caused by an increase in temperature to 180 ^{o}C, which increased the particles size and also broadened the emission spectrum. This simply justifies the size increase of the particles as confirmed by the TEM image (Figure 4.16b). The presence of a single smooth peak for both the samples suggested that the particles were well passivated.

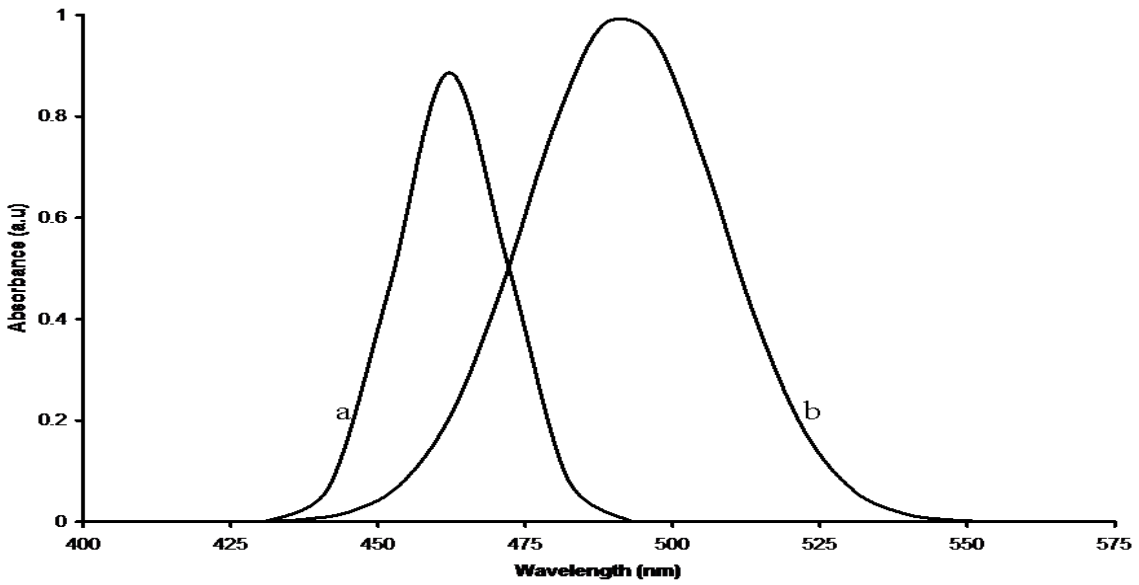

Figure 4.13: Photoluminescence spectra of CdS nanoparticles capped by HDA synthesized from complex **I** at 120 ^{o}C (a) and 180 ^{o}C (b).

Figure 4.14 shows the absorption and emission spectra of Co_3S_4 synthesized from complex **VI** at 120 ^{o}C for 1 h. The band edge of bulk Co_3S_4 was reported to be 1078 nm (1.15 eV) [35, 36]. The absorption spectrum showed three excitonic peaks. Bulk cobalt sulfide is composed of a continuous valence and conduction bands resulting in a fixed energy band characterized by a single absorption peak. As the cobalt sulfide becomes quantized, discrete atomic-like states with energies that are determined by the properties of the nanoparticles arise. Therefore, the observed three peaks in the absorption spectrum of cobalt sulfide nanoparticles are therefore due to the 1S, 1P and 1D transition, with the third excitonic peak categorized as the band gap of the material. The band edge, which is far blue shift as compared to the bulk cobalt sulfide band gap energy, is positioned at 514 nm (2.41 eV), while the excitonic peak is located at 474 nm (2.62 eV). The pronounced excitonic peak as well as high energy absorption feature indicates a stable and narrow size distribution. The emission peak, which appears at 518 nm (2.39 eV) is red shifted to the as prepared-absorption spectrum. This red shift in relation to the absorption band edge was generally observed in II-VI semiconductor nanoparticles [37, 38]. However, the photoluminescence spectrum is broad. The relatively broad emission spectrum has also been reported previously for semiconductor nanoparticles [39, 40]. The broad emission could be attributed to recombination from the surface defects. The appearance of more than one absorption peak is not new as it had been reported before. Liu *et al.* [41] synthesized CdSe

QDs with sharp absorption doublets and were attributed to two exciton transitions: 1S(e)-$1S_{3/2}$(h) and 1S(e)-$2S_{3/2}$(h).

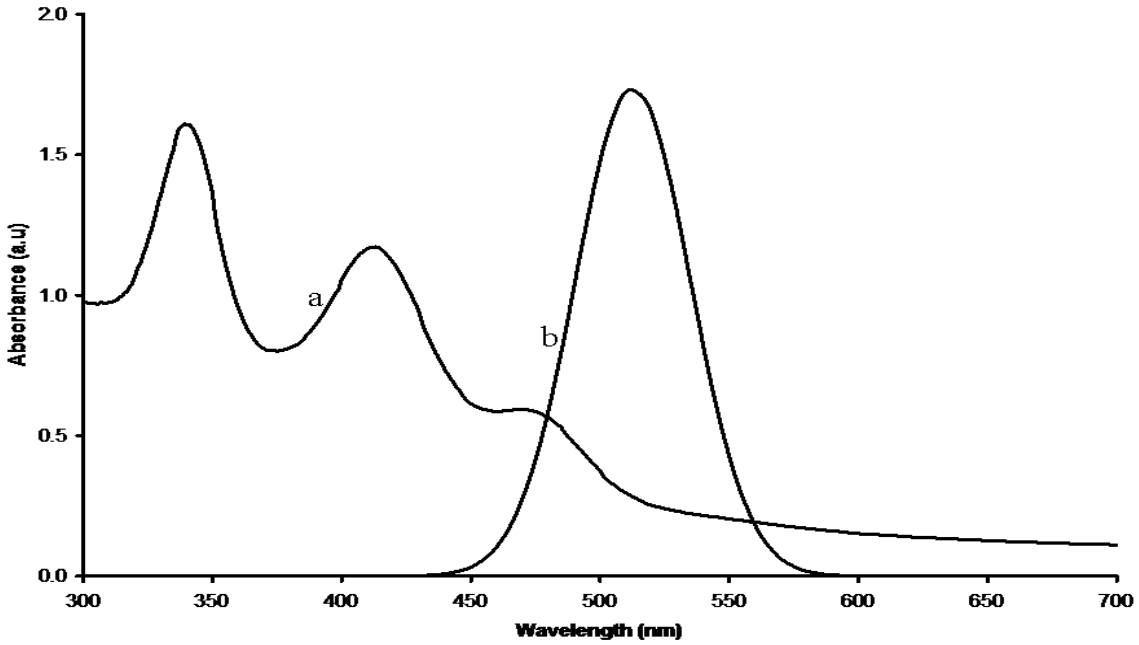

Figure 4.14: Absorption (a) and emission (b) spectra of Co_3S_4 nanoparticles capped by HDA synthesized from complex **VI** at 120 ^oC for 1h.

Figure 4.15 shows the absorption (a) and emission spectra of ZnS capped by HDA synthesized from complex **X** at 120 ^oC for 1 h. The absorption spectrum is blue shifted to the bulk ZnS band edge, with a band edge of 325 nm corresponding to band gap energy of 3.81 eV. A comparison with the value of bulk ZnS band edge, 340 nm (3.65 eV) [42], shows a blue shift of 15 nm indicating the quantum size effect of ZnS quantum dots. The photoluminescence spectrum is red shifted to the as-prepared absorption spectrum, with a maximum emission peak positioned at 368 nm (3.37 eV). However, the photoluminescence spectrum of ZnS capped by HDA synthesized from complex **X** is very broad. Similar phenomena have been observed by Choi *et al.* [43] who synthesized cubic ZnS nanoparticles capped by sodium dodecyl sulfate, with the size ranging from 2 to 5 nm. The broad emission from 375 to 600 nm was observed. It is well known that the nanocrystals of ZnS exhibits broad PL emission which can be contributed by sulfur vacancies, cation vacancies and surface states in the nanocrystals [44, 45].

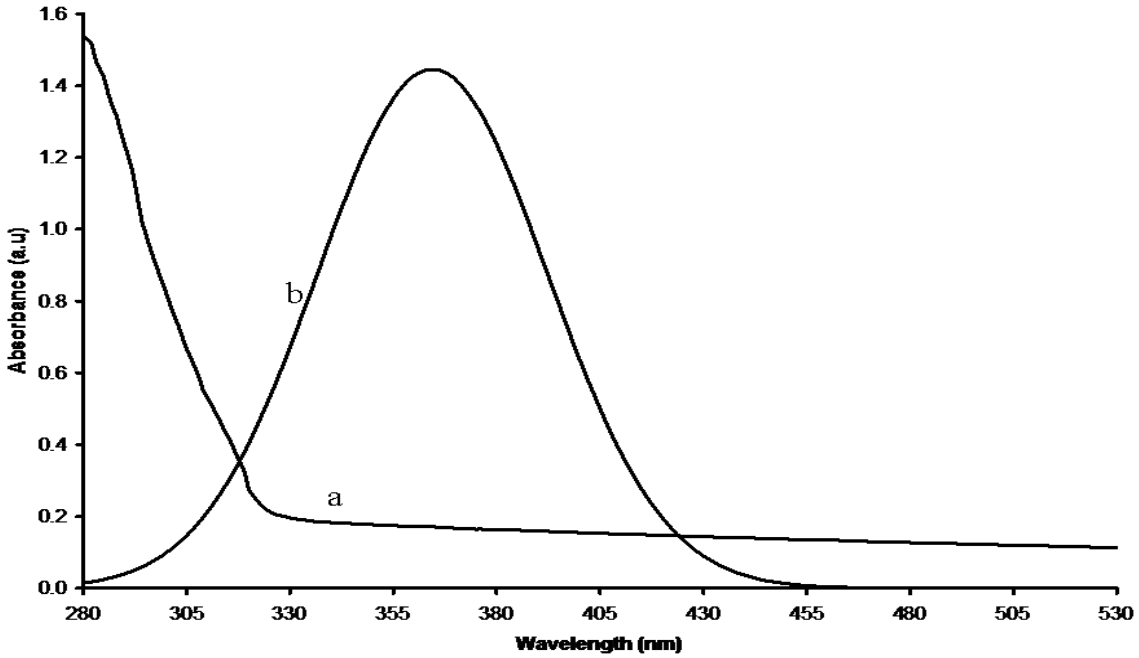

Figure 4.15: Absorption (a) and photoluminescence (b) spectra of ZnS capped by HDA synthesized from complex **X** at 120 ^{o}C for 1 h.

(b) Structural properties

The TEM images of CdS nanoparticles capped by HDA synthesized at 120 ^{o}C (a) and 180 ^{o}C (c), and their corresponding particle size distribution histograms (b – 120 ^{o}C and d – 180 ^{o}C) are depicted in Figure 4.16. Both images show rods shape particles. The histograms of CdS nanoparticles capped by HDA revealed a narrow distribution of particle size and the average diameters were found to be 4.2 nm for CdS nanoparticles synthesized at 120 ^{o}C (Figure 4.14b) and 7.1 nm for CdS nanoparticles synthesized at 180 ^{o}C (Figure 4.14d). Thus, the size of the produced CdS nanoparticles increased with the reaction temperature. It is due to the fact that higher temperature favours the fusion of smaller particles into larger ones. From the images, it was observed that some of those rods particles were fused together at the centre forming multiple pods like bipods and tripods. Although not employing the same precursor or complex, Li *et al.* [46] thermolysed cadmium ethylxanthate, [$Cd(C_2H_5OCS_2)_2$], in the synthesis of CdS nanoparticles. Their report showed that formation of four armed, three armed and two armed rods at 120 ^{o}C were observed.

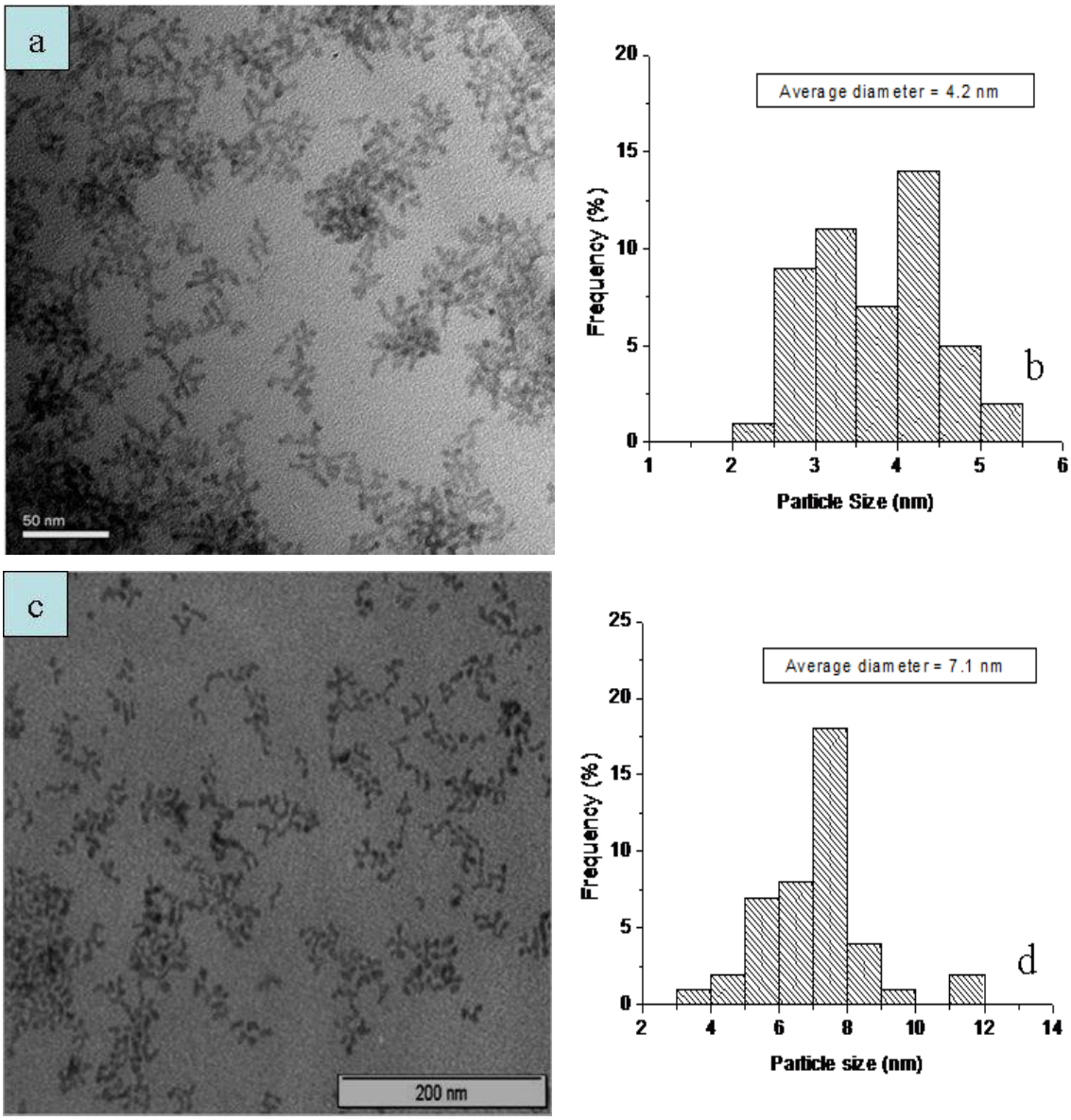

Figure 4.16: TEM images of CdS nanoparticles capped by HDA synthesized from complex **I** at 120 ^{o}C (a) and 180 ^{o}C (c) for 1 h, and their corresponding size distribution histograms (b, d).

Bulk CdS usually exists in the hexagonal phase from room temperature to the melting point [47]. However, CdS nanocrystallites can exist as either cubic or hexagonal phase. Figure 4.17 shows the XRD patterns of HDA-capped CdS nanocrystals synthesized from complex **I** at 120 ^{o}C (a) and 180 ^{o}C (b), for duration of 1 h. Both patterns show obvious broadened diffraction peaks compared to those of the bulk CdS crystals, indicating that the particles are in the nanosize regime. The characteristic diffraction peaks are all clearly indicated between 20^{o} and 80^{o}. The CdS nanoparticles synthesized at 120 ^{o}C show patterns that can be indexed as hexagonal phase with characteristic 44.4^{o} (110), 48.5^{o} (103) and 52.9^{o} (112)

peaks. As the temperature was increased to 180 ^{o}C, no change in phase was observed. Hexagonal-phase CdS with characteristic 44.4^{o} (110), 48.5^{o} (103), 52.9^{o} (112) peaks was still maintained. This showed that temperature did no affect the phase of CdS nanoparticles.

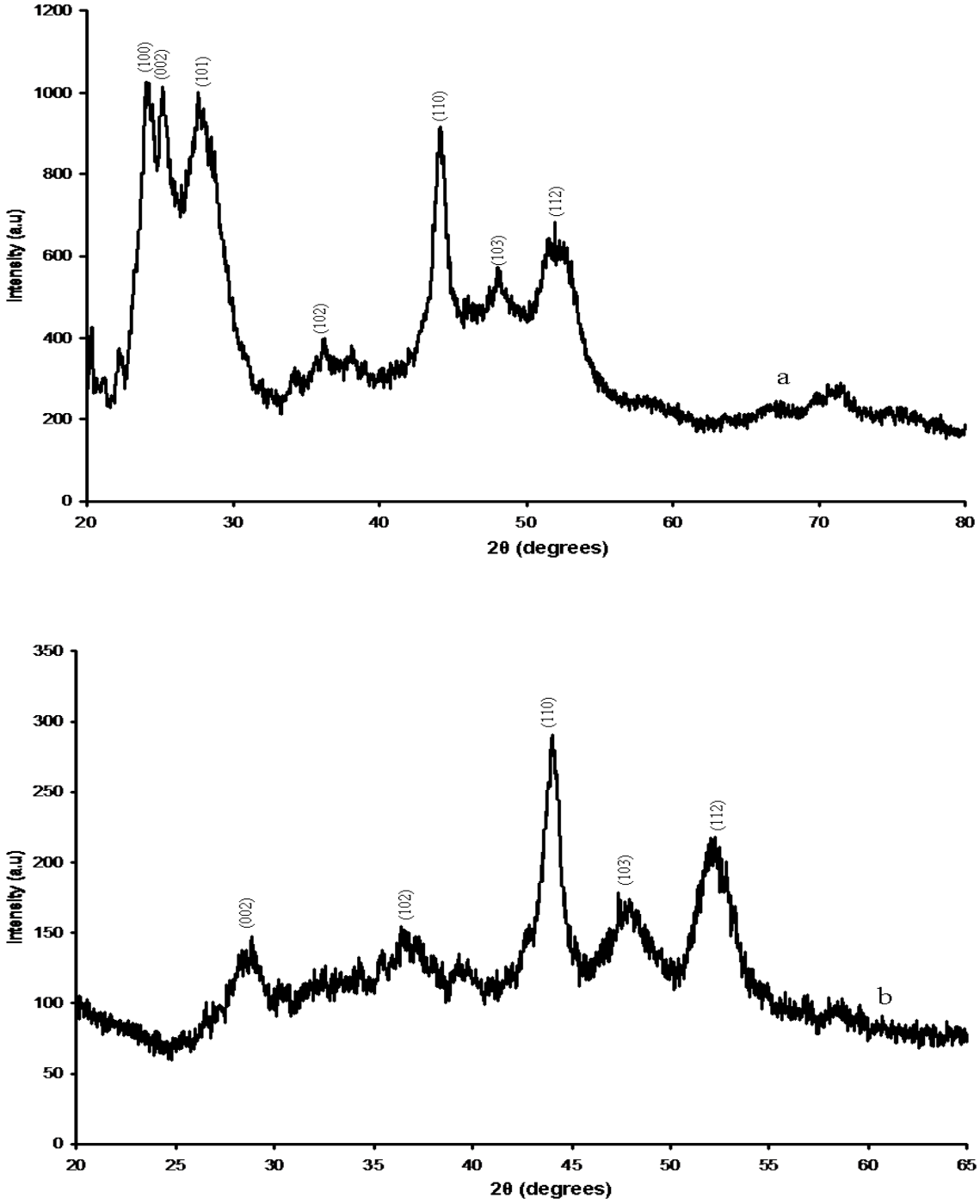

Figure 4.17: XRD patterns of CdS nanoparticles capped by HDA synthesized from complex **I** at 120 ^{o}C (a) and 180 ^{o}C (b) for 1 h.

Figure 4.18 shows TEM image of Co_3S_4 nanoparticles capped by HDA synthesized from

complex **VI** at 120 ^{o}C (a) for an hour and histogram of particles size distribution (b). The TEM image revealed signs of small and big spherical-like-shaped particles with an average diameter of 11.3 nm. A broader size distribution from 4 to 20 nm was observed due to the ineffectiveness of long-chain alkyamines in regulating the size of particles toward nanoscopic regime, as previously reported by Agostiano *et al.* [48]. However, the quantum size effect is seen in the absorption spectrum for the Co_3S_4 nanoparticles (Figure 4.14). Similar results were also obtained by P. Saravanan *et al.* [49] who synthesized ZnO by means of thermal decomposition of zinc (II) Cupferron complex in alkylamines, and then attributed the scenario to the minimal aggregation effects between primary clusters on dilution of ZnO colloidal solution. The X-ray diffraction pattern of the as-prepared cobalt sulphide nanoparticles capped by HDA synthesized from complex **VI** at 120 ^{o}C for 1 h is shown in Figure 4.19. All the main reflection peaks can be indexed as face-centered cubic Co_3S_4 (15.8^{o} (111), 27.3^{o} (220), 30.1^{o} (311), 31.8^{o} (222), 36.4^{o} (400), 37.9^{o} (331), 45.9^{o} (422), 47.9^{o} (551)), consistent with those reported values for bulk Co_3S_4 crystal (JCPDS Card 73-1703).

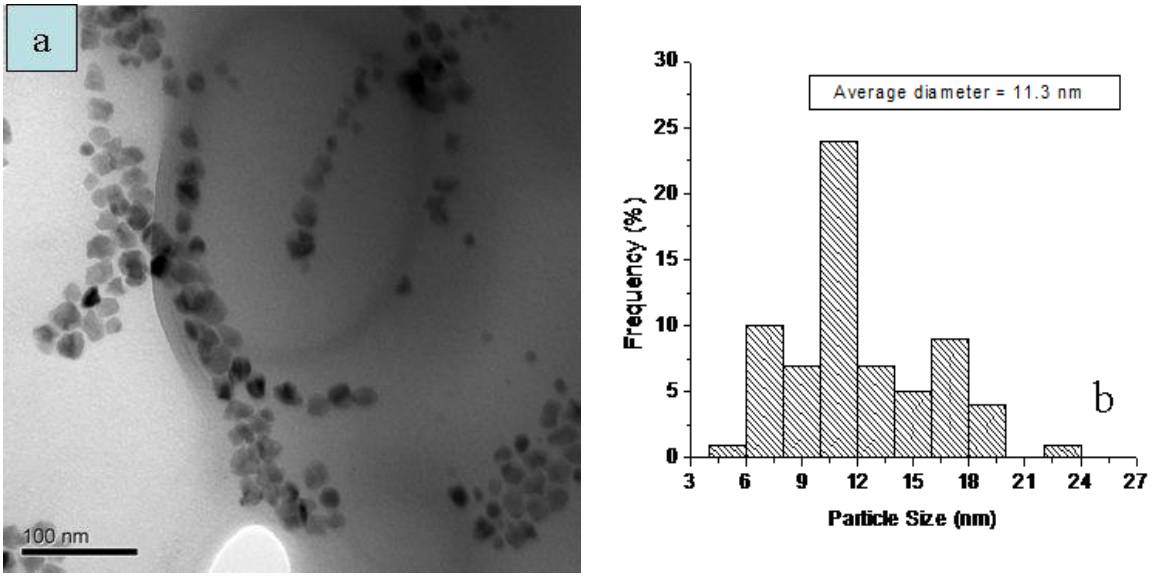

Figure 4.18: TEM image of Co_3S_4 nanoparticles capped by HDA synthesized from complex **VI** at 120 ^{o}C for 1 h (a) and its corresponding size distribution histogram (b).

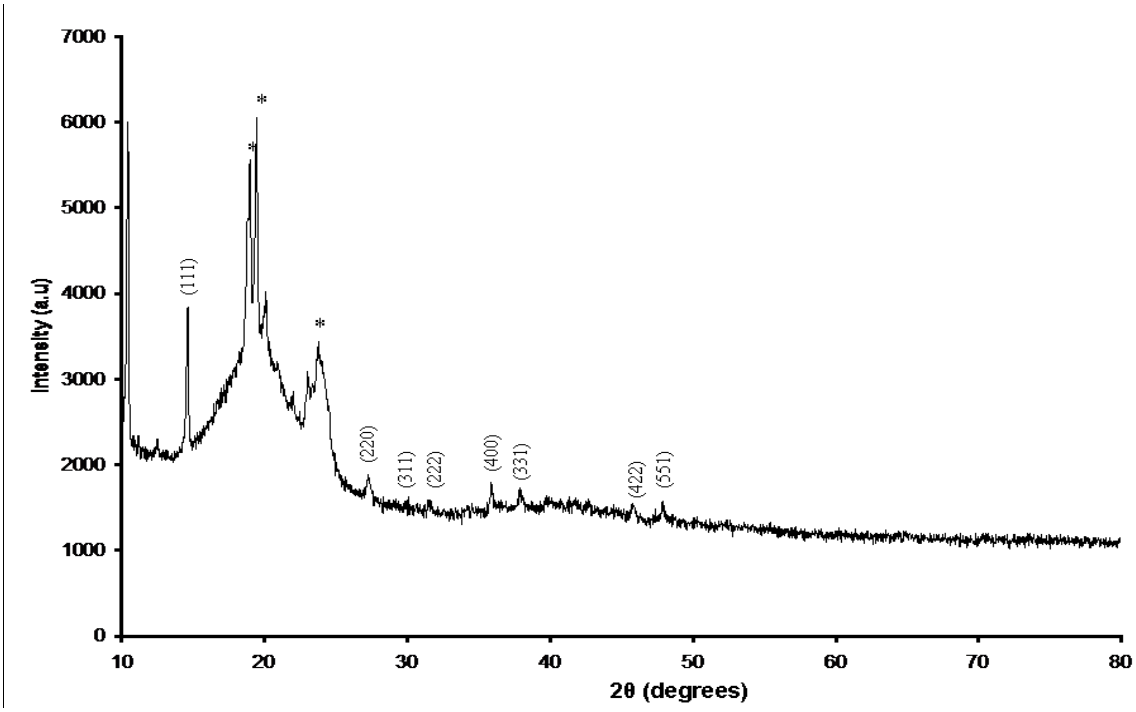

Figure 4.19: XRD pattern of Co_3S_4 nanoparticles capped by HDA synthesized from complex **VI** at 120 ^oC for 1 h.

Figure 4.20 shows the TEM image of ZnS nanoparticles capped by HDA synthesized from complex **X** at 120 ^oC for 1 h (a) and histogram of particle size distribution (b). The sample was prepared by dispersing a small amount of the prepared particles (solid material) in chloroform and then placed a drop on the copper grid. The particles obtained, with short rods dominating and some traces of small dots (spherical) morphology, have an average diameter of 3.1 nm. The phase of the as-synthesized products was characterized using X-ray diffraction. Figure 4.21 shows the XRD pattern of ZnS nanoparticles capped by HDA synthesized from complex **X** at 120 ^oC for an hour. The XRD peaks are significantly broadened which indicates the very fine size of the grain or particle. The XRD pattern exhibit the prominent broad peaks at 2θ values of 28.6^o (111), 47.9^o (220) and 56.7^o (311), corresponding to the cubic phase of ZnS (JCPDS Card 05-0566). The peaks marked with asterisks are due to the capping agent, which is hexadecylamine.

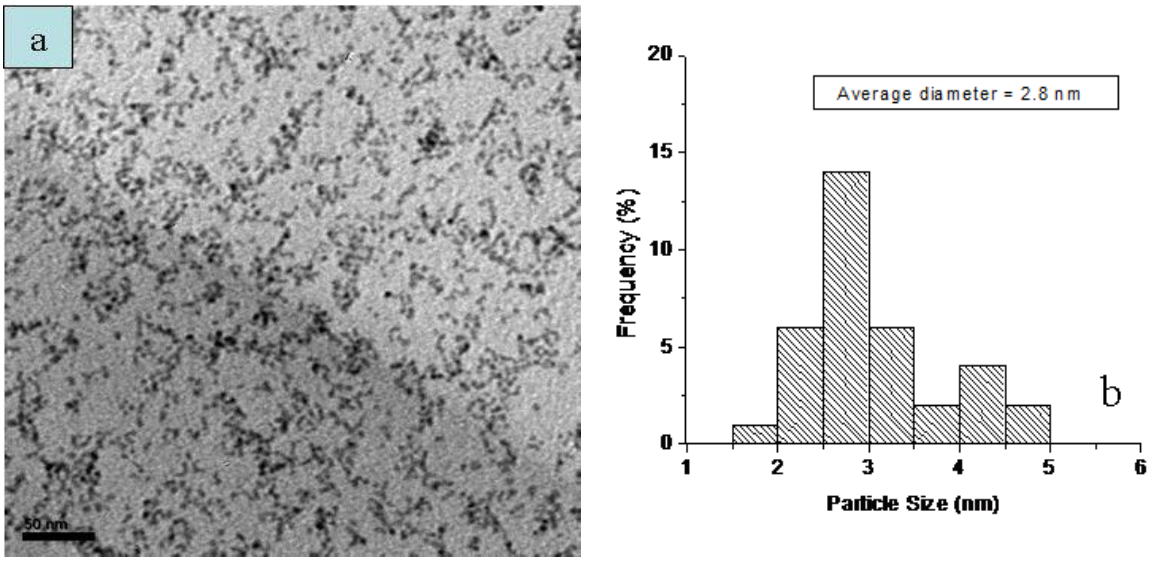

Figure 4.20: TEM image of ZnS nanoparticles capped by HDA synthesized from complex **X** at 120 ^{o}C for 1 h (a), and its corresponding size distribution histogram (b).

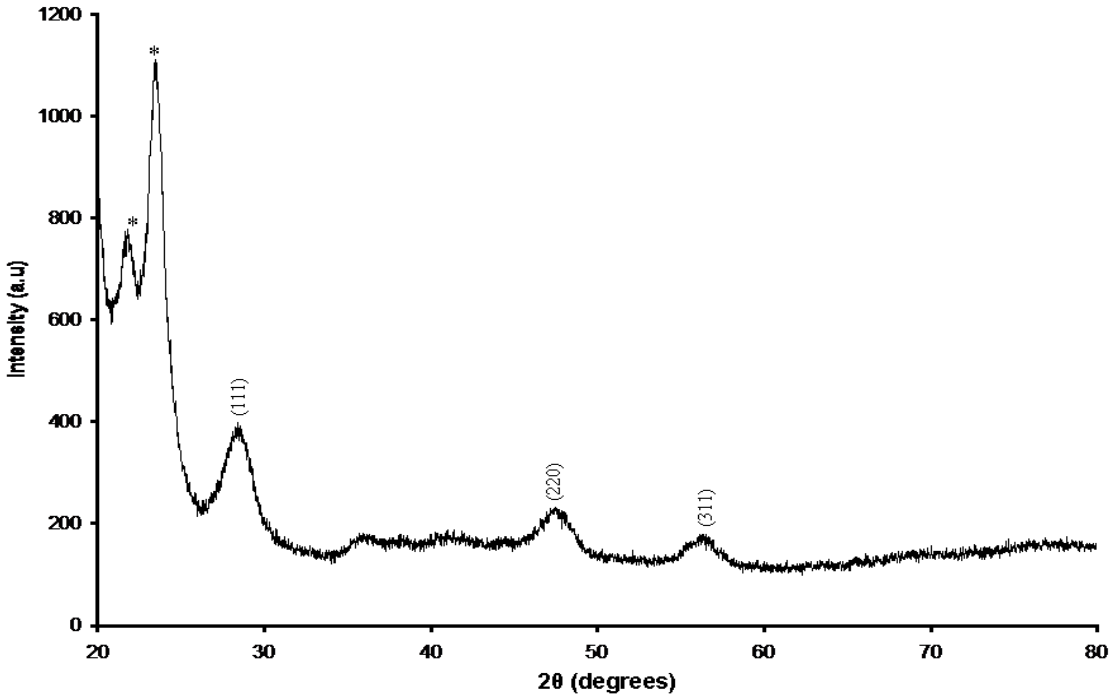

Figure 4.21: XRD pattern of ZnS nanoparticles capped by HDA synthesized from complex **X** at 120 ^{o}C for 1 h.

4.3.2 Synthesis of CdS nanoparticles from $[CdCl_2\{CS(NHC_6H_5)_2\}_2]$ II and $[ZnCl_2\{CS(NHC_6H_5)_2\}_2]$ XI

(a) Optical properties

The optical spectra of these particles measured in an organic solvent can be used to calculate the approximate emission band edge using the direct band gap method. The band edge for CdS nanoparticles synthesized from single-source precursors are blue shifted to the bulk material. This is associated with the CdS nanoparticles being smaller than the exciton of bulk CdS. There are several factors that influence the size and shape of the particles. The effect of concentration on CdS nanoparticles was investigated using complex **II**. During synthesis there is a generally increase of particle size of nanoparticles with time, which is consistent with Ostwald ripening [50]. After injection of the precursor there is a critical size dependence on the concentration of the precursor. The depletion of the precursor causes the size distribution to broaden because smaller, less stable particles aggregate to form bigger particles. Absorption spectra have also been used to determine the optimum time for growth of particles at specific temperatures from various precursors.

Figure 4.22(a – c) shows the absorption spectra of CdS nanoparticles capped by HDA at different monomer concentration, i.e., 0.5 g, 1 g and 2 g. The absorption spectra were measured at room temperature by dispersing the particles in toluene. The absorption band edges for HDA-capped CdS nanoparticles are slightly increasing as the monomer concentration increases. They appear at (a) 458 nm (2.71 eV), (b) 464 nm (2.67 eV) and (c) 474 nm (2.62 eV), which are blue shifts of about (a) 57, (b) 51 and (c) 41 nm from the bulk CdS (515 nm). The shifts signify finite size of the nanoparticles, resulting from the fact that as the size of the particles decreases band gap energy increases. All the HDA-capped CdS nanoparticles experiments were performed at 120 ^{o}C for an hour. Figure 4.23 shows the photoluminescence spectra of HDA-capped CdS nanocrystals at different monomer concentration, (a) 0.5 g, (b) 1 g and (c) 2 g. The emission maxima vary with the samples of different concentration. However, the broad photoluminescence spectra are blue shifted to their as-prepared absorption spectra. The maximum emission peaks are positioned at 436 nm (a), 448 nm (b) and 461 nm (c). This is an uncharacteristic trend of the CdS nanoparticles but has been fairly reported for CdSe nanoparticles. The blue shifts are attributed to the shape of the nanoparticles thus altering the emission maxima. Maseko *et*

al. [51] synthesized CdSe nanoparticles capped by HDA and TOPO and reported emission maximum peaks (593 nm and 584 nm) that were blue shifted as compared to the as-synthesized CdSe absorption band edges (608 nm and 628 nm).

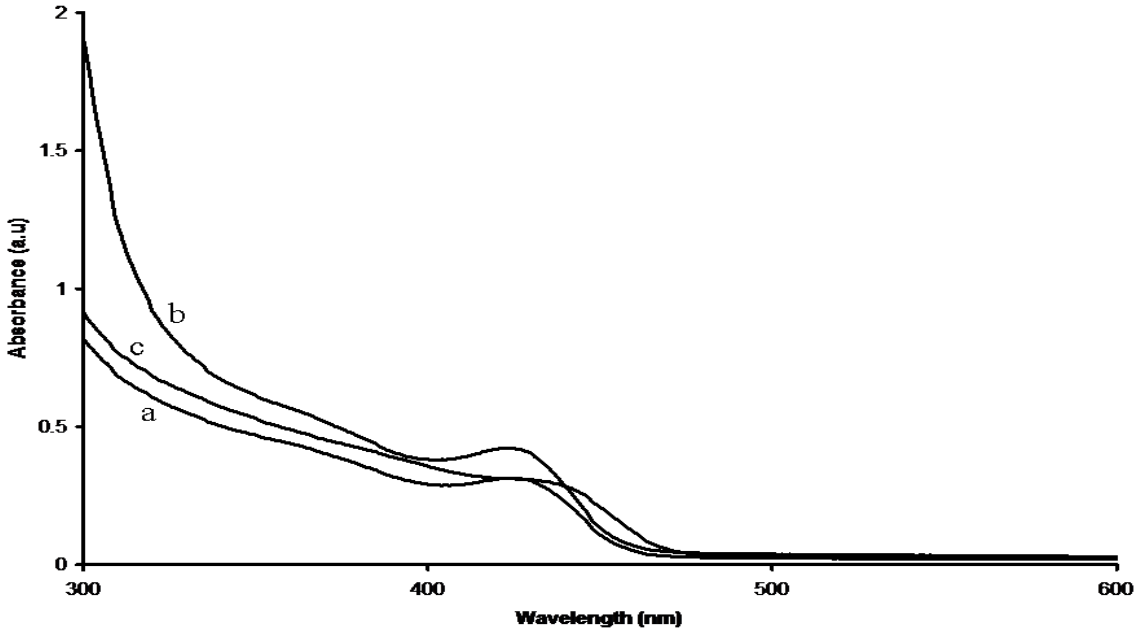

Figure 4.22: Absorption spectra of CdS nanoparticles capped by HDA at different complex amount, 0.5 g (a), 1 g (b) and 2 g (c).

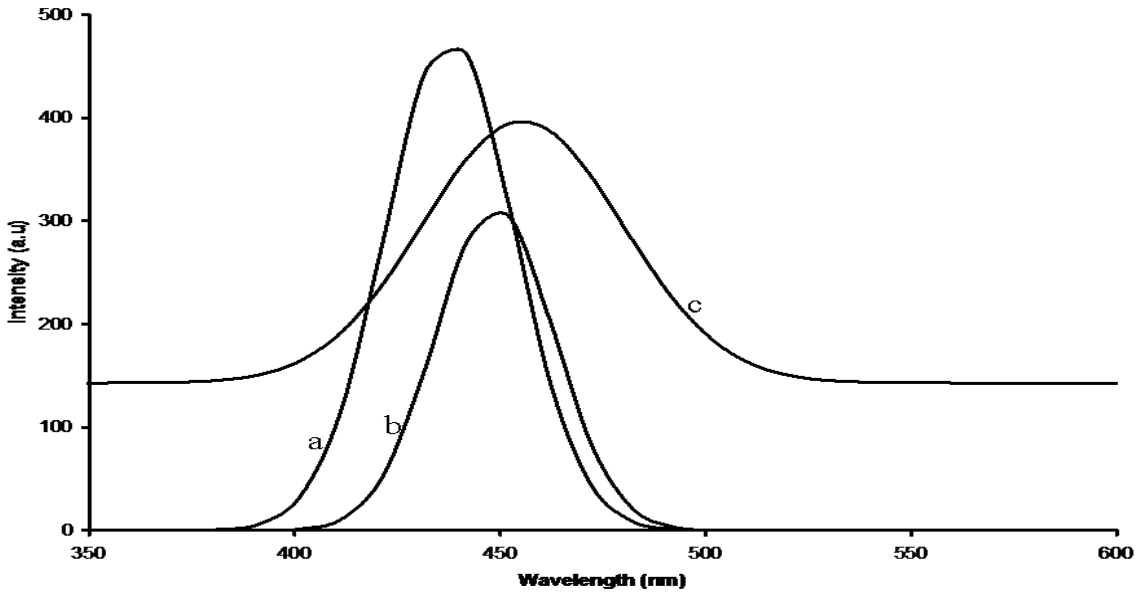

Figure 4.23: Photoluminescence spectra of CdS nanoparticles capped by HDA at different complex amount, 0.5 g (a), 1 g (b), and 2 g (c).

Zinc sulphide is a white to yellow coloured powder or crystal. This compound is typically encountered in the more stable cubic form, which is also known as zinc blende or sphalerite, and hexagonal form which is also known as a synthetic material and as the mineral wurtzite. Both sphalerite and wurtzite are intrinsic, wide band gap semiconductors [52]. Figure 4.24 represents the room-temperature absorption (a) and photoluminescence (b) spectra of the as-synthesized ZnS nanoparticles capped by HDA synthesized from complex **XI**. The particles were grown at 120 ^{o}C for an hour. Samples characterization was prepared by dispersing ZnS capped by HDA in toluene. The particles were sonicated for 15 minutes to improve solubility before analysis. From the absorption spectrum (Figure 4.24a), it can be clearly observed that band edge which is 312 nm, corresponding to 3.97 eV, is blue shifted compared to the bulk ZnS band edge (340 nm). The photoluminescence spectrum, which is red shifted to the as-prepared absorption spectrum, has a maximum emission peak positioned at 351 nm. Although the photoluminescence spectrum is not narrow, a single smooth peak was observed. This indicates that the particles are composed of single shape. The broadness of the photoluminescence spectrum signifies the presence of some larger particles, as will be confirmed by the TEM results.

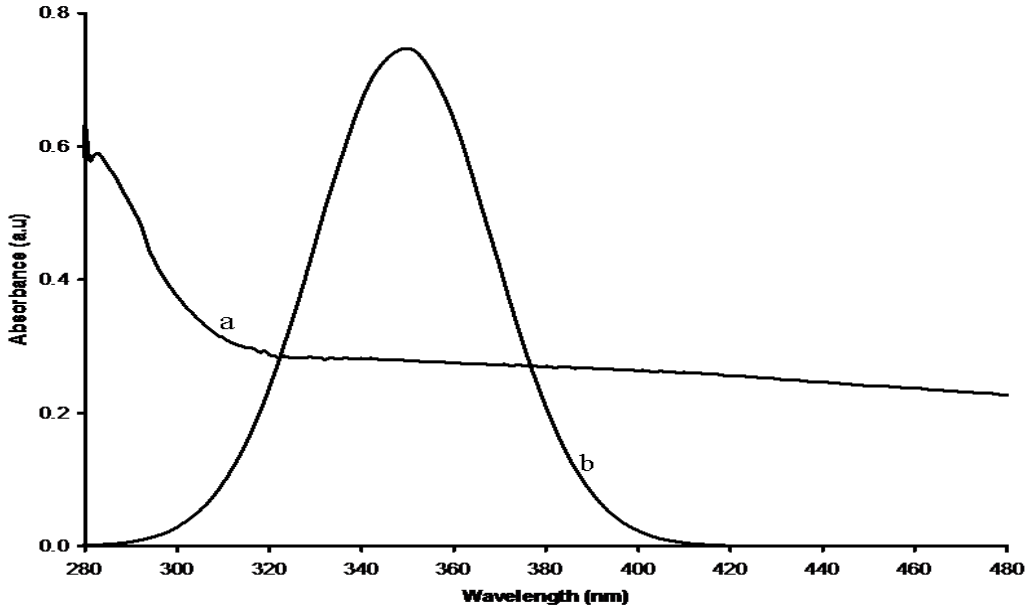

Figure 4.24: Absorption (a) and photoluminescence (b) spectra of ZnS capped by HDA synthesized from complex **XI** at 120 ^{o}C for 1 h.

(b) Structural properties

In order to investigate the effect of precursor concentration on the morphology of CdS nanocrystals, CdS samples were synthesized under different precursor concentration at the same conditions, 120 ^{o}C for 1 h. TEM images of HDA-capped CdS nanoparticles at different monomer concentrations, 0.5 g (a), 1 g (c) and 2 g (e), and their size distribution histograms (b – 0.5 g, d – 1 g and f – 2 g) are shown in Figure 4.25. A mixture of short rods and close-to-spherical particles were observed with an average diameter of 2.4 nm, 3.6 nm and 4.8 nm, respectively. When 0.5 g of the precursor was thermolysed in HDA, very small particles dominated by short rods were observed. However, as the precursor concentration was increased from 0.5 g to 2 g, traces of close-to-spherical particles that were in dominance were observed. The change in morphology as the precursor concentration increases agrees well with the published work by Cai *et al.* [53].

However, the group reported a change from close-to-spherical particles to nanorods as the precursor concentration was increased. The difference between the results above is attributed to the different precursors used. The particles diameter increased as the concentration was increased. An increase of the particles size in diameter (TEM) as the monomer concentration increases confirms the results obtained above from the absorption and emission spectra. The crystallinity of the prepared CdS samples was investigated by X-ray diffraction (XRD), as shown in Figure 4.26. It was interesting to find that the pattern of the CdS nanoparticles capped by HDA (2 g **II** in 5g HDA) sample could be indexed to hexagonal phase with predominant peaks indexed to 28.2^{o} (002), 37.1^{o} (102), 43.9^{o} (110), 48.2^{o} (103) and 52.2^{o} (112). The XRD peaks were considerable broadened as compared to those of the macrocrystalline CdS which signified finite size of the particles. The peak marked with an asterisk was due to the presence of the capping agent (HDA). The clear diffraction peaks indicate that the CdS semiconductor nanoparticles or quantum dots were well crystallized.

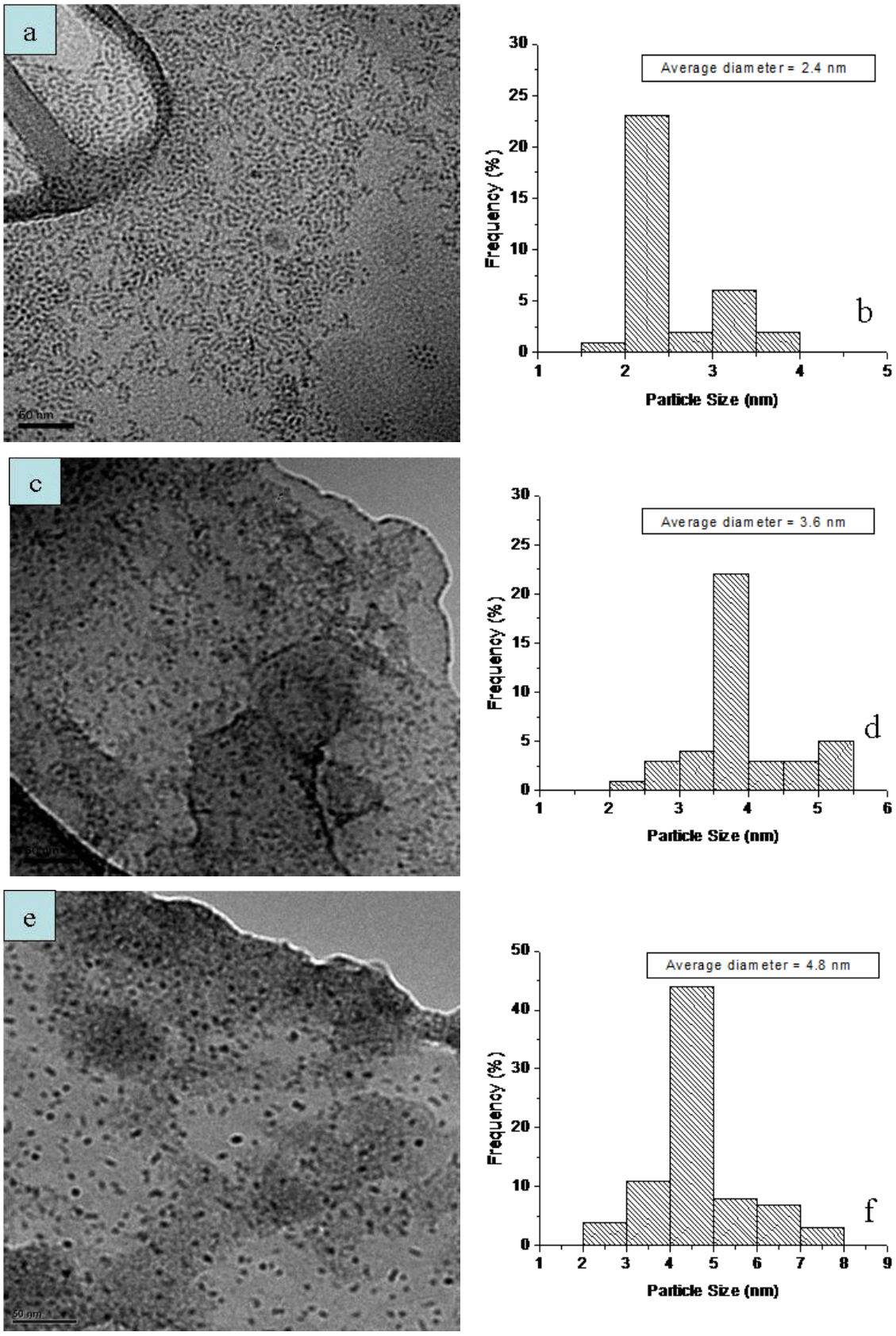

Figure 4.25: TEM images of CdS nanoparticles capped by HDA at different complex amount, 0.5 g (a), 1 g (c), and 2 g (e), and their corresponding size distribution histograms (b, d, f).

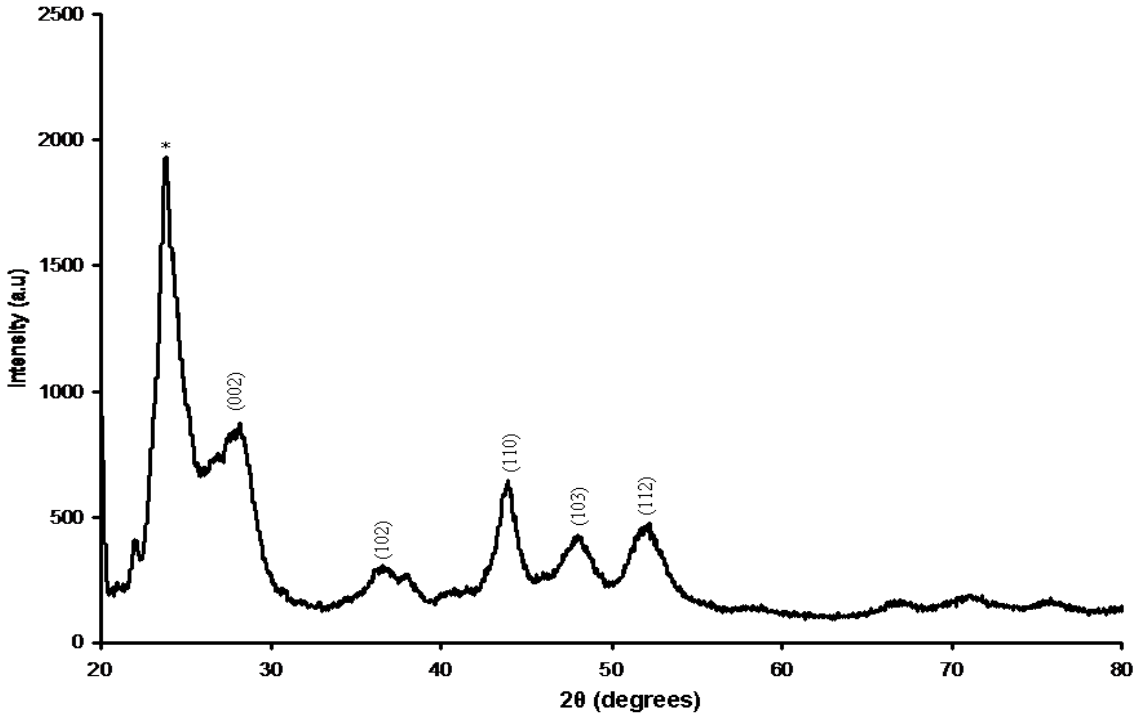

Figure 4.26: XRD pattern of CdS nanoparticles capped by HDA synthesized from diphenylthiourea cadmium complex **II** at 120 ^{o}C for 1 h.

The TEM image of ZnS nanoparticles capped by HDA synthesized from complex **XI** and histogram of particle size distribution (b) are shown in Figure 4.27. The spherical particles with an average diameter of 3.6 nm were grown at 120 ^{o}C for 1 h. The sample was prepared by dispersing a small amount of the as-prepared ZnS in toluene and then placed a drop of solution on the copper grid. The XRD pattern of ZnS nanoparticles capped by HDA synthesized from complex **XI** at 120 ^{o}C for an hour is shown in Figure 4.28. Three broad and symmetric peaks were observed at 2θ = 28.9^{o}, 36.9^{o}, 48.2^{o}, 56.4^{o} belonging to (111), (200), (220), (311) corresponding to the cubic phase of ZnS.

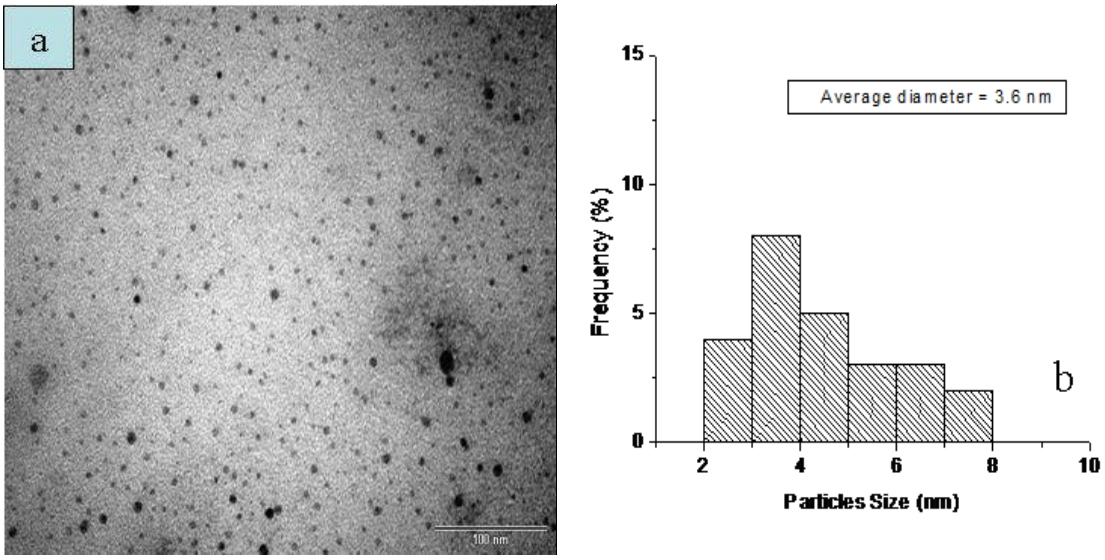

Figure 4.27: TEM image of ZnS nanoparticles capped by HDA (a) synthesized from complex **XI** at 120 ^{o}C for 1 h (a), and its corresponding size distribution histogram (b).

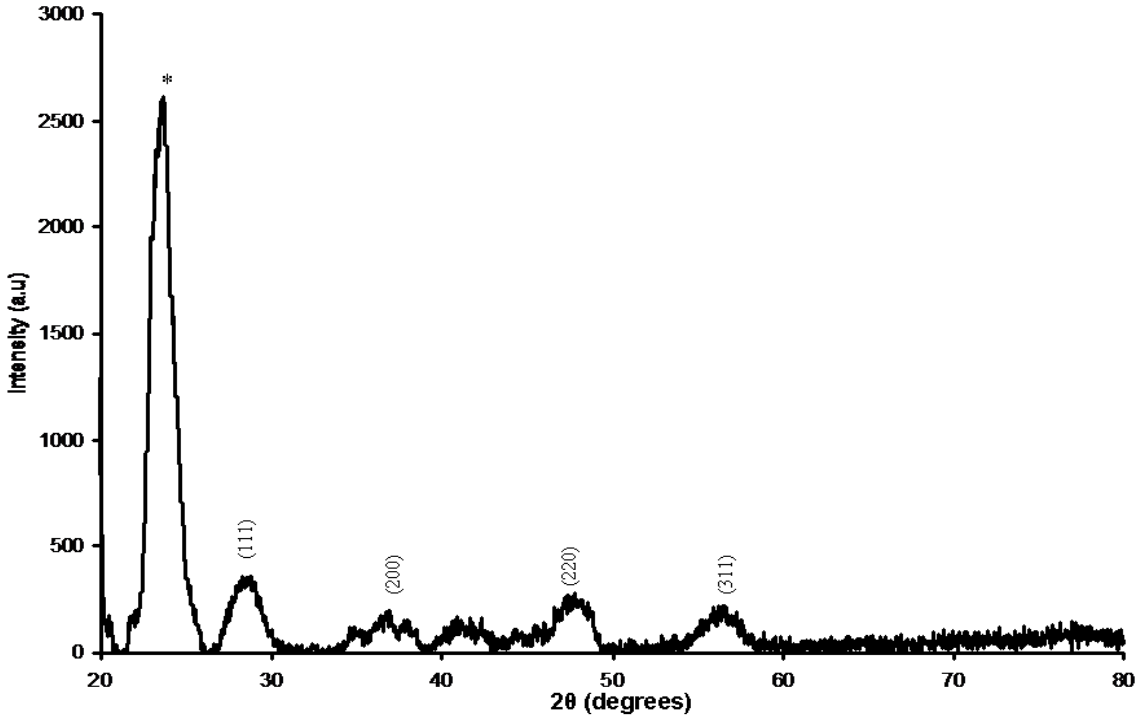

Figure 4.28: XRD pattern of ZnS nanoparticles capped by HDA synthesized from complex **XI** at 120 ^{o}C for 1 h.

4.3.3 Synthesis of CdS nanoparticles from $[CdCl_2\{CS(NHCH_3)_2\}_2]$ III, $[CoCl_2\{CS(NHCH_3)_2\}_2]$ VII and $[ZnCl_2\{CS(NHCH_3)_2\}_2]$ XII.

Metal complexes of alkylthioureas have been prepared and found to be very good precursors for the synthesis of semiconductor nanoparticles. Moloto *et al.* [20] synthesized a number of cadmium (II) complexes with N-alkyl/aryl and N,N'-dialkyl/aryl thioureas (RNHCSNHR'; where R=R'=CH_3, CH_2CH_3, C_5H_5, and /or R'=H). The $[CdCl_2(CS(NH_2)NHCH_3)_2]$, $[CdCl_2(CS(NH_2)NHCH_2CH_3)_2]$, and $[CdCl_2(CS(NH_2)_2]$ complexes were thermolyzed in TOPO at 200 ^oC to give CdS crystallites.

(a) Optical properties

Figure 4.29 represents the room-temperature absoprtion (a) and photoluminescence (b) spectra of CdS nanoparticles capped by HDA. The particles were synthesized from complex **III** at 120 ^oC for a duration of an hour. The samples were prepared by dispersing the particles in toluene. The bulk crystallites reveal the interband absorption spectrum with a band edge of 515 nm. When the crystalline size decreases there was a blue shift of the CdS nanoparticles absorption band edge. Thermolysis of complex **III** yielded CdS nanoparticles with a sharp excitonic peak appearing at 429 nm. The appearance of the strong excitonic peak in the absoprtion apectrum is an indication of particles that are well dispersed and small size. The band edge of the absorption spectrum was estimated to be 450 nm, which corresponds to 2.76 eV. The photoluminescence broad spectra showed a maximum peak appearing at 452 nm.

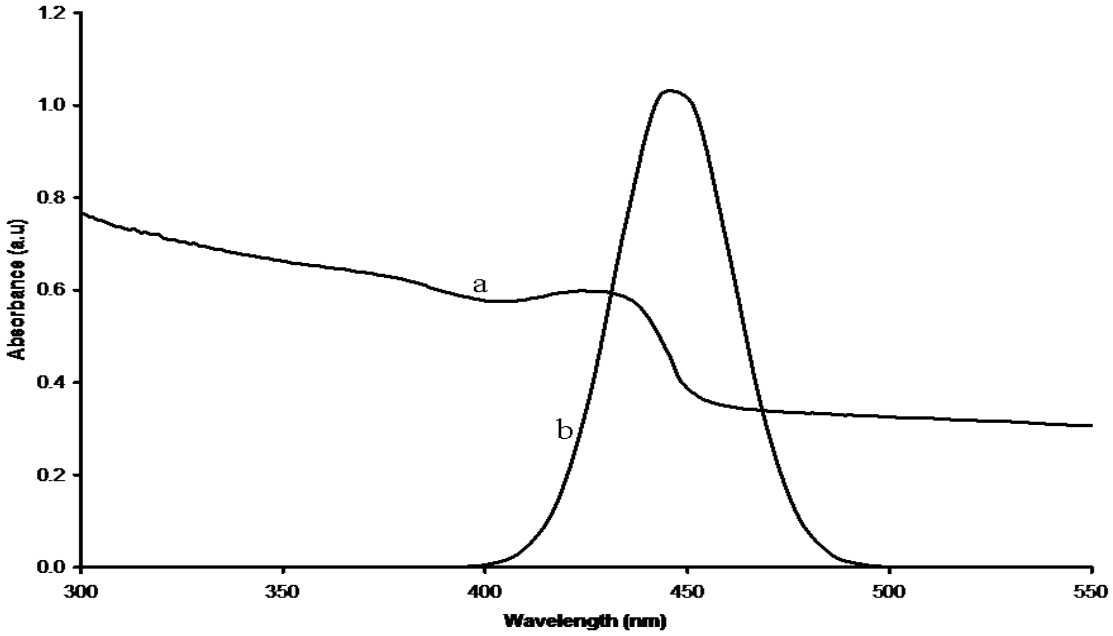

Figure 4.29: Absorption (a) and photoluminescence (b) spectra of CdS nanoparticles capped by HDA synthesized from complex **III** at 120 ^{o}C for 1 h.

The absorption (a) and emission (b) spectra of Co_xS_y nanoparticles capped by HDA are shown in Figure 4.30. The particles samples which were grown at 120 ^{o}C for a maximum of an hour, was dispersed in toluene for characterization. The blue shifted absorption spectrum (a) to the bulk Co_xS_y band edge has a weak absorption peak with a maximum appearing at 395 nm, with a band edge of 443 nm. The weak absorption peak might be an indication of particles that are poorly passivated, have aggregated or depicting an irregular shape. The photoluminescence or emission spectrum (b) is red shifted to the as-prepared absorption spectrum, which is indicative of the large Stokes shift of the nanoparticles. The red emission is assigned to the the trap emission, which is observed in poorly passivated and/or defect-containing materials. The maximum emission peak is positioned at 518 nm, corresponding to a band gap of 2.39 eV.

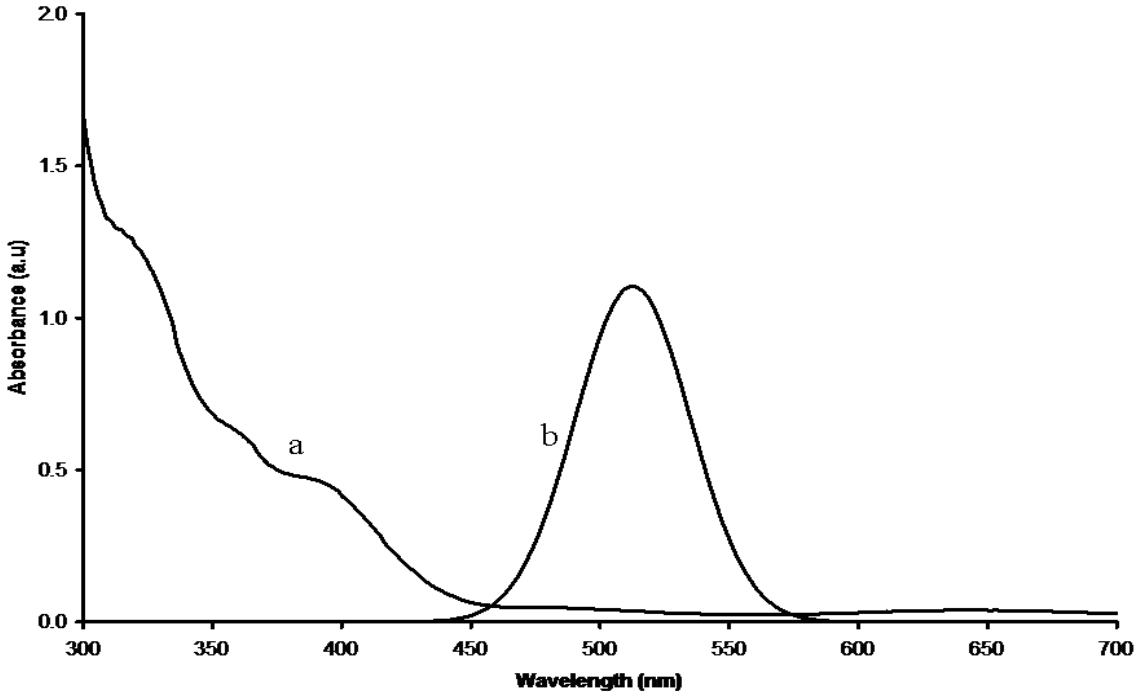

Figure 4.30: Absorption and photoluminescence spectra of Co_xS_y nanoparticles capped by HDA synthesized from complex **VII** at 120 ^oC for 1 h.

The blue shift of the band gap energy due to quantum size confinement of ZnS nanoparticles capped by HDA is demonstrated by the UV-visible absorption spectrum in Figure 4.31a. The particles were grown from complex **XII** at 120 ^oC for 1 h and then dispersed in toluene for optical properties characterization. The spectrum band edge of 310 nm corresponds to band gap energy of 4.0 eV. The band edge appears at lower wavelength compared to the bulk ZnS which is 350 nm (3.54 eV). The photoluminescence spectrum (Figure 4.31b), is red shifted to the absorption spectrum, with an emission maximum peak of 350 nm (3.57 eV).

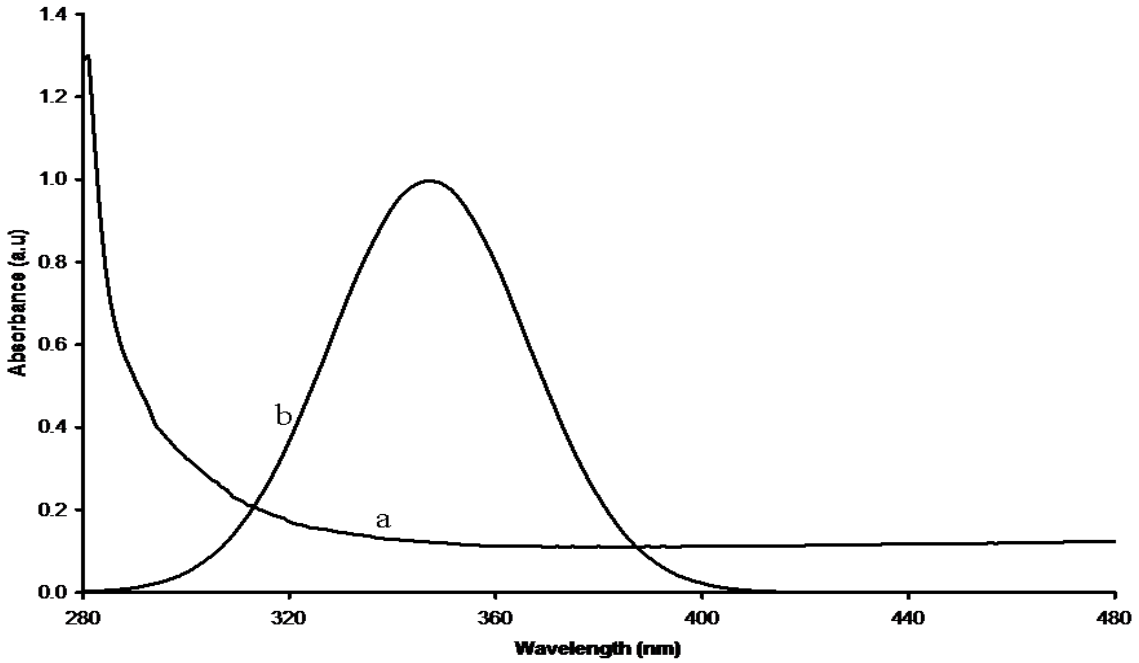

Figure 4.31: Absorption (a) and photoluminescence (b) spectra of ZnS nanoparticles capped by HDA synthesized from complex **XII** at 120 ^{o}C for 1 h.

(b) Structural properties

Figure 4.32 depicts the TEM image of CdS nanoparticles capped by HDA synthesized from complex **III** at 120 ^{o}C for duration of 1 h (a) and histogram of particle size distribution (b). The image depicts short rods shape particles with an average diameter of 4.7 nm. The XRD pattern of this material is shown in Figure 4.33. Six major peaks of hexagonal phase positioned at 26.7^{o}, 28.5^{o}, 36.8^{o}, 43.9^{o}, 48.2^{o}, 52.2^{o} are present in the sample. These peaks correspond to (002), (101), (102), (110), (103) and (112). Compared to the bulk CdS, the diffraction peaks of the CdS nanoparticles are broadened due to the reduced size. The broad peak marked with an asterisk is due to hexadecylamine ligand.

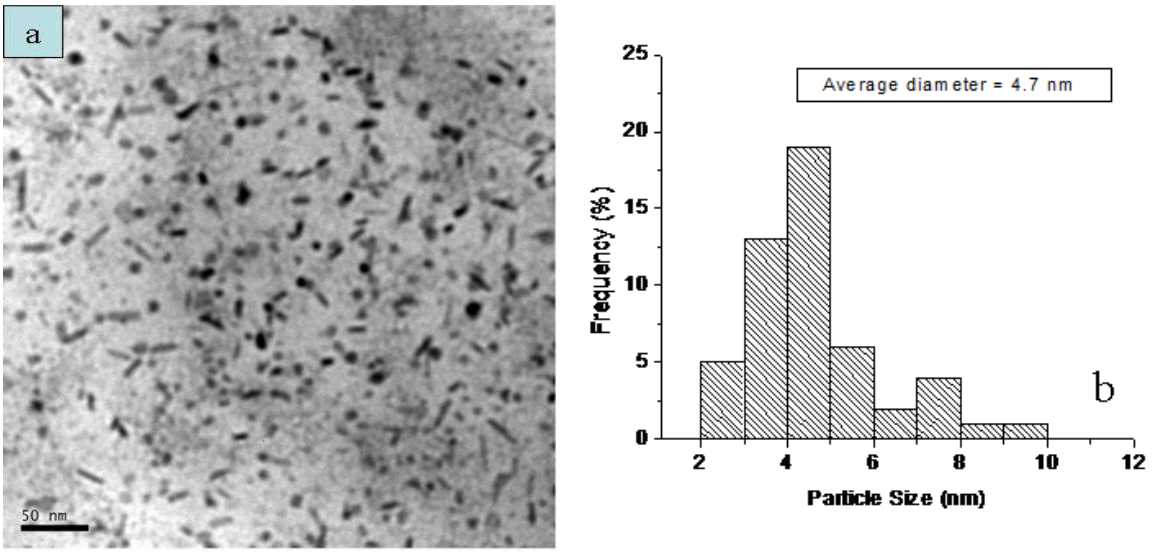

Figure 4.32: TEM image of CdS nanoparticles capped by HDA synthesized from complex **III** at 120 ^{o}C for 1 h (a), and its corresponding size distribution histogram (b).

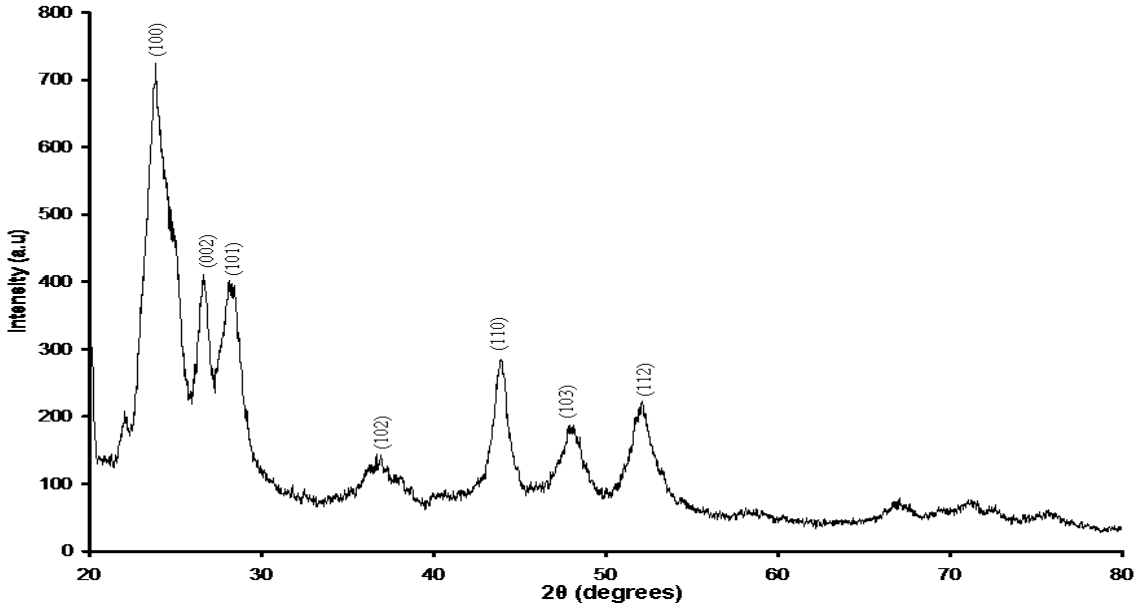

Figure 4.33: XRD pattern of CdS nanoparticles capped by HDA synthesized from complex **III** at 120 ^{o}C for 1 h.

Figure 4.34 shows TEM image of Co_xS_y capped by HDA synthesized from complex **VII** at 120 ^{o}C for 1 h (a) and histogram of particle size distribution (b). It was not easy to detect the exact morphology of the particles since they looked irregular. However, there are some few traces of roddish-like particles observed. The particles have been measured to have an average diameter of 7.5 nm. The XRD pattern of Co_xS_y nanoparticles capped by HDA

synthesized from complex **VII** at 120 ^{o}C for 1 h is shown in Figure 35. The XRD pattern presented here was similar to the one previously presented by Fen *et al.* [54], and no obvious peaks were observed in the pattern, demonstrating the amorphous nature of the as-synthesized cobalt sulphide nanoparticles.

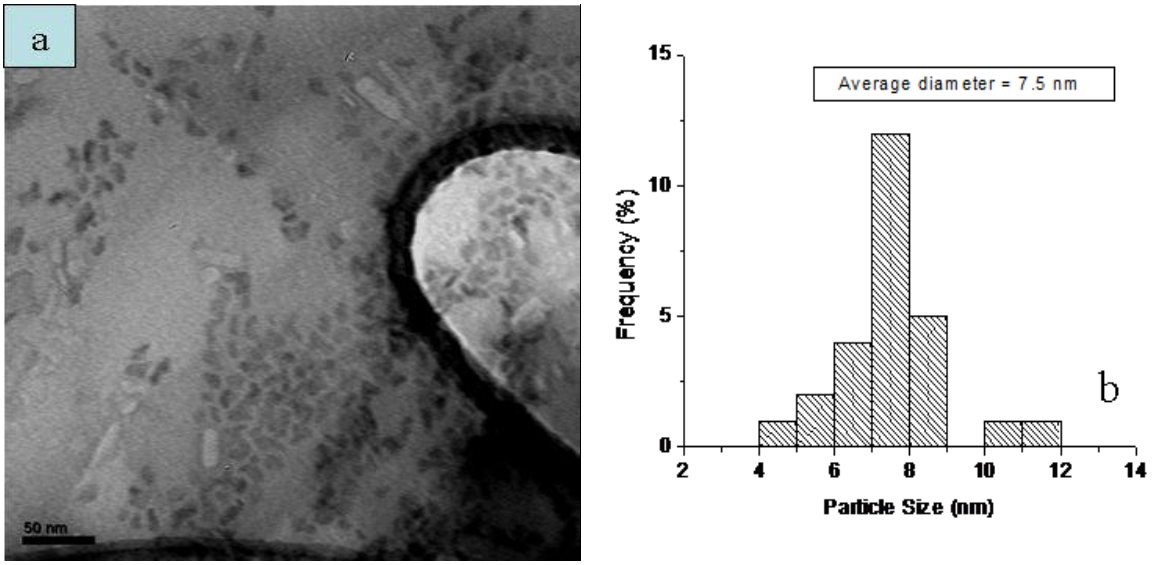

Figure 4.34: TEM image of Co_xS_y nanoparticles capped by HDA synthesized from complex **VII** at 120 ^{o}C for 1 h (a), and its corresponding size distribution histogram (b).

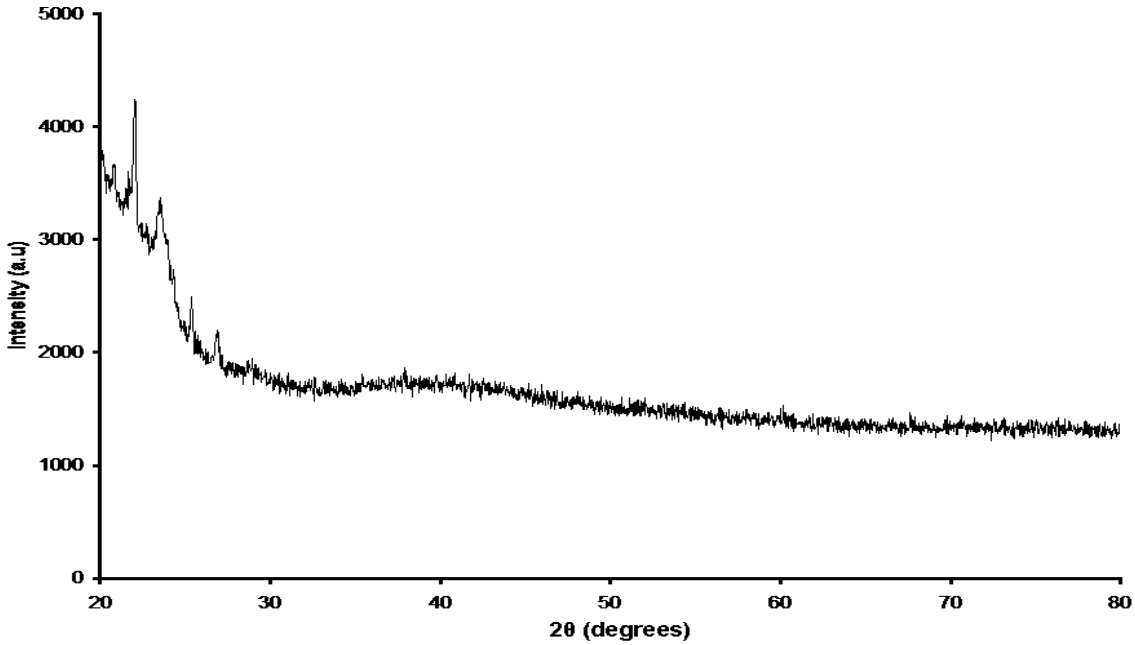

Figure 4.35: XRD pattern of Co_xS_y nanoparticles capped by HDA synthesized from complex **VII** at 120 ^{o}C for 1 h.

The TEM image of ZnS nanoparticles capped by HDA grown from complex **XII** at 120 ^{o}C for 1 h (a) and histogram of particle size distribution (b) are shown in Figure 4.36. The morphology of the particles shows spherical-like-shaped ZnS nanoparticles, with an average diameter of 3.1 nm. Figures 4.37 shows the wide-angle X-ray diffraction pattern of the ZnS nanocrystallites capped by HDA synthesized from complex **XII**. The XRD peaks for this pattern are considerable broadened as compared to those of the macrocrystalline ZnS which signifies finite size of the particles. The 2θ peaks at 28.8^{o}, 36.7^{o}, 48.2^{o} and 56.4^{o}, indexed to (111), (200), (220) and (311), respectively, are consistent with the cubic crystal ZnS structure.

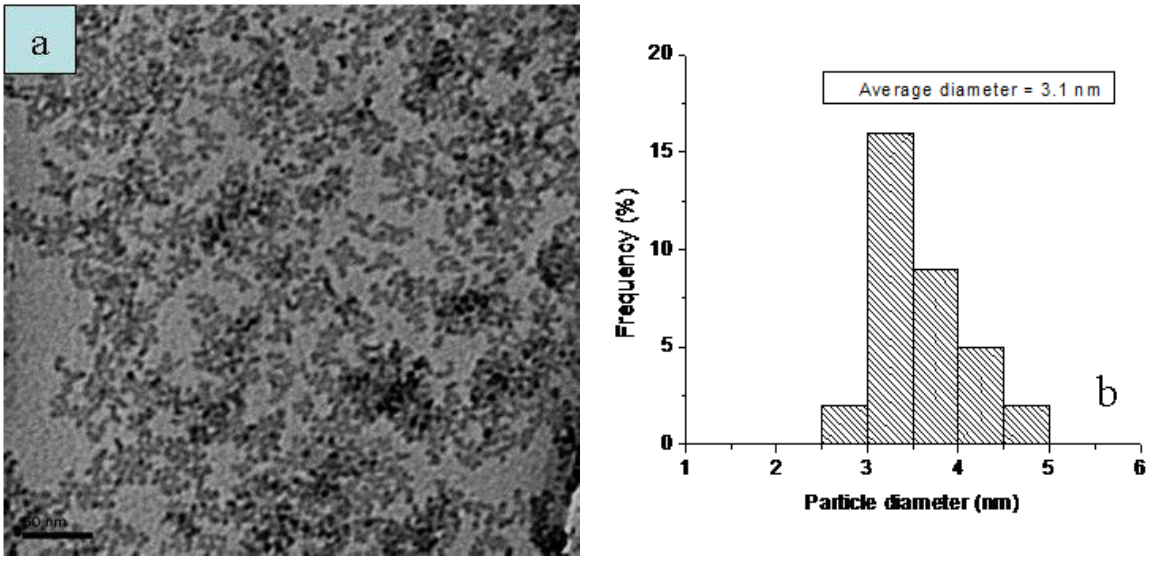

Figure 4.36.: TEM image of ZnS capped by HDA synthesized from complex **XII** at 120 ^{o}C for 1 h (a), and its corresponding size distribution histogram (b).

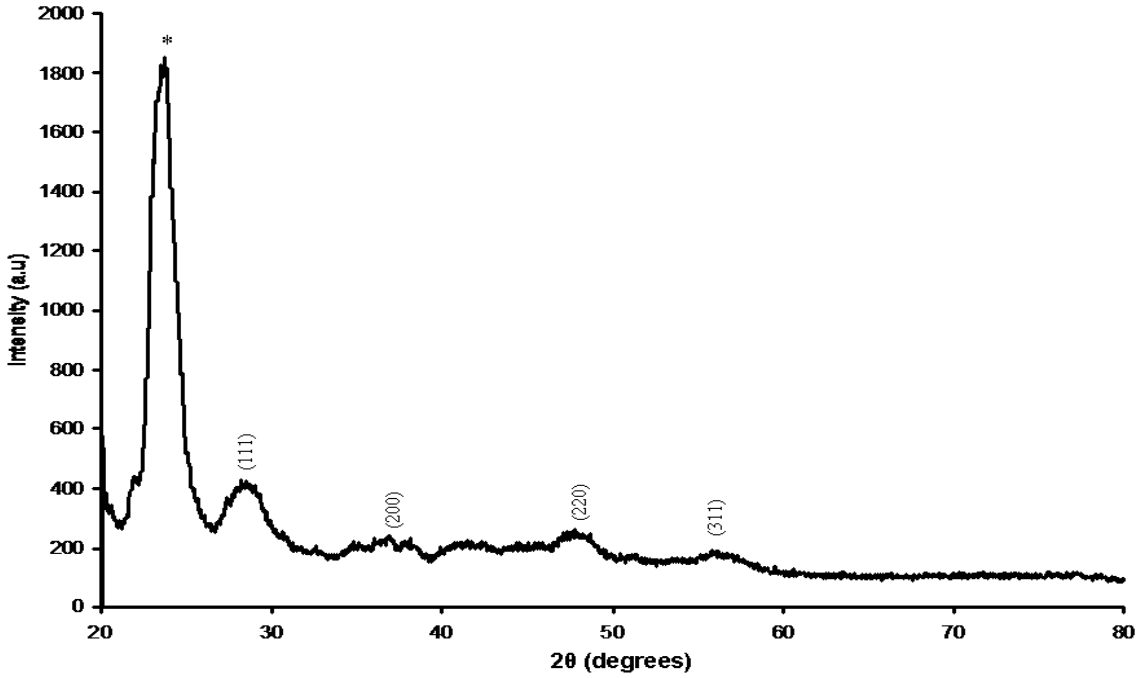

Figure 4.37: XRD pattern of ZnS nanoparticles capped by HDA synthesized from complex **XII** at 120 ^{o}C for 1 h.

4.3.4 Synthesis of CdS nanoparticles from $[CdCl_2\{CSNH_2(NHCH_3)\}_2]$ IV, $[CoCl_2\{CSNH_2(NHCH_3)\}_2]$ VIII and $[ZnCl_2\{CSNH_2(NHCH_3)\}_2]$ XIII.

(a) Optical properties

The absorption (a) and photoluminescence (b) spectra of CdS nanoparticles capped by HDA synthesized from complex **IV** is shown in Figure 4.38. The absorption spectrum revealed a sharp excitonic peak (417 nm) with a band edge of 447 nm (2.77 eV). The photoluminescence spectrum, which is slightly red shifted to the as-prepared CdS nanoparticles absorption spectrum, has a maximum emission peak of 451 nm. It is interesting to observe that the photoluminescence spectrum is narrow, since it signified small particles size.

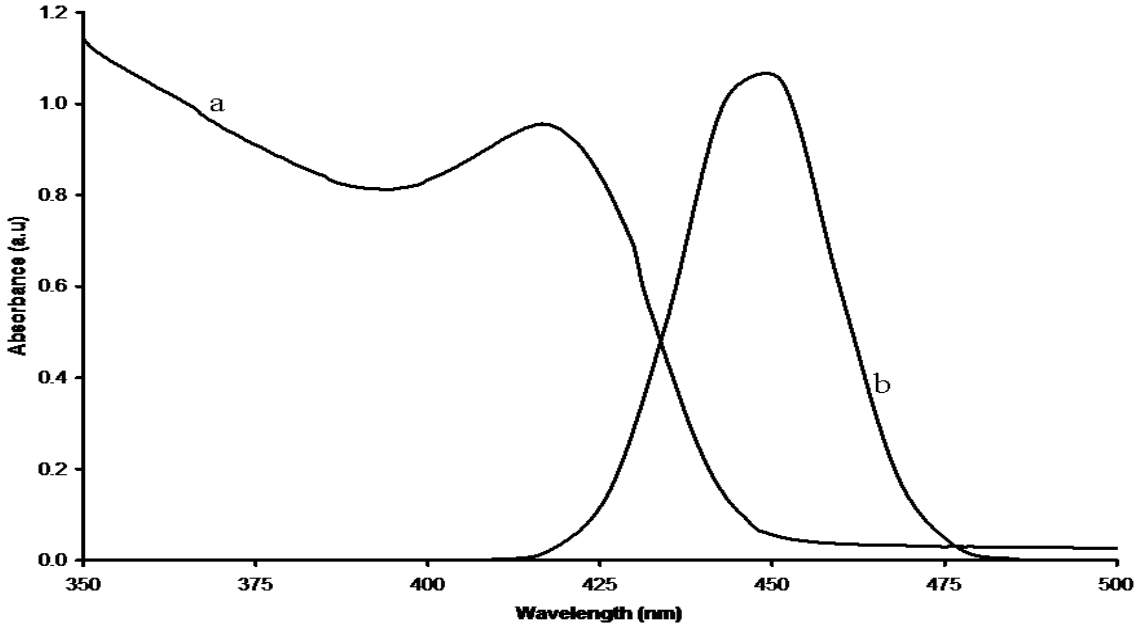

Figure 4.38: Absorption (a) and photoluminescence (b) spectra of CdS nanoparticles capped by HDA synthesized from complex **IV** at 120 ^{o}C for 1 h.

Figure 4.39 shows the absorption (a) and photoluminescence (b) spectra of Co_3S_4 nanoparticles capped by HDA synthesized from complex **VIII** at 120 ^{o}C for 1 h. The blue shifted absorption spectrum to bulk Co_3S_4 band gap energy depicts an estimated band edge of 516 nm, corresponding to 2.40 eV, while the photoluminescence spectrum, which is red shifted to the as-prepared absorption spectrum, has a maximum emission peak appearing at 532 nm (2.33 eV). The photoluminescence spectrum of these Co_3S_4 nanoparticles is narrow, signifying monodispersed particles that are well passivated or capped. The presence of the smooth single peak is an indicative of the existence of predominantly single morphology.

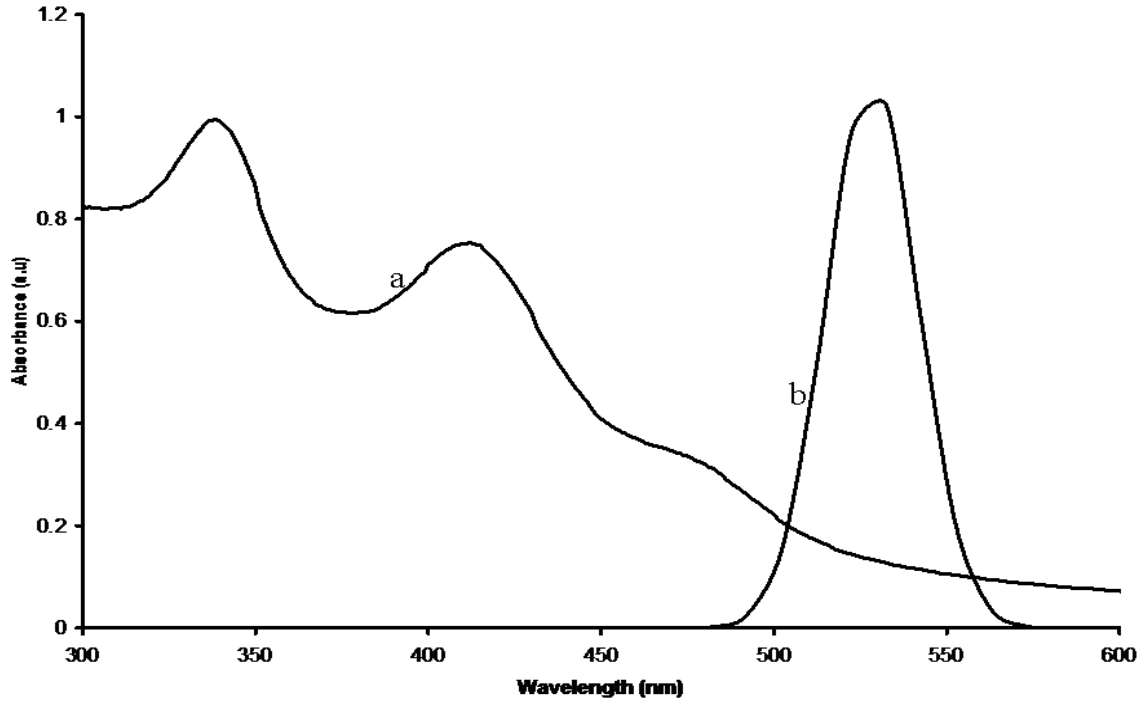

Figure 4.39: Absorption and photoluminescence spectra of Co_3S_4 nanoparticles capped by HDA synthesized from complex **VIII** at 120 ^oC for 1 h.

Figure 4.40 shows the absorption (a) and photoluminescence spectra of ZnS capped by HDA synthesized from complex **XIII** at 120 ^oC for 1 h. The band edge of the absorption spectrum is 342 nm (3.62 eV), which is blue shifted to bulk ZnS band edge. The red shifted photoluminescence spectrum to the as-prepared ZnS nanoparticles absorption spectrum band edge depicts a maximum emission peak of 350 nm, corresponding to an energy band gap of 3.54 eV. The photoluminescence spectrum only shows single smooth peak which is an indicative of the existence of predominantly single morphology.

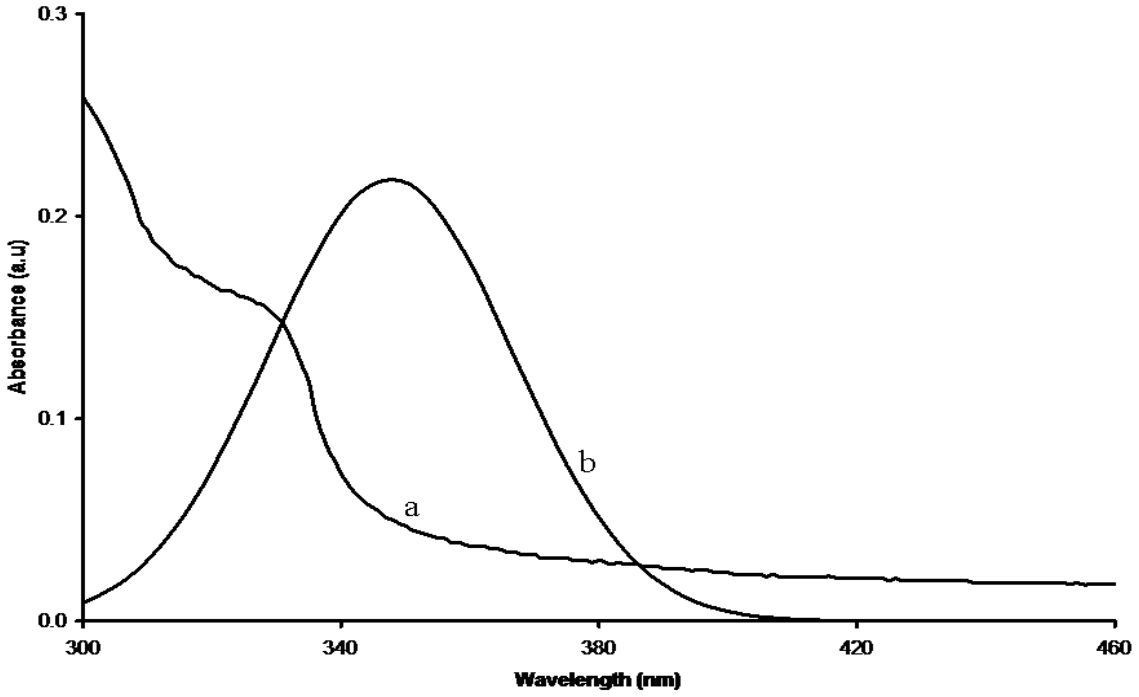

Figure 4.40: Absorption (a) and photoluminescence (b) spectra of ZnS nanoparticles capped by HDA synthesized from complex **XIII** at 120 ^{o}C for 1 h.

(b) Structural properties

Figure 4.41 shows the TEM image of CdS nanoparticles capped by HDA (a) and histogram of particle size distribution (b). The particles were grown from complex **IV** at 120 ^{o}C for a maximum of an hour. Short rods particles with some signs of close-to-spherical particles were observed. The average diameter of the particles measured is 6.2 nm. However, the particles are very close to each other showing some form of aggregation due to their small size and surface energy. The presence of close-to-spherical particles even though the crystal phase wurtzite favors rods could be due to the lack of stability of the nanoparticles due to their small size, thus resume a shape that requires less energy. Broad peaks signifying finite size of CdS nanoparticles are observed in Figure 4.42. The peaks are positioned at 2θ values of 25.2^{o}, 26.9^{o}, 28.2^{o}, 37.2^{o}, 44.1^{o}, 48.2^{o} and 52.3^{o}, corresponding to (100), (002), (101), (102), (110), (103) and (112), respectively. All these peaks are indexed to hexagonal phase of CdS.

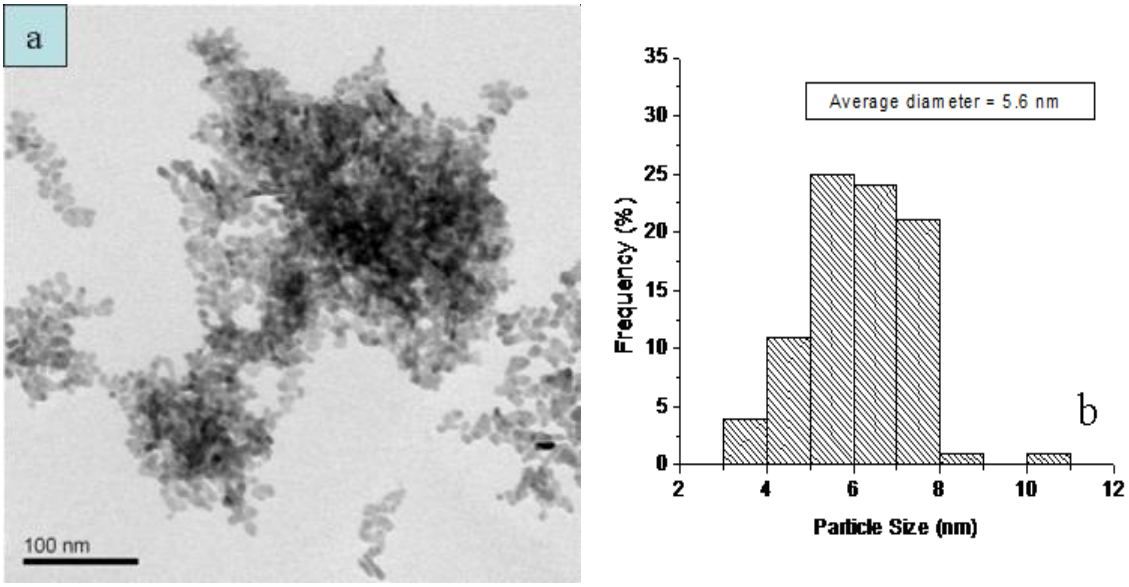

Figure 4.41: TEM image of CdS nanoparticles capped by HDA synthesized from complex **IV** at 120 ^{o}C for 1 h (a), and its corresponding size distribution histogram (b).

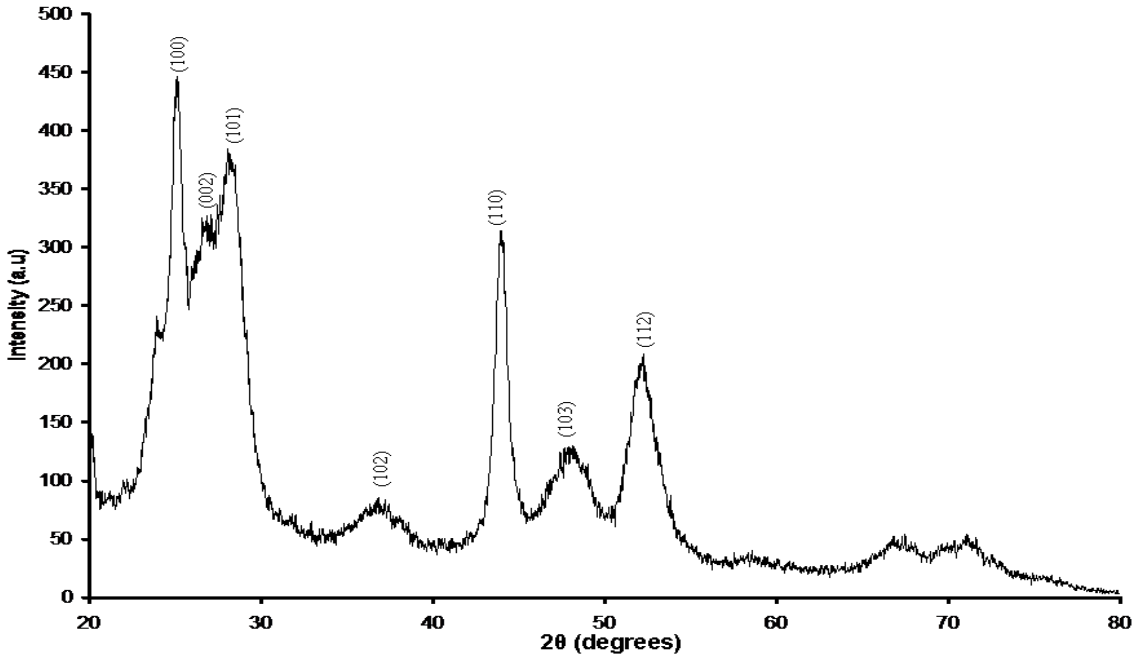

Figure 4.42: XRD pattern of CdS nanoparticles capped by HDA synthesized from complex **IV** at 120 ^{o}C for 1 h.

Figure 4.43 shows the TEM image of Co_3S_4 nanoparticles capped by HDA synthesized from complex **VIII** at 120 ^{o}C for 1 h (a) and histogram of particle size distribution (b). No obvious aggregation was visible in the sample. Small close-to-spherical particles with an average diameter of 1.7 nm were observed. Figure 4.44 shows the XRD pattern of Co_3S_4

nanoparticles capped by HDA synthesized from complex **VIII** at 120 ^{o}C for 1 h. All the main reflection peaks in Figure 4.44 can be indexed as face-centered cubic Co_3S_4, consistent with those of the reported values for bulk Co_3S_4 crystal (JCPDS Card 73-1703).

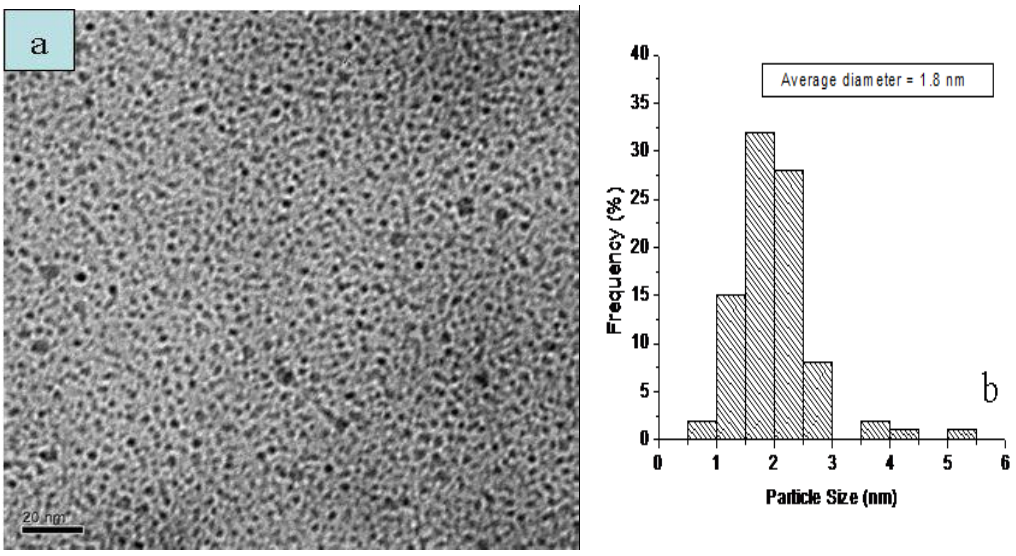

Figure 4.43: TEM image of Co_3S_4 nanoparticles capped by HDA synthesized from complex **VIII** at 120 ^{o}C for 1 h (a), and its corresponding size distribution histogram (b).

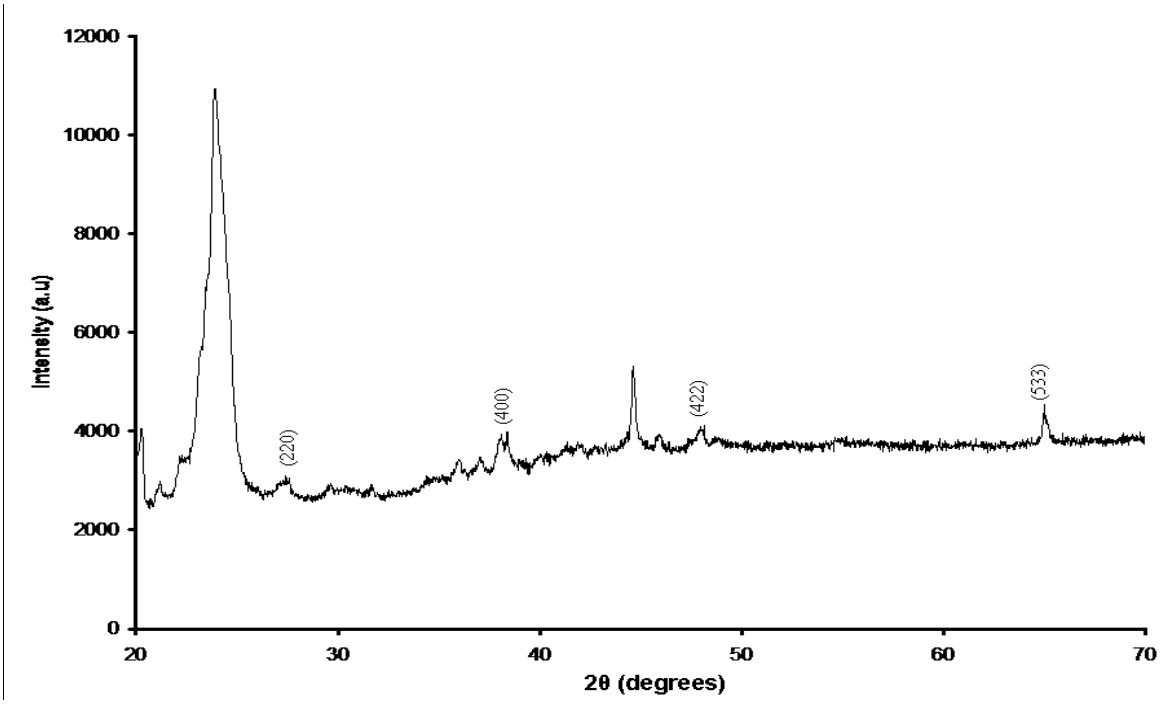

Figure 4.44: XRD pattern of Co_3S_4 nanoparticles capped by HDA synthesized from complex **VIII** at 120 ^{o}C for 1 h.

Figure 4.45 shows TEM image of ZnS nanoparticles capped by HDA synthesized from complex **XIII** at 120 ^{o}C for 1 h (a) and histogram of particle size distribution (b). The rod-shaped particles observed have an average diameter of 3.8 nm. There are signs of some particles fusing together at the centre to form bipods and tetrapods. Figure 4.46 shows the XRD pattern of ZnS capped by HDA grown from complex **XIII** at 120 ^{o}C for a maximum of an hour. The XRD peaks are found to be very broad which is a good indication of the crystallinity as well as the small size of the particles. The XRD pattern exhibits important broad peaks at 2θ values of 28.5^{o} (111), 48.2^{o} (220) and 56.8^{o} (311). All the three peaks are indexed to cubic phase of ZnS (JCPDS Card 05-0566). However, there are some peaks appearing between 20^{o} and 25^{o}. Those peaks are marked with asterisks and are due to the capping agent used.

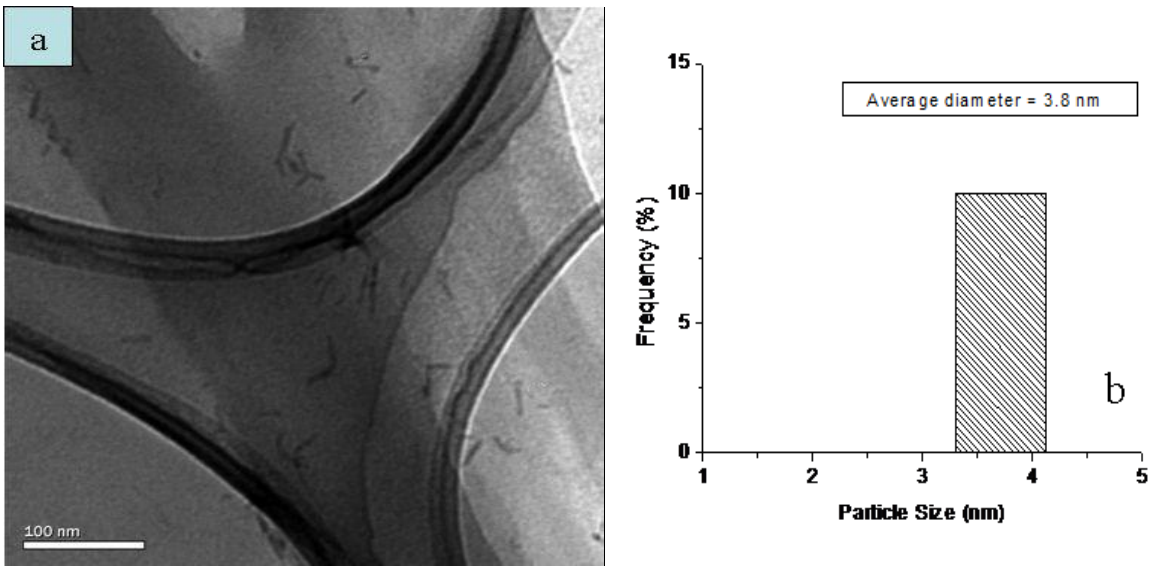

Figure 4.45: TEM image of ZnS capped by HDA synthesized from complex **XIII** at 120 ^{o}C for 1 h (a), and its corresponding size distribution histogram (b).

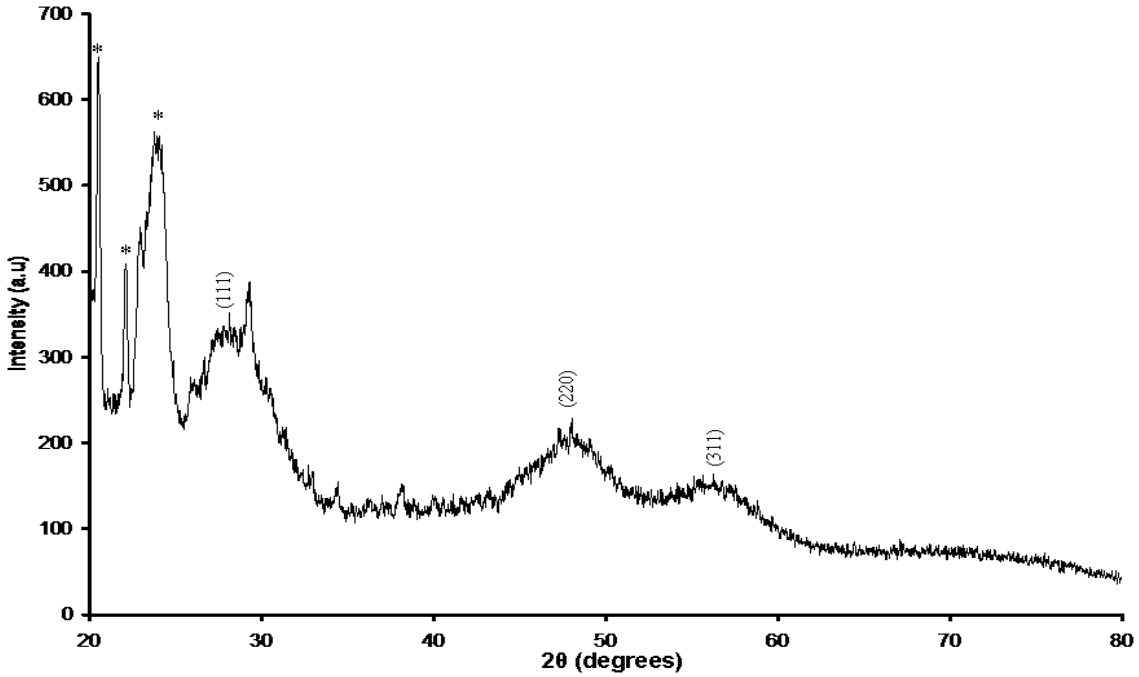

Figure 4.46: XRD pattern of ZnS nanoparticles capped by HDA synthesized from complex **XIII** at 120 ^{o}C for 1 h.

4.3.5 Synthesis of CdS, Co_xS_y and ZnS nanoparticles from $[Cd\{(C_2H_5)_2NCS_2\}_2]$ V, $[Co\{(C_2H_5)_2NCS_2\}_2]$ IX and $[Zn\{(C_2H_5)_2NCS_2\}_2]$ XIV

Metal dialkyldithiocarbamates have been widely used as active accelerators in the sulphur vulcanization of rubber [55] and as metal sulfide precursors in metal-organic chemical vapour deposition (MOCVD) applications [56, 57]. This is because they are moisture insensitive, air stable, less toxic, easy to synthesize and handle. The bis(diethyldithiocarbamato) cadmium compounds have the advantage of stability as compared to other sulphur containing precursors. Precursors based on bis(methyl^{n}hexyldiselenocarbamato) zinc or cadmium decompose particularly cleanly in MOCVD to metal selenides [58, 59, 60]. Below are the results obtained when bis(diethyldithiocarbamato) cadmium was used as a single source precursor for the synthesis of CdS nanoparticles. The effect of temperature and capping agent on the size and shape of the nanoparticles was investigated.

(a) Infrared spectroscopy

Figure 4.47 shows the FT-IR spectrum of CdS nanoparticles capped by HDA synthesized from complex **V** at 180 ^{o}C for an hour. It can be seen that the C-N vibration peak at 1468 cm^{-1} and C-H peak at 1570 cm^{-1} of HDA are observed, whereas the N-H asymmetric stretch peak at 3238 cm^{-1} is weaker due to the amine ligands bound to the nanocrystal surfaces. This observation demonstrates that the nanoparticles were stabilized by HDA. Simiilar phenomena have been observed in HDA-capped semiconductor nanoparticles [53, 61]. To further elucidate whether pods were obtained due to the nature of the complex used, thermolysis was also done at 180 ^{o}C using TOPO as the capping agent instead of HDA. In order to confirm the presence of the capping agent, which is TOPO on the surface of the nanomaterial, infrared spectroscopy was used. TOPO is known to absorb strongly at 1146 and 1466 cm^{-1} corresponding to P=O stretching and CH_2 bending, respectively [62]. In the spectrum of CdS nanoparticles capped by TOPO (Figure 4.48), the P=O stetching vibration peak at 1141 cm^{-1} and CH_2 bending peak at 1462 cm^{-1} have moved to lower wavenumbers. The shift of these peaks to lower wavenumbers has also been reported before for CdSe nanoparticles capped by TOPO and attributed to the binding of TOPO to Cd^{2+} sites on the CdSe nanocrystallites surface [63].

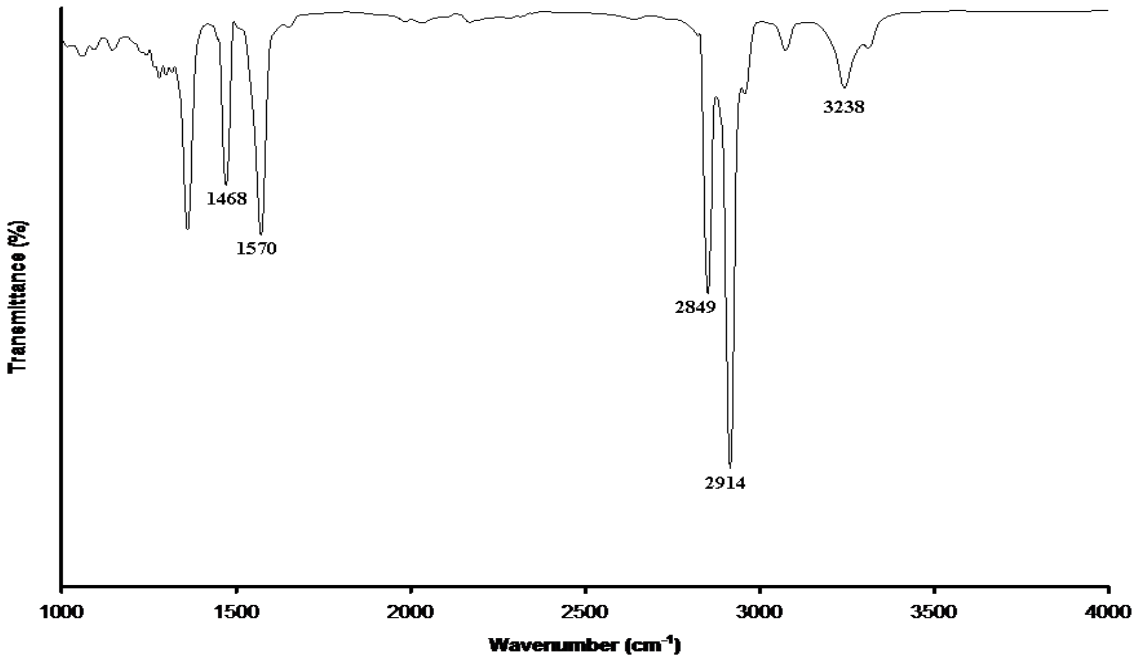

Figure 4.47: FT-IR spectrum of CdS nanoparticles capped by HDA synthesized from complex **V.**

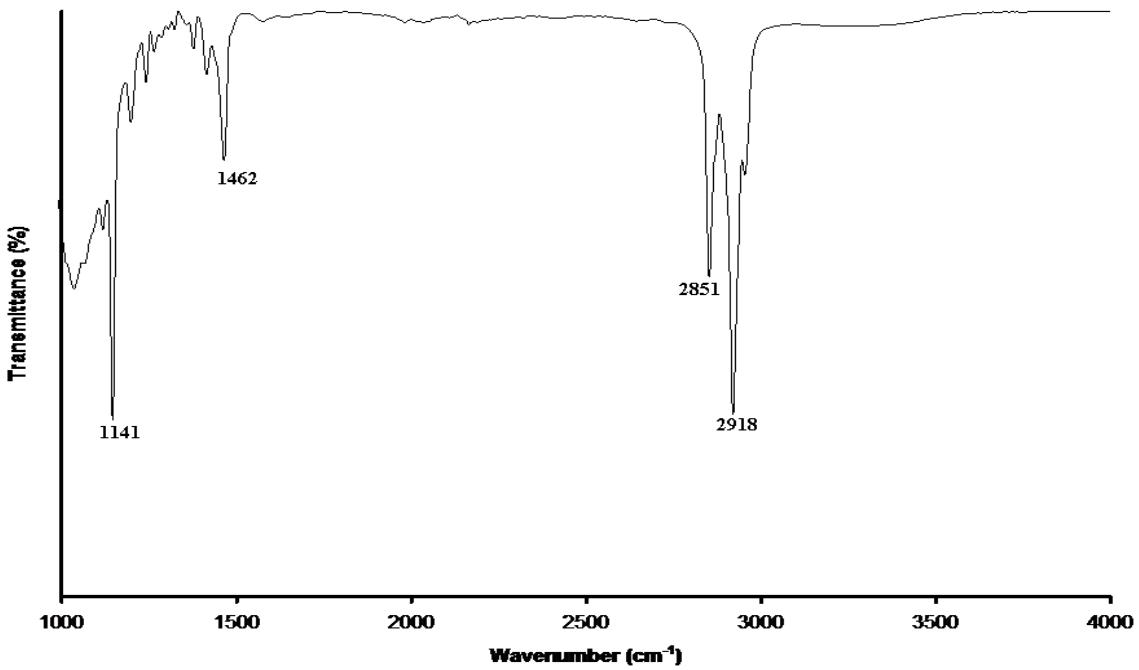

Figure 4.48: FT-IR spectrum of CdS nanoparticles capped by TOPO synthesized from complex **V.**

Figure 4.49 shows the FT-IR spectrum of CdS nanoparticles capped by a mixture of HDA and TOPO synthesized at 120 ^{o}C for 1 h. The spectrum has peaks matching all of the pure HDA and TOPO peaks. It displayed a shift of ν(N-H) to lower wavenumbers compared to that of free HDA (for free HDA ν(N-H) = 3325 cm^{-1}), with the peak being less intense as compared to the peak for pure HDA indicating coordination of HDA. This is supported by results that were reported by Kedarnath *et al.* [64] who synthesized CdSe capped by a mixture of HDA and TOPO. In the C-H stretch spectral region, the strong sharp peaks at 2916 and 2850 cm^{-1} are due to antisymmetric and symmetric CH_2 stretching vibrations. The peak at 1464 cm^{-1} is due to $\delta(CH_2)$, while peak appearing at 1143 cm^{-1} indicate the presence of ν(P=O). This confirms that both HDA and TOPO are present in the surface of the CdS nanoparticles.

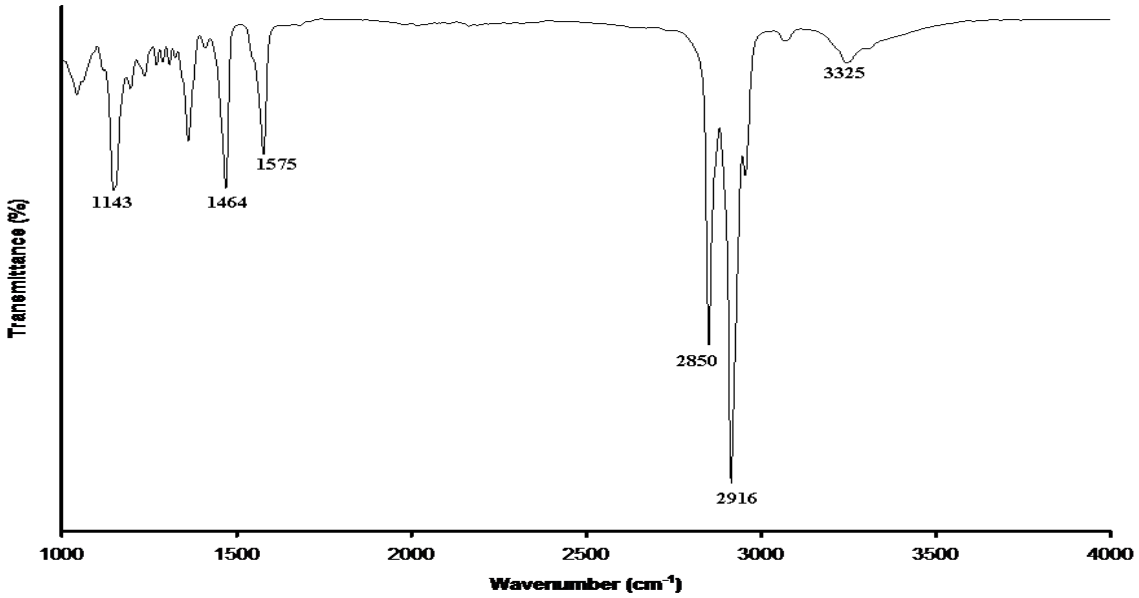

Figure 4.49: FT-IR spectrum of CdS nanoparticles capped by a mixture of HDA and TOPO synthesized from complex **V** at 120 ^{o}C for 1 h.

(b) Optical properties

Thermolysis of diethyldithiocarbamate cadmium complex in hexadecylamine was carried out at 120 ^{o}C and 180 ^{o}C for an hour. The main feature on the properties of quantum dots is their band gap, which is the energy separation between the filled valence band and the empty conduction band. Figure 4.50 depicts the absorption spectra of CdS nanoparticles capped by HDA synthesized from complex **V** at 120 ^{o}C (a) and 180 ^{o}C (b) for duration of an hour. Both absorption spectra show band edges that are blue shifted from the bulk CdS, signifying small sizes of the nanoparticles. However, due to an increase in temperature, the absorption band edges do not appear at the same region. It appears that as the temperature increases the size increases at a slower rate when the band edge is approaching bulk. This could also mean that at lower temperatures there are smaller particles, confirmed by Nair [65] where nanoparticles from the same precursor at 100 ^{o}C gave a band edge of 460 nm, and as the temperature increases the rate of particle growth increases up until an optimum temperature where the rate begins to be constant. The sharpness of the excitonic peaks which was stronger for CdS at 120 ^{o}C was lost when the temperature was increased to 180 ^{o}C. The band edges of CdS nanoparticles capped by HDA at 120 ^{o}C (a) is 485 nm (2.57 eV), while the one prepared at 180 ^{o}C (b) appeared at 502 nm (2.47 eV). The excitonic peaks of the absorption spectra at 120 ^{o}C and 180 ^{o}C are 458 nm (2.71 eV) and 475 nm

(2.61 eV), respectively. To further elucidate the argument of the temperature effect on the particles, photoluminescence spectroscopy was employed. Figure 4.51 shows the photoluminescence spectra of CdS capped by HDA synthesized from complex **V** at 120 ^{o}C (a) and 180 ^{o}C (b) for an hour. It is clear to observe that when the temperature was increased, the pholuminescencce spectrum also increased in width. Therefore, this broadening was probably caused by a higher temperature resulting partly in new nucleation of nanocrystals. Similar phenomena have been observed by Liu *et al.* [66] who synthesized CdS capped by N-oleoylmorpholine nanoparticles at different temperatures (180 ^{o}C, 210 ^{o}C and 240 ^{o}C) and reported an increase of full width at half maxima as the temperature was increased. The pholuminescence spectrum of the bulk CdS has been reported to have a broad emission maximum in the region 500 – 700 nm [67]. The emission maximum observed at 488 nm (2.54) for HDA-capped CdS nanoparticles synthesized at 120 ^{o}C is narrower than the one synthesized at 180 ^{o}C, 510 nm (2.43 eV), which further confirms nanocrystals of small size. The CdS nanoparticles at 120 ^{o}C have a full width at half maximum of 24 nm, while the one synthesized at 180 ^{o}C is 33 nm. Besides that difference, both spectra still signifies nanosized particles and are red shifted to their as-prepared absorption spectra. A blue shift of band edge emission with decrease in size of CdS arising from quantum confinement has been reported by several authors [68, 69].

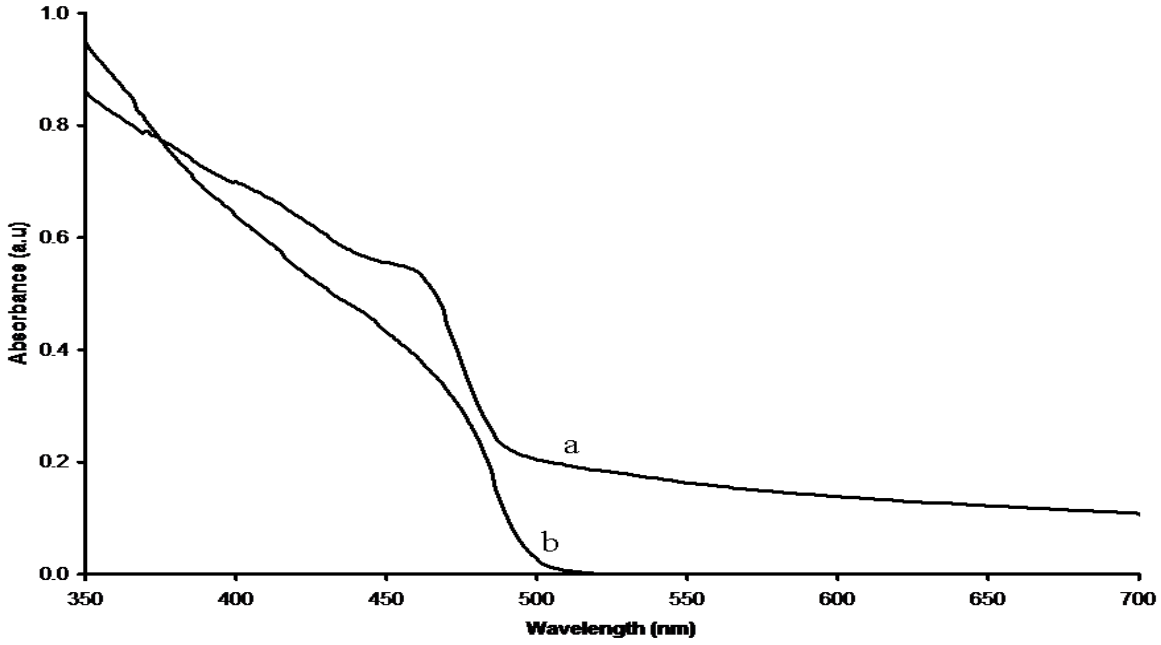

Figure 4.50: Absorption spectra of CdS nanoparticles capped by HDA synthesized from complex **V** at 120 ^{o}C (a) and 180 ^{o}C (b) for 1 h.

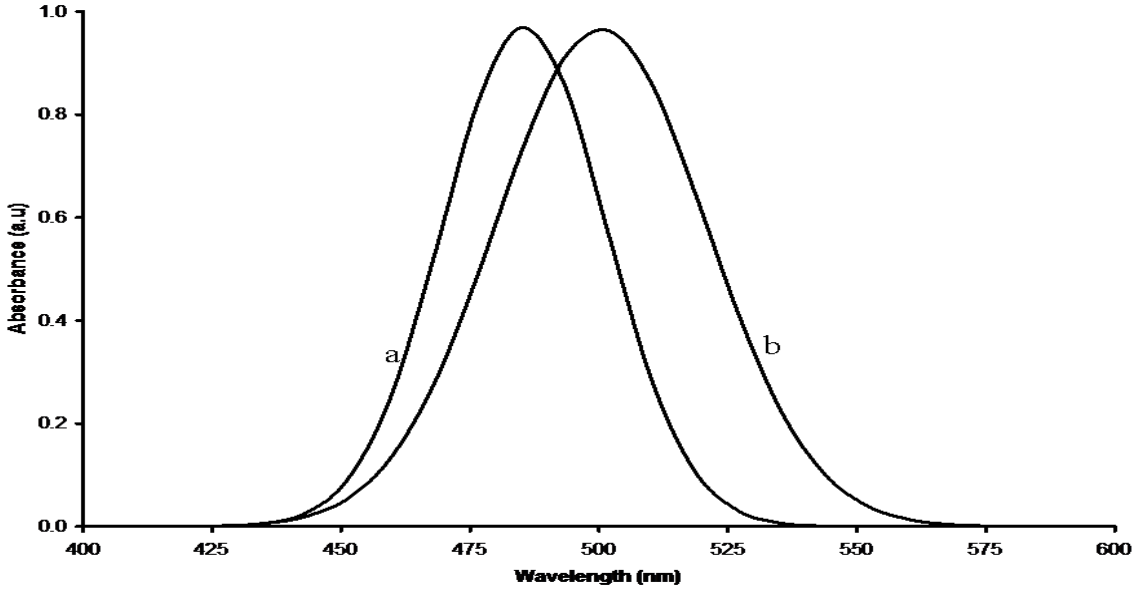

Figure 4.51: Photoluminescence spectra of CdS nanoparticles capped by HDA synthesized from complex **V** at 120 ^{o}C (a) and 180 ^{o}C (b) for 1 h.

Cadmium diethyldithiocarbamate is a well known compound and was prepared by the stoichiometric reaction of diethyldithiocarbamate with the metal chloride in water [57]. In this case, same method was used with high yield obtained. TOPO, which is one the most utilized capping ligand, was used. The use of TOPO method has emerged as a significant and powerful route to prepare high quality nanocrystals of a wide range of semiconductors. Initial work by O'Brien group involved the use of bis(alkyl/selenocarbamato) cadmium (II)/zinc (II) compounds which were thermolyzed in TOPO to give MS and MSe (M = Cd, Zn) nanoparticles [62, 70]. The synthesis of these precursors followed a simple procedure in which CSe_2 or CS_2 was reacted with an excess of the amine and hydroxides at temperatures below 0 ^{o}C to give the dithio- and diselenocarbamates as a salt. The compounds were then reacted with a stoichiomertic quantity of aqueous solution cadmium (II)/zinc (II) chloride to give bis(dialkyl/dithio/diselenocarbamato) cadmium (II)/ zinc (II) compounds of the type $M(E_2CNRR')_2$ either containing symmetric amine alkyl) groups (R = R' = alkyl) or having asymmetric groups on the amine (R = Me or Et and R' = ^{n}He, ^{n}Bu) [62, 70, 71, 72, 73]. The absorption and photoluminescence spectra of CdS nanoparticles capped by TOPO synthesized from complex **V** are shown in Figure 4.52. The absorption spectrum is blue shifted compared to the CdS bulk, with the photoluminescence spectrum being red shifted to the as-prepared absorption spectrum. The absorption spectrum of

TOPO-capped CdS nanoparticles with an excitonic peak appearing at 405 nm (3.06 eV), has an estimated band edge of 444 nm which correspond to 2.79 eV. The strong emission peak has maximum of 450 nm (2.76 eV). Comparison of CdS nanoparticles capped by either HDA (reported above) or TOPO synthesized from diethyldithiocarbamate cadmium complex **V** at 180 ^{o}C differed in terms of band edges. Both the spectra (absorption and emission) of TOPO-capped CdS nanoparticles appear at higher energy while HDA-capped CdS appear far at lower energy. Oluwafemi and Revaprasadu [74] synthesized HDA-capped CdSe and TOPO-capped CdSe using same precursor under similar conditions, except capping agents. The report shows that the band energy of CdSe capped by TOPO is lower as compared to that of CdSe capped by HDA. The sizes of the particles also differed, with TOPO capped CdSe depicting bigger particles size. Similar results were also obtained by Talapin *et al*. [3]. The authors attributed the difference in sizes to the redistribution of electronic density in the semiconductor core under the influence of passivating groups or loss of surface Cd and Se atoms with leaving TOPO molecules. However, in our case, the opposite was observed but with similar trend. For example, the band energy of TOPO-capped CdS was higher, with the particles size being smaller, whilst the opposite was observed for CdS capped by HDA. In summary, employing same complex at constant temperature and time, but different ligands or capping agents does not lead to similar results (for example, band edges, emission maximum, TEM images, etc).

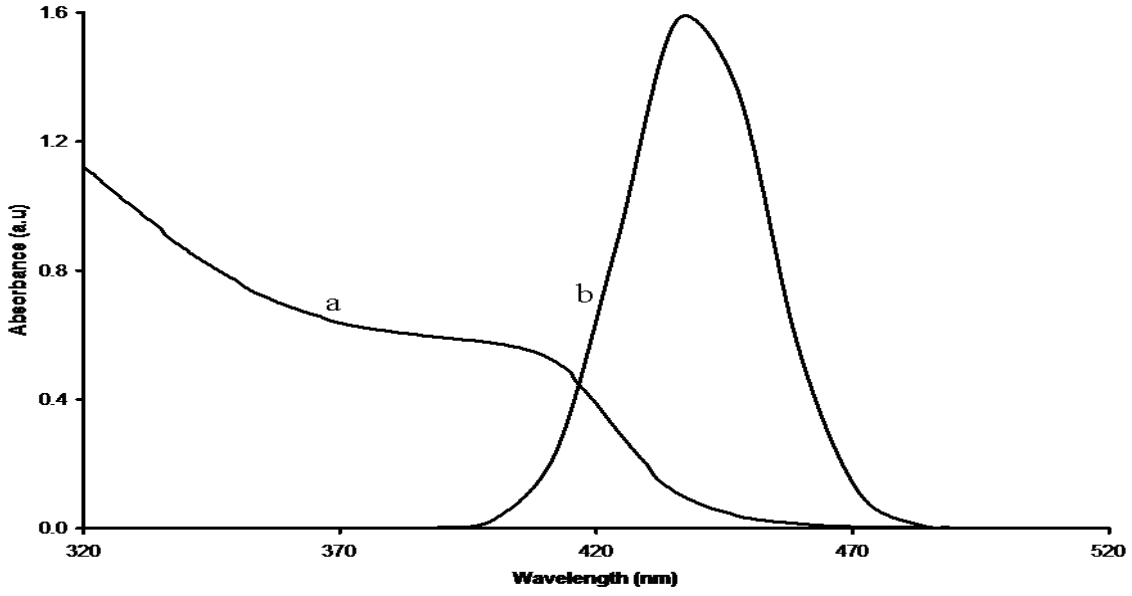

Figure 4.52: Absorption (a) and emission (b) spectra of CdS nanoparticles capped by TOPO synthesized from complex **V** at 180 ^{o}C for 1 h.

The diethyldithiocarbamato cadmium complex was achieved in high yield, which gave us opportunity to further explore it. It is one complex that is easy to synthesize at room temperature, where water is used as a solvent. After decomposition of the same complex into CdS with different capping agents led to different shapes, we then decided to use a mixture of capping agents (HDA and TOPO) to investigate the influence of those shapes. As stated before, the capping agents play an important role in the shape of the nanoparticles. Previous reports show CdS nanoparticles capped by TOPO influencing the formation of spheres [75] while rods are formed when HDA is used [46]. Over the past decades, reports showed the formation of the above shapes especially when cadmium was used as the metal.

HDA-TOPO was used to stabilize CdS nanoparticles synthesized from complex **V** at 120 ^{o}C for duration of an hour. The objective of employing double ligands or capping agents was to prove whether similar or different shapes would be obtained due to the influence of capping agents as HDA was reported to influence the formation of rods with TOPO favouring spheres. In most cases where these shapes were reported due to the above capping agents, cadmium was used as a metal. Figure 4.53 shows the absorption and emission spectra of CdS nanoparticles capped with HDA-TOPO synthesized from complex **V** at 120 ^{o}C for duration of an hour. The ratio used between HDA and TOPO was 1:1. The absorption spectrum which is blue shifted to the bulk CdS has a band edge appearing at 504 nm (2.46 eV), with an excitonic peak appearing at 462 nm (2.68 eV). The emission spectrum is red shifted as compared to the as-prepared CdS nanoparticles, with an emission maximum peak appearing at 506 nm (2.45 eV). Comparison between CdS nanoparticles capped with HDA and CdS nanoparticles capped by HDA-TOPO shows a blue shift in both absorption and emission spectra in the HDA-capped CdS nanoparticles. Similar results were reported by Talapin *et al.* [3] in the preparation of HDA-TOPO capped CdSe nanoparticles. In their report, they concluded that CdSe particles capped by HDA-TOPO are more stable.

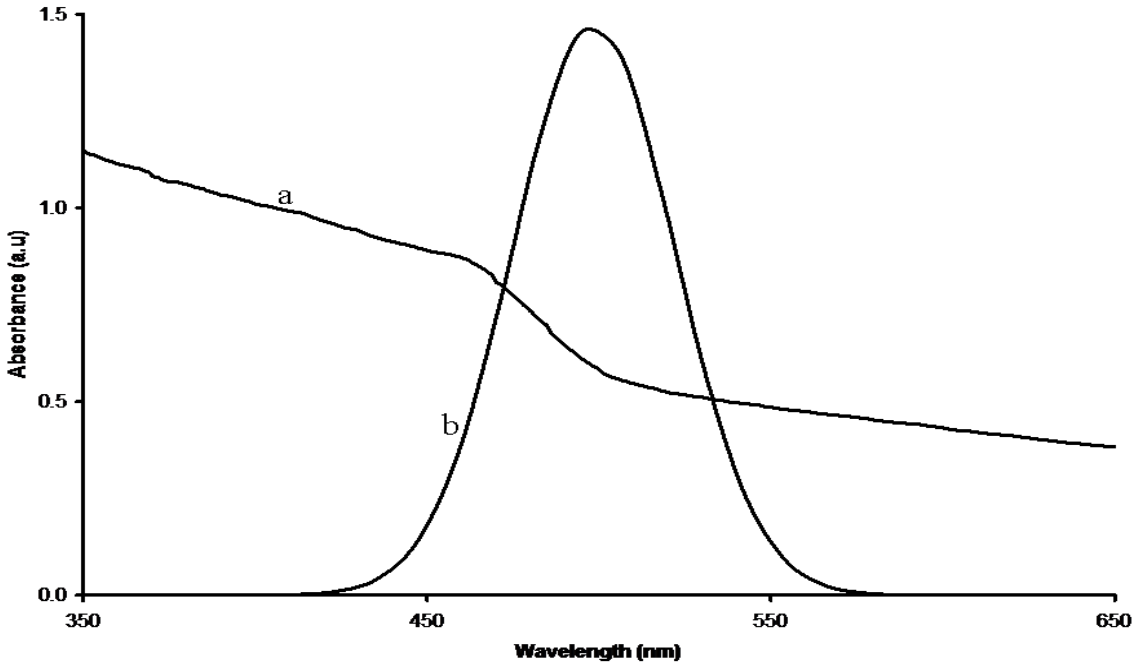

Figure 4.53: Absorption (a) and emission (b) spectra of CdS nanoparticles capped by HDA-TOPO synthesized from complex **V** at 120 ^{o}C for 1 h.

The absorption (a) and photoluminescence (b) spectra of Co_3S_4 nanoparticles capped by HDA synthesized from complex **IX** are shown in Figure 4.54. The particles were grown at 180 ^{o}C for an hour. The bulk band gap energy of Co_3S_4 is 1.15 eV. The blue shifted absorption spectrum has a band edge appearing at 505 nm (2.46 eV) with an excitonic peak appearing at 478 nm (2.59 eV), while the red shifted photoluminescence spectrum to the as-prepared absorption spectrum is positioned at 507 nm (2.45 eV). The absorption (a) and photoluminescence (b) spectra of the same material but capped by TOPO are shown in Figure 4.55, with a band edge of 513 nm (2.42 eV) and a maximum emission peak of 519 nm (2.39 eV), respectively. Similarity between the absorption spectra (Figures 4.54a and 4.55a) is that each spectrum exhibited three absorption peaks. The positions of the three absorption peaks equally remained almost the same irrespective of the capping agent used, sugesting that the cobalt sulphide QDs capped by HDA or TOPO had quite high stability. However, the intensities of absorbance decreased for cobalt sulphide capped by TOPO, which meant that the concentration of cobalt sulphide QDs decreased.

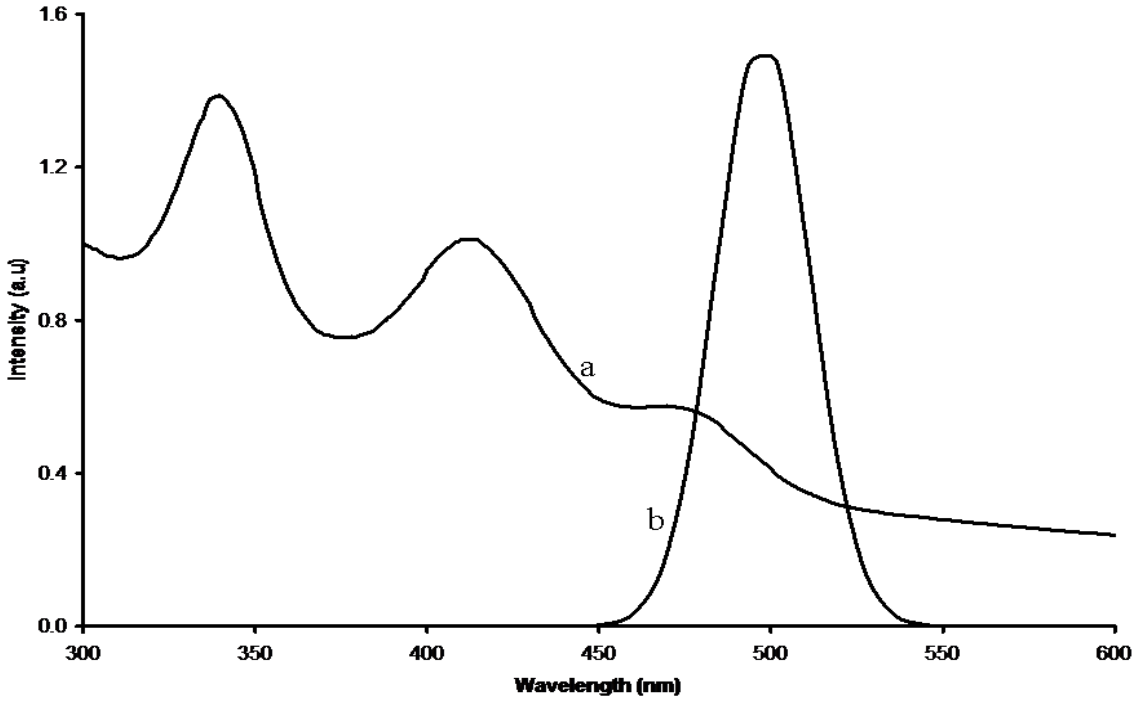

Figure 4.54: Absorption (a) and photoluminescence (b) spectra of Co_3S_4 nanoparticles capped by HDA synthesized from complex **IX** at 180 ^oC for an hour.

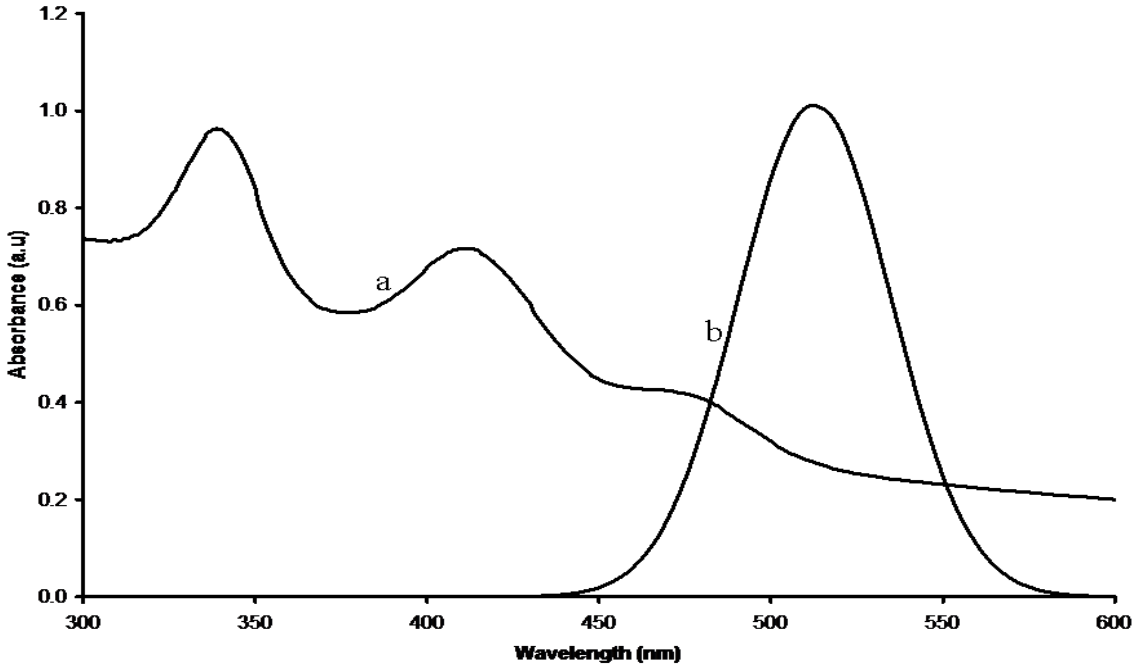

Figure 4.55: Absorption (a) and photoluminescence (b) spectra of Co_3S_4 nanoparticles capped by TOPO synthesized from complex **IX** at 180 ^oC for an hour.

Figure 4.56 shows the absorption (a) and photoluminescence (b) spectra of ZnS capped by HDA. Particles were grown from complex **XIV** at 180 ^{o}C for an hour. The absorption spectrum with a band edge of 320 nm (3.87 eV), is blue shifted to bulk ZnS band edge which signifies particles of small size. The photoluminescence spectrum, which is red shifted to the as-prepared absorption spectrum, has a maximum emission peak appearing at 354 nm (3.50 eV). The absorption (a) and photoluminescence (b) spectra of ZnS nanoparticles capped by TOPO are shown in Figure 4.57. The particles were synthesized from complex **XIV** at 120 ^{o}C for a maximum of an hour. The absorption spectrum, which is blue shifted to the absorption bulk band edge, has a band edge appearing at 314 nm (3.95 eV), with the maximum emission peak of the photoluminescence spectrum, which is red shifted to the as-prepared absorption spectrum, positioned at 349 nm (3.55 eV). The absorption spectrum of ZnS nanoparticles capped by HDA shows a broad shoulder, whilst TOPO-capped ZnS nanoparticle does not reveal any shoulder. However, both absorption spectra revealed neither any sharp absorption peak. The absence of sharp absorption peak signifies poor capping or passivation of the particles.

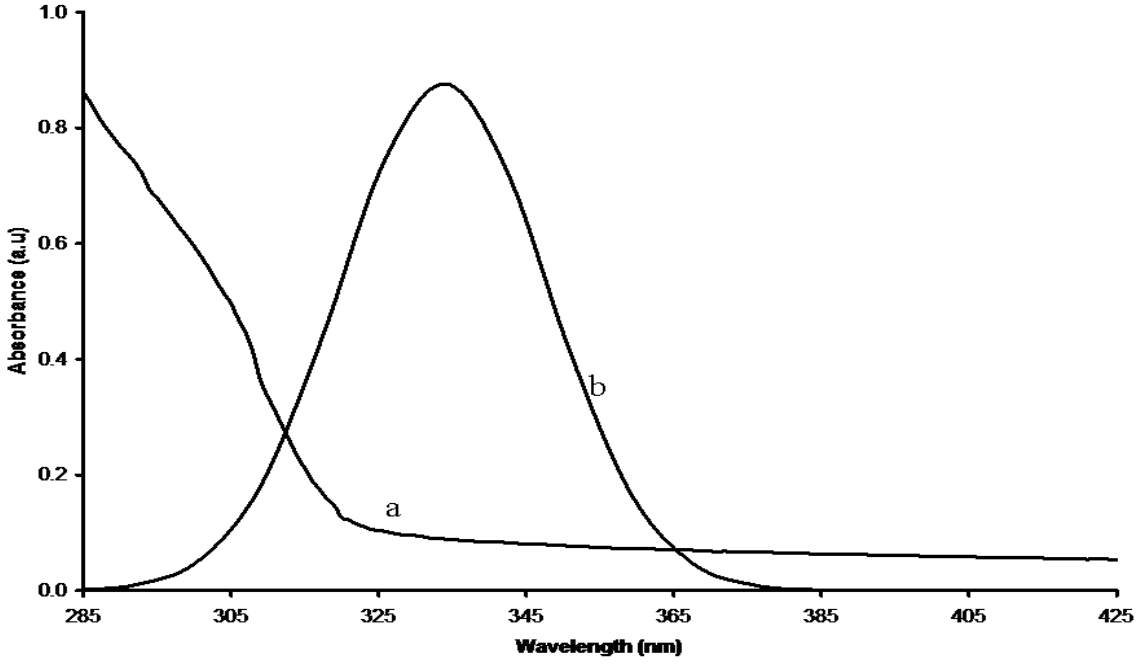

Figure 4.56: Absorption (a) and photoluminescence (b) spectra of ZnS nanoparticles capped by HDA synthesized from complex **XIV** at 180 ^{o}C for 1 h.

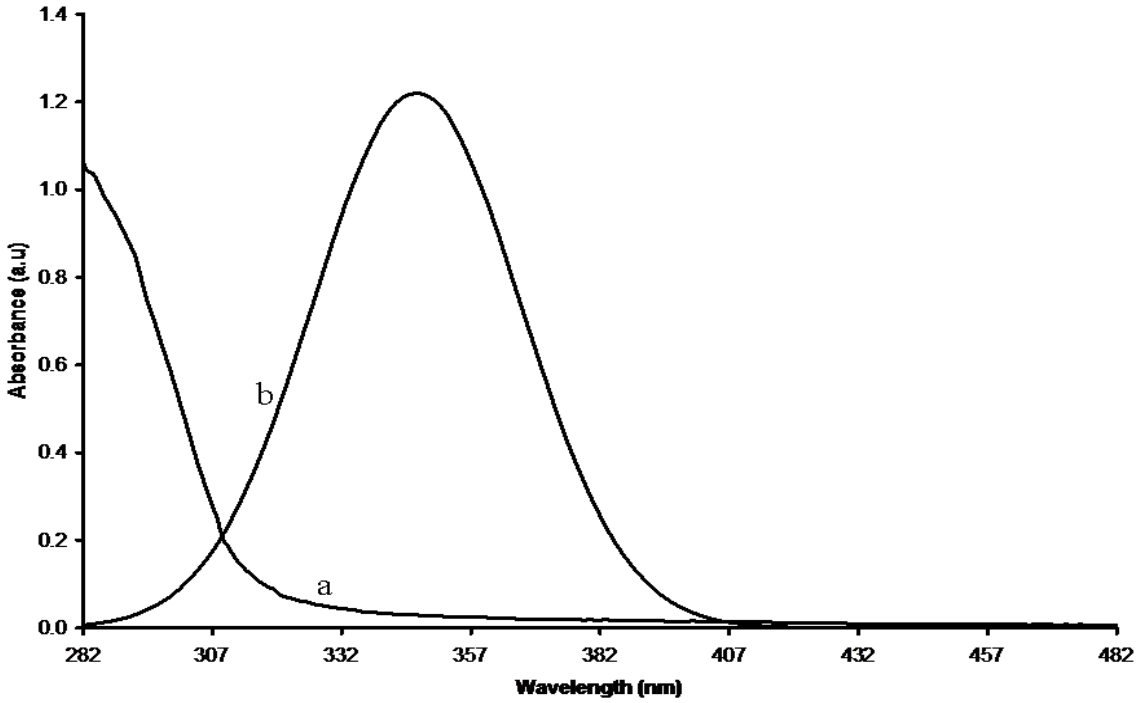

Figure 4.57: Absorption (a) and photoluminescence (b) spectra of ZnS nanoparticles capped by TOPO synthesized from complex **XIV** at 180 ^{o}C for 1 h.

(c) Structural properties

Figure 4.58 depicts the TEM images of CdS nanoparticles capped by HDA synthesized from complex **V** at 120 ^{o}C for duration of 1 h (a) and 180 ^{o}C (c), and histograms of particle size distribution (b – 120 ^{o}C and d – 180 ^{o}C). The images of both HDA-capped CdS show particles with rod shape, with some rods fused together at the centre to form bipods and tripods. More evidence of bi- and tripods is clearly observed when the temperature is increased to 180 ^{o}C (Figure 4.58b). The formation of this type of rods is not new as was reported before. Li *et al.* [46] thermolysed cadmium ethylxanthate $\{Cd(C_2H_5OCS_2)_2\}$ and reported the formation of four armed, three armed and two armed rods at 120 ^{o}C. The formation of two armed and three armed rods augurs well with our results, except the four armed ones, which were not observed in our case. The particles diameters as determined from the TEM images are 3.2 nm for CdS synthesized at 120 ^{o}C, and 5.6 nm for CdS nanoparticles synthesized at 180 ^{o}C.

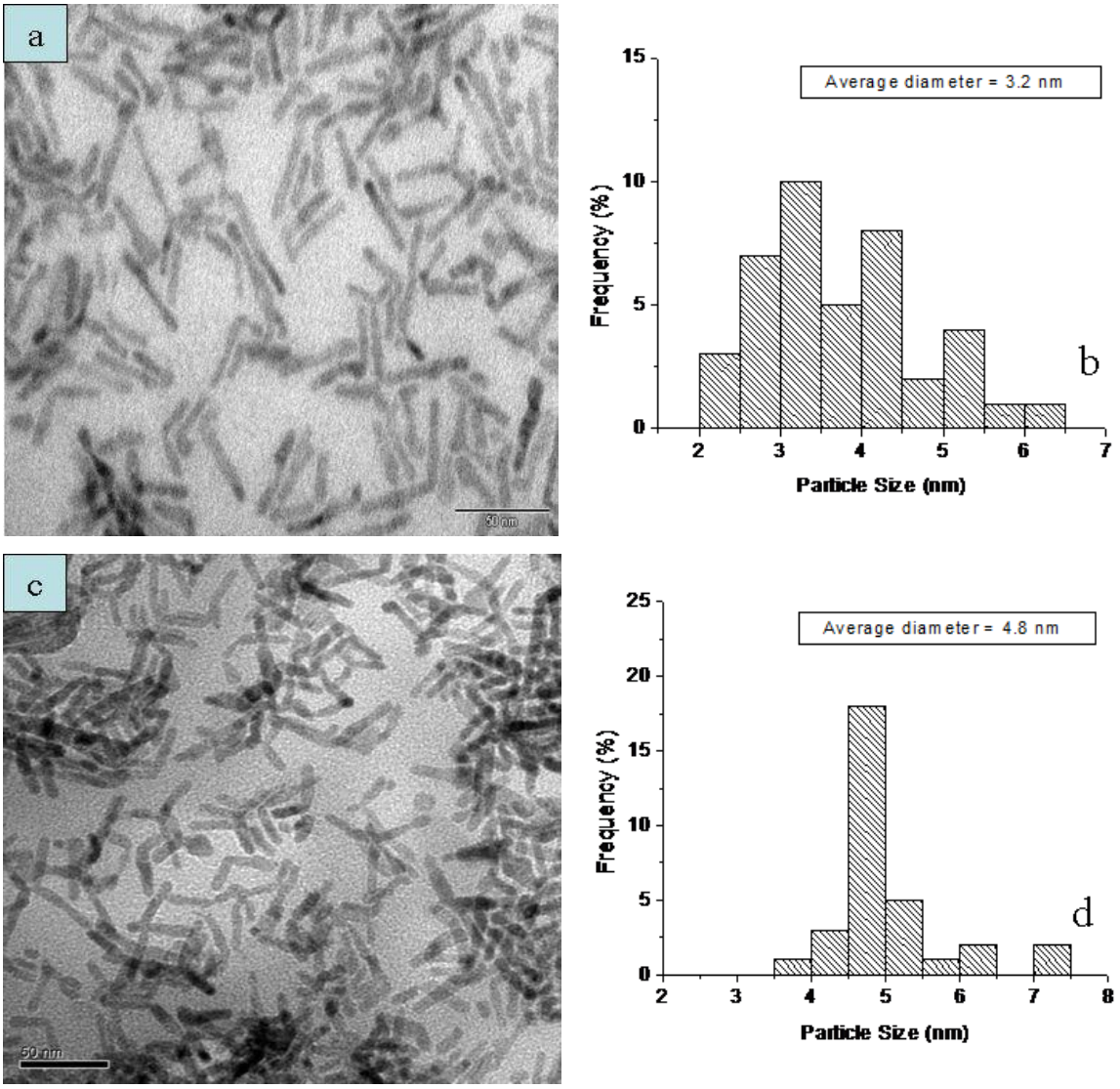

Figure 4.58: TEM images of CdS nanoparticles capped by HDA synthesized from complex **V** at 120 ^{o}C (a) and 180 ^{o}C (c) for 1 h, and their corresponding size distribution histograms (b, d).

Figure 4.59 shows the XRD patterns of CdS nanoparticles capped by HDA synthesized at 120 ^{o}C (a) and 180 ^{o}C (b), for an hour. The patterns of all two samples are indexed to wurtzite phase with characteristics 44.2^{o} (110), 48.1^{o} (103) and 52.4^{o} (112) peaks (JCPDS41-1049). One of the interesting aspects is the preferred orientation of nanocrystals. At higher growth temperature (180 ^{o}C), a strong and narrower (002) peak is observed in contrast to other peaks signifying that the samples are elongated along the *c*-axis. At the lower growth temperature (120 ^{o}C), a preferred orientation along (100) plane is observed. In general, higher reaction temperature, the stronger and narrower the XRD peaks, which signify that the size of the nanocrystals increased with increasing reaction temperature.

Some recent examples have drawn attention to the formation of mixed cubic and hexagonal phase structures of CdS and ZnS materials [76, 77]. There was no indication of a mixed phase in the materials synthesized.

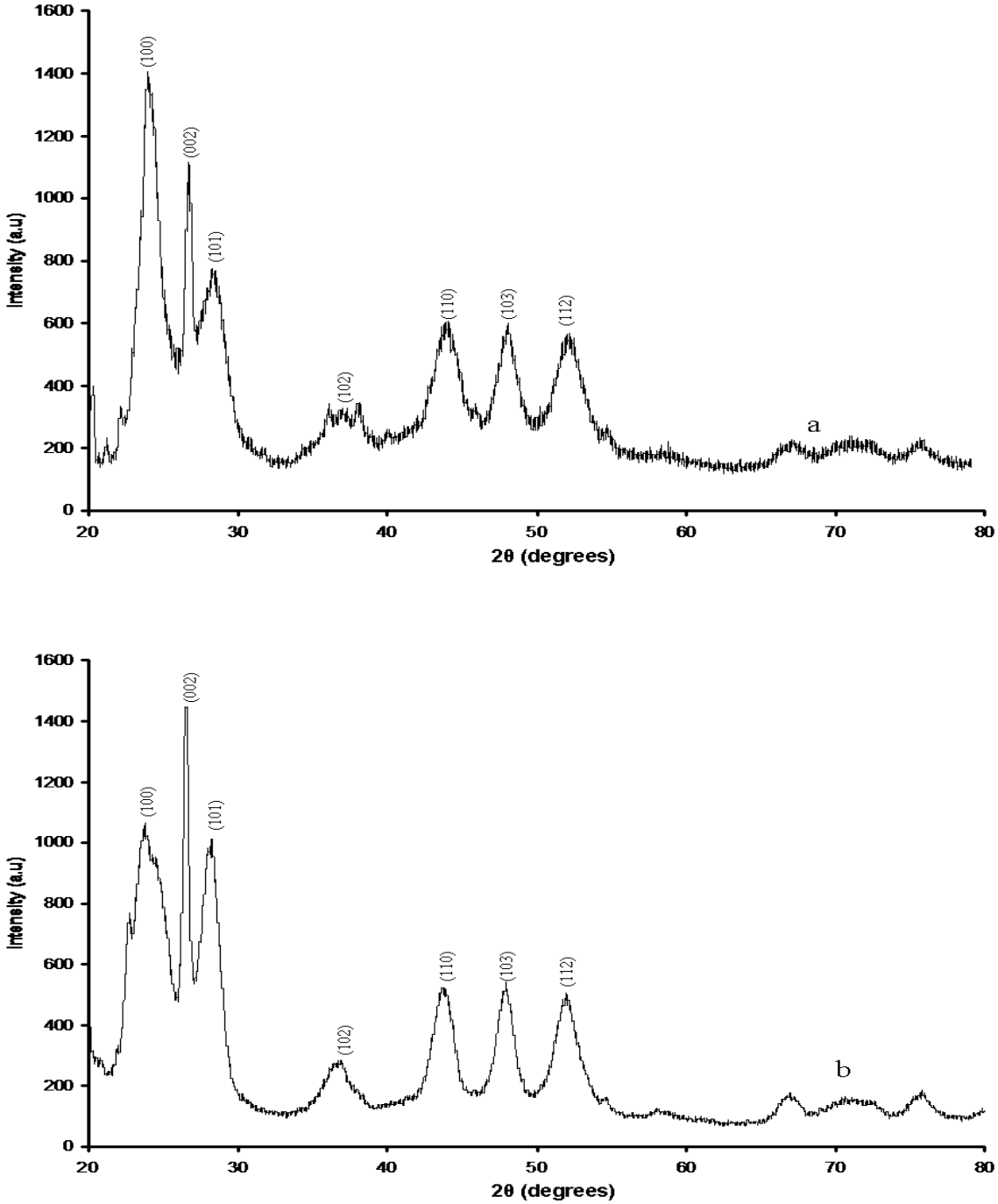

Figure 4.59: XRD patterns of CdS nanoparticles capped by HDA synthesized from complex **V** at 120 ^{o}C (a) and 180 ^{o}C (b) for 1 h.

Figure 4.60 shows the TEM image of CdS nanoparticles capped by TOPO synthesized from

complex **V** at 180 ^{o}C for 1 h (a) and histogram of particle size distribution (b). The small spherical particles with an average diameter of 2.6 nm were obtained. The appearance of spherical particles when a similar monomer that was employed for HDA, was used for TOPO is an indication that the selective adsorption nature of HDA favors the formation of anisotropic morphology. The spherical shape particles in this case was in contrast to the rod shaped HDA-capped CdS nanoparticles synthesized under similar reaction conditions, confirming that the capping agent plays a pivotal role in the morphology of the particles. The HDA molecule strongly binds on 100 plane of the nanoparticles, promoting growth along that axis whilst the TOPO molecule has no preferential growth. Various types of precursors, with metal sulphur bond for the synthesis of CdS nanoparticles have been utilized before. The closeness in structure of xanthates in relation to dithiocarbamates makes them ideal precursors for CdS nanoparticles. Cadmium ethylxanthate was thermolyzed in TOPO at 160 ^{o}C to give monodispersed, spherical TOPO-capped CdS nanparticles [76]. Thermolysis of the same xanthate precursors in HDA under the same conditions gave rod-shaped CdS nanoparticles [46]. Figure 4.61 shows the XRD pattern of CdS nanoparticles capped by TOPO. The particles were grown at 180 ^{o}C for 1 h. The pattern which revealed broad peaks as an indication of small size crystallites, depicts hexagonal phase with characteristic 24.9^{o} (100), 26.6^{o} (002), 28.1^{o} (101), 36.6^{o} (102, 43.8^{o} (110), 48.0^{o} (103) and 52.2^{o} (112).

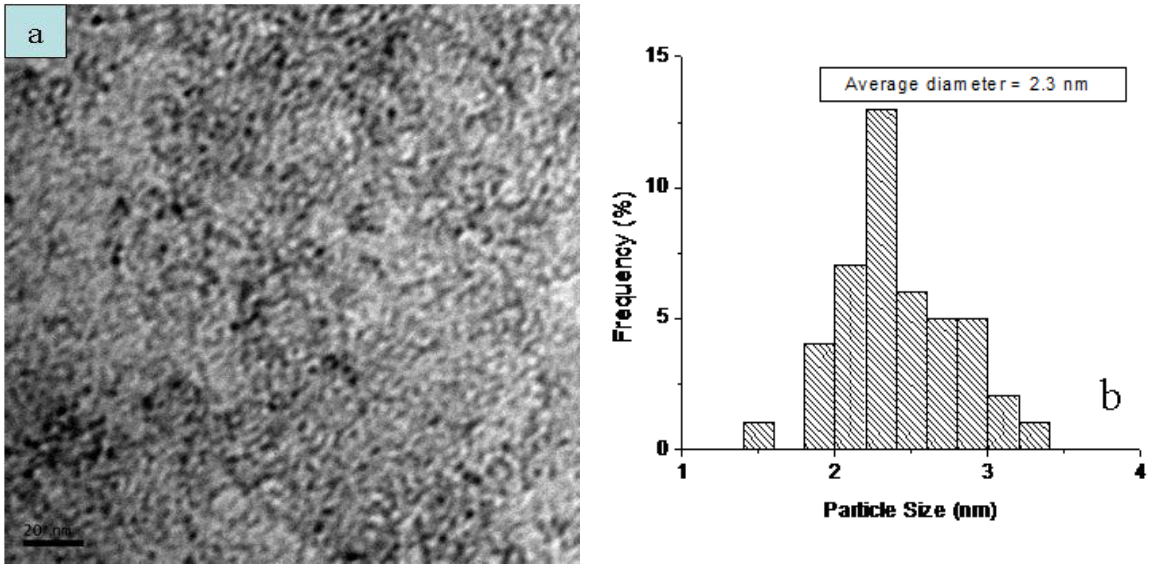

Figure 4.60: TEM image of CdS nanoparticles capped by TOPO (a) synthesized from complex **V** at 180 ^{o}C for 1 h, and its corresponding size distribution histogram (b).

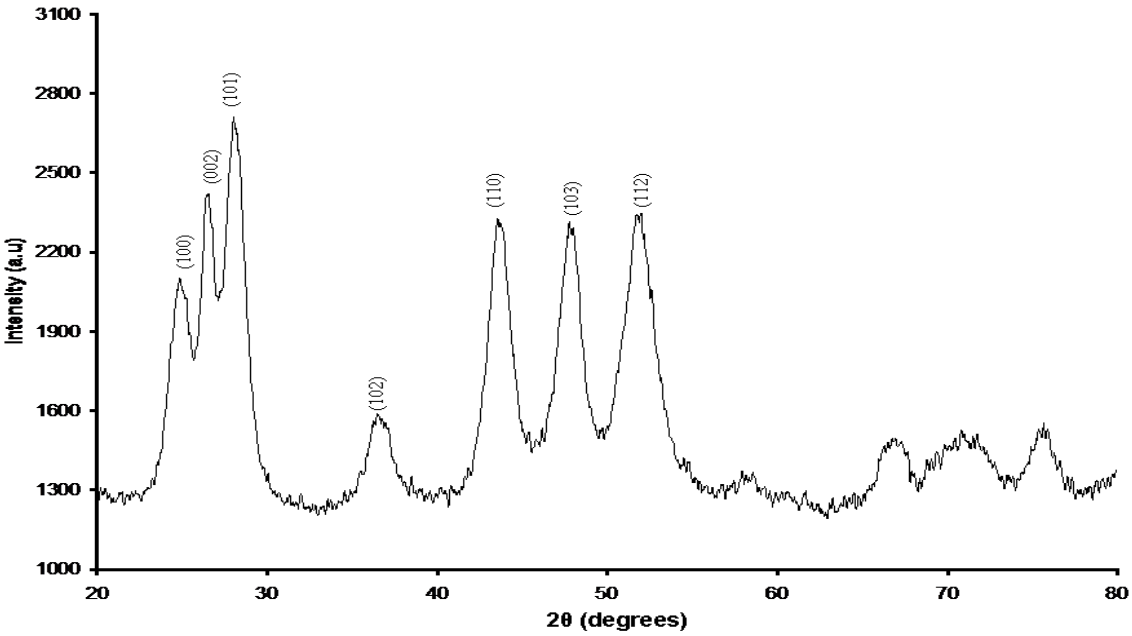

Figure 4.61: XRD pattern of CdS nanoparticles capped by TOPO synthesized from complex **V** at 180 ^{o}C for 1 h.

Figure 4.62 shows TEM images of CdS nanoparticles capped by HDA-TOPO synthesized from complex **V** at 120 ^{o}C for duration of 1 h (a,b) and histogram of particle size distribution (c). TEM images revealed a mixture of rods and spherical shape particles, with rods dominating in one area (Figure 4.62a) and spherical particles dominating in another (Figure 4.62b). The rods shown were not only monorods, there were also traces of bipods and tripods which are not in majority. The shape differences were influenced by the two capping agents where HDA is known to influence the formation of rods while TOPO influences spheres. In this case, the conclusion was that the presence of HDA-TOPO, which was determined by infrared spectral analysis, had an effect on the shape of the particles. The rod-shape particles were due to HDA, while spherical particles were due to TOPO. This was previously confirmed by thermolysing complex **V** in HDA (Figure 4.58) to give rods, and TOPO (Figure 4.60) to give spherical particles. The size of the particles capped by HDA-TOPO, determined from the TEM instrument was found to be on the average of 4.7 nm in diameter. Figure 4.63 shows the XRD pattern of CdS nanoparticles capped by HDA-TOPO. The particles were grown from complex **V** at 120 ^{o}C for an hour. It was interesting to notice that all peaks were broad signifying finite size of CdS crystals. The broadened peaks were positioned at 2θ values of 26.7^{o}, 36.9^{o}, 44.1^{o}, 48.0^{o} and 52.2^{o},

corresponding to (002), (102), (110), (103) and (112). The pattern can be indexed to hexagonal phase of CdS.

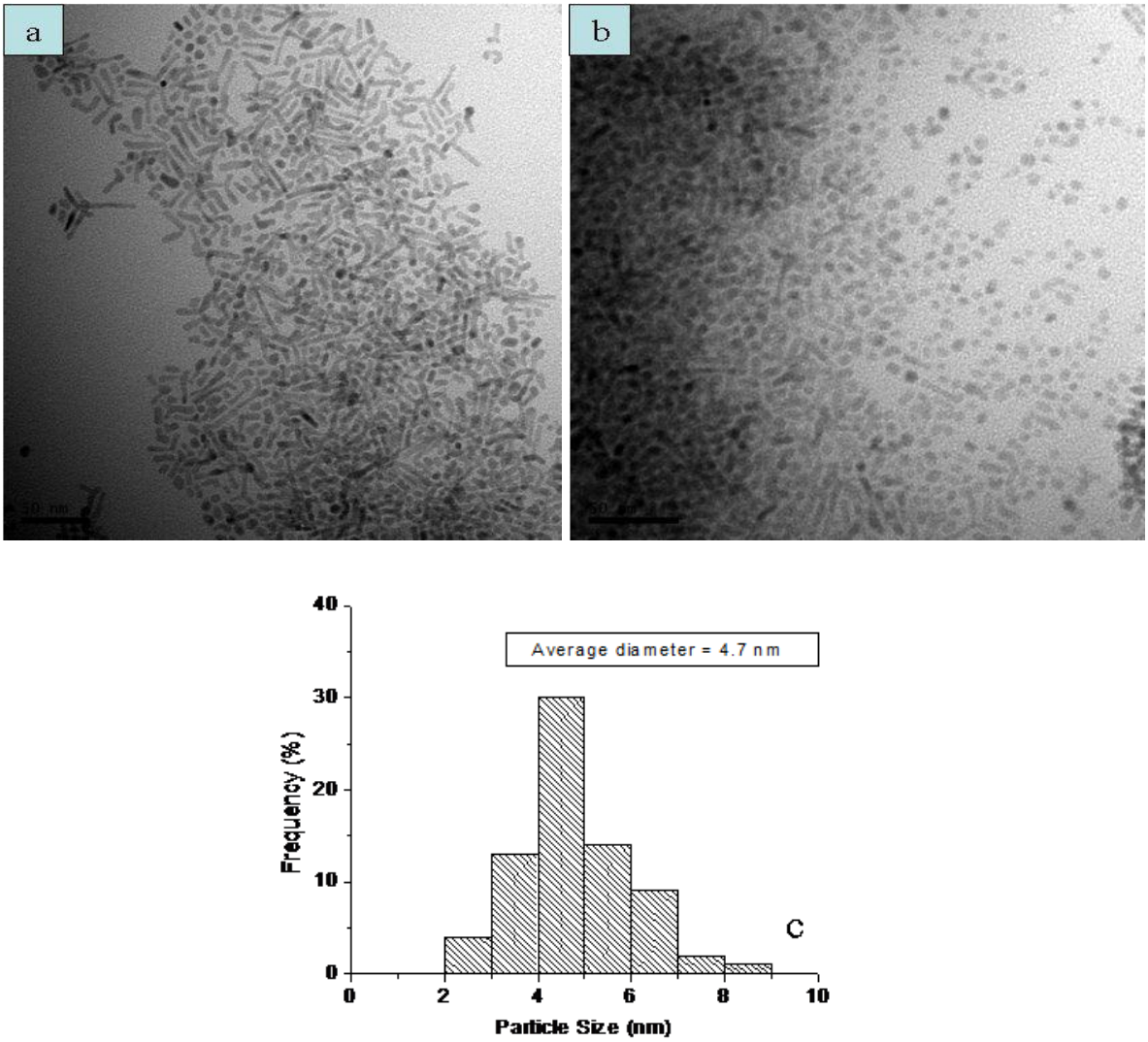

Figure 4.62: TEM images of CdS nanoparticles capped by HDA-TOPO synthesized from complex **V** at 120 ^{o}C (a, b) for 1 h, and their corresponding size distribution histogram.

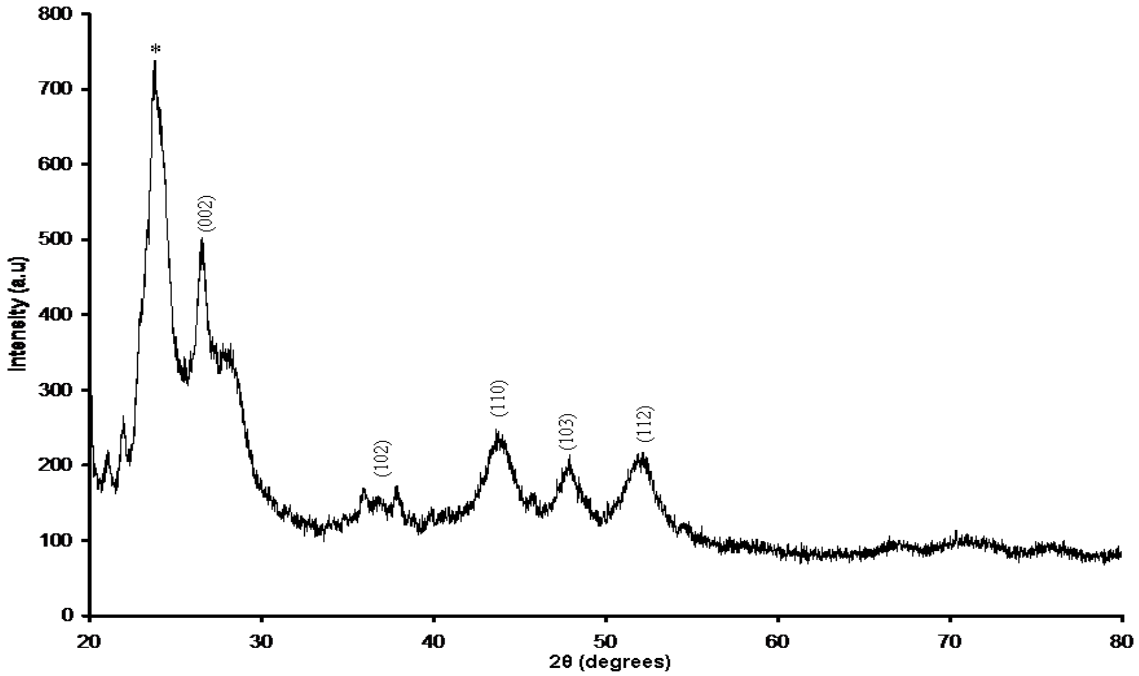

Figure 4.63: XRD pattern of CdS nanoparticles capped by HDA-TOPO synthesized at from complex **V** at 120 ^{o}C for 1 h.

The TEM images of Co_xS_y nanoparticles capped by HDA (a) and TOPO (c) synthesized from complex **IX** at 120 ^{o}C for 1 h, and histograms of particle size distribution (b – HDA and d- TOPO) are shown in Figure 4.64. The particles capped by HDA revealed a mixture of cubic and close-to-spherical morphology with an average diameter of 5.7 nm, while small spherical particles with an average diameter of 4.2 nm for similar material synthesized under the same conditions but capped by TOPO were obtained. The XRD patterns of as-synthesized samples capped by HDA (a) and TOPO (b) prepared from complex **IX** at 120 ^{o}C for 1 h are shown in Figure 4.65. The XRD patterns revealed similar characteristics with peaks appearing at the same region, and all the labelled peaks can be indexed as face-centred cubic Co_3S_4 nanoparticles.

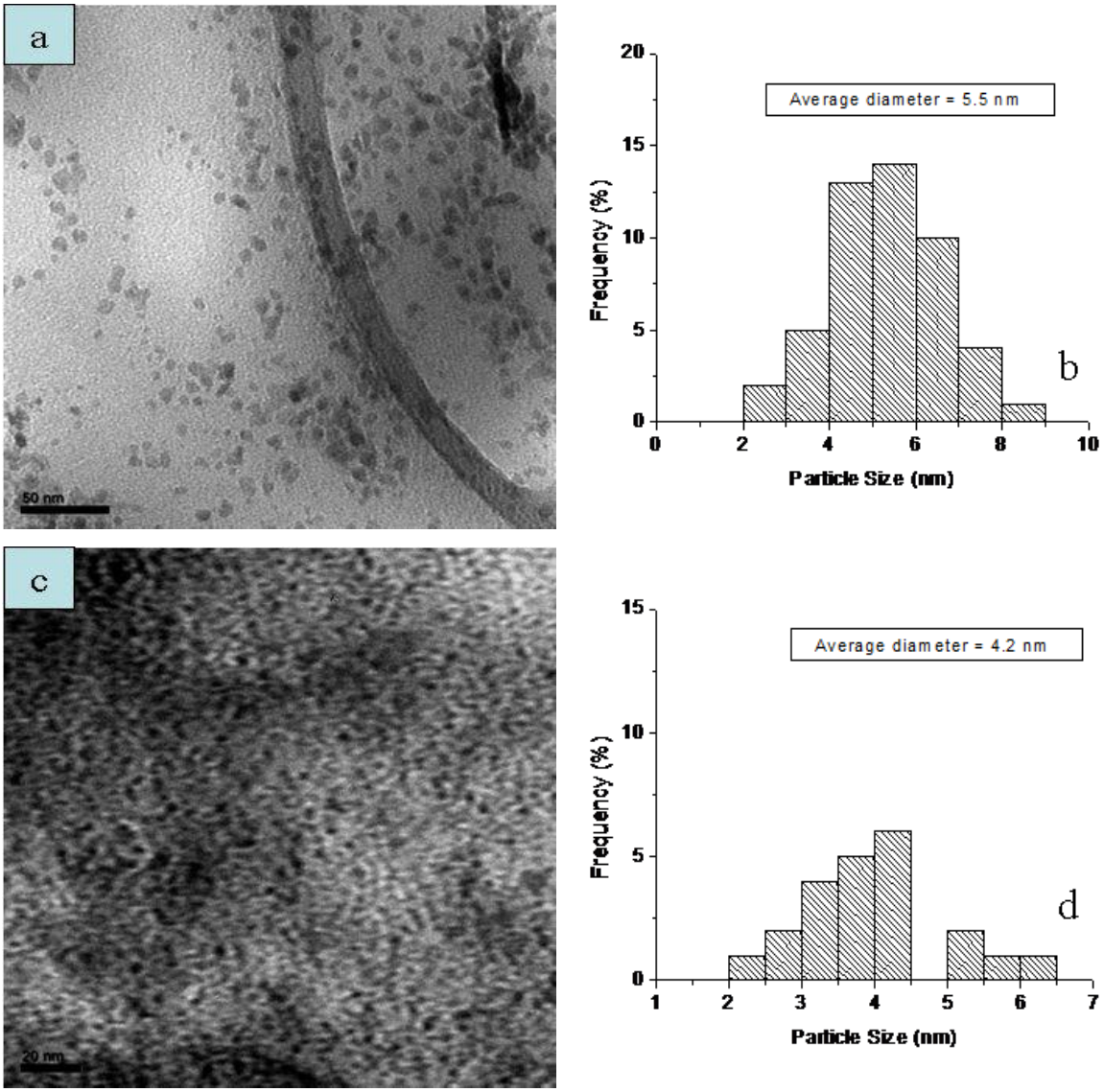

Figure 4.64: TEM images of Co_3S_4 nanoparticles capped by HDA (a) and TOPO (b) synthesized from complex **IX** at 120 ^oC for 1 h, and their corresponding size distribution histograms (b, d).

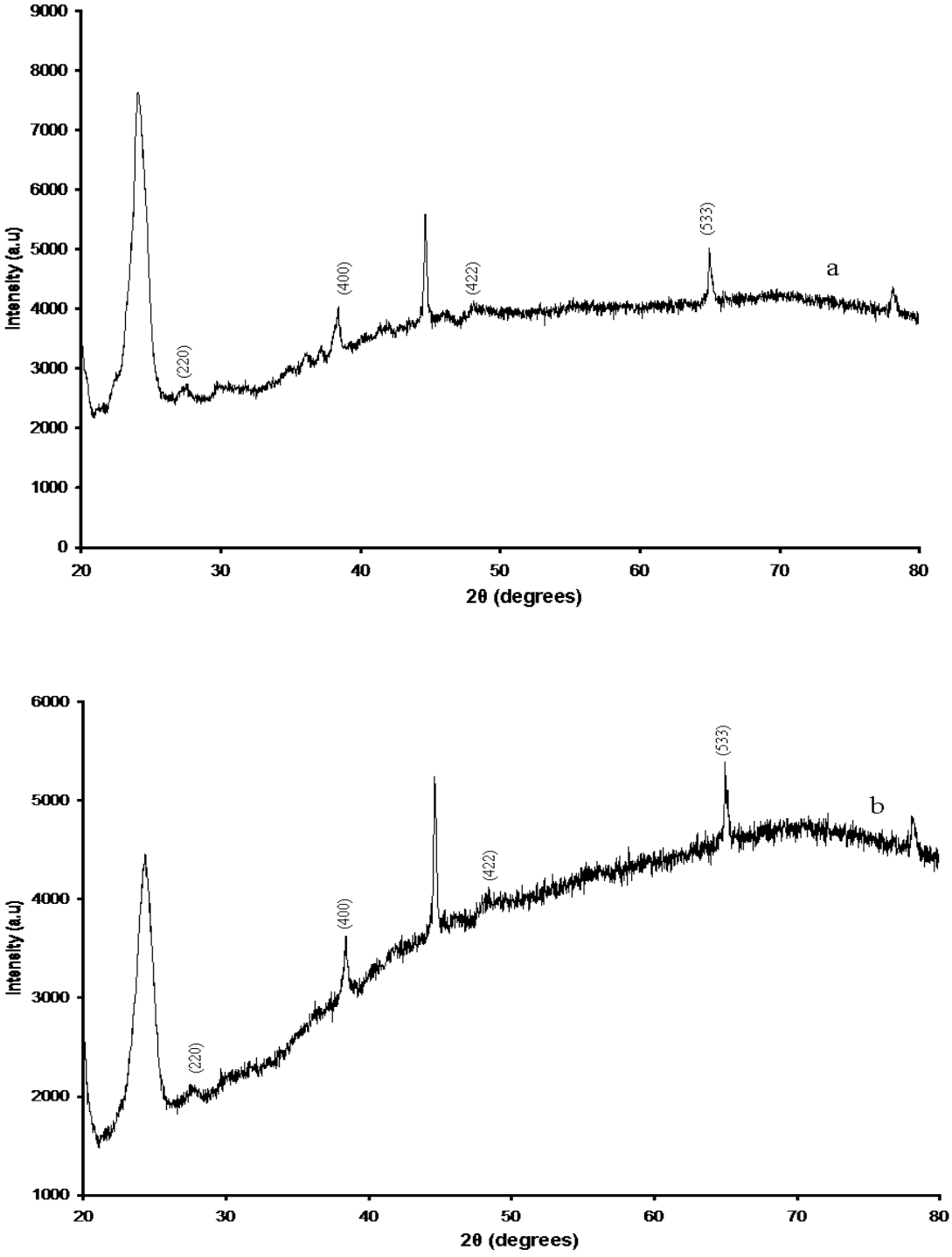

Figure 4.65: XRD patterns of Co_3S_4 nanoparticles capped by HDA (a) and TOPO (b) synthesized from complex **IX** at 120 ^{o}C for 1 h.

Figure 4.66 shows the TEM images of ZnS nanoparticles capped by HDA (a) and TOPO (c) synthesized from complex **XIV** at 180 ^{o}C for 1 h, and histograms of particle size distribution (b - HDA and d - TOPO). Particles capped by HDA reveal very small particles with an average diameter of 2.2 nm, while TOPO-capped ZnS nanoparticles depict an

average diameter of 2.7 nm. Particles capped by HDA are rods which are very short, showing some form of aggregation in other parts, while TOPO-capped ZnS depicted spherical or dot-shaped morphology. The HDA molecule strongly binds on 100 plane of the nanoparticles, promoting growth along that axis whilst the TOPO molecule has no preferential growth. It has been reported that variation of capping agents or ligands influences changes in the morphology of the particles. As stated before, Nair *et al.* [76] and Li *et al.* [46] used similar complex under same conditions, but with different capping agents, HDA and TOPO, to obtain rods and spherical-like-shaped particles, respectively. The XRD patterns of ZnS nanoparticles capped by HDA (a) and TOPO (b) grown from complex **XIV** at 120 ^{o}C for an hour are shown in Figure 4.67. Both XRD patterns can be indexed to cubic crystalline ZnS (JCPDS Card 05-0566). The 2θ values for ZnS nanoparticles capped by HDA were positioned at 28.9^{o} (111), 48.3^{o} (220) and 56.7^{o} (311), while those of TOPO-capped ZnS nanoparticles are positioned at 28.7^{o} (111), 48.1^{o} (220) and 56.2^{o} (311).

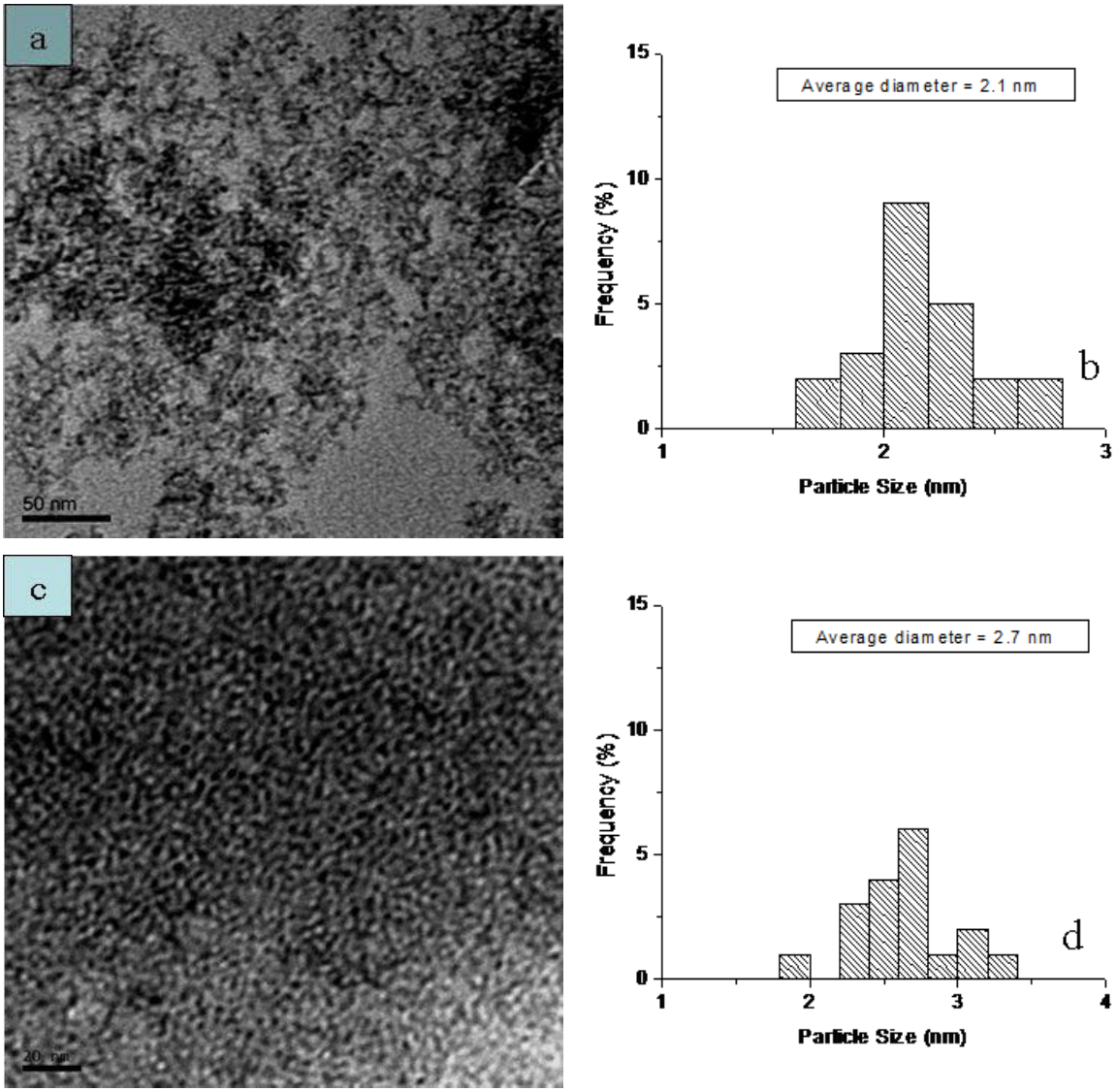

Figure 4.66: TEM images of ZnS nanoparticles capped by HDA (a) and TOPO (c) synthesized from complex **XIV** at 180 ^{o}C for 1 h, and their corresponding size distribution histograms (b, d).

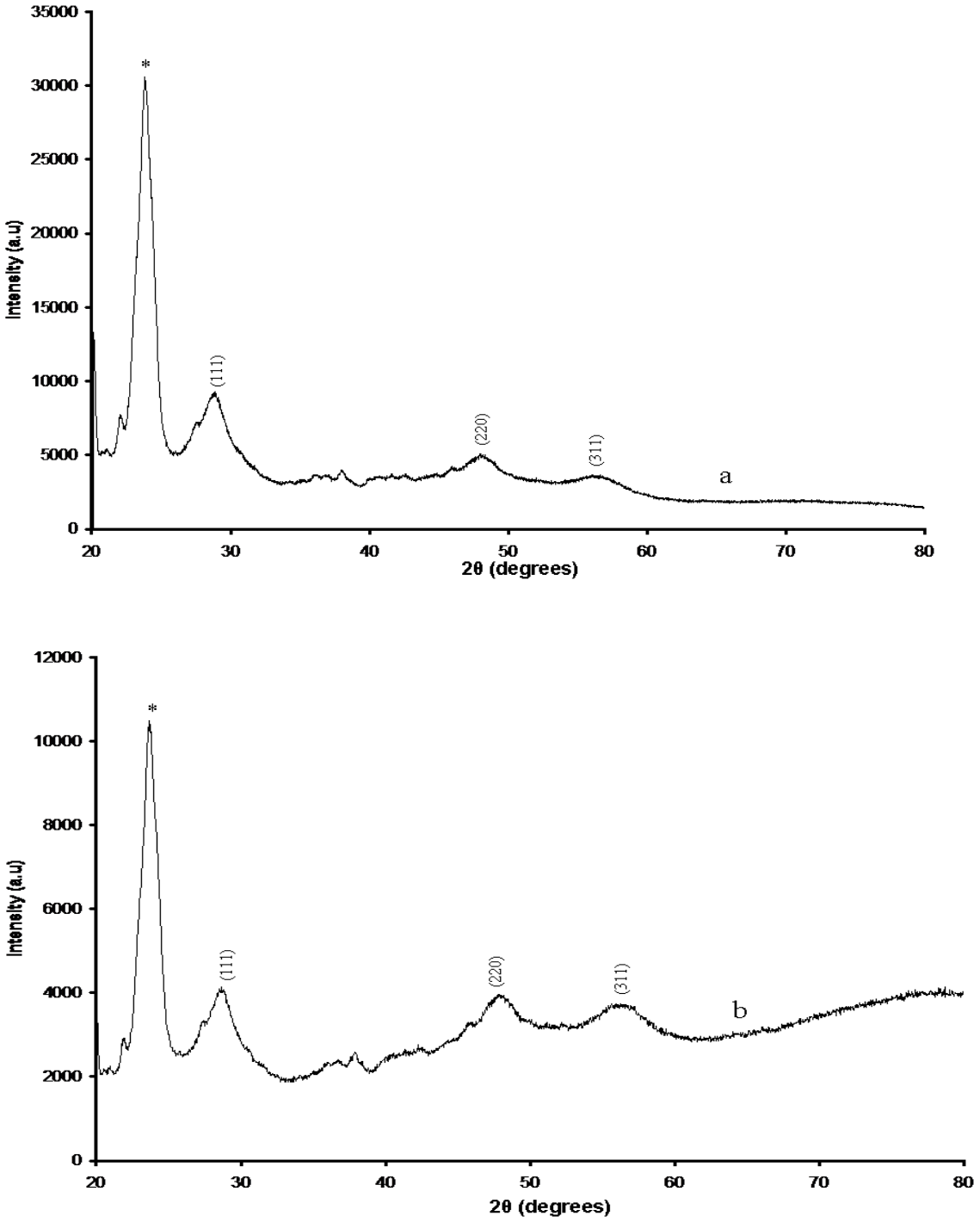

Figure 4.67: XRD patterns of ZnS nanoparticles capped by HDA (a) and TOPO (b) synthesized from complex **XIV** at 180 ^{o}C for 1 h.

4.4 Conclusion

In the preparation of hydrophobic semiconductor nanoparticles or quantum dots, single source precursor route was used due to its advantages over other methods. Some examples

of this method are that reactions could be run at low temperatures, and the chemicals used are cheap. Different parameters such as temperature and concentration of the precursor were investigated in this chapter. The absorption spectra of the nanomaterials synthesized were blue shifted to the bulk materials, which was an evidence of quantum confinement. The photoluminescence spectra, which were red shifted to their as-prepared absorption spectra revealed one emission peak indicating that particles were well capped. Narrow and broad emission peaks were observed. For example, when increasing the temperature or concentration, the emission peaks also broadens. However, there were some broad emission peaks that never resulted in an increase of temperature of precursor concentration. Those broad emissions could be attributed to recombination from the surface defects. Rods and spherical-like particles dominated in this chapter. However, the most interesting part in this chapter is that monodispersed particles with a diameter range of 1 to 12 nm were synthesized. The XRD patterns differed due to the materias synthesized. Hexagonal phase dominated for CdS nanoparticles while ZnS produced cubic phase pattern irrespective of the capping agent used. In the case of cobalt sulphide nanoparticles, Co3S4 phase was observed. However, there was a case where the XRD revealed no obvious peaks in the pattern, demonstrating the amorphous nature of the as-prepared cobalt sulphide nanoparticles.

4.5 Reterences

1. M. L. Steigerwald, A. P. Allivisatos, J. M. Gibson, T. D. Harris, R. Korten, A. J. Muller, A. M. Thayer, T. M. Duncan, D. C. Douglass, L. E. Brus, *J. Am. Chem. Soc.*, **110,** 3046, 1988.
2. C. B. Murray, D. J. Norris, M. G. Bawendi, J. Am. Chem. Soc., 115, 8706, 1993.
3. D. V. Talapin, A. L. Rogach, A. Kornowski, M. Haase, H. Weller, *Nano Lett.*, **1,** 207, 2001.
4. S. A. Empedocles, R. Neuhauser, K. Shimizu, M. G. Bawendi, *Adv. Mater.*, **11,** 1243, 1999.
5. A. A. Memon, M. Afzaal, M. A. Malik, C. Q. Nguyen, P. O'Brien, *Dalton Trans.*, 4499, 2006.
6. N. Moloto, M. J. Moloto, N. J. Coville, R. S. Sinha, *J. Nanosci. Nanotechnol.*, **10**(9), 5594, 2010.
7. N. Moloto, N. Revaprasadu, P. L. Musetha, M. J. Moloto, *J. Nanosci.*

Nanotechnol., **9**(8), 4760, 2009.

8. M. J. Moloto, N. Revaprasadu, P. O'Brien, M. A. Malik, *J. Mat. Sci. -Mater. Electron.*, **15**(5), 313, 2004.
9. N. Moloto, N. Revaprasadu, M. J. Moloto, P. O'Brien, J. Raftery, *S. Afr. J. Sci.*, **105,** 258, 2009.
10. N. Moloto, N. Revaprasadu, M. J. Moloto, P. O'Brien, M. Helliwell, *Polyhedron*, **26,** 3947, 2007.
11. R. Ionov, D. Nesheva, *Thin Solid Films*, **213,** 230, 1992.
12. K. Subbaramaiah, V. S. Raja, *Sol. Enery Mater. Sol. Cells*, **32,** 1, 1994.
13. P. O'Brien, *Chemtronics*, **5,** 61, 1991.
14. Y. L. Chang, C. L. Munse, G. S. Herman, J. F. Wager, P. Mugdur, D. H. Lee, C. H. Chang, *Surf. Interface Anal.*, **37,** 398, 2005.
15. J. Pouzet, J. C. Bernede, A. Khellil, H. Essaidi, S. Benhida, *Thin Solid Films*, **208,** 252, 1992.
16. D. Fan, P. J. Thomas, P. O'Brien, *J. Mater. Chem.*, **17,** 1381, 2007.
17. R. Ortega-Borges, D. Lincot, *J. Electrochem. Soc.*, **140,** 3464, 1993.
18. P. O'Brien, T. Trindade, *Chem. Mater.*, **9,** 523, 1997.
19. A. Yamaguchi, R. B. Penland, S. Mizushima, T. J. Lane, C. Curran, J. V. Quagliano, *J. Am. Chem. Soc.*, **80,** 527, 1958.
20. M. J. Moloto, M. A. Malik, P. O'Brien, M. Motevalli, G. A. Kolawole, *Polyhedron*, **22,** 595, 2003.
21. U. Belluco, M. Graziani, P. Rigo, *Inorg. Chem.*, **5,** 1123, 1966.
22. G. Macrotrigiano, G. Peyronel, R. Battistuzzi, *J. Inorg. Nucl. Chem.*, **37,** 1675, 1975.
23. B. Galabov, G Vassilev, N. Neykova, A. Galabov, *J. Mol. Struct.*, **44,** 15, 1978.
24. B. T. Brown, G. F. Katekar, *Tetrahedron Lett.*, **28,** 2343, 1969.
25. D. R. Williams, *Chem. Rev.*, **3,** 202, 1972.
26. J. Maslowska, A. Baranowska, *J. Thermal Anal.*, **29,** 309, 1984.
27. E. Jona, T. Sramko, *Chem. Zvesti*, **20,** 569, 1966.
28. V. I. Spitsin, I. D. Kolli, *Russ. J. Inorg. Chem.*, **9,** 99, 1964.
29. J. Maslowska, E. Chruscinska, *Polish J. Chem.*, **52,** 1261, 1978.
30. G. D. Thorn, R. Ludwig, *The Dithiocarbamates and Related Compounds, Elsevier, Amsterdam*, 1981.
31. F. H. Allen, O. Kennard, D. G. Watson, L. Brammer, A. G. Orpen, R. Taylor, *in:*

A. J. C. Wilson (Ed.). International Tables of Crystallography, Vol. C. Kluwer Publishers.Dordrecht, 685, 1991.

32. L. V. Victoriano, *Polyhedron,* **19,** 2269, 2000.
33. I. Ojima, T. Onish, T. Iwamoto, N. Inamoto, K. Tamaru, *Inorg. Nucl. Chem.,* **6,** 65, 1970.
34. N. Moloto, N. Revaprasadu, P. L. Musetha, M. J. Moloto, *J. Nanosci. Nanotechnol.,* **9**(8), 4760, 2009.
35. N. Mathur, R. K. Joshi, G. V. Subbaraju, H. K. Sehgal, *Physica*, **E23,** 56, 2004.
36. Z. Yu, J. Du, S. Guo, J. Zhang, Y. Matsumoto, *Thin Solid Films,* **415,** 173, 2002.
37. M. A. Malik, P. O' Brien, N. Revaprasadu, *S. Afr. J. Sci.,* **96,** 55, 2000.
38. M. Green, P. O' Brien, *Chem. Commun.,* 2235, 1999.
39. S. Sapra, J. Nanda, D. D. Sarma, F. Abedi El-Al, G. Hodes, *Chem. Commun.,* 2188, 2001.
40. A. Chatterjee, A. Priyam, S. K. Das, A. Saha, *J. Colloid. Interface Sci.,* **294,** 334, 2006.
41. X. Liu, Y. Jiang, C. Wang, S. Li, X. Lan, Y. Chen, *Phys. Status Solidi A.,* **207,** 2472, 2010.
42. N. A. Dhas, A. Zaban, A. Gedanken, *Chem. Mater.,* **11,** 806, 1999.
43. S. H. Choi, T. Sasaki, Y. Shimizu, J.W. Yoon, W. T. Nichols, Y. E. Sung, N. Koshizaki, *J. Phys. Conference Series,* **59,** 388, 2007.
44. H. Tang, X. Guoyue, L. Weng, L. Pan, L Wang, *Acta Materrialia*, **52**, 1489, 2004.
45. K. Manzoor, S. R. Vadera, N. kumar, T. R. N. Kutty, *Mater. Chem. Phys.,* **82,** 718, 2003.
46. Y. Li, X. Li, C. Yang, Y. Li, *J. Mater. Chem.,* **13,** 2641, 2003.
47. M. L. Steigerwald, L. E. Brus, *Acc. Chem. Res.,* **23,** 183, 1990.
48. P. D. Cozzoli, M. L. Curri, A. Agostiano, *J. Phys. Chem., B* **107,** 4756, 2003.
49. P. Saravanan, S. Alam, G. N. Mathur, *Mater. Lett.,* **58,** 3528, 2004.
50. Y. Wang, N. Herron, *J. Phys. Chem.,* **91,** 257, 1987.
51. N. N. Maseko, N. Revaprasadu, V. S. R. Rajasekhar, Pullabhotla, R. Karthik, P. O' Brien, *Mater. Lett.,* 64, 1037, 2010.
52. A. F. Wells, *Structural Inorganic Chemistry (5th Ed.), Oxford: Clarendon Press,* 1984.
53. W. Cai, Z. Li, J. Sui, *Nanotechnology*, **19,** 465606, 2008.
54. T. Fen, Y. Q. Zhao, G. Q. Zhang, H. L. Li, *Electrochem. Commun.,* **9,** 128, 2007.
55. G. M. C. Higgins, B. Saville, *J. Chem. Soc.,* 2812, 1963.

56. R. D. Pike, H. Cui, R. Kershaw, K. Dwight, A. Wold, T. N. Blanton, A. A. Wernberg, H. J. Gysling, *Thin Solid Films*, 224, 1993.
57. D. M. Frigo, O. F. Z. Khan, P. O'Brien, *J. Cryst. Growth*, **96,** 989, 1989.
58. M. Chunggaze, J. M. McAleese, P. O'Brien, D. J. Otway, *Chem. Commun.,* **833,** 1998.
59. P. O'Brien, D. J. Otway, J. R. Walsh, *Chem. Vap. Deposition*, **3,** 227, 1997.
60. M. Chunggaze, M. A. Malik, P. O'Brien, *J. Mater. Chem.*, **9,** 2433, 1999.
61. R. W. Meulenberg, S. Bryan, C. S. Yun, G. F. Strouse, *J. Phys. Chem. B.*, 106, 7774, 2002.
62. T. Trindade, P. O'Brien, *Chem. Mater.,* **9,** 523, 1997.
63. J. E. Bowen-Katari, V. L. Colvin, A. P. Allivisatos, *J. Phys. Chem.*, **98**, 4109, 1994.
64. Kerdanath, G; Dey, S; Jain, V. K; Dey, G. K; Varghese, B. *Polyhedron*, **25,** 2383, 2006.
65. P.S. Nair, M. M. Chili, T. Radhakrishnan, N. Revaprasadu, P. Christian, P. O'Brien, *S. Afr. J. Sci.,* **101,** 466, 2005.
66. X. Liu, Y. Jiang, X. Lan, S. Li, D. Wu, T. Han, H. Zhong, Z. Zhang, *J. Colloid. Interface Sci.,* **354,** 15, 2011.
67. D. R. Eaton, K. Zaw, *J. Inorg. Nucl. Chem.,* **38,** 1007, 1976.
68. Z. Sedaghat, N. Tagavinia, M. Marandi, *Nanotechnology*, **19,** 3812, 2006.
69. A. E. Saunders, I. Popov, U. Banin, *J. Phys. Chem. B.,* **110,** 25421, 2006.
70. T. Trindade, P. O'Brien, *Adv. Mater.,* **8,** 161, 1996.
71. M. A. Malik, N. Revaprasadu, P. O'Brien, *Chem. Mater.*, **13,** 913, 2001.
72. B. Ludolph, M. A. Malik, P. O'Brien, N. Revaprasadu, J. *Chem. Soc., Chem. Commun.,* 1849, 1998.
73. N. Revaprasadu, M. A. Malik, P. O'Brien, M. M. Zulu, G. Wakefield, *J. Mater. Chem.,* **8,** 1885, 1998.
74. O. S. Oluwafemi, N. Revaprasadu, *New. J. Chem.,* **10**, 1432, 2008.
75. P. S. Nair, T. Radhakrishnan, N. Revaprasadu, G. A. Kolawole, P. O'Brien, *J. Mater. Chem.,* **12,** 1, 2002.
76. H. Zhang, B. Chin, B. Gilbert, J. Banfield, *J. Mater. Chem.,* **16,** 249, 2006
77. P. Christian, P. O'Brien, *Chem. Commun.,* **2817,** 2005.

Chapter 5

Water soluble semiconductor nanoparticles or quantum dots using ligand exchange route or method

5.1 Introduction

In the last decade semiconductor nanoparticles or quantum dots have been introduced as a new type oof colloids for biolabelling. The fluorescence wavelength of these semiconductor nanoparticles or QDs are size dependent. Biological applications have been discussed in many news and views/ feature articles [1, 2, 3, 4, 5, 6] and reviews [7, 8, 9]. Since these fluorescence nanoparticles are inorganic solids, they can be expected to be more robust than organic fluorophores (e.g. towards photobleaching) and in addition they can also be observed with high resolution by electron microscope. The use of QDs in biology and medical applications is a multidisciplinary field of science where aspects of synthetic chemistry, physics and biology are equally important. It is difficult to find common language and thinking among these scientific disciplines.

High quality nanocrystals of various semiconductor materials such as CdS, CdSe, ZnS, CdTe or CdSe/ZnS can be synthesized by a variety of approaches [10, 11, 12, 13], with the particles well dispersed in solvents such as toluene and chloroform. Due to their hydrophobic surface layer they are not soluble in aqueous media. However, experiments involving biological applications require water soluble materials. In practice, hydrophobic QDs can be made hydrophillic by several methods. Most of them rely on the exchange of hydrophobic surfactant coatings with ligand molecules that carry funtional groups that are reactive towadrs nanocrystal surface, and hydrophilic groups on the other end, which ensure water solubility. The most frequent used anchoring groups reactive to the surface of QDs are thiol, hydroxyl and carboxyl functionalities [14, 15, 16, 17]. Biological mollecules can be linked to the surface of QDs in order to introduce specific funtionalities [18]. Stated from another perspective, biological molecules can be fluorescence labelled by attaching QDs. Conjugation of QDs with biological molecules is well established and has been demonstrated for a whole variety of molecules, including small molecules like biotin [19], folic acid [18], the neurotransmitter serotonin [20], peptides [16, 21], proteins like avidin or

streptavidin [22, 23], albumin [24], transferrin [14], trichosanthin [15], the lectin wheat germ agglutinin [17], or antibodies [16, 22, 25, 23, 26] and DNA [27, 28, 29, 30, 31, 32]. For potential applications it is important to know if the functionality of the molecules is retained or whether it is impaired by the QD. Since QDs have the size of a few nanocrystals, the attachment of such objects to a biological molecule might well influence its properties. Functionality of biological molecules can be regarded from different perspectives. One main idea of applying QDs in cell biology is their use as fluorescence markers to label structures/compartments/molecules in cells. For this purpose QDs are conjugated to ligand molecules such as antibodies which recognize specific receptors, that is the structure/compartments/molecules which is to be labelled. Therefore, it is important that the QDs do not interfer with molecular recognition. However, the most significant key in employing QDs for biological applications is their water solubility, which will be adressed in this chapter.

In the preparation of water soluble semiconductor nanoparticles/quantum dots reported in this chapter, glucuronic acid, glucose and sucrose were used as capping agents due to the functional groups they possess, water solubility and non-toxicity. In the results obtained, we found that in most cases glucose and sucrose give similar results. For example, when semiconductor nanoparticles capped by glucose and sucrose were characterized through FT-IR, no significant difference was observed. Both capping agents possess an OH group which appeared almost at the same region as a broad peak. Due to this reason, there are cases where one of the two was used instead of both. However, in the case of glucuronic acid, it was used or applied in all reactions since it differed from the two by containing carboxylic acid group.

5.2 Results and discussions

5.2.1 Transfer of hydrophobic semiconductor nanoparticles/QDs to water soluble *via* ligand exchange method

Different methods have been employed in the preparation of water soluble semiconductor nanoparticles/quantum dots. Ligand exchange method, which is one of the methods employed, is favoured because it does not alter the size of the particles completely [33].

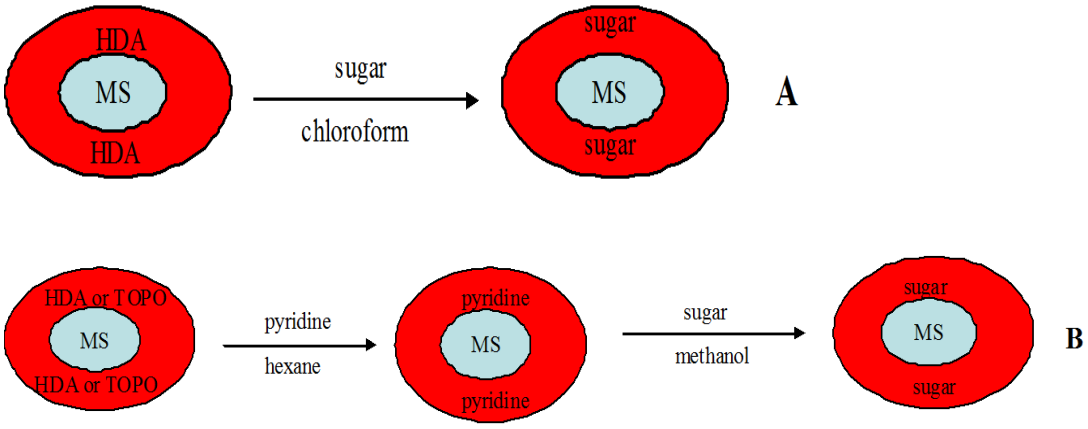

M = Cd, Co or Zn Sugar = glucose, sucrose or glucuronic acid

Scheme 5.1: Preparation of water soluble semiconductor nanoparticles using ligand exchange method (**A** - chloroform route, **B** - pyridine route)

Semiconductor nanoparticles can be prepared directly from water, however, they often give large full width at half maximum. In our case, ligand exchange method was employed, with hydrophobic material or nanoparticles dispersed in either chloroform or pyridine (Scheme 4.1) to achieve water soluble semiconductor nanoparticles. Different instruments were utilised to detect if we managed to synthesize semiconductor nanoparticles or quantum dots. However, the FT-IR and XRD results of semiconductor nanoparticles or QDs using pyridine route were not discussed, except the ones used for the published paper (subsection 5.3.1.3). For example, the infrared spectra of semiconductor nanoparticles or QDs capped by glucuronic acid were the same irrespective of the complex used. In the case of XRD patterns, multiple peaks were observed which made it too difficult to peak the important peaks of the synthesized material.

5.2.1.1 Sugars-capped CdS nanoparticles from HDA-capped CdS nanoparticles prepared from complex I using chloroform route

In this method, a small amount of HDA-capped CdS nanoparticles (180 ^{o}C) that was prepared from complex **I** was dissolved in chloroform and mixed with a mixture of either glucose or sucrose and methanol. The chloroform was then allowed to evaporate and particles were then transferred into water soluble. A suspension of sugar-capped CdS

nanoparticles was obtained. The capping agents or ligands used to stabilize semiconductor nanoparticles, that is glucose and sucrose, were chosen because of their solubility in water and their are non-toxicity.

(a) Optical properties

The CdS nanoparticles prepared using chloroform route yielded particles that were partially soluble in water. This is simply an indication of the presence of HDA which was not completely removed. Instead of achieving ligand exchange, hydrophobic interaction might have prevailed, with the sugars forming an outer layer instead of displacing the hydrophobic ligand. Figure 5.1 represents the absorption spectra of CdS nanoparticles capped by glucose (a) and sucrose (b) synthesized from CdS nanoparticles capped by HDA prepared from complex **I**. Both absorption spectra show weak excitonic peaks as compared to the CdS nanoparticles capped by HDA. Macrocrystalline hexagonal CdS particles have an optical band edge of 515 nm (2.14 eV). The band edge for both CdS capped by either glucose or sucrose is located at approximately 499 nm (2.48 eV), with the weak excitonic peaks appearing at 473 nm (2.62 eV). The absorption spectra are blue shifted in relation to the bulk CdS material which signifies strong quantum size effect.

Luminescence spectroscopy is well known to be very sensitive towards small changes of the surface chemistry of the semiconductor nanoparticles [34]. Photoluminescence in nanoparticles arises from the radiative recombination of electron-hole pairs. The fate of photogenerated electron-hole pair in the solid state is critically tied to applications of these materials. Slight defects in the solid such as vacancies, impurities or adsorbates at the surface cause the formation of trap states into which the photo-excited electrons can fall, or the photo-excited hole can float [35]. The resulting photoluminescence can therefore be quite Stokes-shifted from the absorbance, depending on the energies of these trap states compared to valence and conduction band edges. Due to the sensitivity of photoluminescence of semiconducting nanoparticles to defects and adsorbates the optical properties of the materials may depend heavily on the synthesis procedure used to make them.The photoluminescence spectra of CdS nanoparticles capped by glucose and sucrose are shown in Figure 5.2. Both spectra show sharp and narrow emission. However, their emission maxima are very close to the band edges. Similar results were reported by Moloto *et al.* [36] who successfully synthesized CdS nanoparticles capped by TOPO. They

obtained broad photoluminescence spectra, which were due to wide distribution of particles size, with the emission maxima that were very close to the band edges.

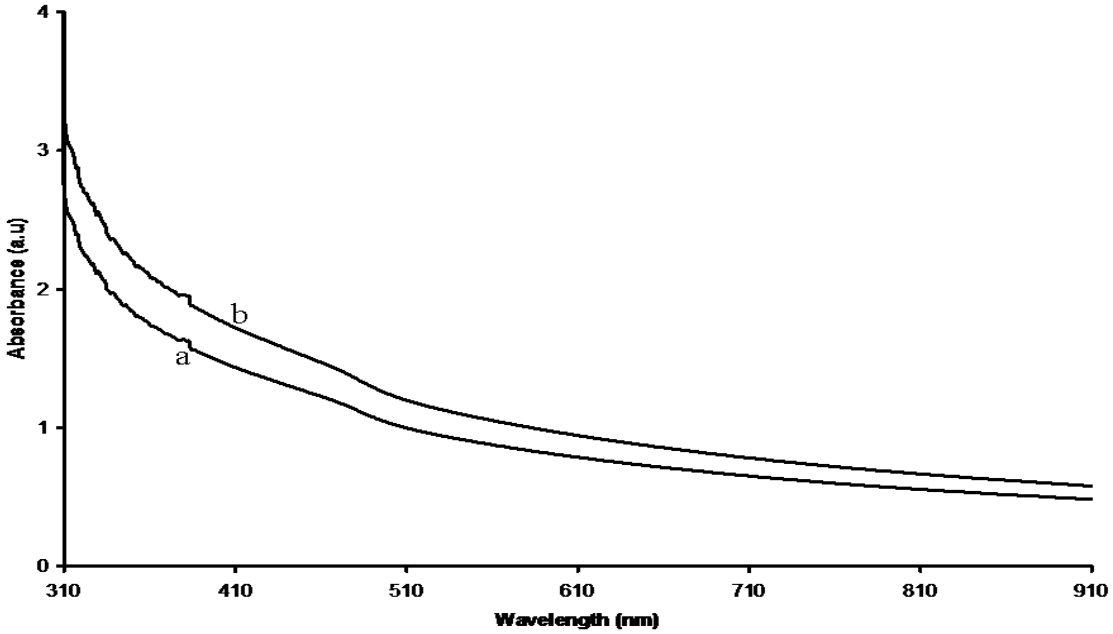

Figure 5.1: Absorption spectra of CdS nanoparticles capped by glucose (a), and sucrose (b) synthesized from HDA-capped CdS nanoparticles prepared from complex **I.**

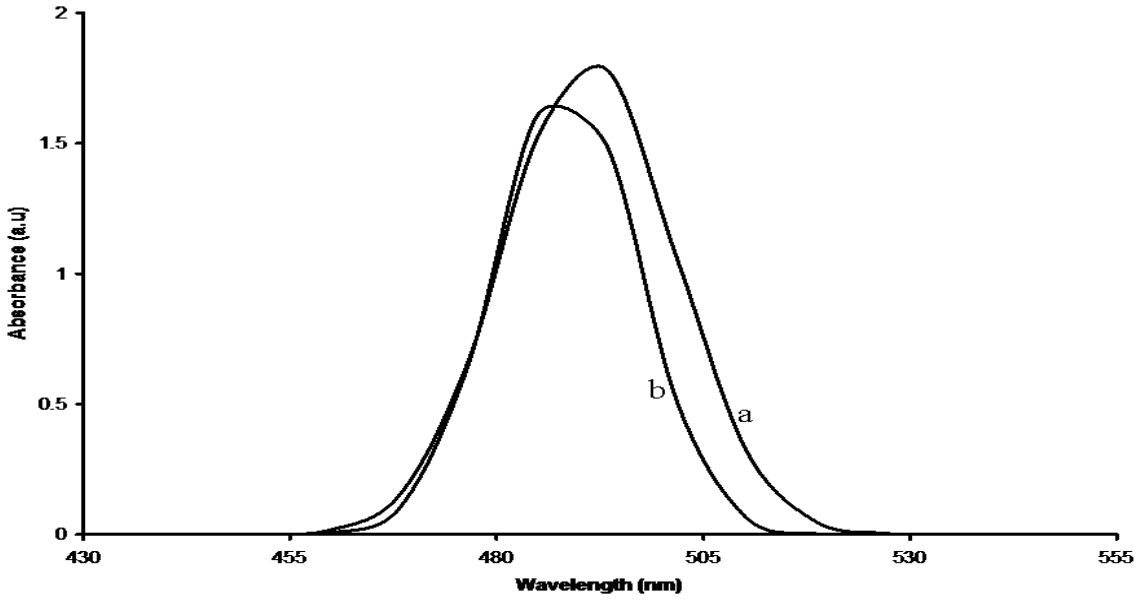

Figure 5.2: Photoluminescence spectra of CdS nanoparticles capped by glucose (a,) and sucrose (b) synthesized from HDA-capped CdS nanoparticles prepared from complex **I.**

(b) Structural properties

Figure 5.3 depicts the TEM images of CdS nanoparticles capped by glucose (a) and sucrose (b). Both images show rod shape particles with an average diameter of 4.8 nm. This indicates that the size and shape of the particles were not affected when attempting to displace the former ligand which was HDA. The crystallinity of the CdS nanoparticles capped by glucose was investigated by X-ray diffraction (XRD), as shown in Figures 5.4. The sample was dried through an oven at 50 ^{o}C before XRD analysis. The characteristic diffraction peaks which are clearly indicated between 20^{o} and 70^{o} show pattern that can be indexed as hexagonal-phase CdS with characteristic 44.4^{o} (110), 48.5^{o} (103), 52.9^{o} (112) peaks. The pattern, which depicts broadened diffraction peaks, compared to those of the bulk CdS crystals, signifying the finite size of these crystallites. Comparison between glucose-capped CdS and HDA-capped CdS nanoparticles show the absence of a peak at 28.5^{o} (002) in the glucose-capped CdS pattern. However, the significant similarity between the two is that of the broad peaks which differs from the bulk material. The competition between the coating agents is a possible source of variation. This explanation is also consistent with the results obtained in the absorption spectra, where the excitonic peaks of the water soluble CdS nanoparticles become weak. However, yields from the glucose and sucrose-capped CdS nanoparticles were very low. Unlike in CdS nanoparticles capped by glucose, the amount obtained for CdS nanoparticles capped by sucrose was not enough for XRD analysis. An alternative route which involved pyridine (explored below), was employed in order to improve the yield.

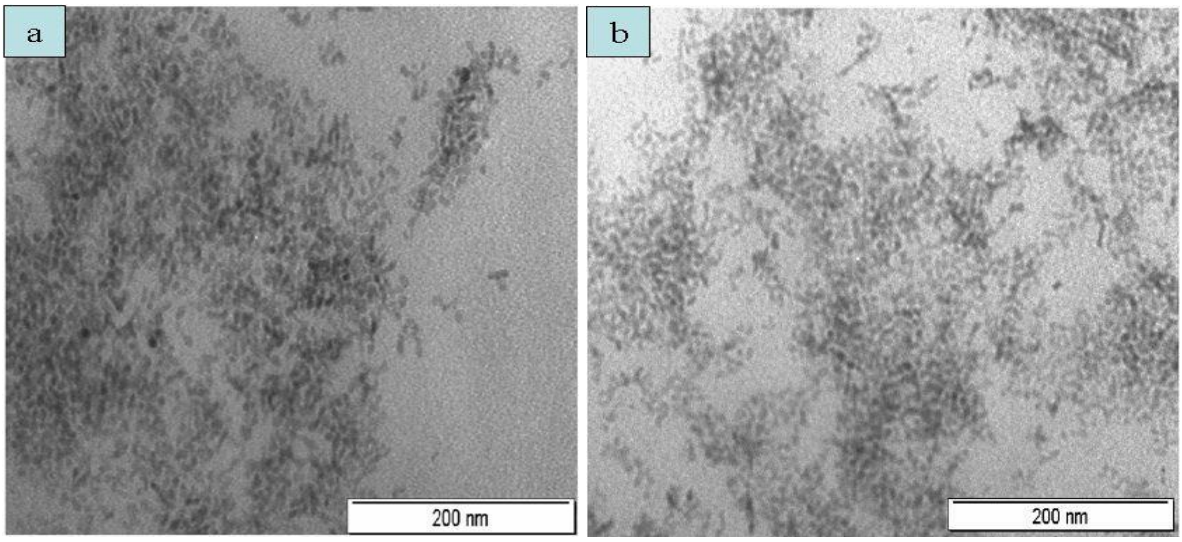

Figure 5.3: TEM images of CdS nanoparticles capped by glucose (a) and sucrose (b) synthesized from HDA-capped CdS nanoparticles (180 ^{o}C) from complex **I.**

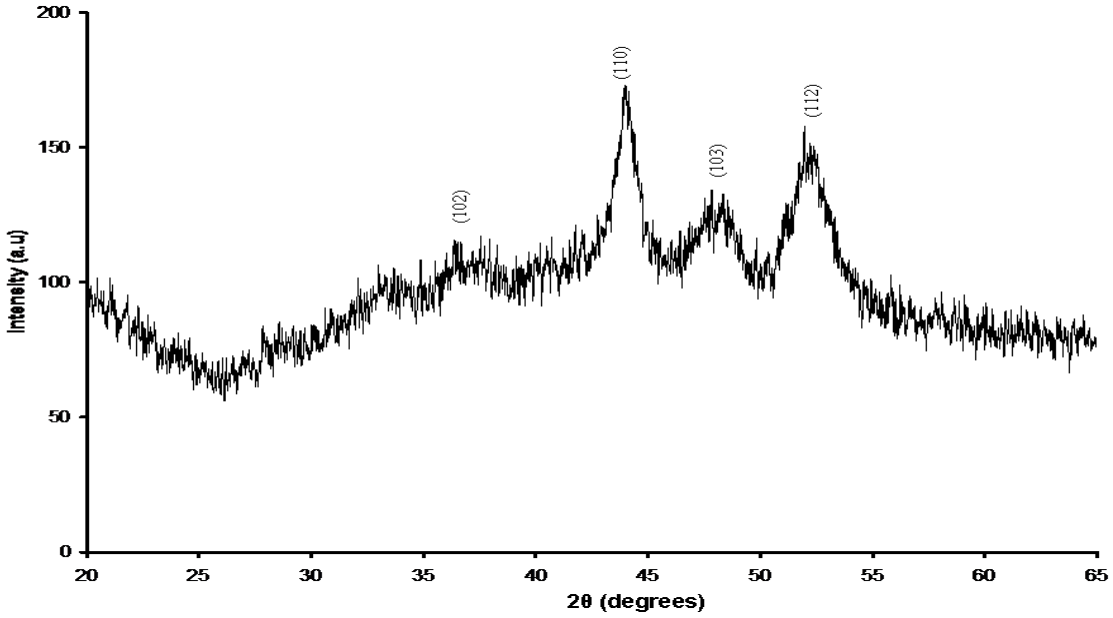

Figure 5.4: XRD pattern of CdS nanoparticles capped by glucose prepared from HDA-capped CdS nanoparticles (180 ^{o}C) from complex **I.**

5.2.1.2 Ligand exchange of HDA-capped CdS nanoparticles prepared from complex I using pyridine route

Pyridine, which can also act as a capping agent, was employed as a solvent. The capping agents such as HDA and TOPO are known to be completely soluble in pyridine. It is a good solvent for displacing HDA or TOPO. Although there is a possibility of pyridine to bind to

the surface of the nanoparticles, the advantage is that it does not bind strongly and hence can be easily displaced by a new capping agents.

(a) Optical properties

The absorption spectra of CdS nanoparticles capped by glucuronic acid (a) and glucose (b) were grown at room temperature for overnight (Figure 5.5). Prior to the introduction of glucuronic acid and glucose, pyridine was used to displace hexadecylamine at 40 ^{o}C for 2 h. The band edge of bulk CdS is recorded as 515 nm (2.41 eV). The absorption spectra of the nanocrystallite samples were recorded by dispersing CdS nanoparticles in de-ionized water. The as-prepared CdS absorption spectra, which are broad, are blue shifted with respect to the bulk CdS, which signifies a finite size of the nanoparticles. Both CdS nanoparticles capped by these sugars depict band edges appearing at 461 nm (2.69 eV), with an excitonic peak positioned at about 431 nm (2.88 eV). Their corresponding photoluminescence spectra (Figure 5.6) show narrow emission curves, with the emission maxima appearing at the same region, which is 469 nm (2.64 eV). It is interesting to observe that absorption and emission spectra of these water soluble nanoparticles absorb and emit at the same wavelength compared to the one capped by HDA. Similar results were reported by Sato *et al.* [37] where they used the coating agent, trioctadecylmethylammonium bromide (TODAB) to stabilize the quantum dots, and then transfer the quantum dots to water soluble using polyacrylic acid (PAA) as the hydrophilic coating agent. In their work, it was reported that the absorption edge and emission peak for PAA-capped CdS nanoparticles were identical to the nanocrystals prior to the phase transfer reaction. Their conclusion was that PAA coating agent did not influence the electronic states on the CdS surface.

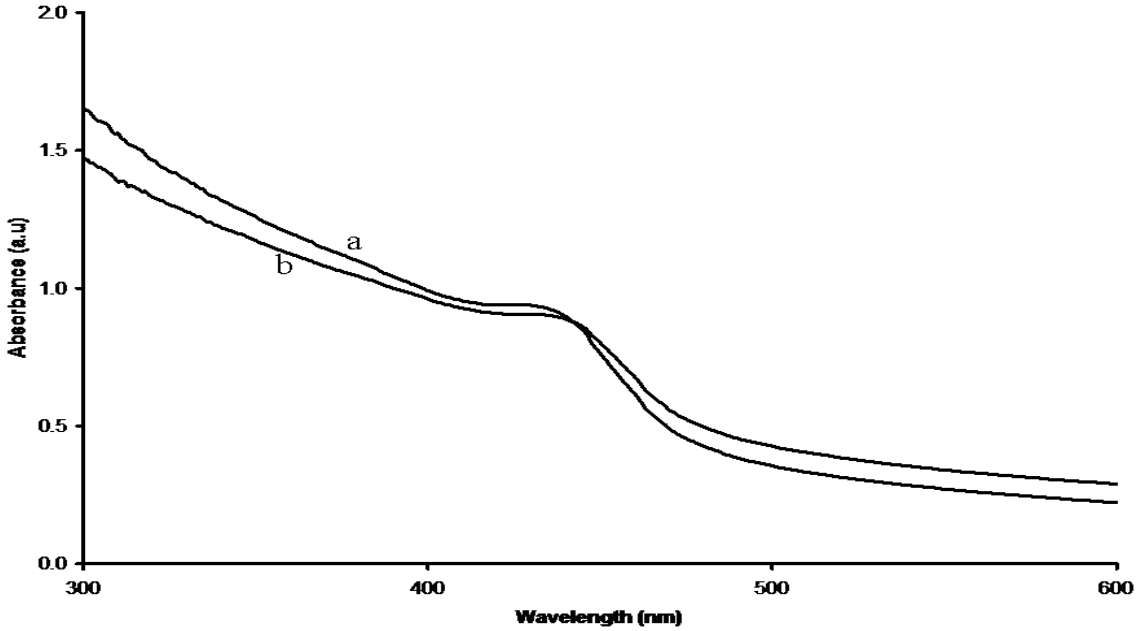

Figure 5.5: Absorption spectra of CdS nanoparticles capped by glucuronic acid (a) and glucose (b) prepared from HDA-capped CdS nanoparticles (120 ^{o}C) from complex **I.**

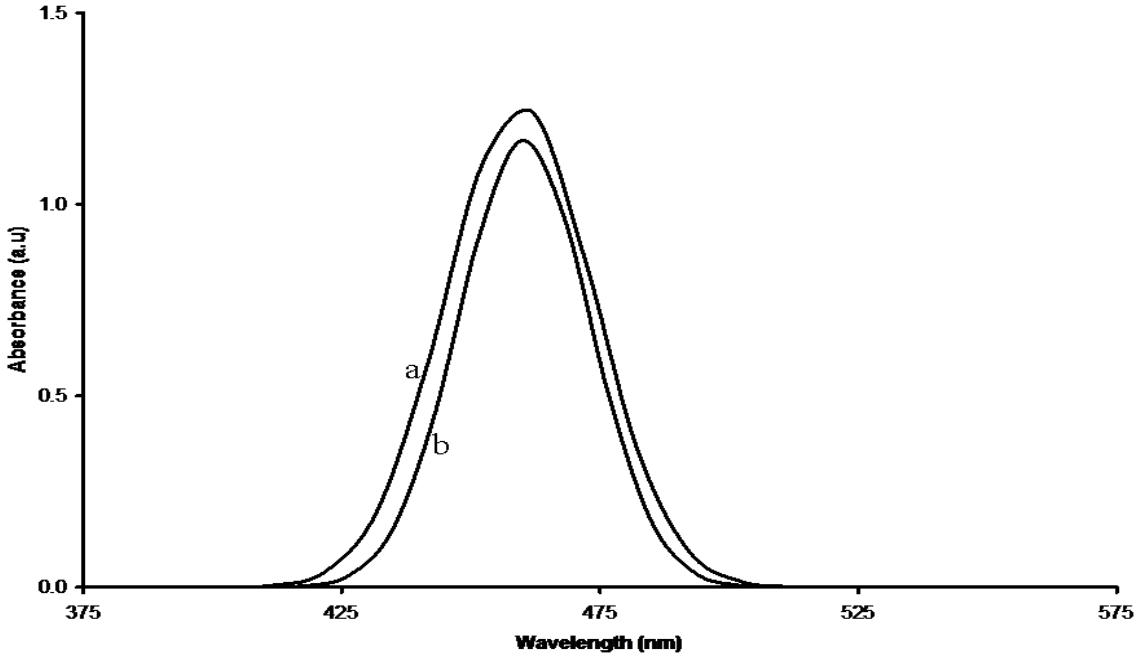

Figure 5.6: Photoluminescence spectra of CdS nanoparticles capped by glucuronic acid (a) and glucose (b) prepared from HDA-capped CdS nanoparticles (120 ^{o}C) from complex **I.**

(b) Structural properties

The TEM images of CdS nanoparticles capped by glucuronic acid (a) and glucose (b) are shown in Figure 5.7. The starting material, which is HDA-capped CdS nanoparticles, was synthesized from complex **I** at 120 ^{o}C. The particles obtained showed rods shape particles with diameter ranging from 1.8-2.8 nm. These small rod-like particles are fused together at the centre to give multipods.

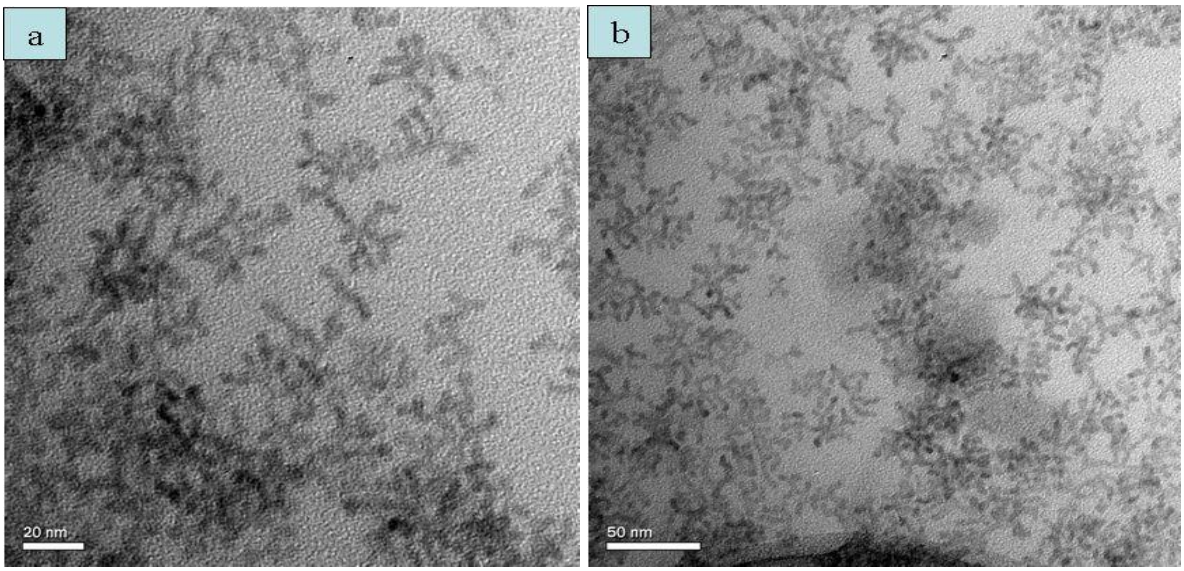

Figure 5.7: TEM images of CdS nanoparticles capped by glucuronic acid (a) and glucose (b) prepared from HDA-capped CdS (120 ^{o}C) from complex **I.**

5.2.1.3 Synthesis of glucuronic acid or glucose-capped CdS nanoparticles *via* pyridine route synthesized from HDA-capped CdS nanoparticles prepared from complex II.

The synthesis of water soluble CdS nanoparticles was achieved by displacing HDA by glucuronic acid and glucose as the capping agents. A certain amount from CdS nanoparticles capped by HDA synthesized from different precursor concentration was dissolved in a minimum volume of pyridine. Pyridine, which acted both as a solvent and capping agent, although weak, was chosen because it solubilises HDA and TOPO completely.

(a) Infrared spectra

FT-IR spectral analyses of glucuronic acid or glucose-capped CdS nanoparticles are shown in Figure 5.8. The prominent peaks are marked with asterisks. Broad band of valence (symmetrical and asymmetrical) oscillations of OH at 3368 cm^{-1} is due to the presence of glucuronic acid (Figure 5.8a), while another broad band of OH appearing at 3230 cm^{-1} is due to glucose (Figure 5.8b). The well defined band (Figure 5.8a) appearing at 1709 cm^{-1} corresponds to valence vibration of the carbonyl group.

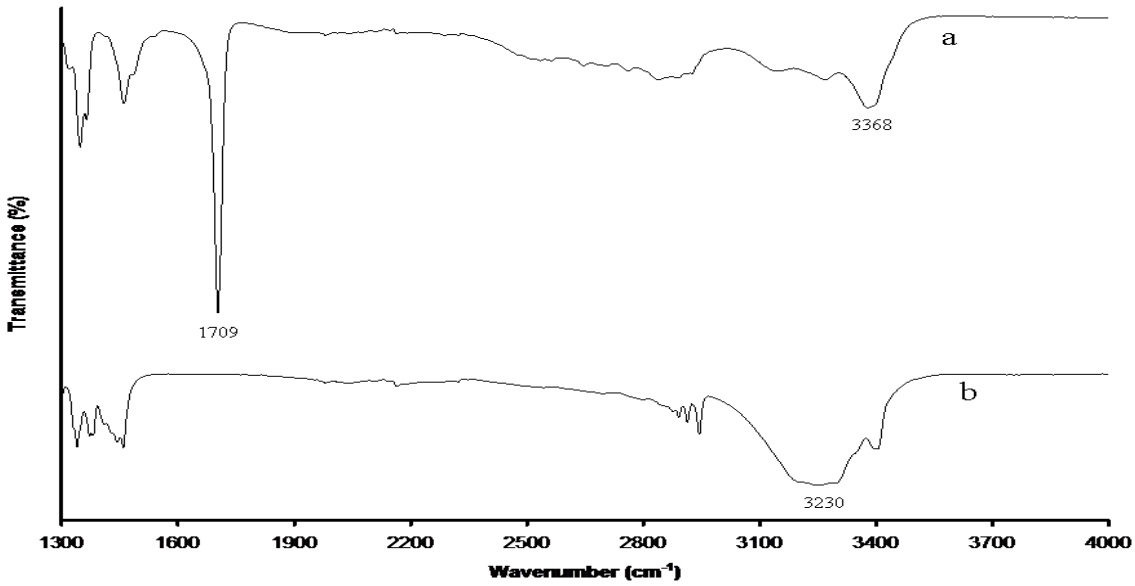

Figure 5.8: Infrared spectra of CdS nanoparticles capped by glucuronic acid (a) and glucose (b) synthesized from HDA-capped CdS (2 g complex **II** in 5 g HDA).

(b) Optical properties

The absorption spectra of water soluble CdS nanoparticles capped by glucose synthesized from 0.5 g complex **II** in5 g HDA (a), glucose synthesized from 1 g complex **II** in 5 g HDA (b), glucuronic acid synthesized from 2 g complex **II** in 5 g HDA (c) and glucose synthesized from 2 g complex **II** in 5 g HDA (d) are shown in Figure 5.9. The absorption and emission spectra were recorded at room temperature by dispersing the particles in de-ionized water. The absorption spectra, which are also blue shift to the bulk CdS, show some tailing as compared to the HDA-capped ones which symbolizes either bigger particles or aggregation of particles. Their band edges are also slightly higher than those capped by

HDA. This is attributed to the ligand exchange which involved the use of pyridine before incorporation of the sugar molecules. The particles might have been exposed before being capped by sugar molecules as pyridine is known not to be a strong capping agent compared to HDA, TOPO, Oleic acid and many more. The emission spectra of CdS nanoparticles capped by glucose (a) from 0.5 g complex **II** in 5 g HDA, glucose (b) from 1 g complex **II** in 5 g HDA, glucuronic acid (c) from 2 g complex **II** in 5 g HDA and glucose (d) from 2 g complex **II** in 5 g HDA (Figure 5.10) appear at higher wavelength (lower energy) as compared to the emission spectra of CdS nanoparticles capped by HDA, which is a good support of their absorption spectra which also appeared at higher wavelength as reported above. Their maximum absorption peaks are positioned at (a) 453 nm, (b) 464 nm and (c, d) 482 nm. Similar trends were observed when glucuronic acid was used instead of glucose in the ligand exchange process.

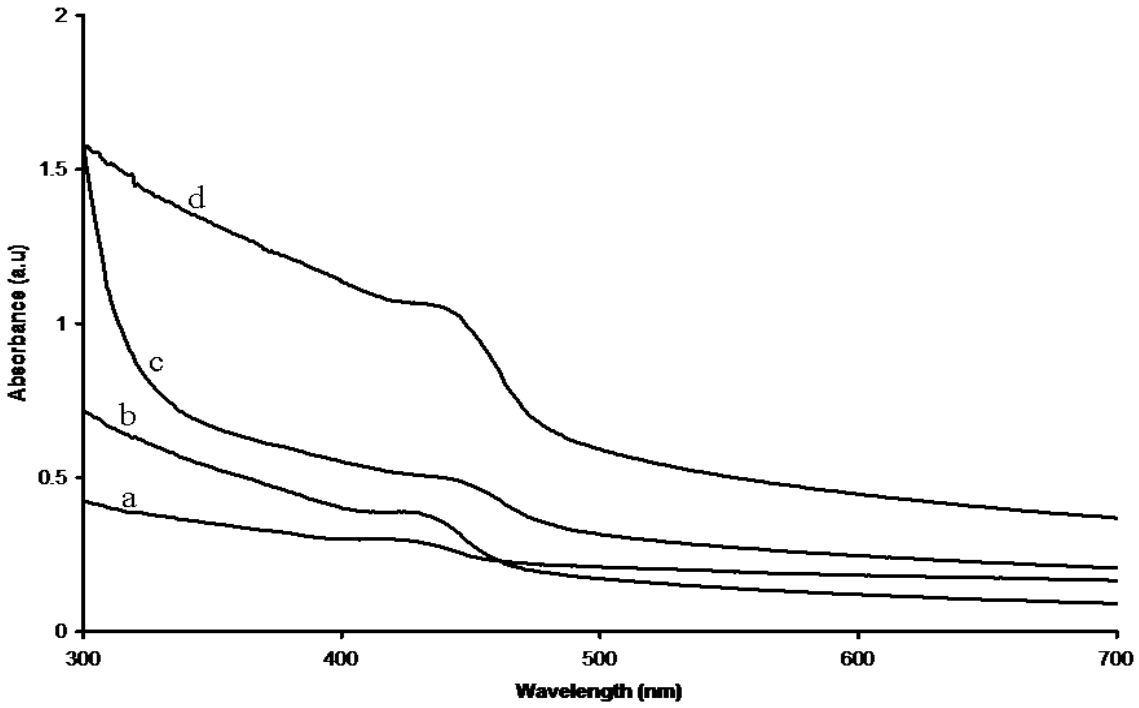

Figure 5.9: Absorption spectra of CdS nanoparticles capped by glucose (a, b, d) and glucuronic acid (c) synthesized from different mass composition of HDA-capped nanopartiles

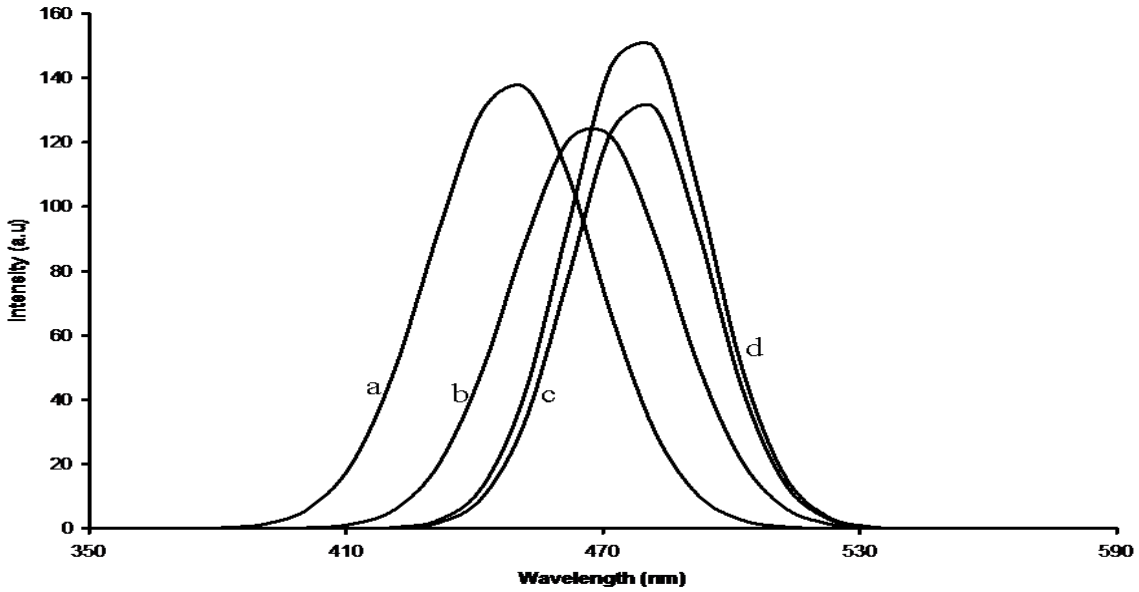

Figure 5.10: Photoluminescence spectra of CdS nanoparticles capped by glucose (a, b, d) and glucuronic acid (c) synthesized from different mass composition of HDA-capped nanopartiles.

(c) Structural properties

Figure 5.11 depicts TEM images of CdS nanoparticles capped by glucose (a) synthesized from 0.5 g complex **II** in 5 g HDA, glucose (b) synthesized from 1 g complex **II** in 5 g HDA, glucuronic acid (c) synthesized from 2 g complex **II** in 5 g HDA and glucose (d) synthesized from 2 g complex **II** in 5 g HDA. No significant changes were observed on the particles from the HDA-capped through ligand exchange to glucose or glucuronic acid-capped ones with an exception of the fine edges being lost on the surface of nanoparticles and some aggregation of the particles especially in (d) glucuronic acid-capped CdS nanoparticles (Figure 5.11d). Figure 5.12 shows the XRD patterns of CdS nanoparticles capped by glucuronic acid (a) and glucose (b). The particles were grown from 2 g of complex **II** in 5 g HDA at room temperature for 12 hours. The XRD patterns could not reveal the crystallinity of CdS nanoparticles because of the multiple peaks that are present due to crystalline sugar molecules being in the same region as the CdS materials. This scenario was observed for all XRD patterns of CdS nanoparticles capped by sugars synthesized at room temperature.

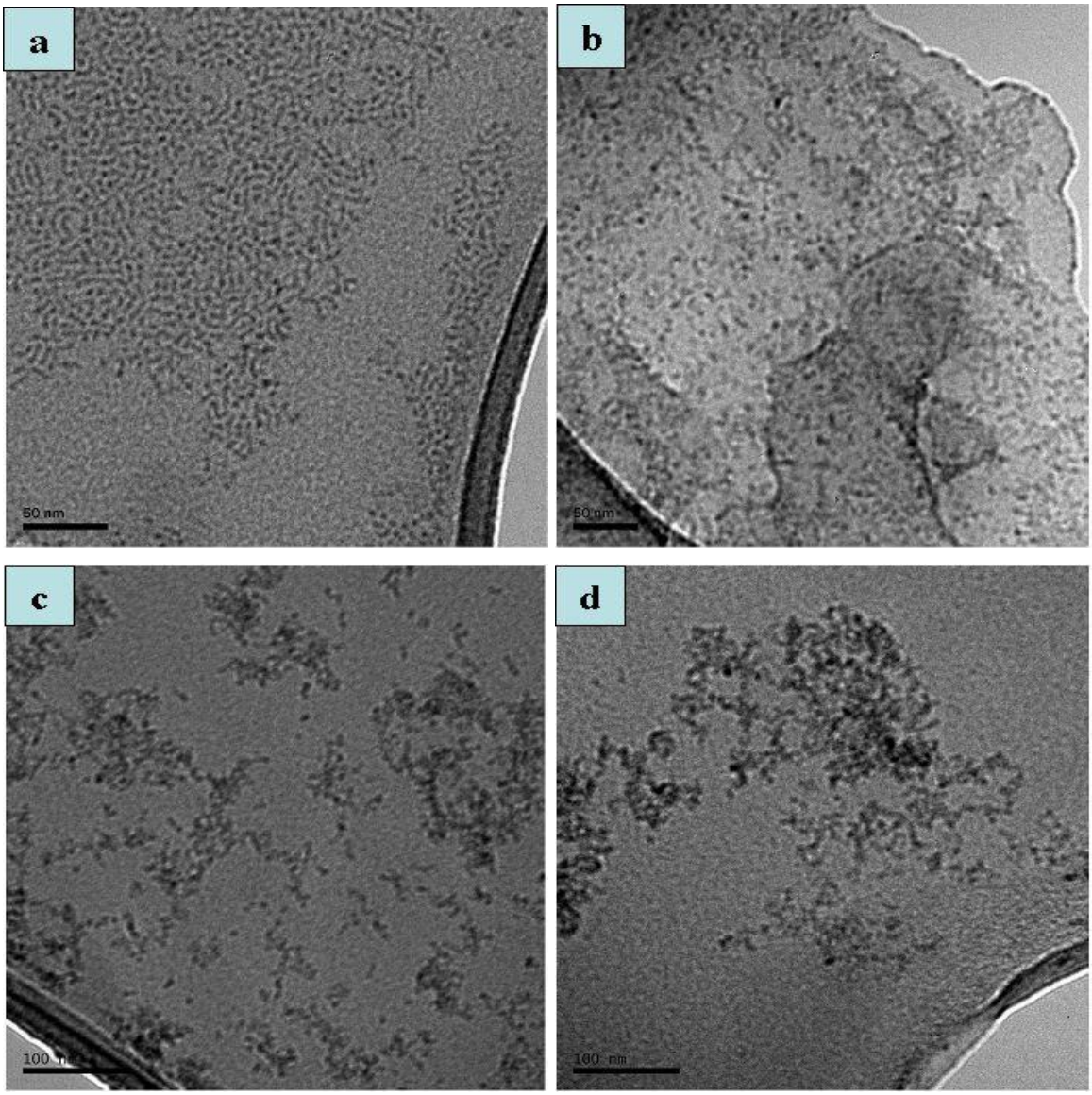

Figure 5.11: TEM images of CdS nanoparticles capped by glucose (a, b, d) and glucuronic acid (c) synthesized from different mass composition of HDA-capped nanopartiles.

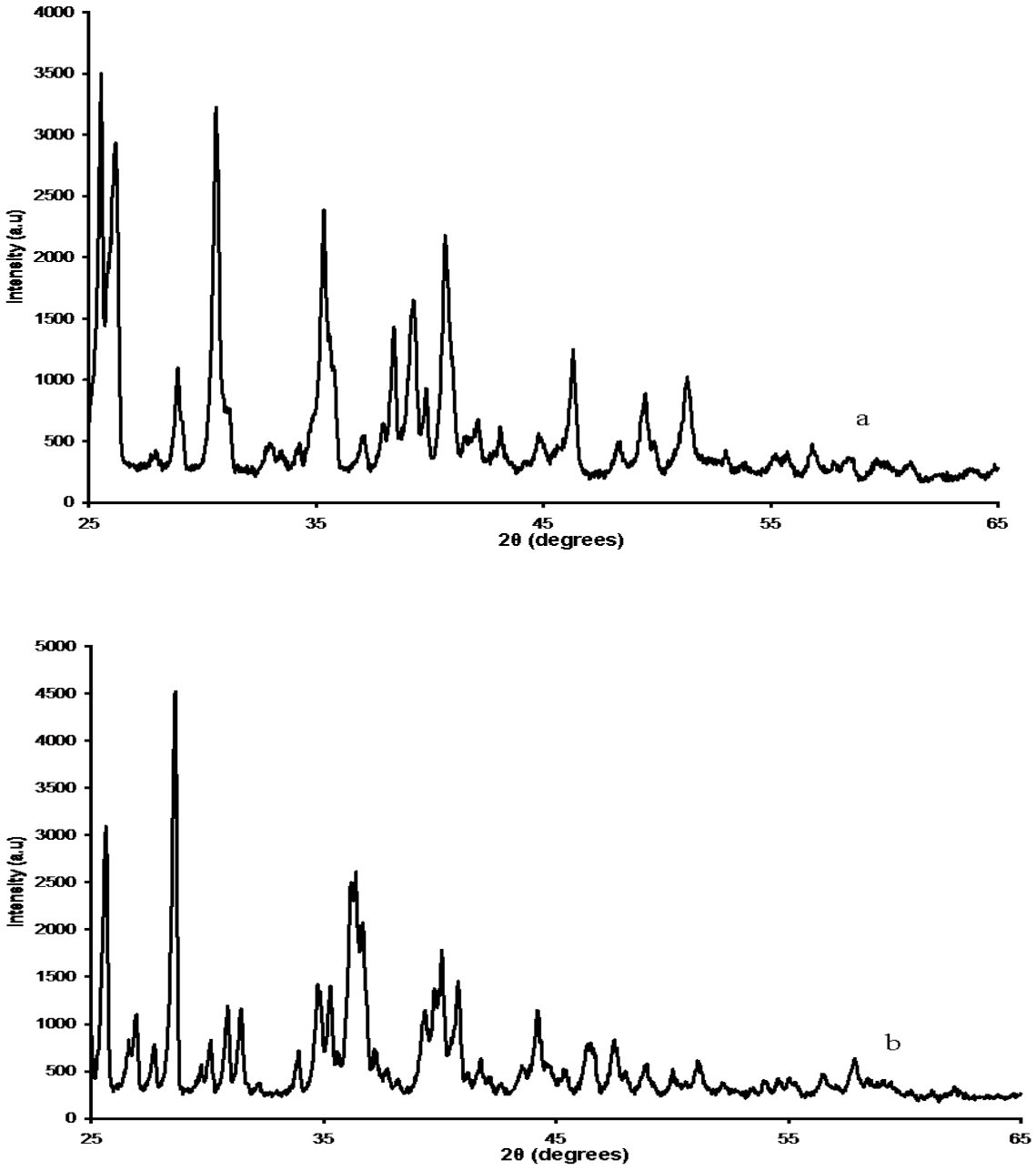

Figure 5.12: XRD patterns of CdS nanoparticles capped by glucuronic acid (a) and glucose (b) synthesized from 2 g complex **II** in 5 g HDA.

5.2.1.4 Sugars-capped CdS nanoparticles synthesized from HDA-capped CdS nanoparticles prepared from complex III

The sugars-capped CdS nanoparticles in this section were synthesized from CdS nanoparticles capped by a hydrophobic long chain ligand, which is hexadecylamine. The water insoluble HDA-capped CdS nanoparticles were synthesized from cadmium complex of dimethylthiourea **(III)**. The hexadecylamine ligand was displaced by the use of pyridine

solvent at lower temperature (40 ^{o}C) for a maximum of 2 h. The sugars-capped CdS nanoparticles reactions were run for overnight at room temperature. Upon completion of the reactions, chloroform, ethyl acetate and diethyl ether were added to precipitate and dry particles.

(a) Optical properties

The absorption spectra of CdS nanoparticles capped by glucuronic acid (a) and sucrose (b) synthesized from HDA-capped CdS (120 ^{o}C) that was prepared from complex **III** (Figure 5.13), are blue shifted to the band edge of bulk CdS, which signifies small nanocrystal size. The band edge of both glucuronic acid and sucrose-capped CdS appear at about 461 nm, corresponding to a band gap of 2.69 eV. The photoluminescence spectra of CdS capped by both glucuronic acid (a) and sucrose (b) synthesized from complex **III** are shown in Figure 5.14. Both spectra are red shifted as compared to their as-prepared CdS nanoparticles absorption spectra (Figure 4.13). The photoluminescence spectra depict sharp emission peaks which are very close to the absorption band edges.

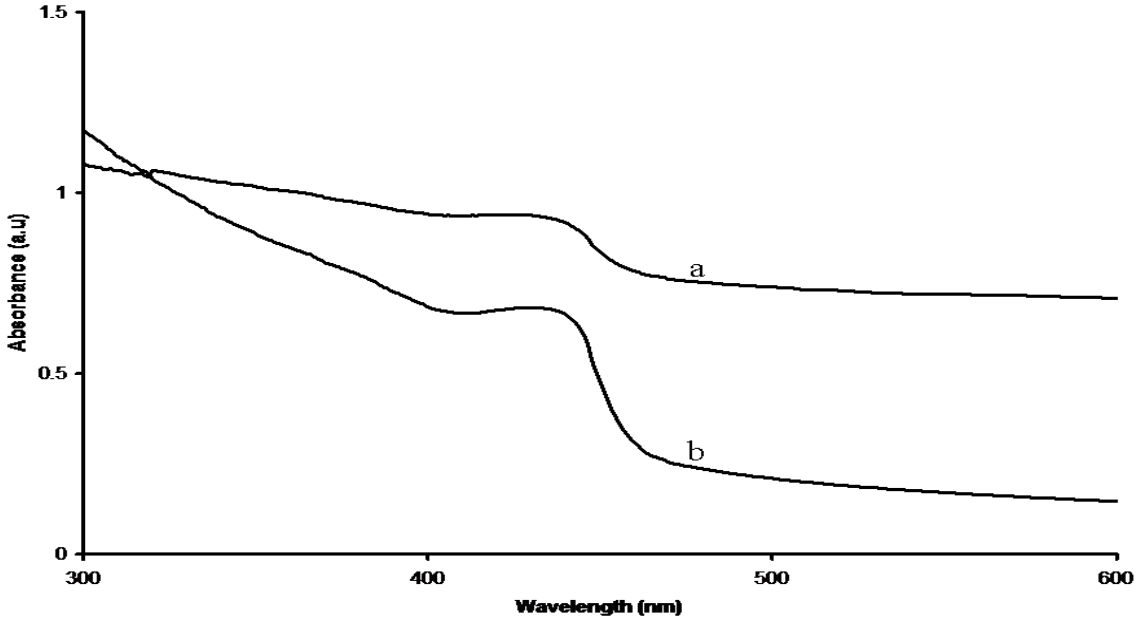

Figure 5.13: Absorption spectra of CdS nanoparticles capped by glucuronic acid (a), and sucrose (b) synthesized from HDA-capped CdS nanoparticles (120 ^{o}C) prepared from complex **III**.

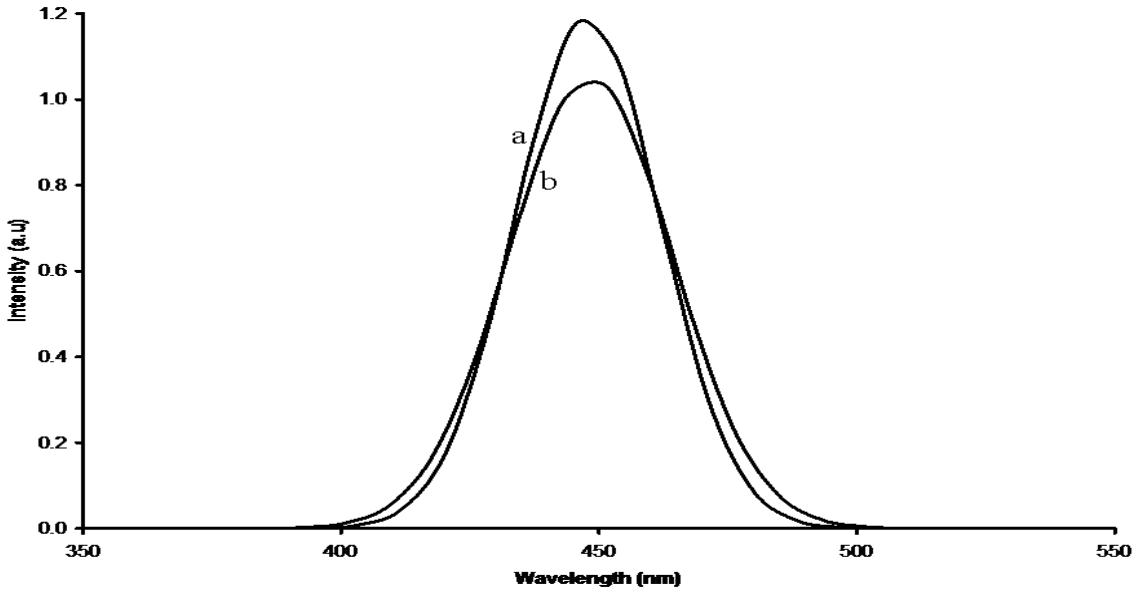

Figure 5.14.: Photoluminescence spectra of CdS nanoparticles capped by glucuronic acid (a) and sucrose (b) synthesized from HDA-capped CdS nanoparticles (120 ^{o}C) prepared from complex **III**.

(b) Structural properties

Figure 5.15 depicts the TEM images of glucuronic acid (a) and sucrose (b) CdS nanoparticles capped synthesized from HDA-capped CdS that was prepared from complex **III**. All images showed a mixture of spherical and short rod shape particles. Beside the observation of a mixture of spherical and rods particles, the particles showed some aggregation which were due to their small size and high surface energy. It was difficult to measure the size or diameter of the particles because of that aggregation. All sugar-capped CdS nanoparticles synthesized were dispersed in de-ionized water and a clear yellow solution was observed. A drop of solution was placed on the copper grid for TEM analysis. The complete solubility of the particles in water confirmed the achievement of ligand exchange method through pyridine route.

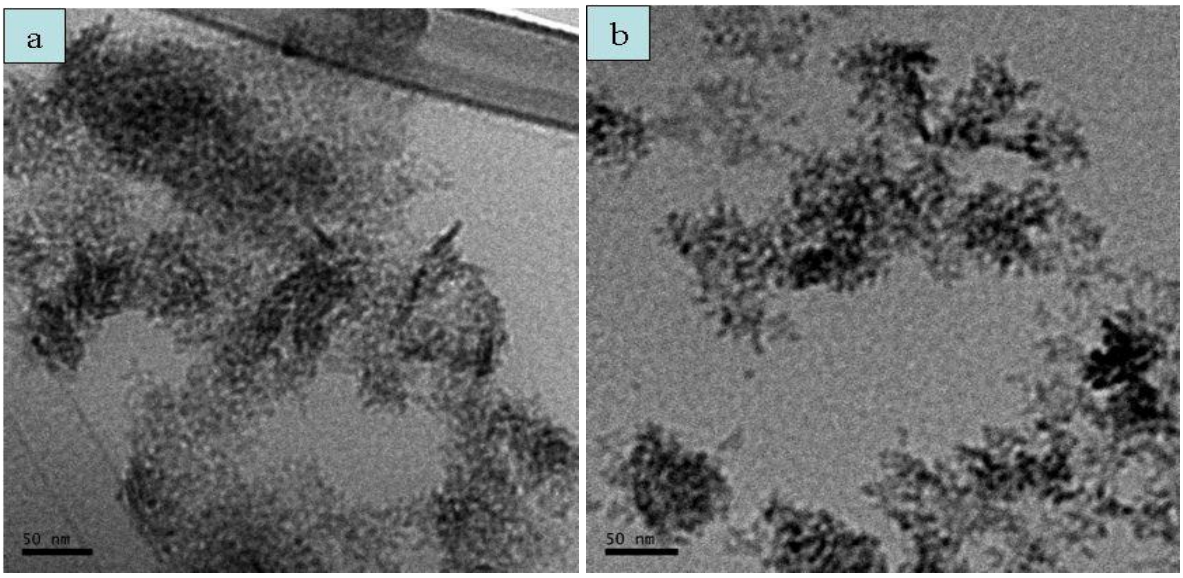

Figure 5.15: TEM images of CdS nanoparticles capped by glucuronic acid (a) and sucrose (b) synthesized from HDA-capped CdS (120 ^{o}C) prepared from complex **III**.

5.2.1.5 Sugars-capped CdS nanoparticles synthesized from HDA-capped CdS nanoparticles from complex IV

(a) Optical properties

The absorption spectra of CdS nanoparticles capped by glucuronic acid (a) and sucrose (b) synthesized from HDA-capped CdS from complex **IV** are represented in Figure 5.16. The band edges of CdS nanoparticles capped by glucuronic acid (a) and sucrose (b) transferred from HDA-capped CdS (120 ^{o}C) that was synthesized from complex **IV** were estimated to be 451 nm (2.75 eV). Both spectra, with sharp and strong excitonic peaks, are blue shifted with respect to bulk CdS material. Their photoluminescence spectra (Figure 5.17), which are narrow (depict smaller particles size), were excited at a wavelength of 230 nm. They both show full width at half maximum (FWHM) of less than 100 nm. Their sharp emission peaks are positioned at almost 459 nm (2.70 eV) for CdS nanoparticles capped by glucuronic acid and 454 nm (2.73 eV) for CdS nanoparticles capped by sucrose.

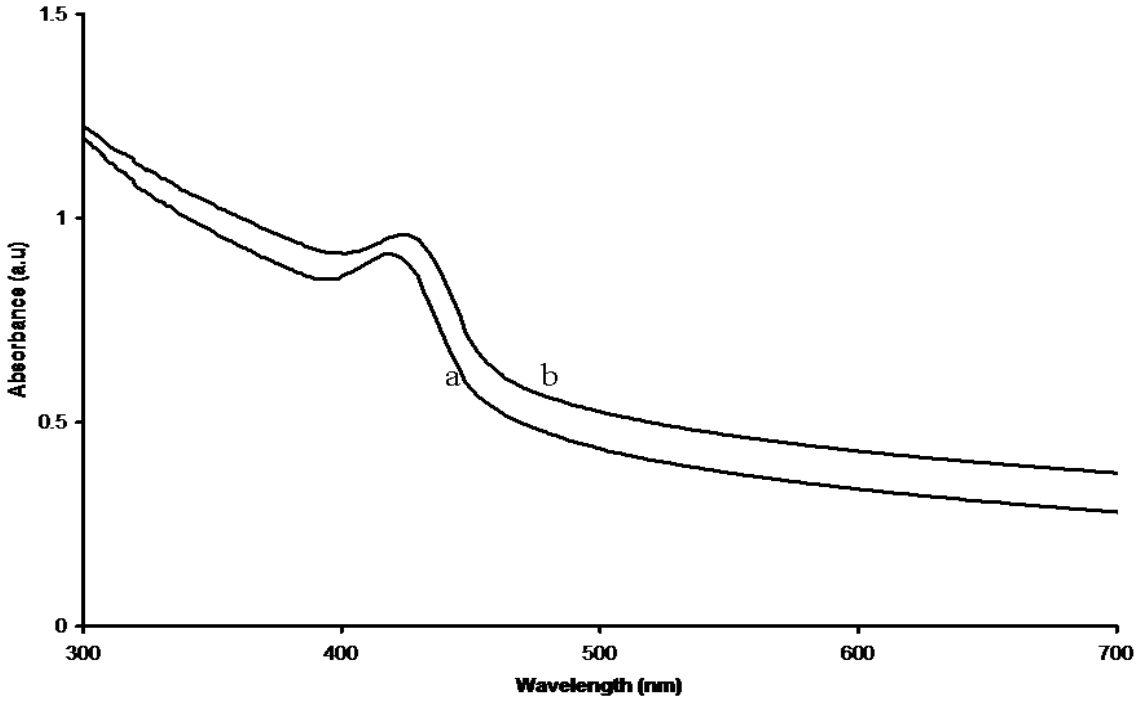

Figure 5.16: Absorption spectra of CdS nanoparticles capped by glucuronic acid (a) and sucrose (b) synthesized from HDA-capped CdS (120 ^{o}C) prepared from complex **IV**.

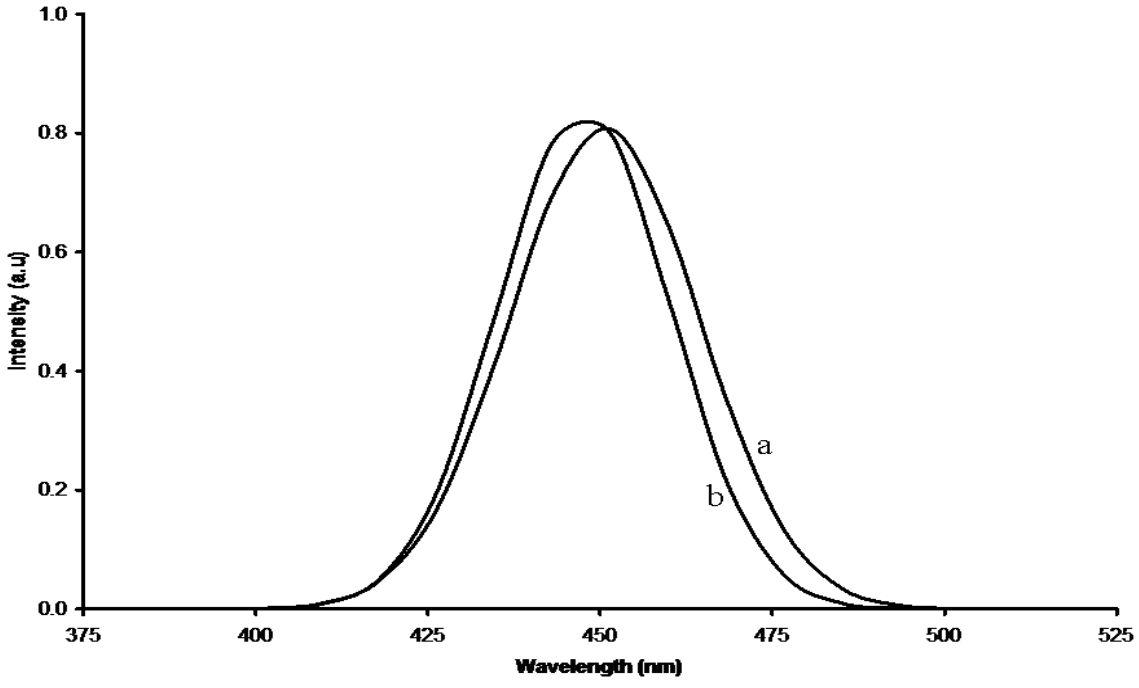

Figure 4.17: Photoluminescence spectra of CdS nanoparticles capped by glucuronic acid (a), and sucrose (c) synthesized from HDA-capped CdS (120 ^{o}C) prepared from complex **IV**.

(b) Structural properties

The particles obtained for CdS nanoparticles (Figure 5.18) capped by glucuronic acid (a) and sucrose (b) synthesized from HDA-capped CdS nanoparticles which was thermolysed from complex **IV**, are short rod-like in shape and very small with an average diameter of 2.7 nm. There are also traces of very small spherical particles in shape. The mixtures of these particles are aggregate together due to their small size and high surface energy. All sugar-capped CdS nanoparticles synthesized were dispersed in de-ionized water and a clear yellow solution was observed. A drop of solution was placed on the copper grid for TEM analysis. The complete solubility of the particles in water confirmed the achievement of ligand exchange method through pyridine route.

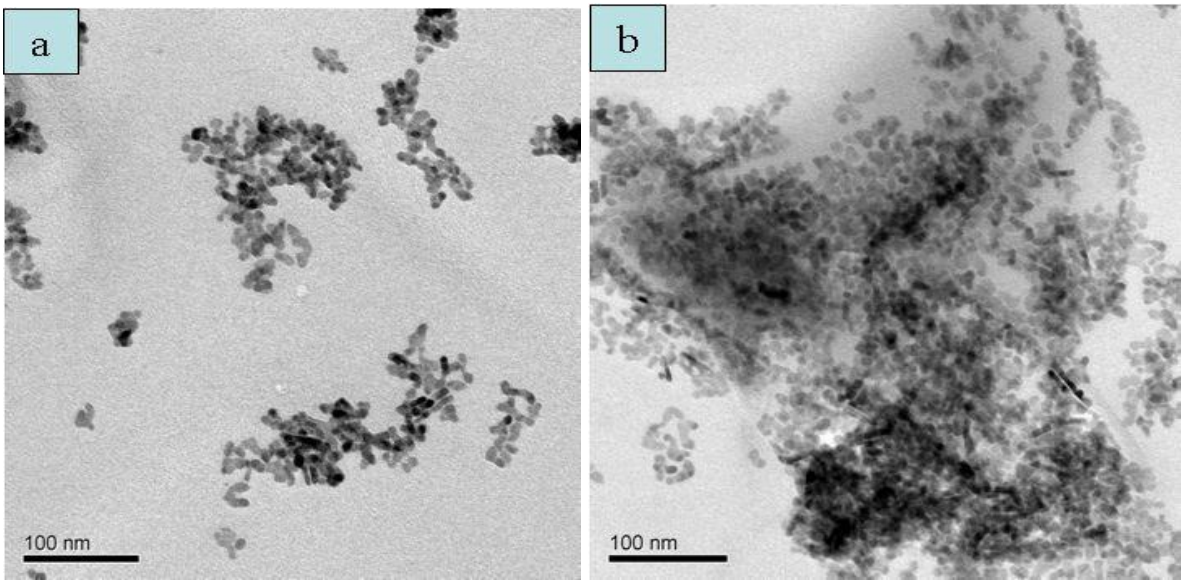

Figure 5.18: TEM images of CdS nanoparticles capped by glucuronic acid (a) and sucrose (b) synthesized from HDA-capped CdS (120 ^{o}C) prepared from complex **IV**.

5.2.1.6 Sugars-capped CdS nanoparticles synthesized from HDA or TOPO-capped CdS prepared from complex V

The glucuronic acid and sucrose-capped CdS nanoparticles experiments were run at room temperature for overnight after the displacement of the water insoluble capping agents through pyridine. The sugar-capped CdS nanoparticles that were synthesized from TOPO-capped CdS were run at 80 ^{o}C instead of room temperature. Pyridine, which worked both as a solvent and weak capping agent, was employed because of its strength in dissolving

hexadecylamine and trioctylphosphine oxide. The CdS nanoparticles capped by HDA used were prepared at 120 ^{o}C and 180 ^{o}C for an hour, while the latter temperature was also employed in synthesizing TOPO-capped CdS nanoparticles. Both HDA and TOPO-capped CdS were synthesized from cadmium complex of sodium diethyldithiocarbamate trihydrate (**V**) at room temperature in water. The absorption and photoluminescence spectra of water soluble nanoparticles revealed some significant differences as compared to CdS capped by water insoluble capping agents (Figure 3.27). The particles were analyzed at room temperature, using water as a solvent. However, the infrared analysis showed some differences after introducing glucuronic acid and sucrose as capping agents.

(a) Optical properties

Figure 5.19 shows the absorption spectra of CdS nanoparticles capped by glucuronic acid (a) and sucrose (b) synthesized from HDA-capped CdS nanoparticles (120 ^{o}C), glucuronic acid (c) and sucrose (d) synthesized from HDA-capped CdS (180 ^{o}C). The HDA-capped CdS material used before for preparing these water soluble nanoparticles was synthesized from complex **V**. The absorption spectra, which were recorded at room temperature using de-ionized water as a solvent, are blue shifted with respect to the bulk CdS, with the emission spectra, shown in Figure 5.20, being red shifted to their as-prepared absorption spectra. Although syntheses were performed at room temperature, the spectra show some distinct features in terms of excitonic peaks and emission peaks. These differences were due to the temperature employed for water insoluble CdS nanoparticles. The absorption spectra (a, b) of CdS nanoparticles capped by glucuronic acid and sucrose, respectively, appear at higher energy with a band edge of 489 nm (2.53 eV), while their excitonic peaks are positioned at 456 nm (2.72 eV). Their emission spectra (Figure 5.20a, b) have sharp peaks appearing at 477 nm (2.60 eV). The absorption spectra (Figure 4.19), in which their material (CdS nanoparticles) was completely soluble in water, were synthesized from CdS nanoparticles capped by HDA (120 ^{o}C).

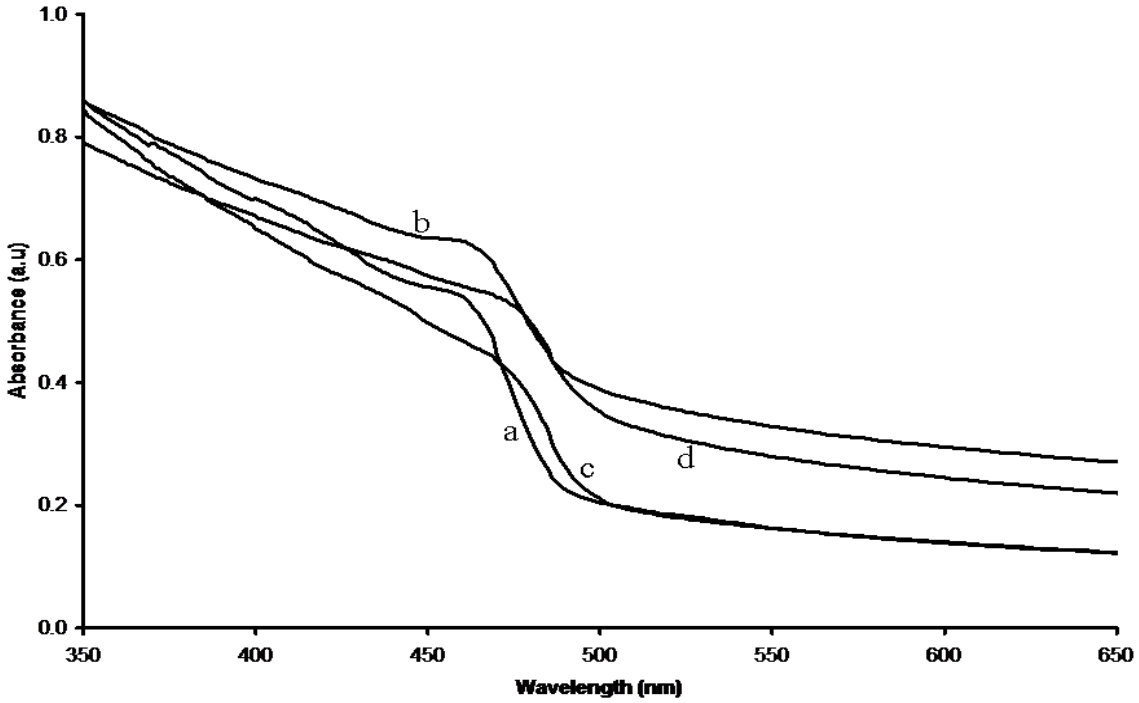

Figure 5.19: Absorption spectra of CdS nanoparticles capped by glucuronic acid (a), and sucrose (b) from HDA-capped CdS (120 ^{o}C), and glucuronic acid (c), and sucrose (d) from HDA-capped CdS (180 ^{o}C).

Comparison of sugars-capped CdS nanoparticles synthesized from HDA-capped CdS nanoparticles (120 ^{o}C and 180 ^{o}C) revealed differences as observed from Figures 5.19 and 5.20. Although all reactions were performed at room temperature, the absorption spectra (Figure 5.19) of CdS nanoparticles capped by glucuronic acid (c) and sucrose (d) synthesized from HDA-capped CdS (180 ^{o}C) and their photoluminescence spectra (Figure 4.20c and d) have clearly shifted to higher wavelength. The band edge of both CdS capped by glucuronic acid (c) and sucrose (d) synthesized from HDA-capped CdS (180 ^{o}C) is 497 nm, corresponding to 2.49 eV. Their excitonic peaks, which can be clearly visualized too, are positioned at 471 nm (2.63 eV) with their emission peaks positioned almost at the same region, 501 nm (2.47 eV).

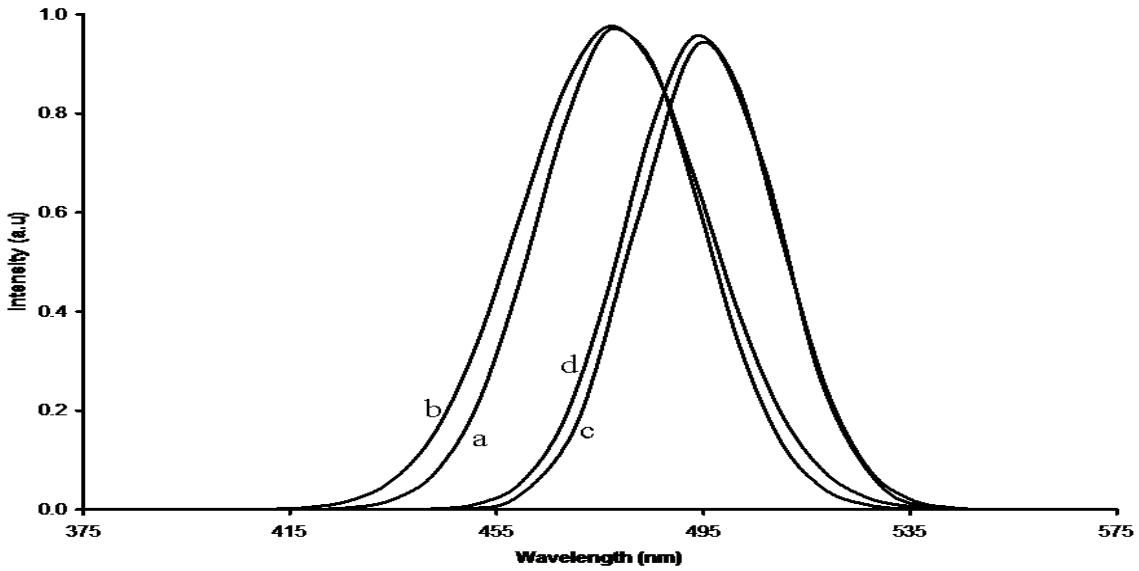

Figure 5.20: Photoluminescence spectra of CdS nanoparticles capped by glucuronic acid (a) and sucrose (b) from HDA-capped CdS (120 ^{o}C), and glucuronic acid (c) and sucrose (d) from HDA-capped CdS (180 ^{o}C)

Figures 5.21 and 5.22 represent the absorption and photoluminescence spectra of CdS nanoparticles capped by glucuronic acid (a) and sucrose (b) synthesized from TOPO-capped CdS (180 ^{o}C) that was thermolysed from complex **V.** The synthesis of CdS nanoparticles capped by glucuronic acid (a) and sucrose (b) from TOPO-capped CdS (180 ^{o}C) were performed at lower temperature, 80 ^{o}C for a duration of 2 h. This temperature was employed in order to speed up the process for the completion of the reaction. In other experiments we have carried, the synthesis of sugar-capped CdS or water soluble CdS nanoparticles *via* ligand exchange route (pyridine route) were performed for a longer time at room temperature. The absorption spectra, which are blue shifted to bulk CdS material, show similarity with a band edge of 467 nm (2.66 eV), and an excitonic peak appearing at 427 nm (2.90 eV). The emission peaks, which are near red shifted to the as-prepared absorption spectra, are positioned at approximately the same region, which is 471 nm (2.63 eV).

Comparison of the spectra between TOPO-capped CdS (180 ^{o}C) (Figure 4.52) and glucuronic acid and sucrose-capped CdS nanoparticles showed some differences. The absorption and emission spectra of CdS nanoparticles capped by glucuronic acid and sucrose prepared from TOPO-capped CdS nanoparticles have shifted to higher wavelength

with the emission spectra being broader due to temperature which was 80 ^{o}C instead of the experiments run at room temperature. From the spectra, it can be deduced that in order to maintain almost the same properties when doing ligand exchange, experiments should be run at room temperature.

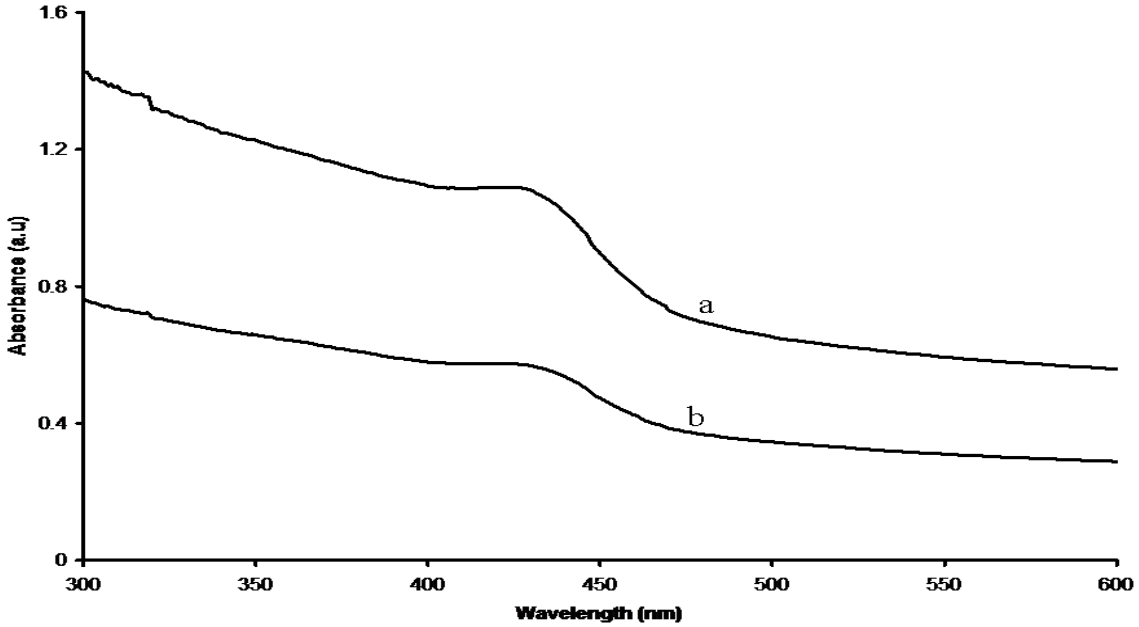

Figure 5.21: Absorption spectra of CdS nanoparticles capped by glucuronic acid (a) and sucrose (b) synthesized from TOPO-capped CdS (180 ^{o}C).

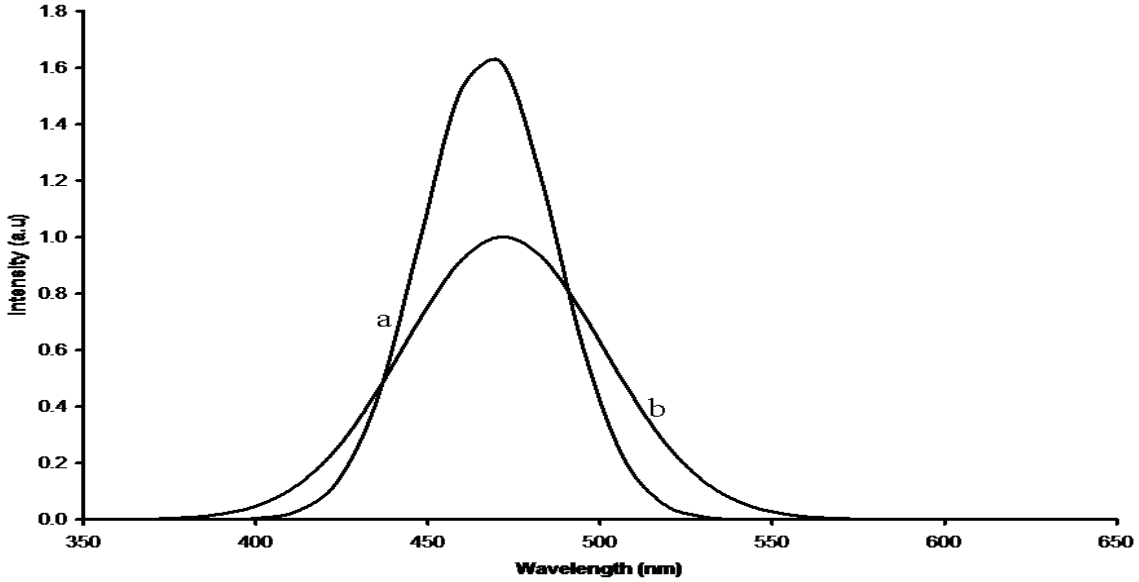

Figure 4.22: Photoluminescence spectra of CdS nanoparticles capped by glucuronic acid (a) and sucrose (b) prepared from TOPO-capped CdS (180 ^{o}C).

(b) Structural properties

Figure 5.23 depicts the TEM images of CdS nanoparticles capped by glucuronic acid (a) and sucrose (b), synthesized from HDA-capped CdS (120 ^{o}C), glucuronic acid (c) and sucrose (d) synthesized from HDA-capped CdS nanoparticles (180 ^{o}C). Both materials, HDA-capped CdS at 120 and 180 ^{o}C, were prepared using complex **V**. It was interesting to observe that rod shaped particles, fused together at the centre were still obtained in some particles. However, although rod-like shaped particles were maintained for glucuronic acid and sucrose-capped CdS nanoparticles images, some of the particles seemed to have lost their sharp edges, particularly in sucrose-capped CdS nanoparticles (Figure 5.23b) image as compared to HDA-capped CdS nanoparticles (120 ^{o}C). There are also signs of short rod particles in Figure 5.21c. This had been caused by the surface interaction that has changed from -NH to -OH. The particles diameter for images synthesized from HDA-capped CdS (120 ^{o}C), as determined from the TEM images is 4.7 nm. The TEM images of CdS nanoparticles capped by glucuronic acid (c), and sucrose (d) synthesized from HDA-capped CdS (180 ^{o}C) has an average diameter of 5.9 nm.

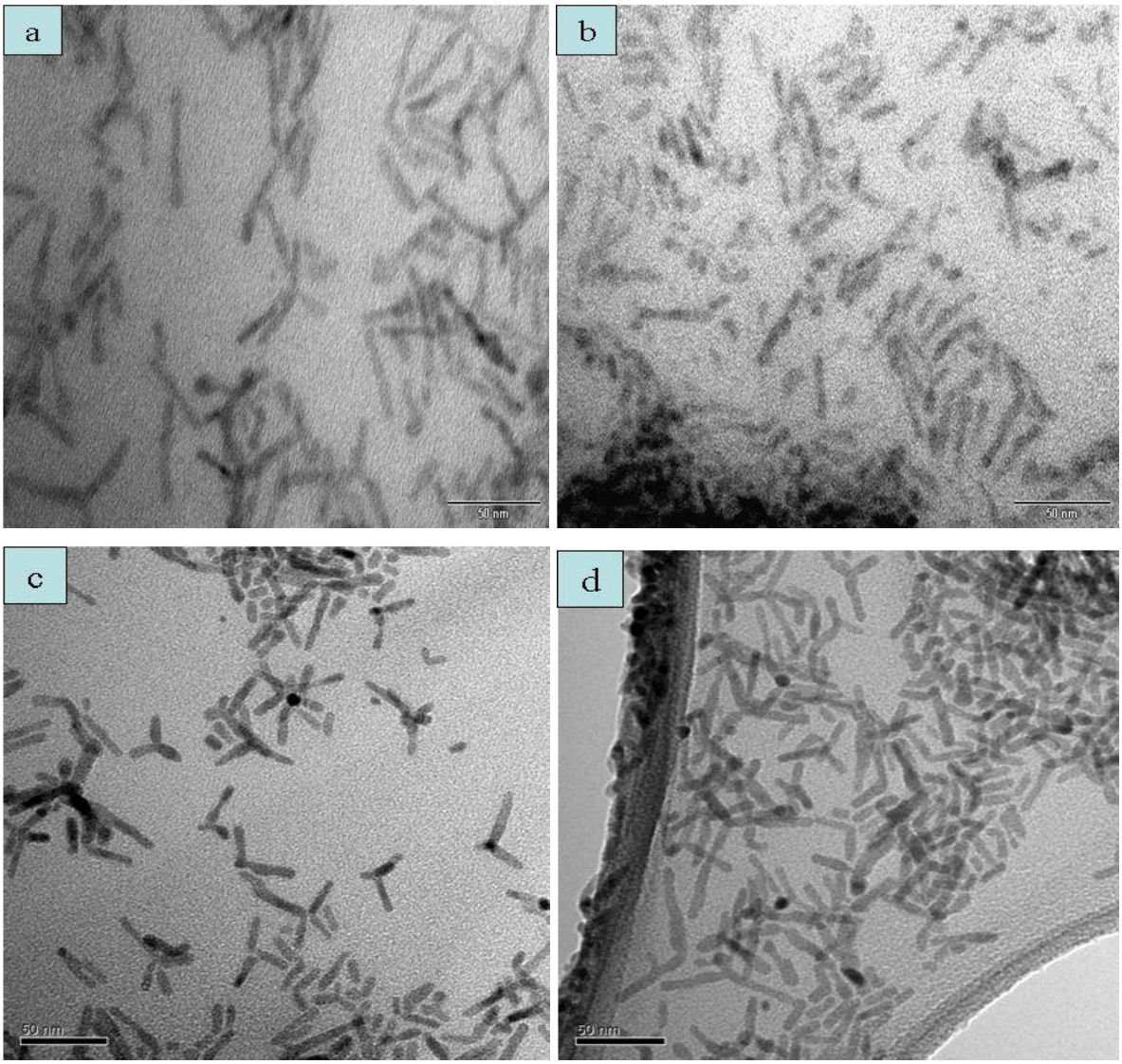

Figure 5.23: TEM images of CdS nanoparticles capped by glucuronic acid (a) and sucrose (b), synthesized from HDA-capped CdS (120 ^{o}C), glucuronic acid (c) and sucrose (d), synthesized from HDA-capped CdS (180 ^{o}C) prepared from complex **V**.

Figure 5.24 shows the TEM image of CdS nanoparticles capped by glucuronic acid (a) and sucrose (b) synthesized from TOPO-capped CdS nanoparticles that were thermolysed from complex **V**. The morphology of water soluble CdS nanoparticles did not change as a result of temperature, as compared to the TOPO-capped CdS nanoparticles (chapter 4, Figure 4.60). The TEM images depict close-to-spherical-like shaped CdS nanoparticles. However, although spheres were obtained, sizes for the particles differed for CdS nanoparticles capped by TOPO. The temperature (80 ^{o}C) used had an effect on the particles size increase. The particles observed from the TEM image are well dispersed, with an average diameter of 4.2 nm. The bigger the size as the temperature increases augurs well with the absorption

and emission spectra that shifted to higher wavelength. In support of the statement reported for the maintenance of the room temperature in order to obtain similar optical properties for absorption and emission spectra, room temperature is also vital for structural properties, that is size and shape.

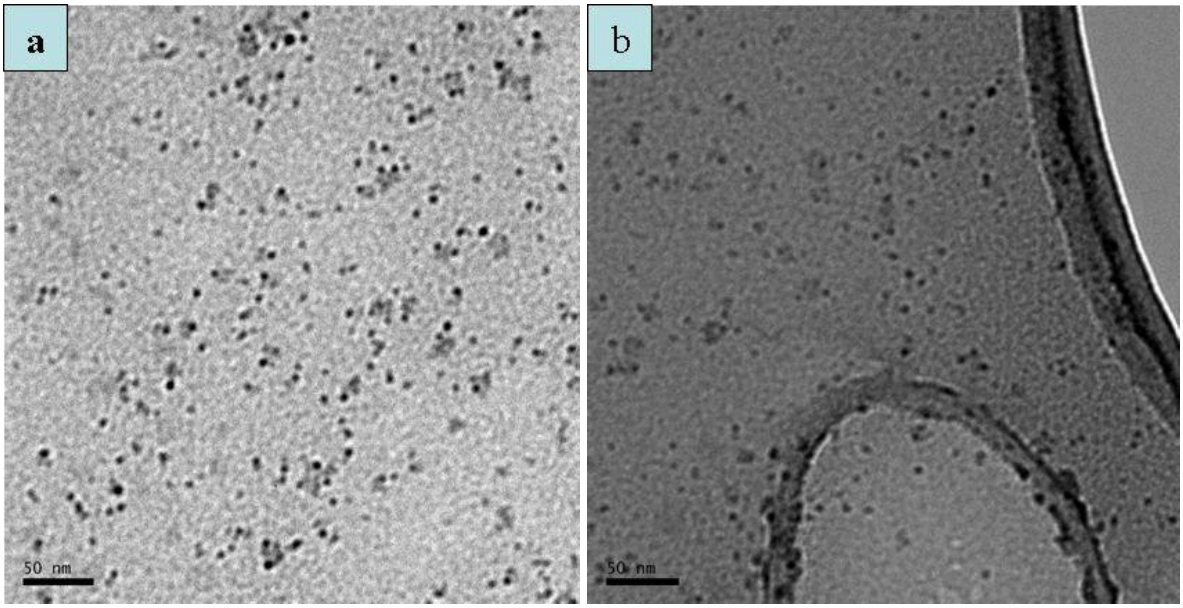

Figure 5.24: TEM images of CdS nanoparticles capped by glucuronic acid (a) and sucrose (b) synthesized from TOPO-capped CdS nanoparticles (180 ^{o}C) that was prepared from complex **V**.

5.2.1.7 Sugar-capped CdS nanoparticles from a mixture of HDA/TOPO-capped CdS nanoparticles prepared using complex V

(a) Optical properties

Figures 5.25 and 5.26 show the absorption and emission spectra of CdS nanoparticles capped by glucuronic acid (a) and sucrose (b) synthesized from CdS nanoparticles (120 ^{o}C) that were capped by a mixture of HDA and TOPO. Both spectra were recorded at room temperature using de-ionized water as a solvent. The absorption spectra are blue shifted to the bulk CdS, with the emission spectra being near red shift to their as-prepared absorption spectra. Both absorption spectra have a band edge of 501 nm (2.47 eV), with an excitonic peak of 462 nm (2.68 eV), with their emission spectra showing a maximum peak positioned at 509 nm (2.43 eV).

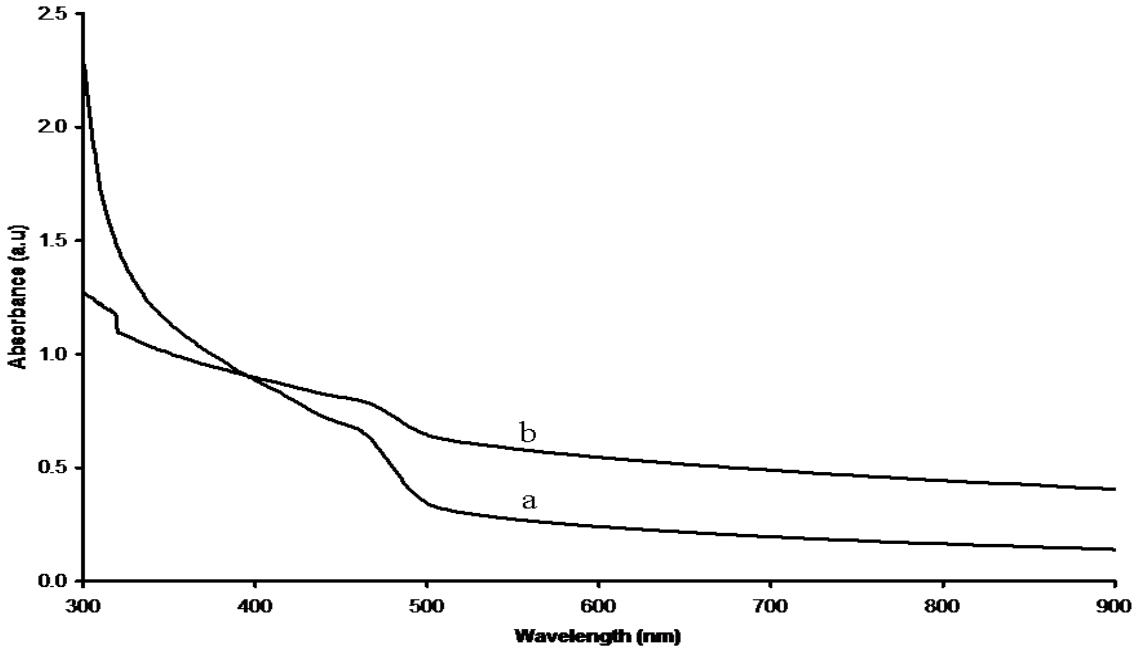

Figure 5.25: Absorption spectra of CdS nanoparticles capped by glucuronic acid (a) and sucrose (b) synthesized from HDA/TOPO-capped CdS nanoparticles from complex **V**.

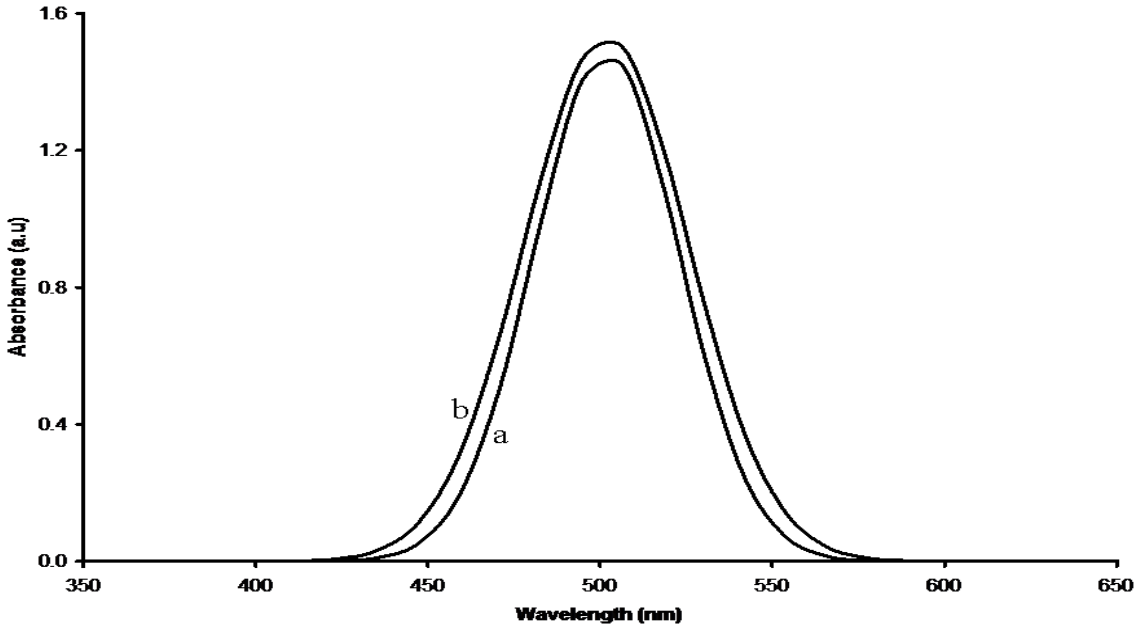

Figure 5.26: Photoluminescence spectra of CdS nanoparticles capped by glucuronic acid (a), and sucrose (b) synthesized from HDA/TOPO-capped CdS nanoparticles from complex **V**.

(b) Structural properties

The TEM images of CdS nanoparticles capped by glucuronic acid (a) and sucrose (b) synthesized from a mixture of HDA and TOPO-capped CdS nanoparticles from complex **V** are shown in Figure 5.27. Both images showed domination of rod shaped particles with an average diameter of 6 nm. There are also traces of spherical shape particles.

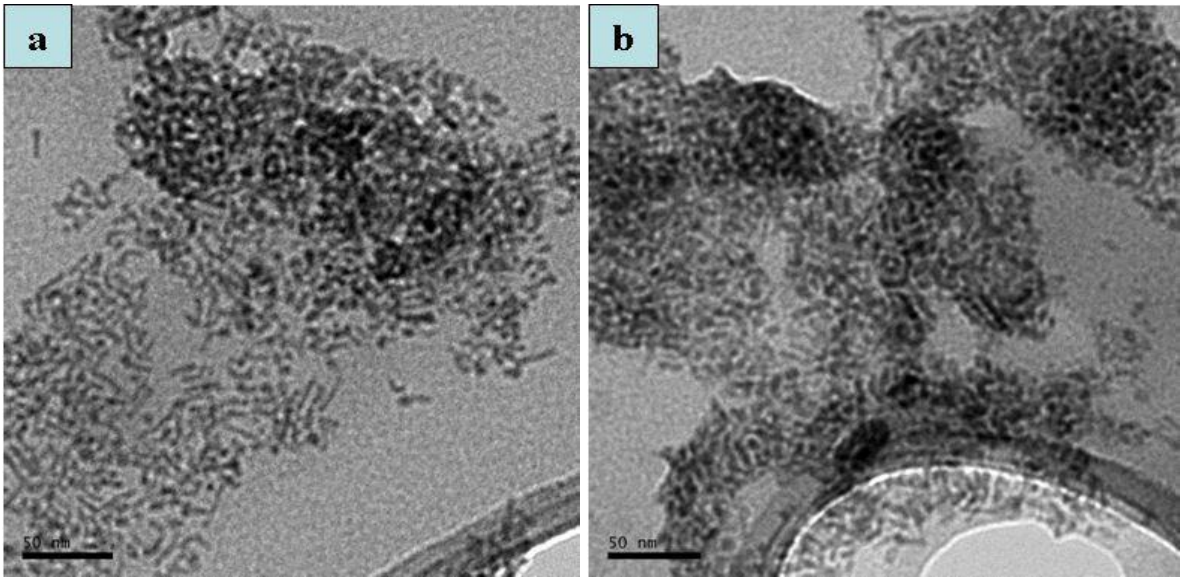

Figure 5.27: TEM images of CdS nanoparticles capped by glucuronic acid (a) and sucrose (b) synthesized from HDA/TOPO-capped CdS nanoparticles from complex **V**.

5.2.1.8 Synthesis of sugars-capped Co_xS_y nanoparticles from HDA-capped Co_xS_y nanoparticles synthesized from complex VI

The Co_xS_y nanoparticles capped by HDA (120 ^oC) used for the synthesis of water soluble nanoparticles was prepared from complex **VI**, which was prepared by refluxing a solution of $CoCl_2$ and tetramethylthiuram monosulfide in ethanol. The $CoCl_2$ was used as a source of cobalt ion, with tetramethylthiuram monosulfide as a source of sulphide ion. The water soluble Co_xS_y experiments were run at room temperature after the removal of the water insoluble capping agent.

(a) Optical properties

In the preparation of water soluble Co_xS_y nanoparticles through pyridine route, hexane was used to precipitate particles after the removal of HDA. The supernatant, which is a mixture of pyridine and hexane, was analysed as shown in Figure 5.28. It was found that the solution still contained Co_xS_y nanoparticles, with the absorption excitonic peaks sharper as the Co_xS_y nanoparticles capped with HDA, while the absorption band edges and the emission peak still appeared in the same region as the one for CdS nanoparticles capped by HDA. The precipitates of Co_xS_y nanoparticles (Figure 5.29) by the addition of excess hexane were also analysed to determine the presence of Co_xS_y nanoparticles. The intensity of the peaks observed in the absorption spectrum is low as compared to those observed in Figure 5.28. This might be due to the material lost during the addition of hexane when precipitating the particles. This also played a role in the tailing of the absorption spectrum. However, it is interesting to note that the band edge and maximum emission peak were still maintained or appeared in the same region as the one in HDA-capped Co_xS_y nanoparticles. Different precursors were tried for ligand exchange, using pyridine as a solvent as in the case of CdS. However, the introduction of sugars after the displacement of HDA or TOPO yielded water insoluble precipitates. When the three solvents, which are chloroform, ethyl acetate and diethyl ether were added, white precipitates settled at the bottom of the centrifuge tube, with some brownish precipitates floating in the solution or supernatant. When the bottom or white precipitates were analysed to investigate the optical properties, a straight line was observed (absorption spectrum). TEM results revealed no formation of the particles. Attempt to analyse the floating precipitates that were separated by filtration was not successful since the material filtered was not soluble in water. The ligand exchange method or route was not efficient for the formation of water soluble or sugars-capped Co_xS_y nanoparticles in our case. The capping agents, which are sugars in our case, and cobalt sulphide, are not miscible.

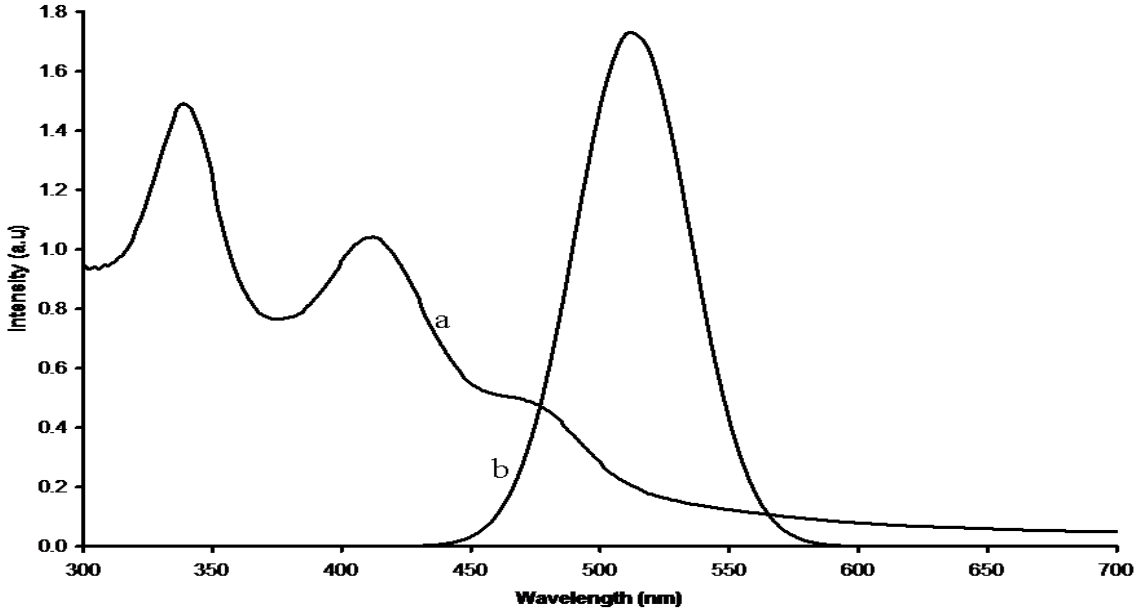

Figure 5.28: Absorption (a) and photoluminescence (b) spectra of Co_xS_y nanoparticles dispersed in pyridine and hexane.

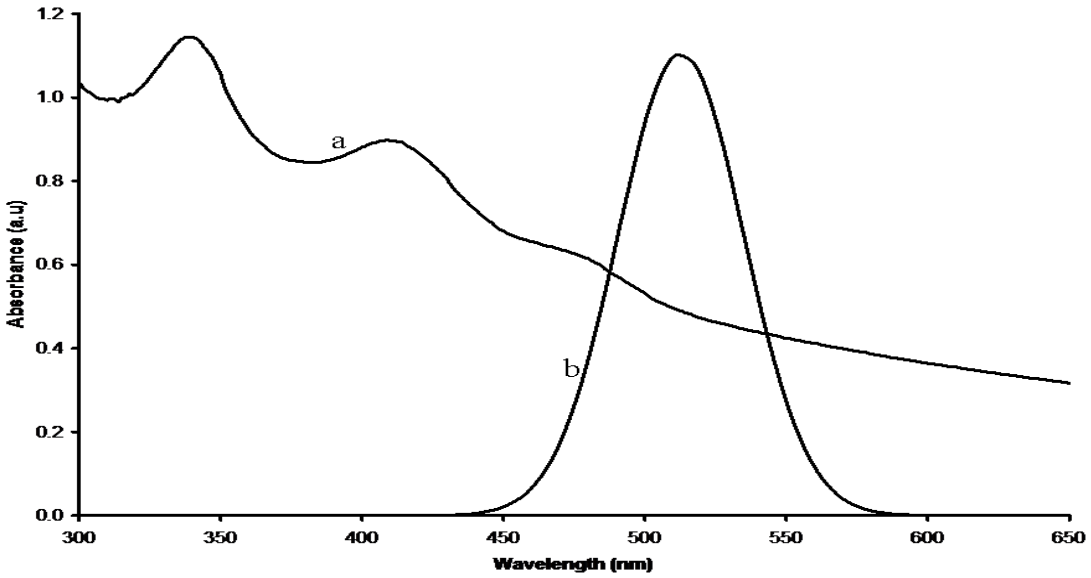

Figure 5.29: Absorption (a) and photoluminescence (b) spectra of Co_xS_y nanoparticles.

5.3 Conclusion

The transformation of hydrophobic semiconductor nanoparticles to hydrophilic semiconductor nanoparticles using ligand exchange did not affect the properties of the particles as expected. All the absorption spectra were still observed to be blue shifted to the

bulk material, while the photoluminescence spectra were red shifted to their as-prepared absorption spectra. Ligand exchange was performed through chloroform route and also pyridine route. The former was found to give small yield which was wet, but did not change the properties. To improve the yield, pyridine route was employed ans aslo did not affect the properties of quantum dots as compared to those that were not soluble in water. It was observed that the best parameter to work with for ligand exchange is room temperature. Pyridine was used as a solvent to displace both HDA and TOPO. In case where low temperature (80 ^{o}C) was used to displace TOPO, properties were affected, although the shape of the particles remained the same. The size of those particles was almost double as compared to the water insoluble one.

Displacement of the water soluble capping agents was investigated by FT-IR and revealed no obvious signs of HDA or TOPO peaks. The materials produced were also soluble in water showing the presence of sugars that were used as capping agents for ligand exchange. However, both chlorooform and pyridine routes yielded no expected results for cobalt sulphide and zinc sulphide nanoparticles. Centrifuging the materials after sugars were introduced presented two different powders, one settling at the bottom while another powder or solid was floating on top of the solution to show that they were not miscible.

5.4 References

1. P. Mitchell, *Nat. Biotechnol.,* **19,** 1013, 2001.
2. E. Klarreich, *Nature,* **413,** 450, 2001.
3. T. M. Jovin, *Nat. Biotechnol.,* **21,** 32, 2003.
4. C. Seydel, *Science,* **3000,** 80, 2003.
5. L. A. Bentolila, S. Weiss, *Phys. World*, **16**(3), 23, 2003.
6. R. F. Uren, *Nat. Biotechnol.,* **22,** 38, 2004.
7. A. Watson, X. Wu, M. Bruchez, *Biotechniques,* **34,** 296, 2003.
8. R. P. Bagwe, X. Zhao, W. Tan, *J. Dispersion Sci. Technol.,* 24, 453, 2003.
9. P. Allivisatos, *Nat. Biotechnol.,* **22,** 47, 2004.
10. B. D. Dabbousi, J. Rodriquez-Viejo, F. V. Mikulec, J. R. Heine, H. Mattoussi, R. Ober, K. F. Jensen, M. G. Bawendi, *J. Phys. Chem. B.*, **101,** 9463, 1997.
11. D. V. Talapin, A. L. Rogach, A. Kornowski, M. Haase, H. Weller, *Nano Lett.*, **1,** 207, 2001.

12. Z. A. Peng, X. Peng, *J. Am. Chem. Soc.*, **123,** 183, 2001.
13. P. Reiss, J. Bleuse, A. Pron, *Nano Lett.*, **2,** 781, 2002.
14. W. C. W. Chan, S. Nie, *Science*, **281,** 2016, 1998.
15. C. Zhang, H. Ma, S. Nie, Y. Ding, L. Jin, D. *Chen, Analyst*, **125,** 1029, 2000.
16. J. O. Winter, T. Y. Liu, B. A. Korgel, C. E. Schmidt, *Adv. Mater.*. **13,** 1673, 2001.
17. J. A. Kloepfer, R. E. Mielke, M. S. Wong, K. H. Nealson, G. Stucky, J. L. Nadeau, *Appl. Environ. Microbiol.*. **69,** 4205, 2003.
18. W. C. W. Chan, D. J. Maxwell, X. Gao, R. E. Bailey, M. Han, S. Nie, *Curr. Opin. Biotechnol.*, **13,** 40, 2002.
19. M. J. Brunchez, M. Moronne, P. Gin, S. Weiss, A. P. Alivisatos, *Science*, **281,** 2013, 1998.
20. S. J. Rosenthal, I. Tomlinson, E. M. Adkins, S. Schroeter, S. Adans, L. Swafford, J. McBride, Y. Wang, L. J. Detelice, R. D. Blakely, *J. Am. Chem. Soc.*, **124,** 4586, 2002.
21. M. E. Akerman, W. C. W. Chan, P. Laakkonen, S. N. Bhatia, E. Ruoslahti, *Proc. Natl Acad. Sci. USA.*, **99,** 12617, 2002.
22. J. K. Jaiswal, H. Mattoussi, J. M. Mauro, S. M. Simon, *Nat. Biotechnol.*, **21,** 47, 2003.
23. M. X. Wu, H. Liu, J. Liu, K. N. Haley, J. A. Treadway, J. P. Larson, N. Ge, F. Peale, M. P. Bruchez, *Nat. Biotechnol.*, **21,** 41, 2003.
24. K. I. Hanaki, A. Momo, T. Oku, A. Komoto, S. Maenosono, Y. Yamaguchi, Y. Yamamoto, *Biochem. Biophys. Res. Commun.*, **302,** 496, 2003.
25. A. Sukhanova, L. Venteo, J. Devy, M. Artemyev, V. Oleinikov, M. Pluot, I. Nabiev, *Lab. Investigation*, **82,** 1259, 2002.
26. E. R. Goldman, G. P. Anderson, P. T. Tran, H. Mattoussi, P. T. Charles, J. M. Mauro, *Anal. Chem.*, **74,** 841, 2002.
27. W. Parak, D. Gerion, D. Zanchet, A. S. Woerz, T. Pellegrino, C. Micheel, S. C. Williams, M. Seitz, R. E. Bruehl, Z. Bryant, C. Bustamante, C. R. Bertozzi, A. P. Alivisatos, *Chem. Mater.*, **14** (5), 2113, 2002.
28. S. Pathak, S. K. Choi, N. Arnheim, M. E. Thompson, *J. Am. Chem. Soc.*, **123,** 4103, 2003.
29. A. Schroedter, H. Weller, R. Eritia, W. E. Ford, J. M. Wessels, *Nano Lett.*, **2,** 1363, 2002.
30. B. Dubertret, P. Skourides, D. J. Norris, V. Noireaux, a. H. Brivanlou, A. Libchaber, *Science*, **298,** 1759, 2002.
31. D. Grion, W. J. Parak, S. C. Williams, D. Zanchet, C. M. Micheel, A. P. Alivisatos, *J.*

Am. Chem. Soc., **124,** 7070, 2002.

32. D. Gerion, F. Chen, B. Kannan, A. Fu, W. J. Parak, D. J. Chen, A. Majumdar, A. P. Alivisatos, *Anal. Chem.*, **75,** 4766, 2003.
33. W. W. Yu, E. Chang, R. Drezek, Vl L. Colvin, *Biochem. Biophys. Res. Commun.*, **348,** 781, 2006.
34. T. Gacoin, K. Lahlil, P. Larregaray, J. P. Boilot, *J. Phys. Chem. B.*, **105,** 10228, 2001.
35. C. J. Murphy, J. L. Coffer, *Appl. Spectrosc.*, **56,** 16A, 2002.
36. M. J. Moloto, N. Revaprasadu, P. O'Brien, M. A. Malik, *J. Mater. Sci. –Mater. Electron.*, **15**(5), 313, 2004.
37. K. Sato, Y. Tachibana, S. Hattori, T. Chiba, S. Kuwabata, *J. Colloid. Inter. Sci.*, **324,** 257, 2008.

Chapter 6

Water soluble semiconductor nanoparticles/QDs synthesized by direct method

6.1 Introduction

Currently, semiconductor nanoparticles/QDs are the most intense research subject of material scientists and engineers due to their fascinating physical properties affected by atomic physics and their wide application in many fields [1]. Thus, to establish well-controlled synthetic methods and to understand the mechanisms by which the size and shape of the nanocrystals can be easily varied are key issues in nanoscience. There have been a numbers of experiments concerned with synthesis and characterization of semiconductor nanoparticles both through colloidal preparation [2, 3, 4] and other methods such as ultrasonic-assisted successive ionic layer adsorption and reaction method [5], microwave irradiation [6], soli-state reaction [7], and wire technique [8]. The polyol compounds, acting both as solvent and reducing agent, have been widely used in the preparation of nanomaterials [9, 10] and their basic reducing mechanism has been monitored and proved [11, 12].

The most recent advances in the field of applications of nanoparticles are in the field of biology. With the bright, photostable fluorescence these semiconductor nanoparticles or quantum dots show promise as alternatives to organic dyes for fluorescent biology labelling (for example, to trace a biological molecule) [13]. Conjugation of semiconductor nanoparticles or QDs with antibodies yields biomarkers that compete with traditional organic fluorescent tags in terms of biocompatibility, excitation and filtering simplicity and photostability [14, 15]. The potential benefits and the use of conjugated quantum dots probes to monitor cellular functions has prompted extensive efforts to develop methods to synthesize water soluble and biocompatible quantum dots that can be used for fluorescent based bio-imaging [13, 16, 17, 18]. In general the key to develop quantum dots as a tool in biological systems is to achieve water solubility, biocompatibility and photostability, and importantly, to provide flexible quantum dots surface chemistry/functionality that will

enable efficient coupling of these fluorescent inorganic probes to reagents capable of targeting and/or sensing ongoing biological processes.

6.2 Results and discussions

6.2.1 Synthesis and characterization of CdS, Co_xS_y and ZnS capped by glucuronic acid, glucose and sucrose using direct chemical synthesis

Different ligands such as tetramethylthiuram monosulfide, dimethylthiourea, 1-methyl-2-thiourea and diethyldithiocarbamate were employed with cadmium chloride, cobalt chloride and zinc chloride in various experiments. The ligands above were used due to their ability to provide sulphur to the metals, to form metal sulphide nanoparticles. All the experiments using the direct method were run for an hour. The temperature employed in these reactions is 160 ^{o}C, with ethylene glycol being used as a solvent. Ethylene glycol is a strong polar and high boiling point solvent. It can also act as a weak capping agent, and can be easily removed at 160 ^{o}C or above. Ethanol was added to precipitate the particles, and then separated by centrifugation. The particles were washed several times by ethanol, followed by the addition of acetone to dry the particles. Scheme 6.1 shows how the sugars-capped metal sulphide nanoparticles were prepared using direct chemical method. The ligand used in the scheme is dimethylthiourea. Other ligands of interest used (not shown in the scheme), are tetramethylthiuram monosulfide, methylthiourea and diethyldithiocarbamate. The significance of employing these ligands is that they contain sulphur element that forms part in the formation of semiconductor nanoparticles or quantum dots. De-ionized water which dissolved the sugar-capped CdS, Co_xS_y and ZnS was used as a solvent for transmission electron microscope, absorption and photoluminescence spectra analysis.

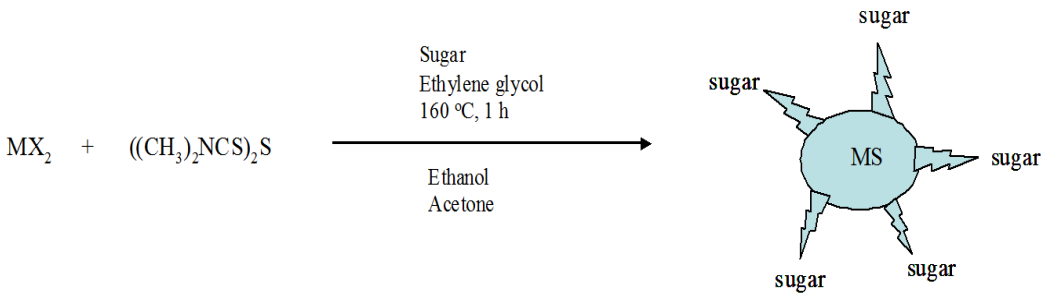

M = Zn, Co, Cd X = Cl Sugars = glucuronic acid, glucose, sucrose

Scheme 6.1: Preparation of sugars-capped metal sulphide nanoparticles using direct chemical reaction method.

6.2.1.1 Sugars-capped CdS, Co_xS_y and ZnS nanoparticles from cadmium chloride, cobalt chloride and zinc chloride and tetramethylthiuram monosulfide

(a) Optical properties

Group II-VI semiconductor nanoparticles are well known to exhibit a strong change of their optical absorption when their size is reduced down to a few nanometers. This is a consequence of quantum confinement of electrons and holes, which is basically a blue shift of the absorption threshold and appearance of discrete energy levels associated to progressive transition from bulk state down to a molecular behaviour [19]. For semiconductor nanoparticles or quantum dots, electronic absorption spectroscopy is a simple and easy way to estimate the band gap energy [20]. Figures 6.1 and 6.2 show the absorption and photoluminescence spectra of CdS nanoparticles capped by glucuronic acid (a), glucose (b) and sucrose (c) using chemical reaction method. The CdS nanoparticles were synthesized from cadmium chloride as a metal source and tetramethylthiuram monosulfide as a sulphur source, with the temperature employed being 160 ^{o}C. All the absorption spectra appear at lower wavelength as compared to the bulk CdS wavelength which is known to be 515 nm. The shift of absorption spectra to lower wavelength is due to quantum confinement. The band edge, which is almost similar for CdS nanoparticles capped by glucuronic acid, glucose and sucrose, was estimated to appear at almost 495 nm which corresponds to a band gap of 2.51 eV. The absorption spectra also show some shoulders at 463 nm (2.68 eV). The photoluminescence spectra are very close to the band

edges of the as-prepared absorption CdS nanoparticles spectra. However, all the photoluminescence spectra are narrow signifying finite size of the nanoparticles.

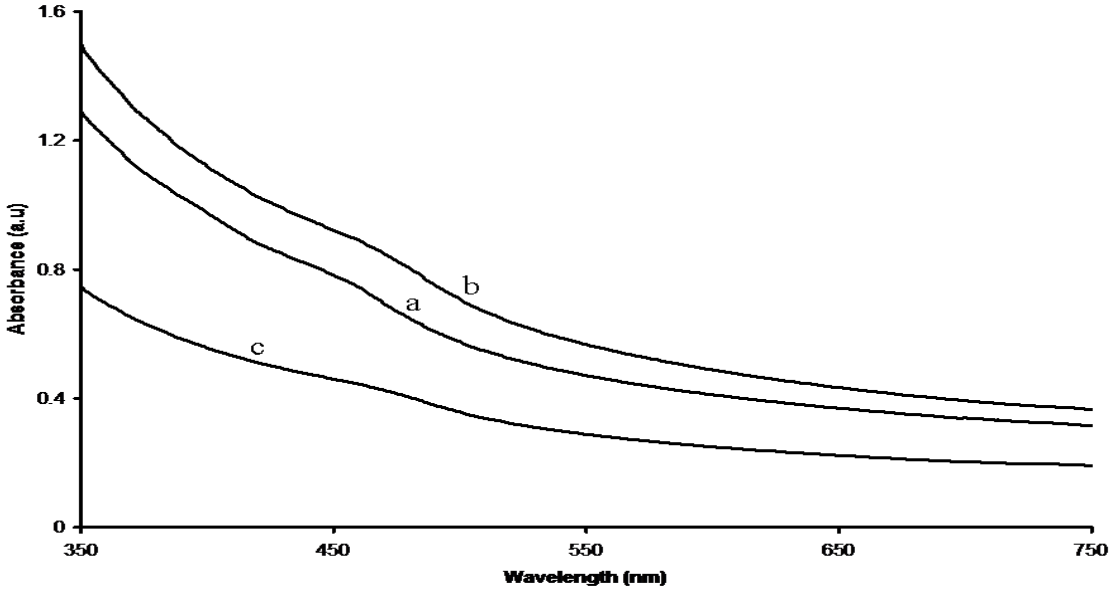

Figure 6.1: Absorption spectra of CdS nanoparticles capped by glucuronic acid (a), glucose (b) and sucrose (c) synthesized from cadmium chloride and tetramethylthiuram monosulfide.

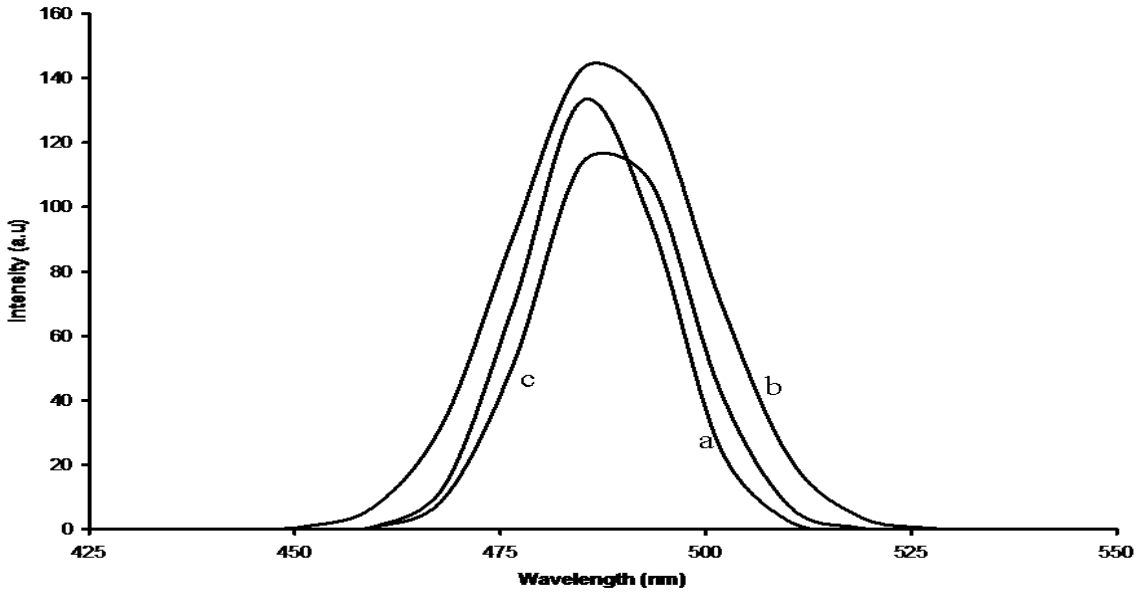

Figure 6.2: Photoluminescence spectra of CdS nanoparticles capped by glucuronic acid (a), glucose (b) and sucrose (c) synthesized from cadmium chloride and tetramethylthiuram monosulfide.

The absorption and pholuminescence spectra of Co_xS_y nanoparticles capped by glucuronic acid (a), glucose (b) and sucrose (c) synthesized from cobalt chloride and tetramethylthiuram monosulfide at 160 ^oC for 1 h, dispersed in de-ionized water, are shown in Figures 6.3 and 6.4. The absorption spectra, which are strongly blue shifted to the bulk Co_xS_y band edge, have broad shoulders appearing at 395 nm for glucuronic acid, glucose and sucrose-capped Co_xS_y nanoparticles. The broad shoulders are indicative of particles that are not of the same size (not monodispersed) or have aggregated. The band edge of all the absorption spectra is located at approximately 438 nm, corresponding to an energy band gap of 2.83 eV. The broad emission spectra are red shifted to their as-prepared absorption spectra, with the maximum peaks of Co_xS_y nanoparticles capped by glucuronic acid and glucose positioned at approximately 444 nm, while the one for sucrose-capped Co_xS_y nanoparticles has shifted to higher wavelength by 5 nm.

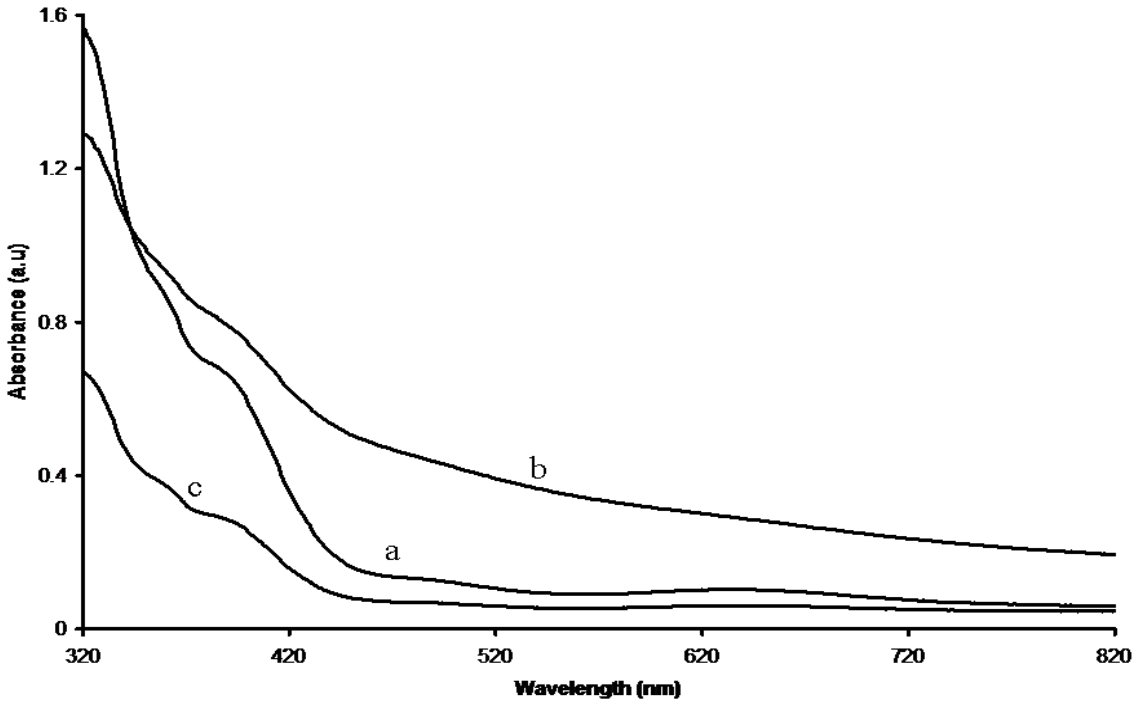

Figure 6.3: Absoption spectra of Co_xS_y nanoparticles capped by glucuronic acid (a) glucose (b) and sucrose (c) synthesized from cobalt chloride and tetramethylthiuram monosulfide.

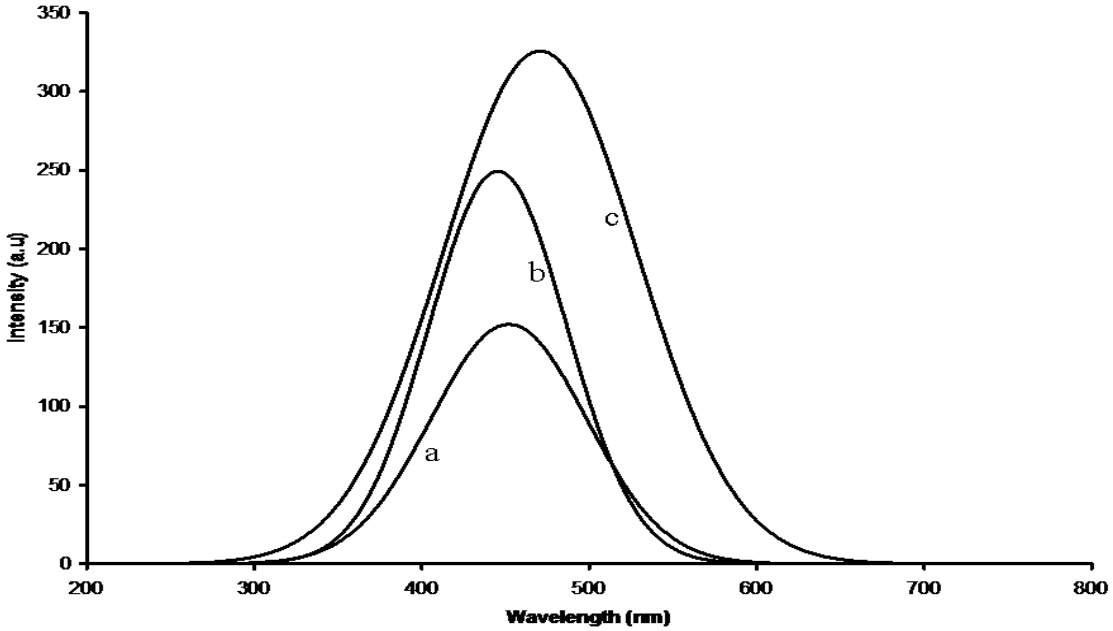

Figure 6.4: Photoluminescence spectra of Co_xS_y nanoparticles capped by glucuronic acid (a), glucose (b) and sucrose (c) synthesized from cobalt chloride and tetramethylthiuram monosulfide.

Figure 6.5 shows the absorption spectra of ZnS nanoparticles capped by glucuronic acid (a), glucose (b) and sucrose (c), respectively. All the spectra appear at lower wavelength, that is, higher energy as compared to the bulk ZnS which simply termed as blue shift. This is an indication of small particles size. The increase in the band gap with decrease in the crystallite size is attributed to size quantum effects. The band edge of the as-prepared ZnS nanoparticles capped by glucuronic acid, glucose and sucrose appears at approximately 343 nm (3.62 eV), which is lower in wavelength as compared to the bulk ZnS which has a band edge of 350 nm (3.54 eV). The photoluminescence/emission spectra of ZnS nanoparticles capped by glucuronic acid (a), glucose (b) and sucrose (c) synthesized from zinc chloride and tetramethylthiuram monosulfide at 160 ^oC for an hour are shown in Figure 6.6. The emission spectra, which are red shifted to their as-prepared absorption spectra, are positioned at approximately 447 nm (2.77 eV). The emission spectrum of sucrose-capped ZnS nanoparticles revealed some broadness as compared to glucuronic acid and glucose-capped ZnS nanoparticles. However, all the photoluminescence spectra are broad signifying that the particles are not well capped, which might lead to aggregation of particles.

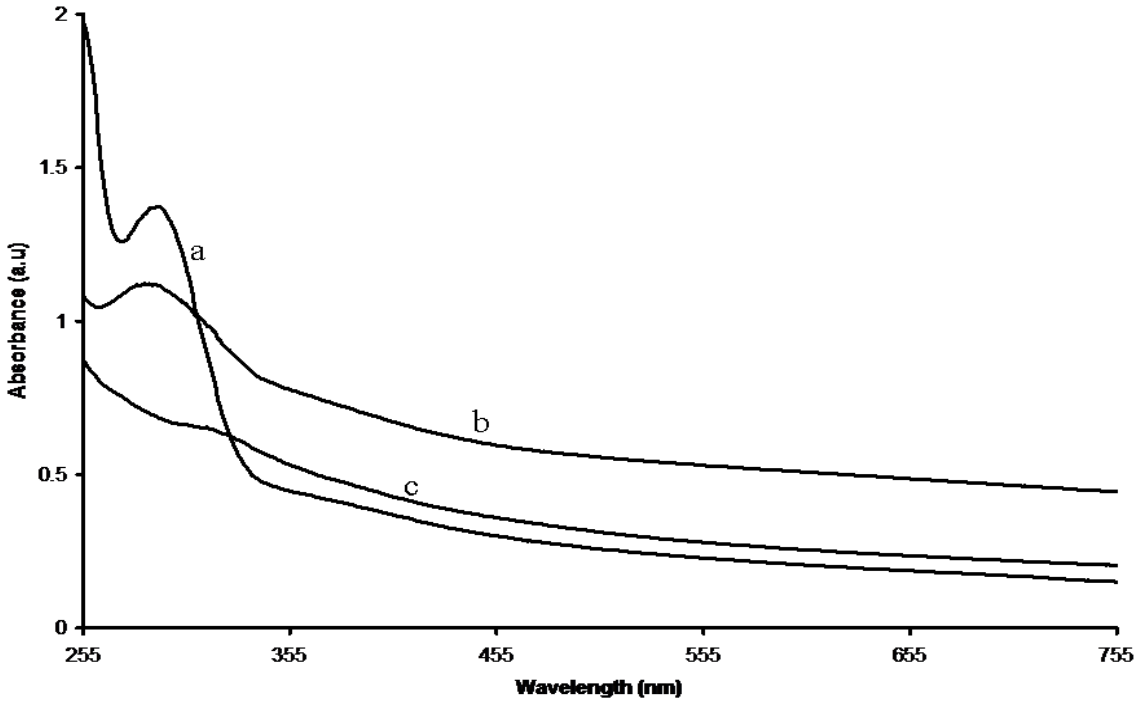

Figure 6.5: Absorption spectra of ZnS nanoparticles capped by (a) glucuronic acid, (b) glucose, and (c) sucrose zinc chloride and tetramethylthiuram monosulfide.

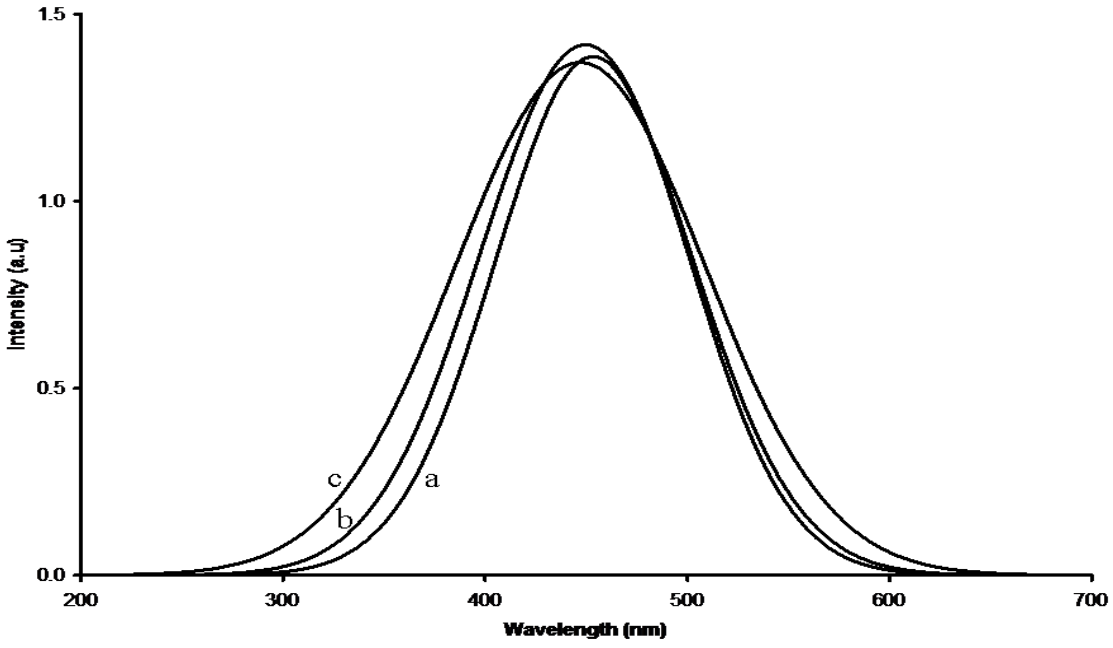

Figure 6.6: Photoluminescence spectra of ZnS nanoparticles capped by glucuronic acid (a), glucose (b) and sucrose (c) zinc chloride and tetramethylthiuram monosulfide.

(b) Structural properties

The TEM images of CdS nanoparticles synthesized by chemical reaction method from cadmium chloride and tetramethylthiuram monosulfide at 160 ^{o}C are shown in Figure 6.7. The stability of the nanoparticles was achieved by employing the ligands glucuronic acid (a), glucose (b) and sucrose (c) as capping agents. The images revealed some agglomeration of uniformly distributed close-to-spherical cadmium sulphide nanoparticles, with an average diameter of 4.3 nm. The reason for the agglometaion of the particles is probably due to their small size and high surface energy. Small particles will aggregate to form large particles due to nucleation effect.

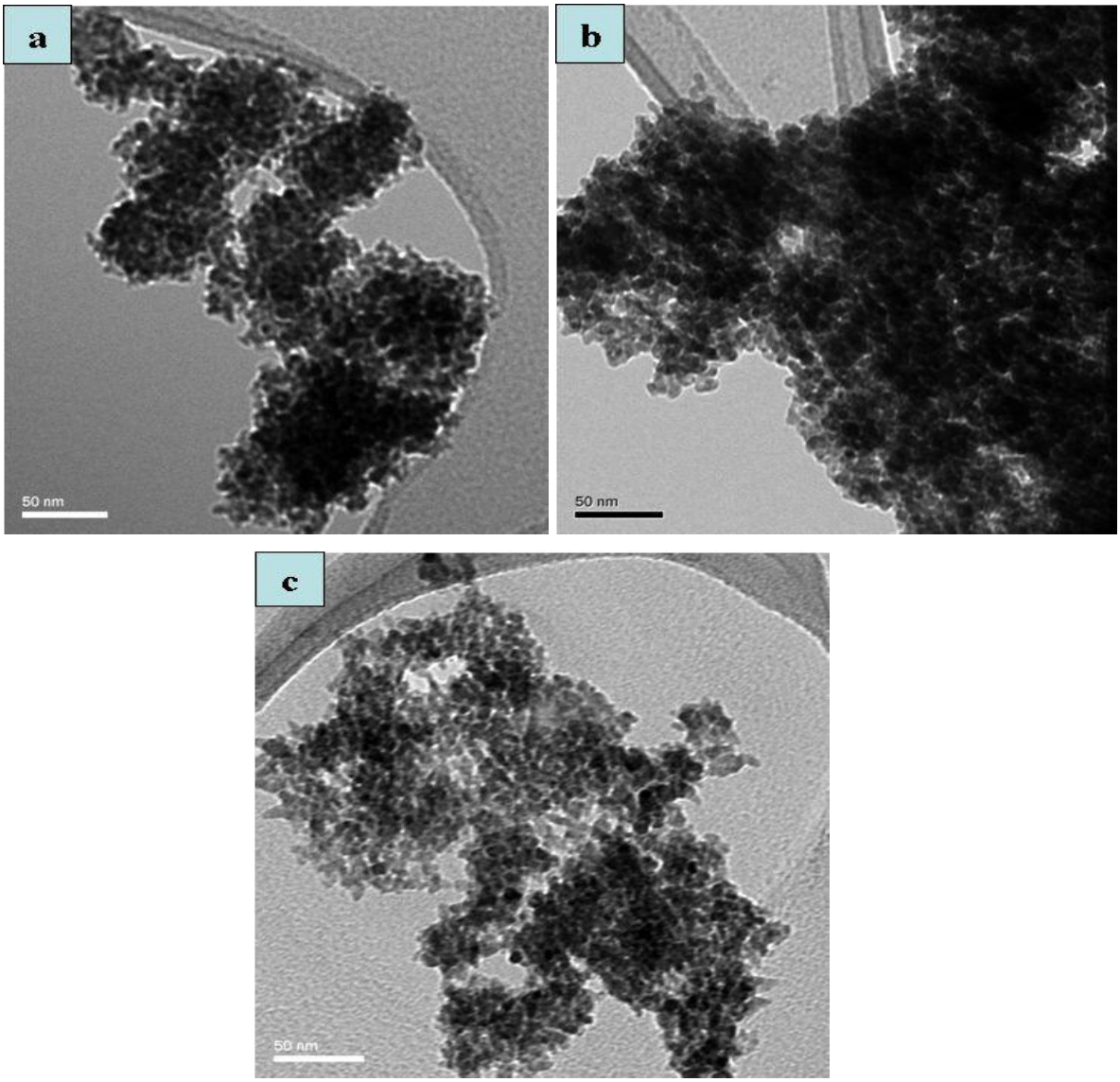

Figure 6.7: TEM images of CdS nanoparticles capped by glucuronic acid (a), glucose (b) and sucrose (c) synthesized from cadmium chloride and tetramethylthiuram monosulfide.

Bulk CdS usually exixts in the hexagonal phase from room temperature to melting point [21]. However, CdS nanocrystals can exist as either cubic or hexagonal phase. Figure 6.8 shows the XRD pattern of CdS nanoparticles capped by sucrose. The CdS diffraction pattern obtained for the powder sample shows broad peaks typical of particles in nanosize regime. The XRD pattern is consistent with predominantly the hexagonal phase [22]. The (002), (110), (103) and (112) planes of wurtzite CdS, positioned at 2θ values of 26.8^{o}, 44.1^{o}, 48.1^{o} and 52.2^{o} are clearly distinguishable in the pattern [JCPDS file no. 41-1049]. The (103) reflection is characteristic of hexagonal CdS. A very strong peak is observed for reflections from (002) plane, while the (102) peak is very weak. This is characteristic of stacking fault along the (002) direction [23]. Similar results were observed when other capping agents such as glucuronic acid and glucose were employed in the preparation of CdS nanoparticles under similar conditions.

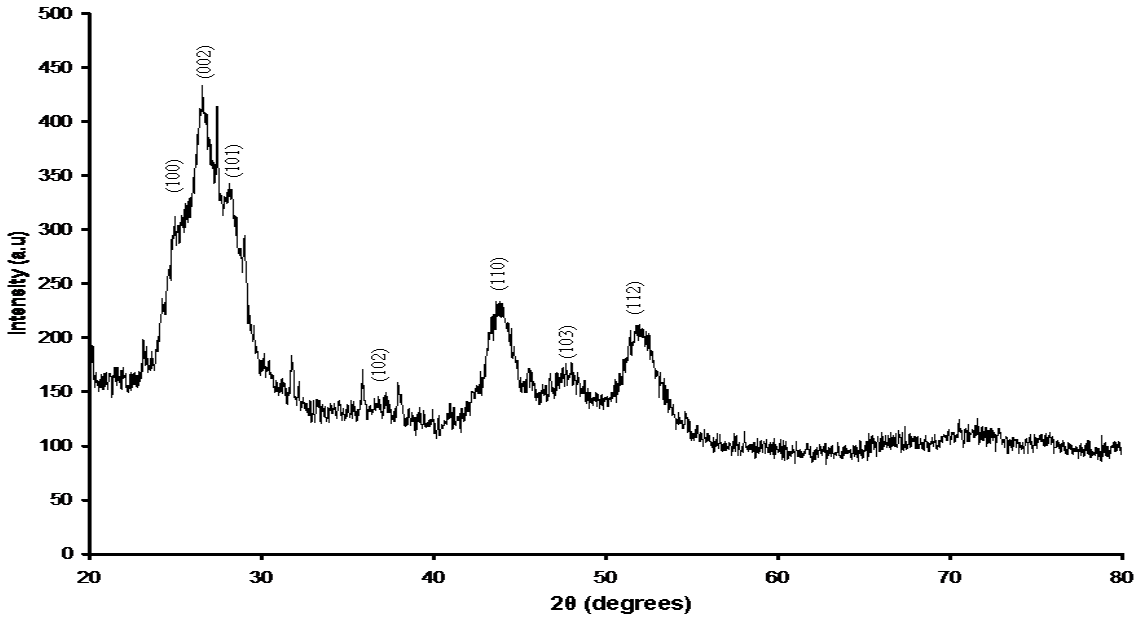

Figure 6.8: XRD pattern of CdS nanoparticles capped by sucrose synthesized from cadmium chloride and tetramethylthiuram monosulfide.

The TEM images of Co_xS_y nanoparticles capped by glucuronic acid (a), glucose (c) and sucrose (d) are shown in Figure 6.9. The particles were grown from cobalt chloride and tetramethylthiuram monosulfide at 160 ^{o}C for an hour. The morphology of the particles revealed spherical-like-shaped Co_xS_y nanoparticles capped by glcuronic acid, glucose and sucrose. The histogram of particle size distribution for Co_xS_y nanoparticles capped by glucuronic acid (Figure 6.9b) is also shown with an average diameter of 4.3 nm. The Co_xS_y

nanoparticles capped by glucose and sucrose revealed signs of aggregation. The XRD pattern of Co_xS_y nanoparticles capped by sucrose is shown in Figure 6.10. The presented XRD pattern revealed no significant peaks showing that the as-prepared cobalt sulphide powder was amorphous. The XRD patterns of the same material capped by glucuronic acid and glucose (not shown), also did not present obvious peaks for cobalt sulphide nanoparticles. The amorphous nature of cobalt sulphide nanoparticles is in agreement with the work reported by Yuan *et al.* [24] who synthesized nanosized amorphous cobalt sulphide by means of the H_2O/CS_2 interface under hydrothermal treatment at 70 ^oC for 48 h.

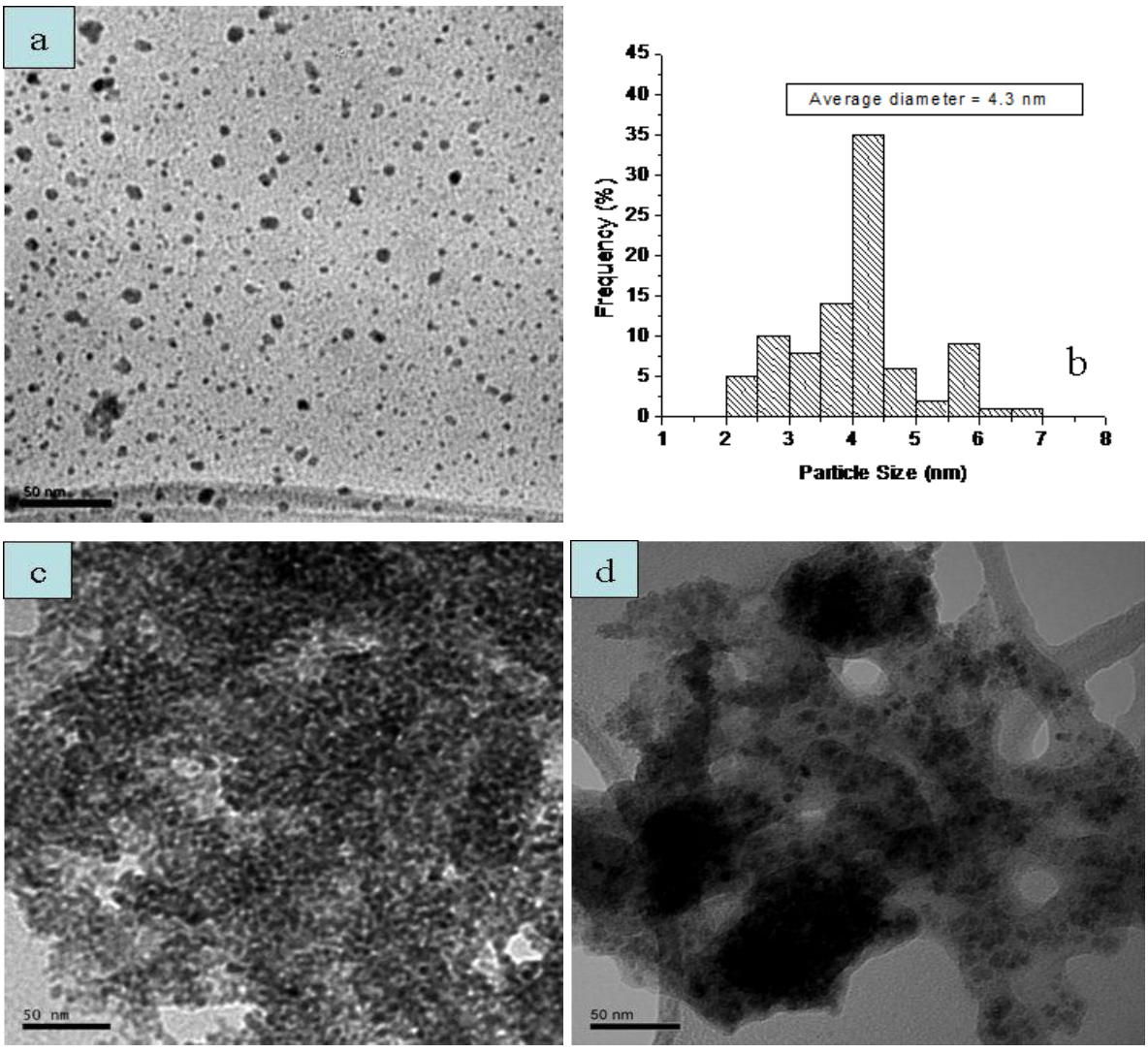

Figure 6.9: TEM images of Co_xS_y nanoparticles capped by glucuronic acid (a), glucose (c) and sucrose (d) synthesized from cobalt chloride and tetramethylthiuram monosulfide, and the corresponding size distribution histogram for Co_xS_y nanoparticles capped by glucuronic acid (b).

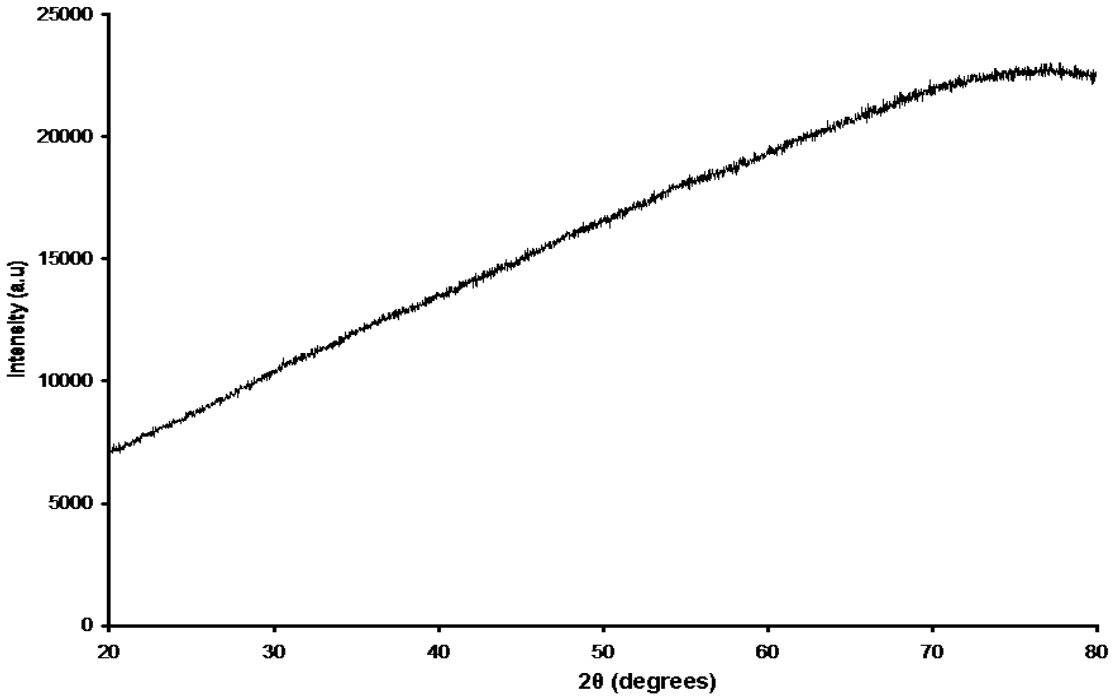

Figure 6.10: XRD pattern of Co_xS_y nanoparticles capped by glucuronic acid (a), glucose (b), and sucrose (c) synthesized from cobalt chloride and tetramethylthiuram monosulfide.

Figure 6.11 shows the TEM images of ZnS nanoparticles capped by glucuronic acid (a), glucose (c), and sucrose (e) synthesized from zinc chloride and tetramthylthiuram monosulfide. The histograms of particle size distriburion for ZnS capped by glucuronic acid (b), glucose (d) and sucrose (f) with an average diameter of 3.9 nm (a), 4.7 nm (b) and 4.4 nm (c), respectively, are also shown in Figure 6.11. The morphology of the particles depicted in the TEM images is spherical. The typical X-ray diffraction (XRD) patterns of ZnS capped by glucuronic acid (a) and sucrose (b) synthesized from zinc chloride and tetramethylthiuram monosulfide are shown in Figure 6.12. The broad peaks observed at 28.9^o, 48.6^o and 57.3^o degree of 2θ for ZnS capped by glucuronic acid are identified to cubic zinc blende (111), (220) and (311) diffraction peaks, whereas the broad peaks for ZnS capped by sucrose can be indexed to hexagonal phase 28.8^o (002), 39.6^o (102), 48.1^o (110), 52.2^o (103) and 56.7^o (112). These observed broad diffraction peaks suggest that the products are composed of the nanocrystals. The XRD studies (Figure 6.12b) of ZnS structures indicated that the diffraction peaks of (100) and (101) were overlapped with (002) diffraction because of widening, which resulted from the small crystallite size. Similar phase, which s hexagonal, was obtained for glucose-capped ZnS nanoparticles (not shown). The characteristic peaks marked with asterisks are due to the impurities.

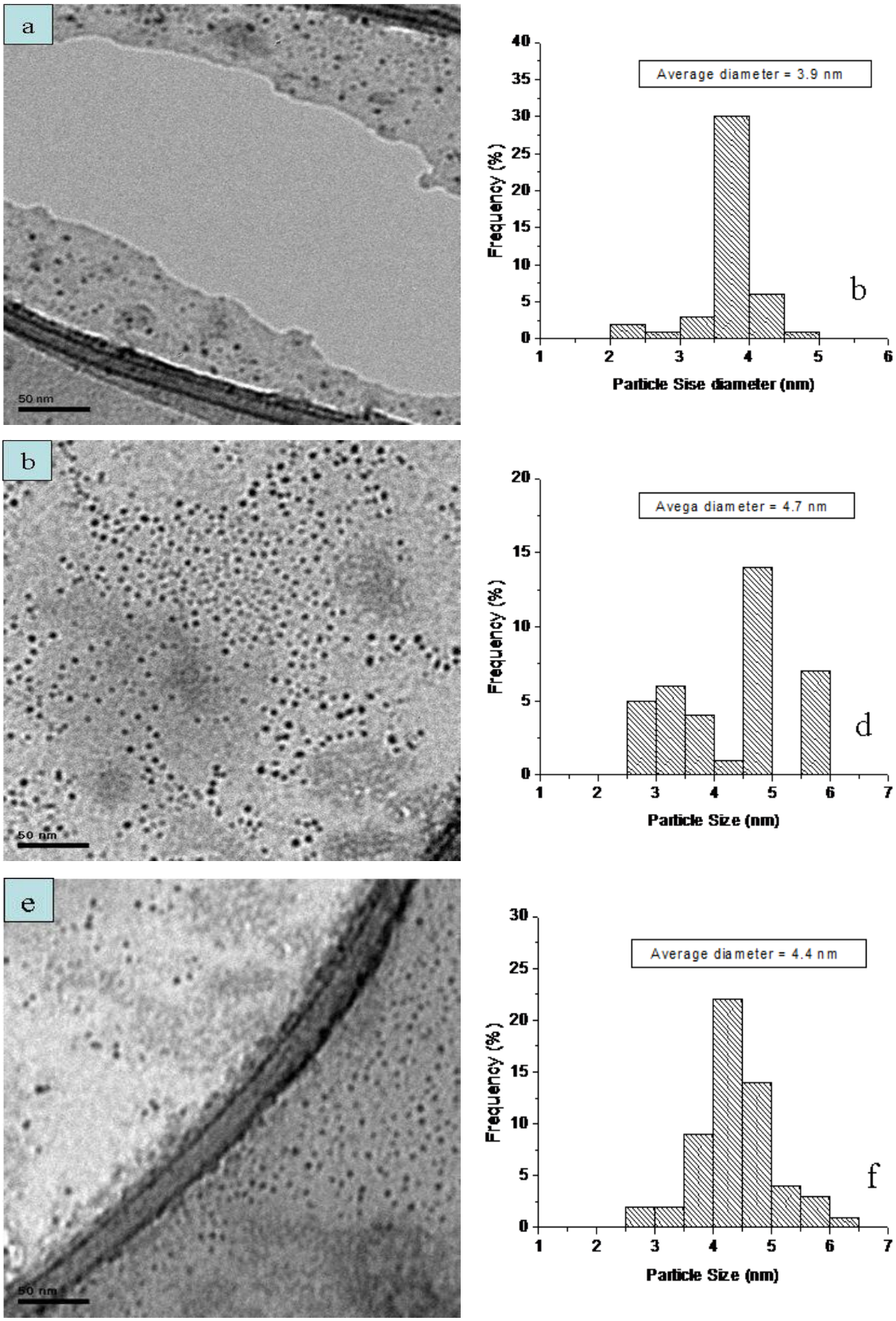

Figure 6.11: TEM images of ZnS nanoparticles capped by glucuronic acid (a), glucose (c) and sucrose (e) synthesized from zinc chloride and tetramethylthiuram monosulfide, and their corresponding size distriburion histograms (b, d, f).

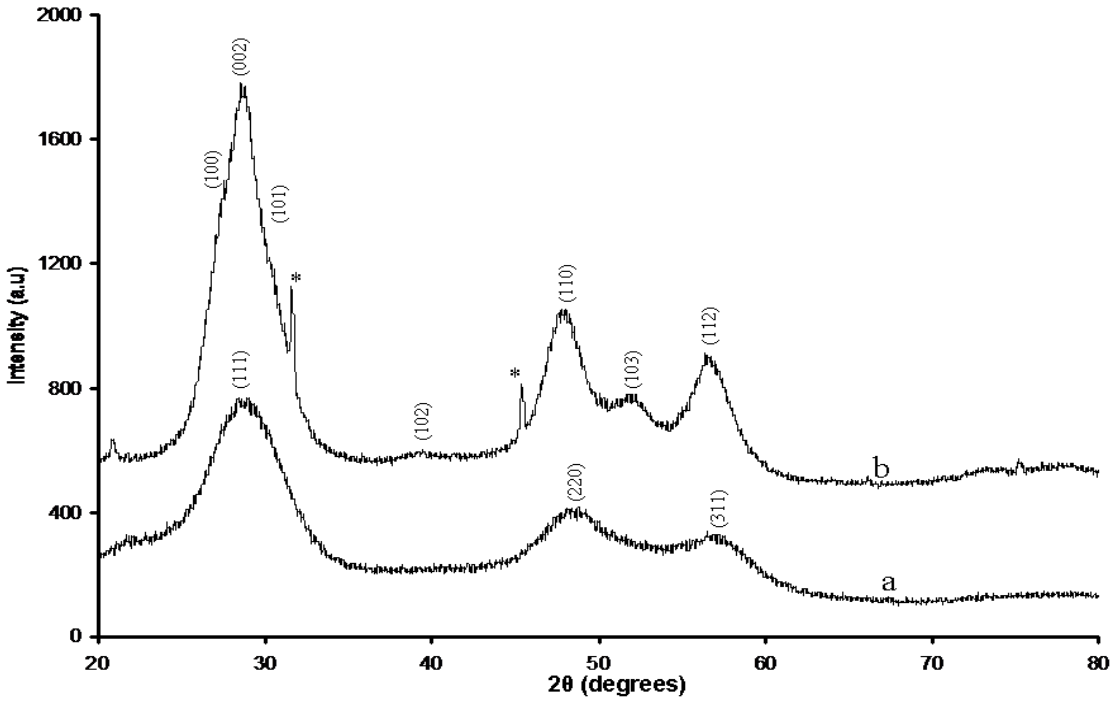

Figure 6.12: XRD patterns of ZnS nanoparticles capped by glucuronic acid (a) and sucrose (b) synthesized from zinc chloride and tetramethylthiuram monosulfide.

6.2.1.2 Sugars-capped CdS, Co_xS_y and ZnS nanoparticles from cadmium chloride, cobalt chloride and zinc chloride, and dimethylthiourea

(a) Optical properties

The absorption spectra of CdS nanoparticles capped by glucuronic acid (a), glucose (b) and sucrose (c) synthesized from cadmium chloride hydrate and dimethylthiourea at 160 ^{o}C are shown in Figure 6.13. The absorption spectra are blue shifted to the bulk CdS band edge. The band edges of CdS nanoparticles capped by glucuronic acid and glucose appear approximately at 486 nm and 482 nm, respectively. The absorption spectrum of CdS nanoparticles capped by sucrose (Figure 6.13c) shows a broad shoulder as compared to CdS nanoparticles capped by glucuronic acid and glucose, with an excitonic peak positioned at 456 nm. This implies that particles are not well distributed, with some signs of aggregation. All the spectra were characterized by dissolving a minimum amount of the solid material in de-ionised water. The photoluminescence spectra (Figure 6.14) of CdS nanoparticles capped by glucuronic acid (a), glucose (b) and sucrose (c) are red shifted to their as-prepared absorption spectra, with maximum emission peaks for CdS nanoparticles capped

by glucuronic acid and glucose positioned approximately at 494 nm. The photoluminescence spectrum of CdS nanoparticles capped by sucrose depicts emission maximum that is very close to the band edge.

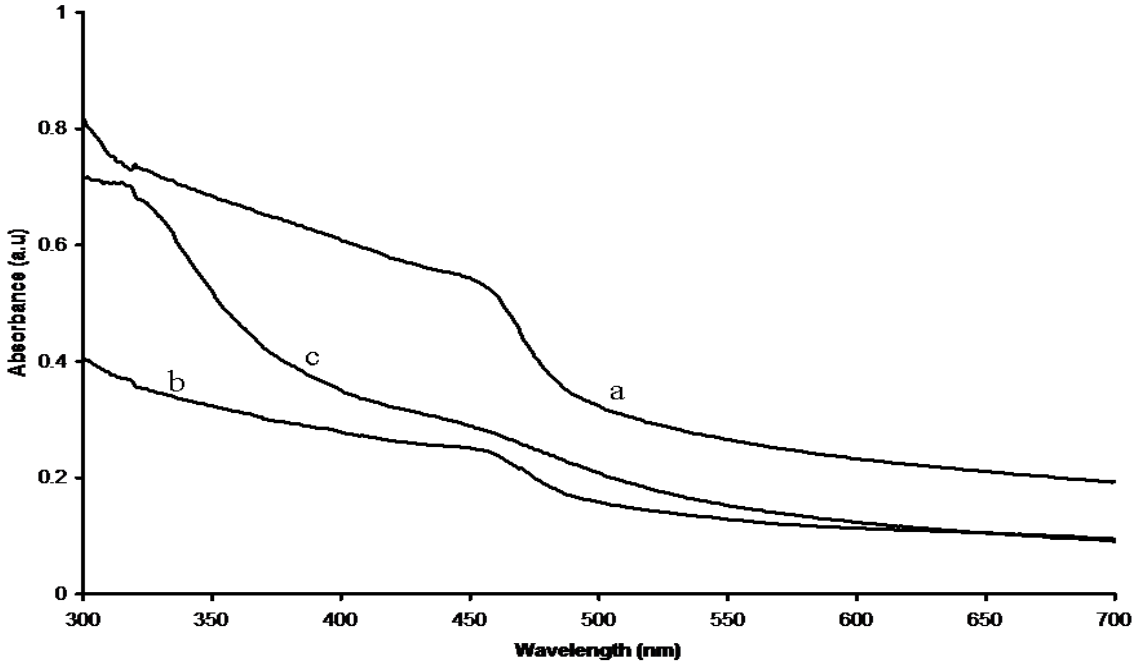

Figure 6.13: Absorption spectra of CdS nanoparticles capped by glucuronic acid (a), glucose (b) and sucrose (c) synthesized from cadmium chloride and dimethylthiourea.

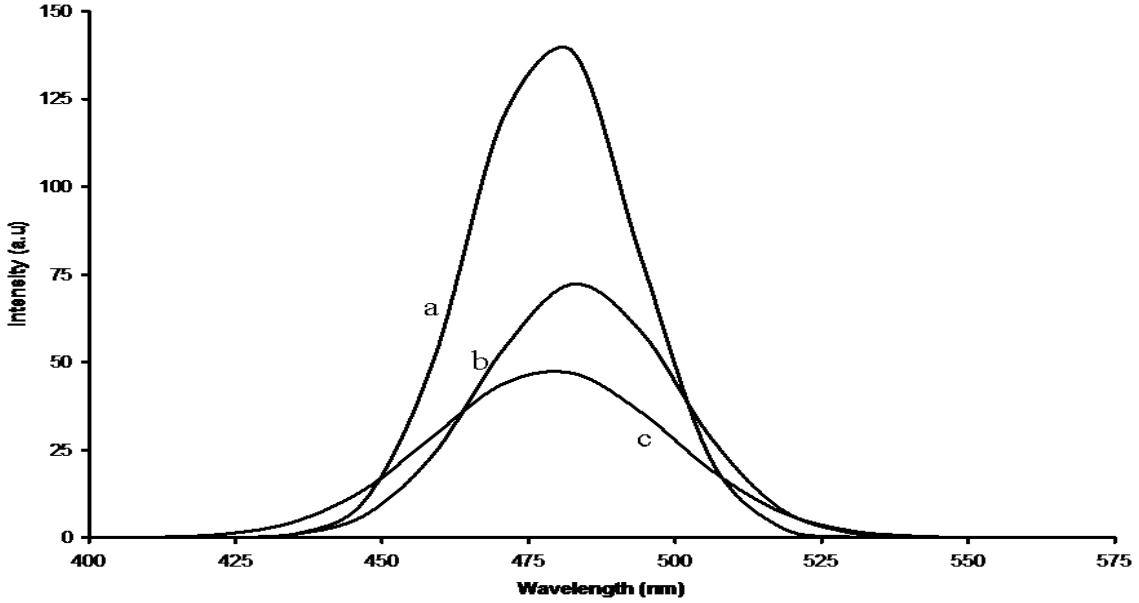

Figure 6.14: Photoluminescence spectra of CdS nanoparticles capped by glucuronic acid (a), glucose (b) and sucrose (c) synthesized from cadmium chloride and dimethylthiourea.

The absorption spectra of Co_xS_y nanoparticles dispersed in de-ionized water are shown in Figure 6.15. The particles, which were synthesized from cobalt chloride and dimethylthiourea at 160 ^oC for an hour, are capped by glucuronic acid (a), glucose (b), and sucrose (c) to prevent agglomeration. The spectra are almost similar, with a broad shoulders appearing approximately at 373 nm. The broad size distribution of the nanoparticles is responsible for the absence of sharp excitonic peaks in these samples. The blue shift of the absorption peaks signifies smaller size of the particles. The band edge of these absorption spectra is at 393 nm, which corresponds to 3.16 eV. The photoluminescence spectra, which are red shifted to their as-prepared absorption spectra, are shown in Figure 6.16. Their emission maximum peaks are positioned at approximately 411 nm.

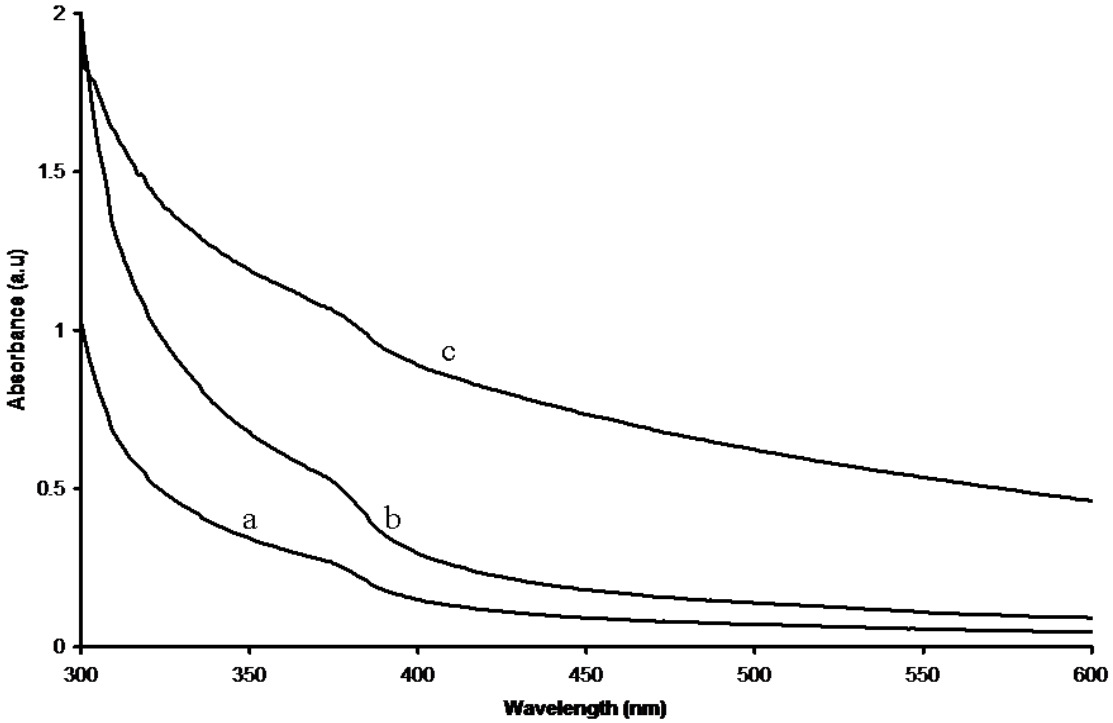

Figure 6.15: Absorption spectra of Co_xS_y nanoparticles capped by glucuronic acid (a), glucose (b), and sucrose (c) synthesized from cobalt chloride and dimethylthiourea.

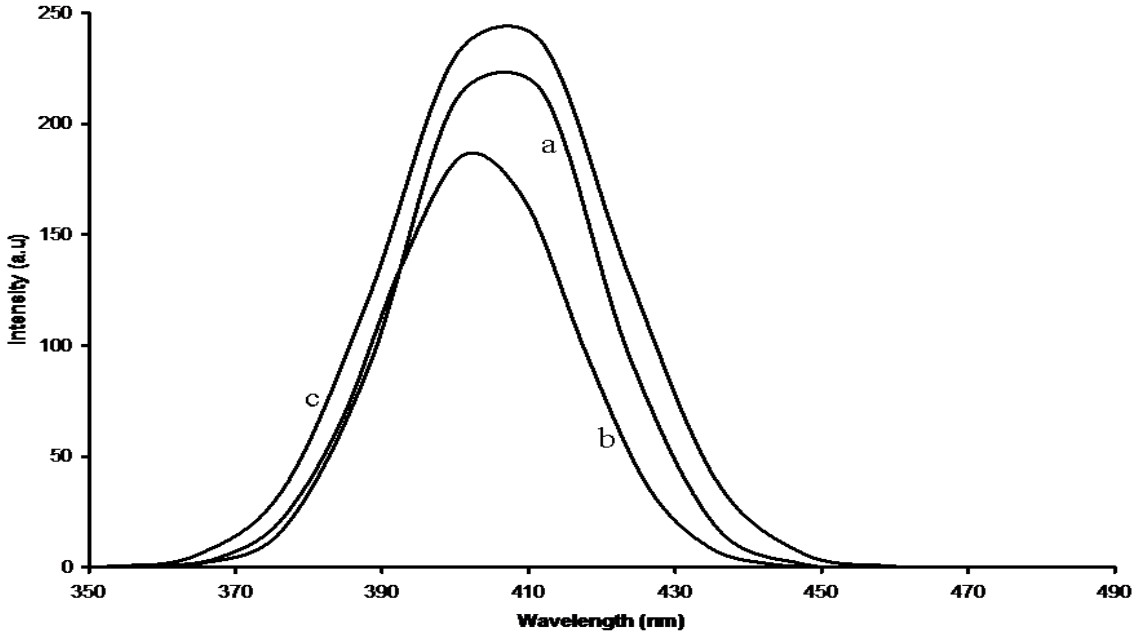

Figure 6.16: Photoluminescence spectra of Co_xS_y nanoparticles capped by glucuronic acid (a), glucose (b), and sucrose (c) synthesized from cobalt chloride and dimethylthiourea.

The absorption spectra of ZnS nanoparticles capped by glucuronic acid (a), glucose (b) and sucrose (c) are shown in Figure 6.17. The particles were grown at 160 ^{o}C for an hour. The spectra, which are blue shifted to bulk ZnS, have an absorption peaks appearing at approximately 263 nm. Their band edges were estimated to appear at approximately 292 nm (4.25 eV), 295 nm (4.20 eV) and 304 nm (4.08 eV), for ZnS nanoparticles capped by glucuronic acid, glucose and sucrose, respectively. The photoluminescence spectra of ZnS nanoparticles capped by glucuronic acid (a), glucose (b) and sucrose (c) are shown in Figure 6.18. Characterization was achieved by dispersing the particles in de-ionized water. All spectra are far red shifted to their as-synthesized absorption spectra. Their emission maximum peaks are positioned at 392 nm, 409 nm and 418 nm, respectively. Different absorption band edges and maximum emission peaks signify different particles size or shape.

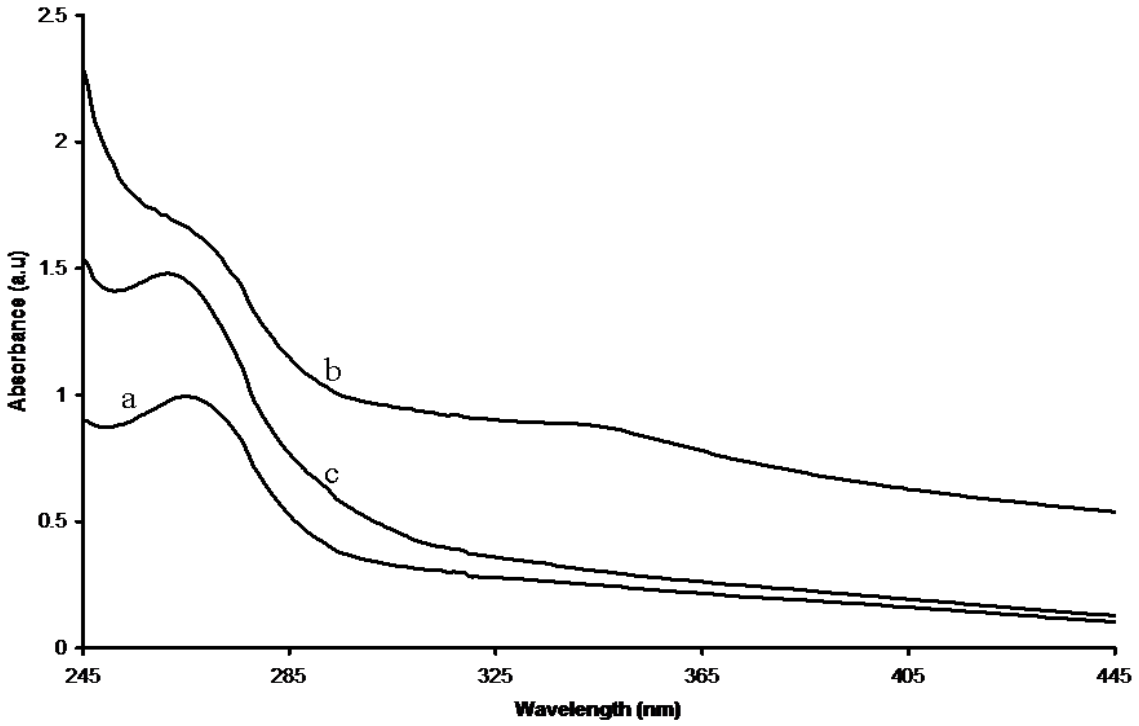

Figure 6.17: Absorption spectra of ZnS nanoparticles capped by glucuronic acid (a), glucose (b) and sucrose (c) synthesized from $ZnCl_2$ and dimethylthiourea.

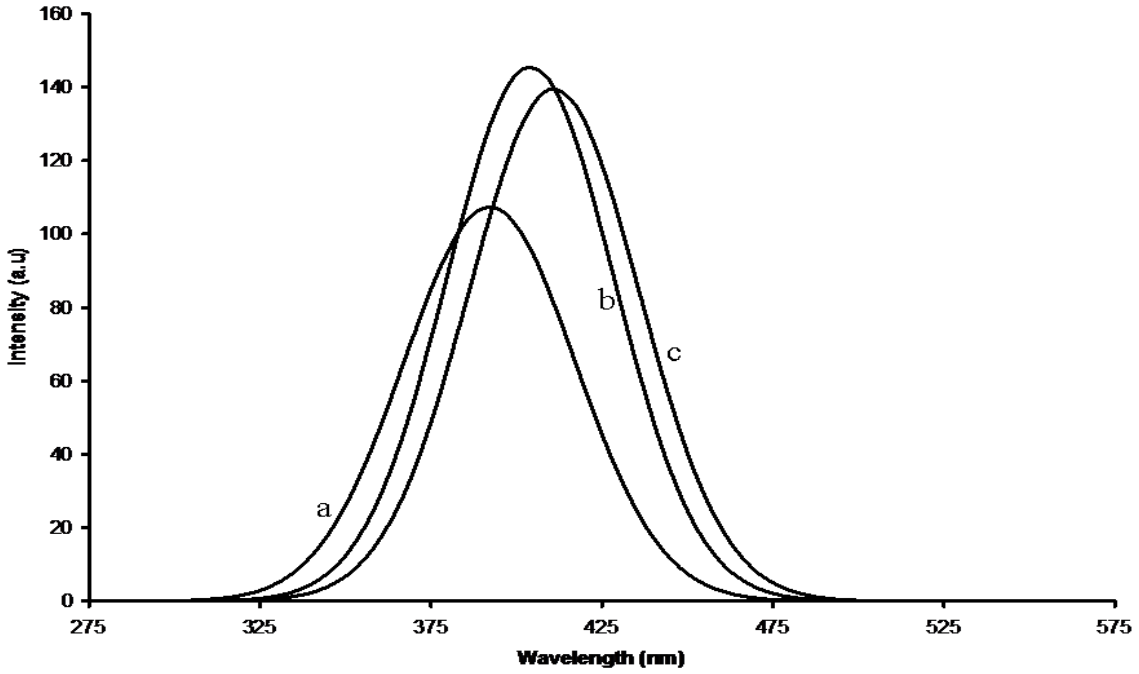

Figure 6.18: Photoluminescence spectra of ZnS nanoparticles capped by glucuronic acid (a), glucose (b) and sucrose (c) synthesized from $ZnCl_2$ and dimethylthiourea.

(b) Structural properties

Figure 6.19 shows TEM images of CdS nanoparticles capped by glucuronic acid (a), glucose (b) and sucrose (c). Particles were grown from cadmium chloride and dimethylthiourea at 160 ^{o}C for an hour. The TEM image of CdS nanoparticles capped by glucuronic acid (Figure 6.19a) revealed some signs of small cubic shaped particles with an average diameter of 5.5 nm. In the case of CdS nanoparticles capped by glucose (Figure 6.19b) and sucrose (Figure 6.19c), close-to-spherical particles were obtained, with average diameters of the particles measured to be 4.6 nm and 4.9 nm, respectively. However, it is also imperative to mention that all images are dominated by aggregation of particles which is due to nucleation effect, where small particles aggregates to form bigger particles. The typical XRD pattern of CdS nanoparticles capped by glucuronic acid synthesized from cadmium chloride and tetramethylthiuram monosulfide at 120 ^{o}C for an hour is shown in Figure 6.20. The broad peaks observed at 28.6^{o}, 48.0^{o} and 56.7^{o} degree of 2θ, are identified to be hexagonal (002), (102), (110), (103) and (112) diffraction peaks of CdS nanoparticles. The XRD pattern exhibits the remarkable broad feature, which is a quite similar diffraction patterns of CdS nanoparticles capped by glucose and sucrose (not shown) synthesized using similar conditions, but different capping agents. The combination of finite size and defect broadening results in a convolution of peaks in the X-ray diffraction spectra giving rise to very broad peaks [25].

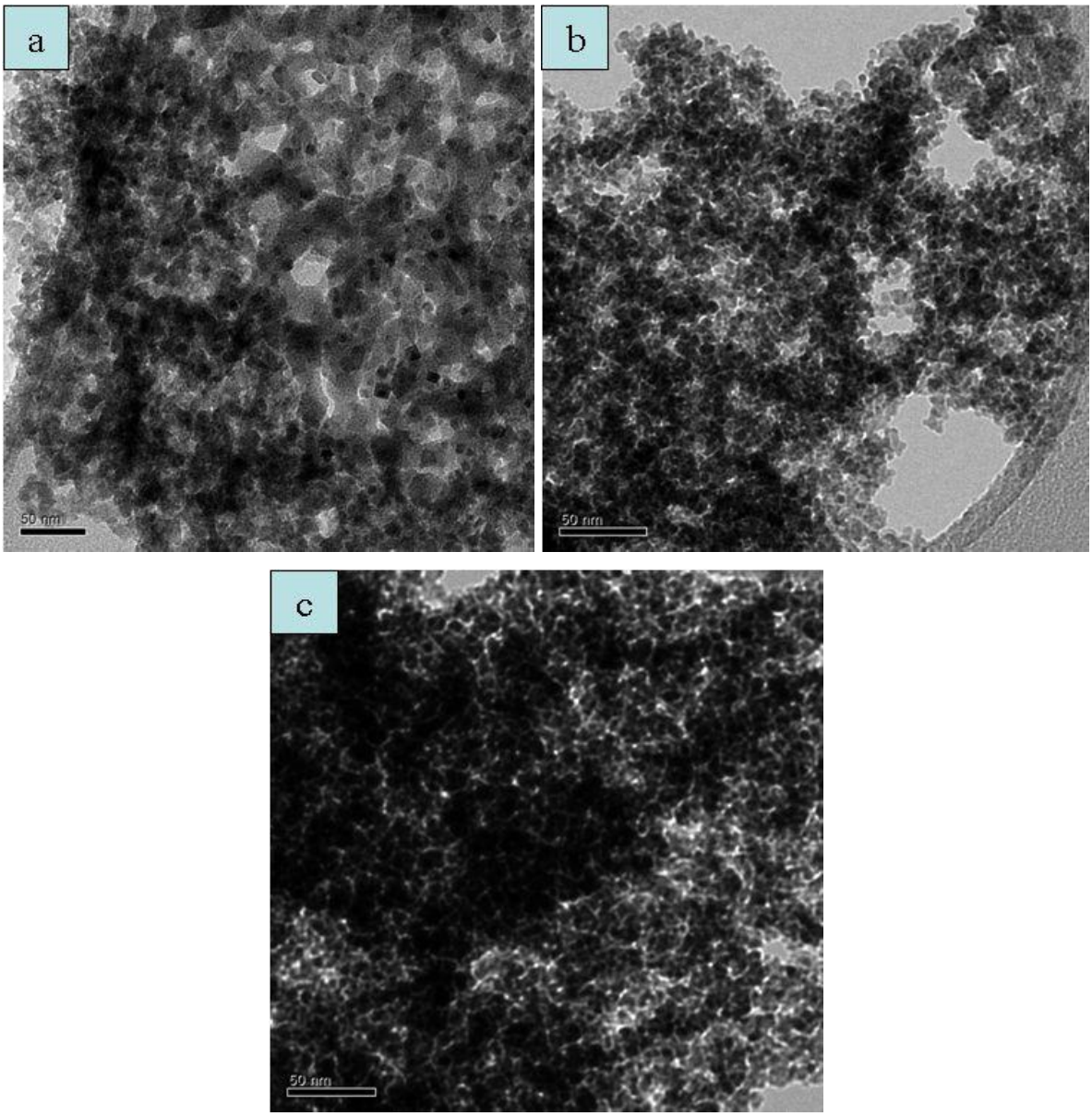

Figure 6.19: TEM images of CdS nanoparticles capped by glucuronic acid (a), glucose (b) and sucrose (c) synthesized from cadmium chloride and dimethylthiourea.

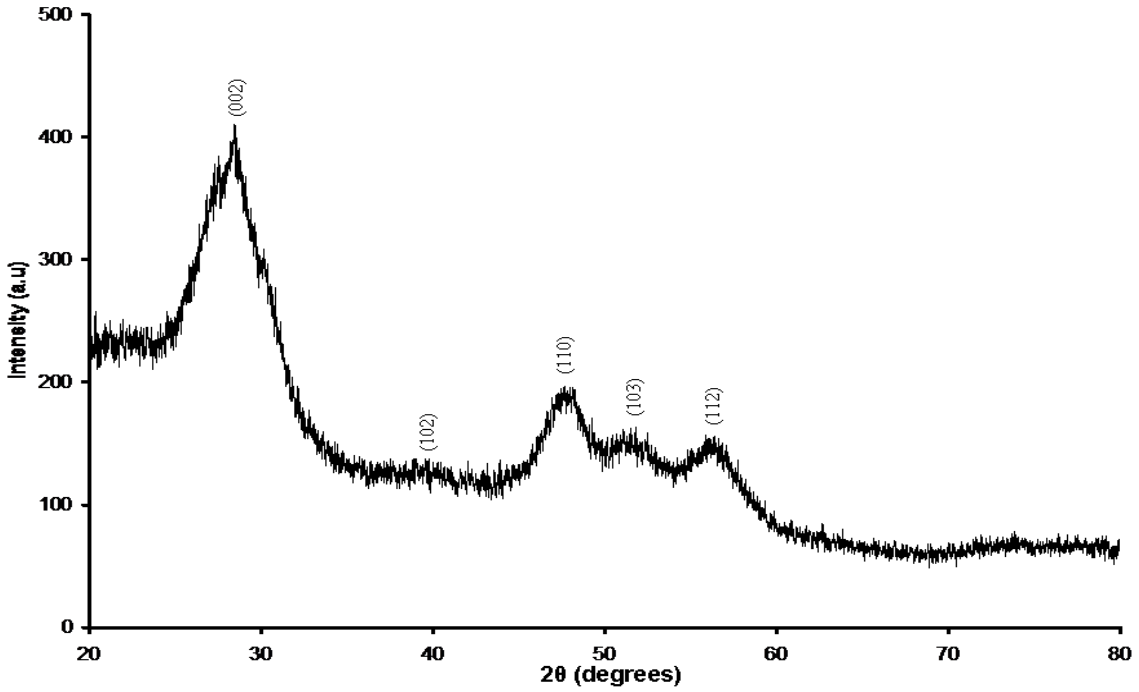

Figure 6.20: XRD pattern of CdS nanoparticles capped by glucuronic acid synthesized from cadmium chloride and dimethylthiourea.

Figure 6.21 shows the TEM images of Co_xS_y nanoparticles capped by glucuronic acid (a), glucose (b) and sucrose (c). The particles were synthesized from cobalt chloride as the metal precursor and dimethylthiourea which was used as the sulphur precursor. Particles were grown at 160 ^oC for a maximum of an hour. All images show particles that are cubic in shape, sitting on top of each other forming a sheet. The particles arrangement made it difficult to detect the diameter. However, there are also some signs of small spherical particles (Figure 6.21a), with an average diameter of 3.0 nm. From the XRD pattern of Co_xS_y nanoparticles capped by glucuronic acid synthesized from cobalt chloride and dimethylthiourea, no sign of significant peaks were observed when the material was subjected to XRD instrument. The introduction of other sugars (glucose and sucrose) as capping agents did not yield any different results. Amorphous nature was still revealed. The as-synthesized cobalt sulphide powder demonstrated amorphous nature. Similar results were reported by Yuan *et al*. [24] in their preparation of cobalt sulphide nanoparticles using cobalt acetate and carbon disulphide as the precursors.

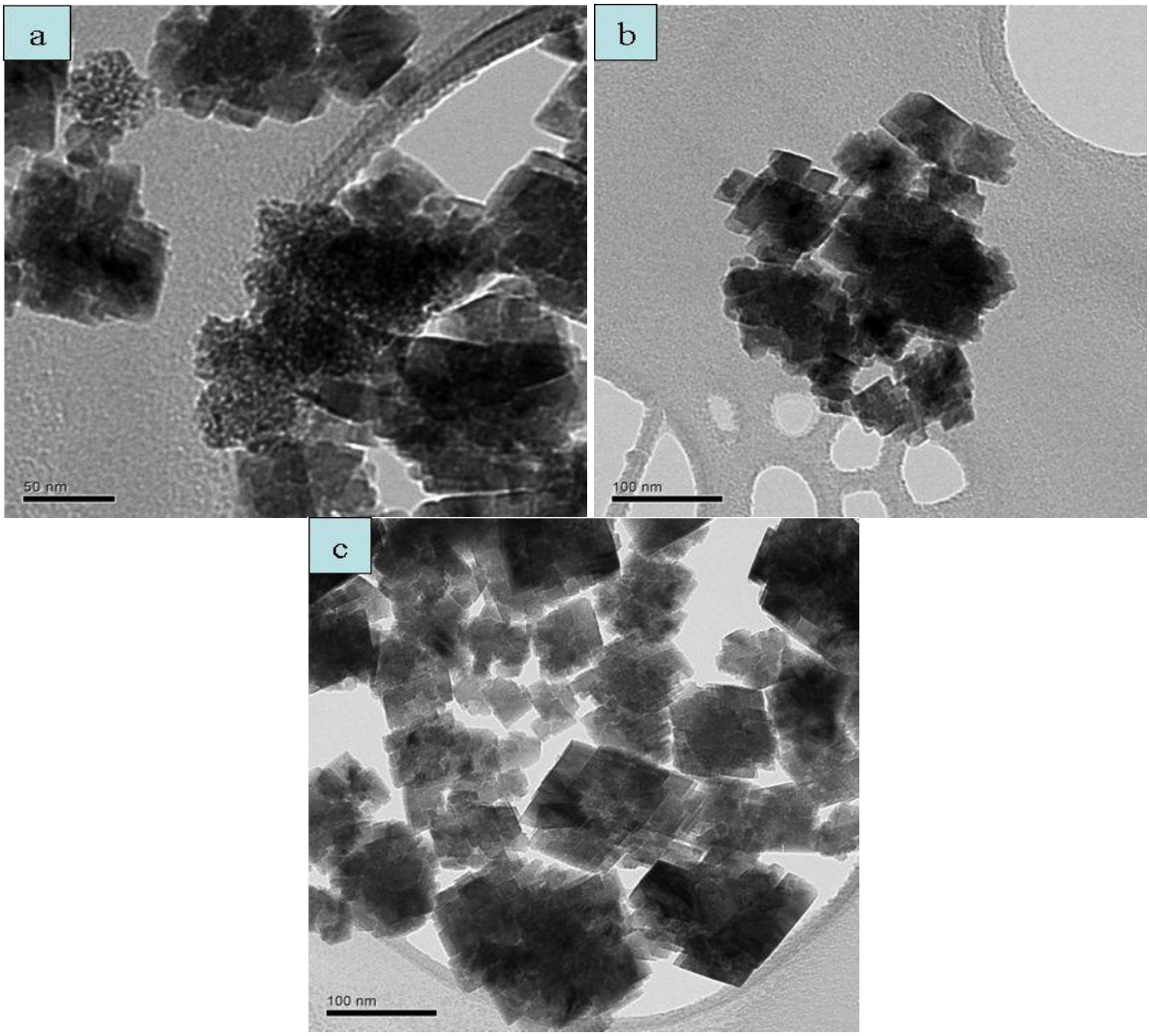

Figure 6.21: TEM images of Co_xS_y nanoparticles capped by glucuronic acid (a), glucose (b) and sucrose (c) synthesized from cobalt chloride and dimethylthiourea.

The TEM images of ZnS nanoparticles capped by glucuronic acid (a), glucose (b) and sucrose (d) synthesized from zinc chloride and dimethylthiourea, together with the histograms of particle size of ZnS capped by glucose (c) and sucrose (e) are shown in Figure 6.22. The particles were grown at 160 ^oC for an hour. The TEM image of ZnS nanoparticles (Figure 6.23a), showed an irregular morphology. Due to particles that did not reveal well defined shape, the diameter of the particles was not recorded. The morphology of the particles observed when ZnS nanoparticles were capped by glucose and sucrose is spherical-like-shaped with an average diameter of 9.9 nm (b) and 11.6 nm (c), respectively. Figure 6.24 shows the XRD pattern of ZnS nanoparticles capped by glucuronic synthesized from zinc chloride and dimethylthiourea at 120 ^oC for an hour. It is interesting to find that the peaks are broad which signify finite size of the particles. The observed broad peaks can

be indexed to hexagonal phase, with 2θ values positioned at 31.8^{o} (100), 34.4^{o} (002), 36.3^{o} (101), 47.6^{o} (102), 56.6^{o} (110), 62.7^{o} (103) and 67.9^{o} (112). The patterns of ZnS nanoparticles capped by glucose and sucrose also depicted hexagonal phase.

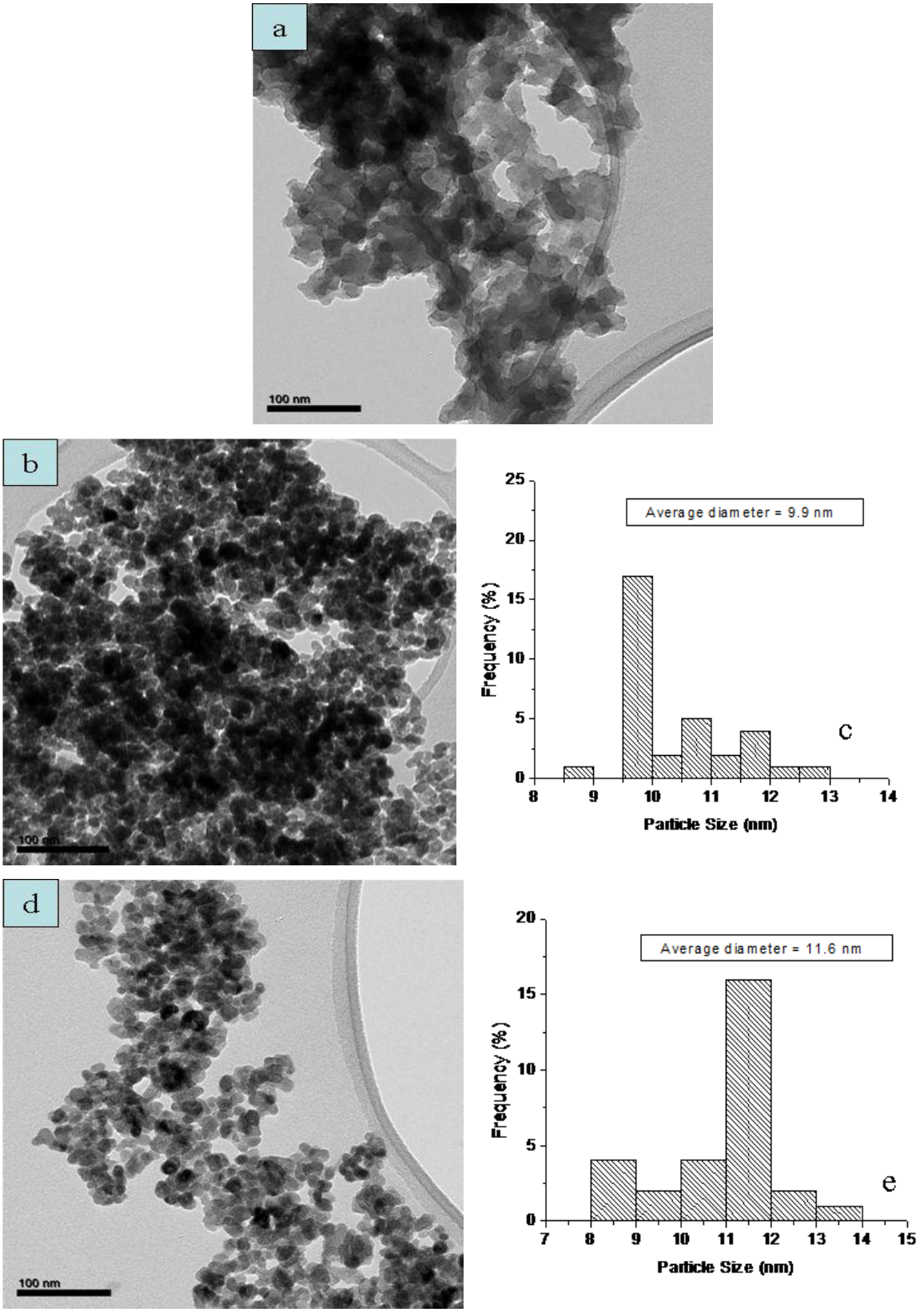

Figure 6.22: TEM images of ZnS nanoparticles capped by glucuronic acid (a), glucose (b) and sucrose (d) synthesized from $ZnCl_2$ and dimethylthiourea, and their corresponding size distribution histograms (c, e).

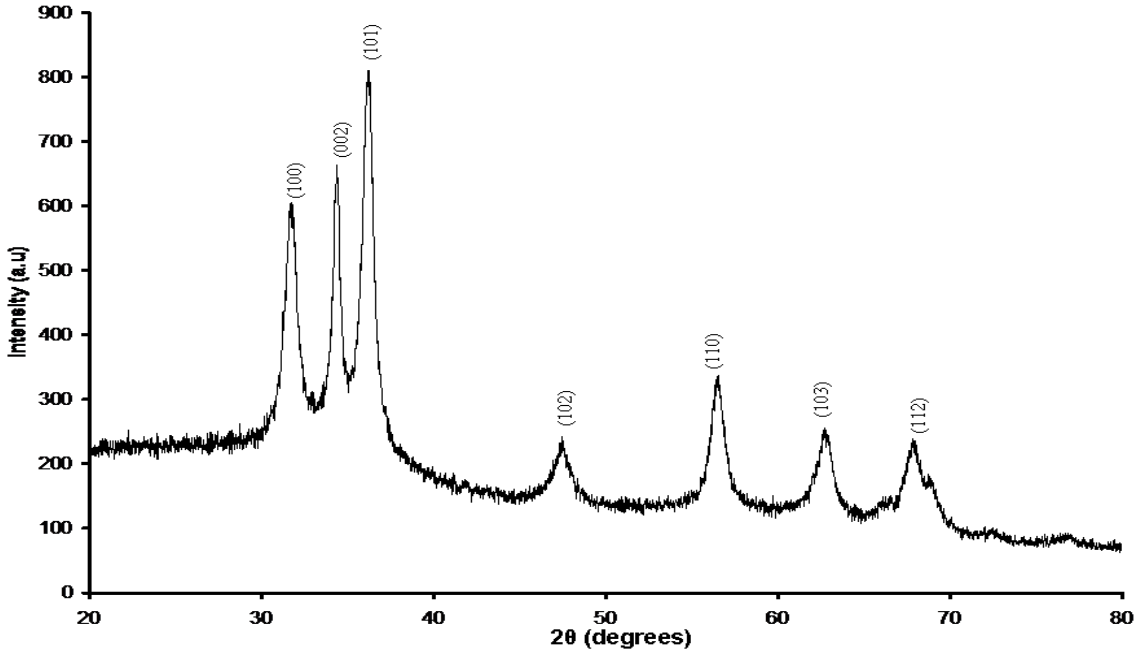

Figure 6.23: XRD pattern of ZnS nanoparticles capped by glucuronic acid synthesized from $ZnCl_2$ and dimethylthiourea.

6.2.1.3 Sugars-capped CdS nanoparticles from cadmium chloride, cobalt chloride and zinc chloride and methylthiourea

(a) Optical properties

Figure 6.24 shows the absorption spectra of CdS nanoparticles capped by glucuronic acid (a), glucose (b) and sucrose (c). The particles were grown from cadmium chloride and 1-methyl-2-thiourea at 160 ^{o}C for an hour. The absorption spectra of CdS nanoparticles capped by glucuronic acid and sucrose reveal a band edge appearing almost at the same region. The estimated band edge is positioned at 436 nm (2.84 eV). However, a difference was observed when glucose was the capping agent, with an absorption broad shoulder appearing. The excitonic peak for CdS nanoparticles capped by glucose appearing at 399 nm (3.11 eV) was observed. All spectra, which appear almost at the same region, have a blue shift of 79 nm as compared to the bulk CdS material. The photoluminescence spectra of CdS nanoparticles capped by glucuronic acid (a), glucose (b) and sucrose (c) are shown in Figure 6.25. The photoluminescence spectra show broad emission due to the wide distribution of particle sizes. The emission maxima are very close to the band edges.

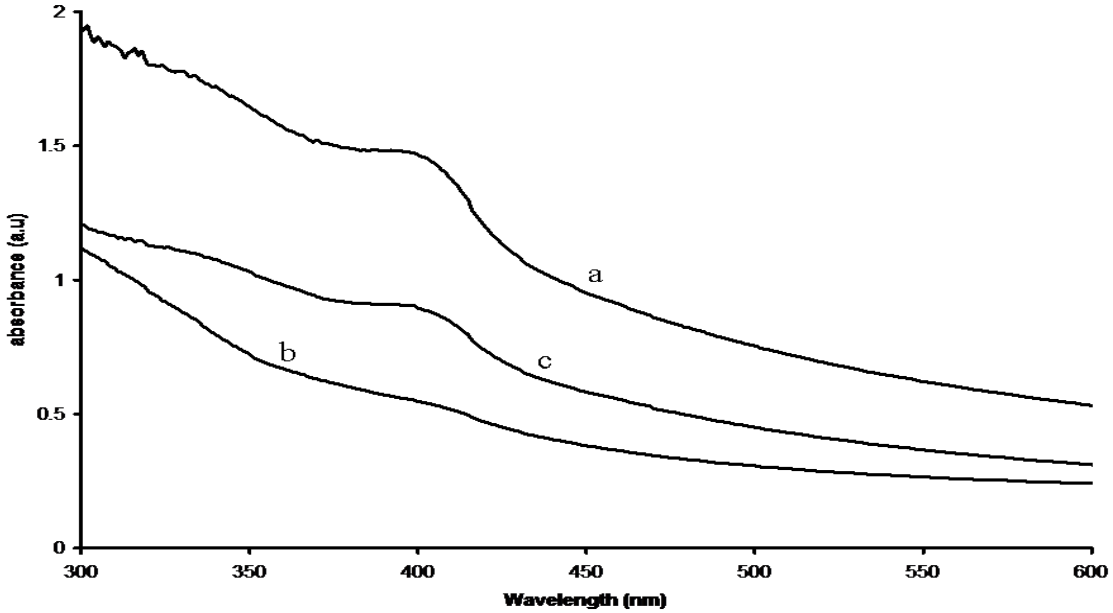

Figure 6.24: Absorption spectra of CdS nanoparticles capped by glucuronic acid (a), glucose (b) and sucrose (c) synthesized from cadmium chloride and 1-methyl-2-thiourea.

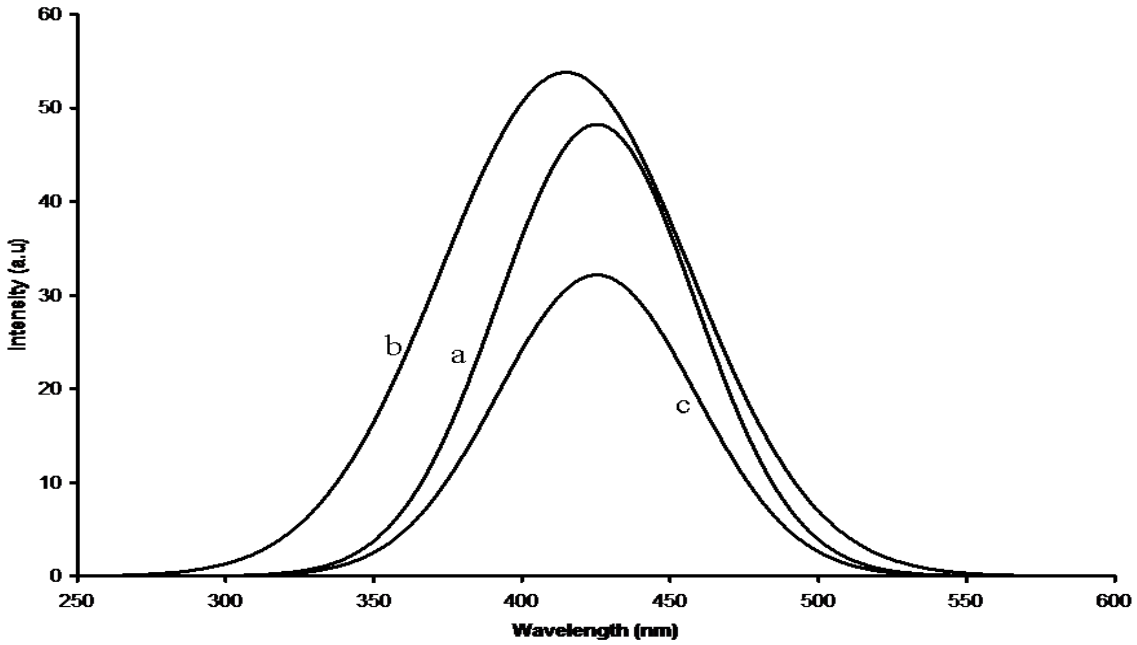

Figure 6.25: Photoluminescence spectra of CdS nanoparticles capped by glucuronic acid (a), glucose (b) and sucrose (c) synthesized from cadmium chloride and 1-methyl-2-thiourea.

Figures 6.26 and 6.27 show the absorption and photoluminescence spectra of Co_xS_y nanoparticles dispersed in de-ionized water, respectively. The particles were synthesized

from cobalt chloride and 1-methyl-2-thiourea at 160 ^{o}C for an hour, with glucuronic acid (a), glucose (b) and sucrose (c) being used as capping agents. All the absorption peaks are strongly blue-shifted (263 nm) indicating smaller size of particles. The spectra have a band edge of 304 nm (4.08 eV), which is lower compared to bulk Co_xS_y band edge of 1078 nm (1.15 eV). The photoluminescence spectra are red shifted to their as-prepared Co_xS_y nanoparticles absorption spectra with maximum emission peaks positioned at approximately 342 nm, which corresponds to 3.15 eV.

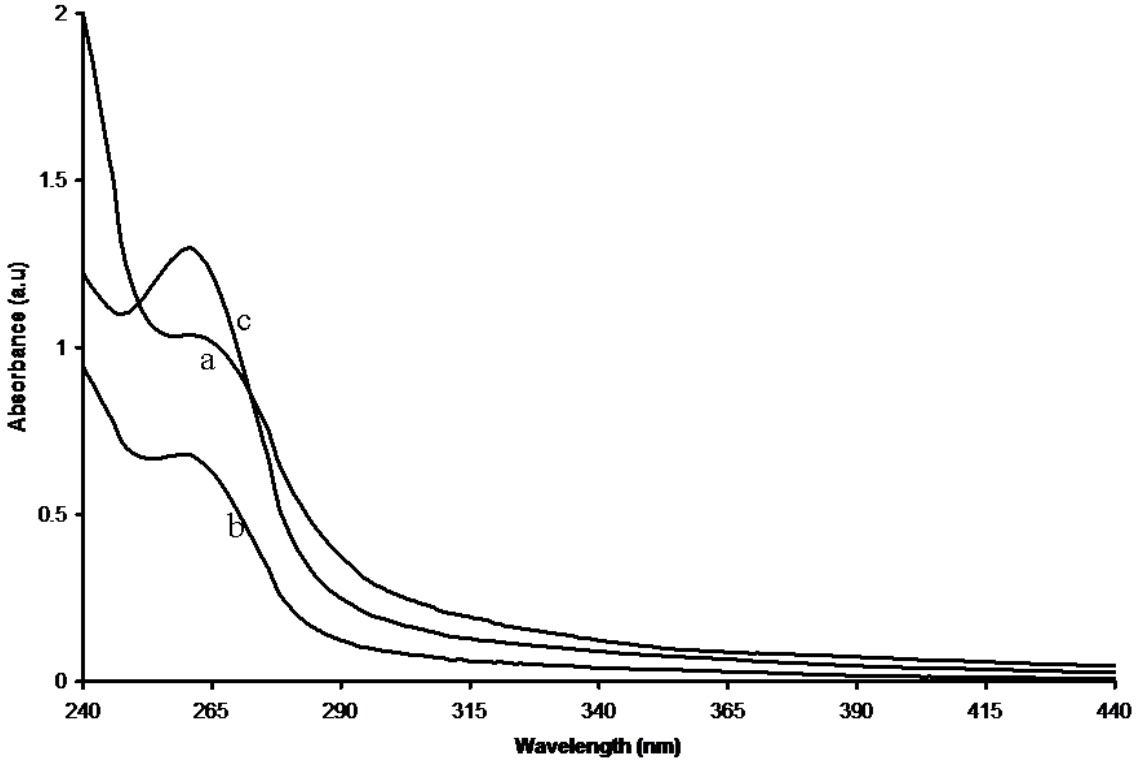

Figure 6.26: Absorption spectra of Co_xS_y nanoparticles capped by glucuronic acid (a), glucose (b), and sucrose (c) synthesized from cobalt chloride and 1-methyl-2-thiourea.

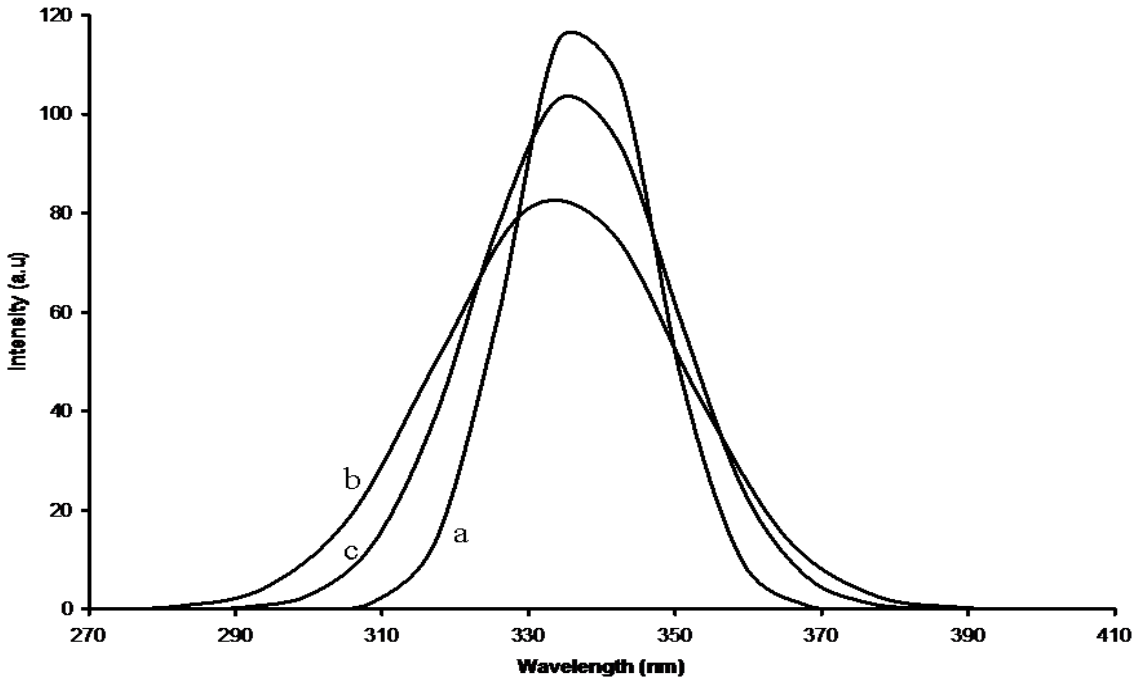

Figure 6.27: Photoluminescence spectra of Co_xS_y nanoparticles capped by glucuronic acid (a), glucose (b), and sucrose (c) synthesized from cobalt chloride and 1-methyl-2-thiourea.

The absorption and photoluminesce spectra of ZnS nanoparticles capped by glucuronic acid (a), glucose (b) and sucrose (c) synthesized from $ZnCl_2$ and 1-methyl-2-thiourea at 160 ^oC for an hour are shown in Figures 6.28 and 6.29. The blue shifted spectra have absorption peaks appearing at approximately 261 nm (4.75 eV), with a band edge of 289 nm (4.29 eV). The red shifted photoluminescence spectra depict emission maximum peaks positioned at approximately 337 nm, which corresponds to 3.68 eV.

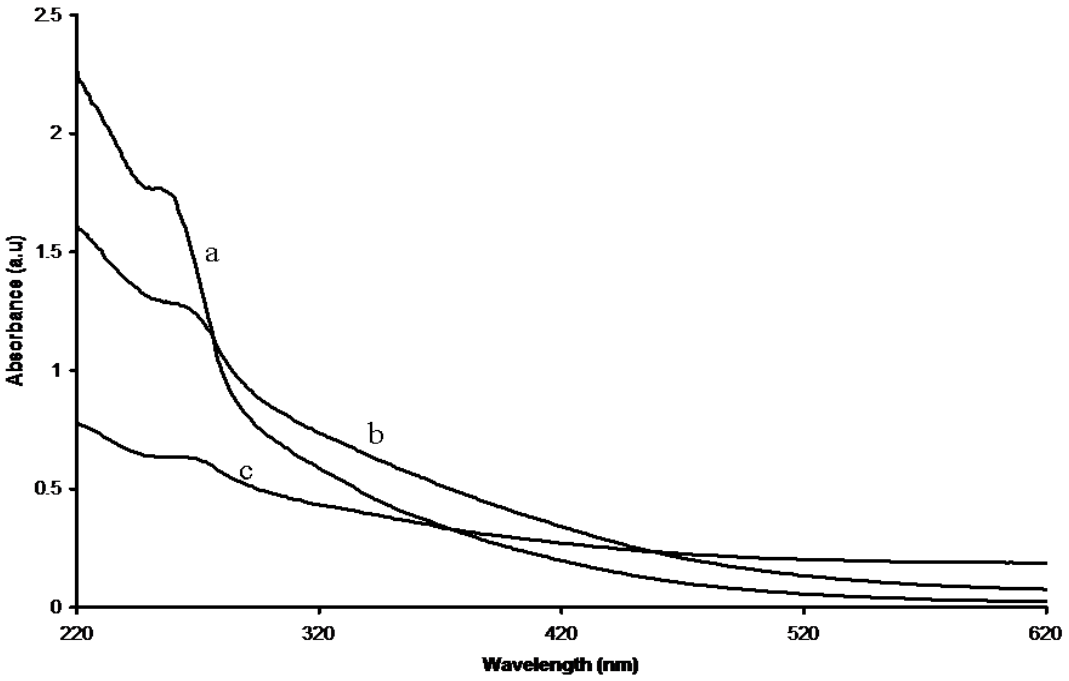

Figure 6.28: Absorption spectra of ZnS nanoparticles capped by glucuronic acid (a), glucose (b) and sucrose (c) synthesized from $ZnCl_2$ and 1-methyl-2-thiourea.

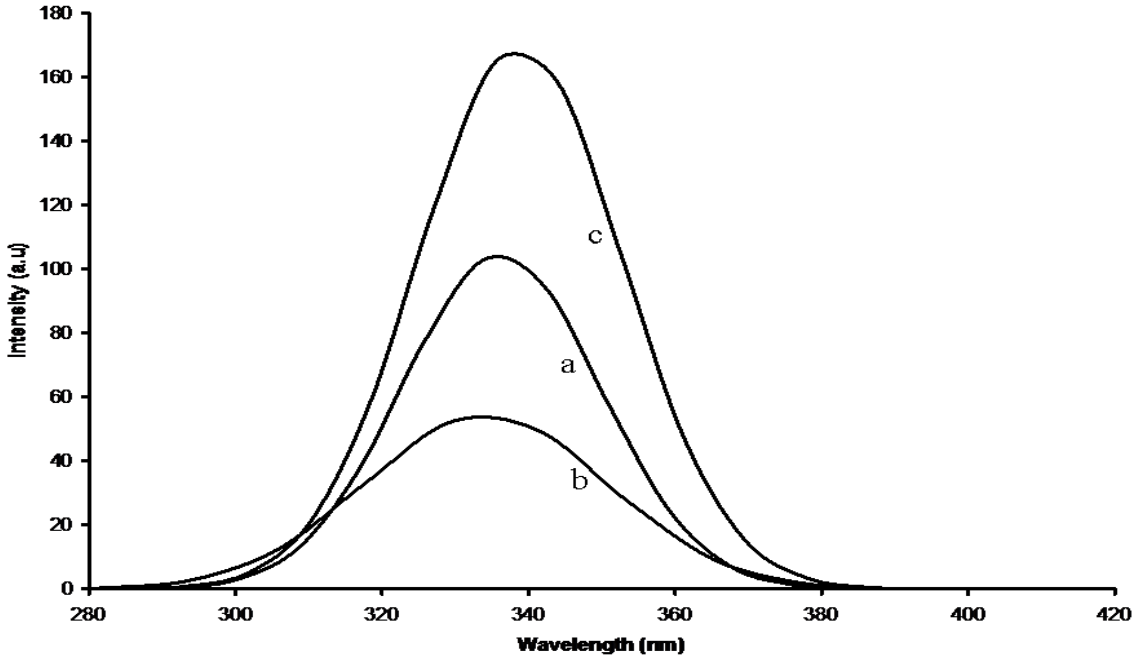

Figure 6.29: Photoluminescence spectra of ZnS nanoparticles capped by glucuronic acid (a), glucose (b) and sucrose (c) synthesized from $ZnCl_2$ and 1-methyl-2-thiourea.

(b) Structural properties

Figure 6.30 shows the TEM images of CdS nanoparticles capped by glucuronic acid (a), glucose (b) and sucrose (c) synthesized from cadmium chloride hydrate and dimethylthiourea. The temperature of the reactions was 160 ^{o}C. The TEM images show some agglomeration of close-to-spherical particles. However, the particles of sucrose-capped CdS (Figure 6.30c) are fused together in the form of a chain. Figure 6.31 shows the XRD patterns of CdS nanoparticles capped by glucuronic acid (a) and sucrose (b). The XRD pattern of CdS nanoparticles capped by glucose was not shown since it revealed similar feature as that of CdS nanoparticles capped by sucrose. The broad peaks of XRD pattern of CdS nanoparticles capped by glucuronic acid can be indexed to cubic phase of CdS, with the 2θ values positioned at 27.1^{o} (111), 44.3^{o} (220) and 51.8^{o} (311). However, when sucrose was used as the capping agent, a change in the phase was observed. Hexagonal phase with the 2θ values positioned at 24.9^{o} (100), 26.6^{o} (002), 28.3^{o} (101), 36.8^{o} (102), 43.8^{o} (110), 48.0^{o} (103) and 51.9^{o} (311) was observed. The change of phase might have been caused by the way the capping agent bound to the surface of the nanoparticles. The glucuronic acid might have bound to the surface of the nanoparticles through the carboxylic acid group, while sucrose and glucose might have used hydroxyl groups.

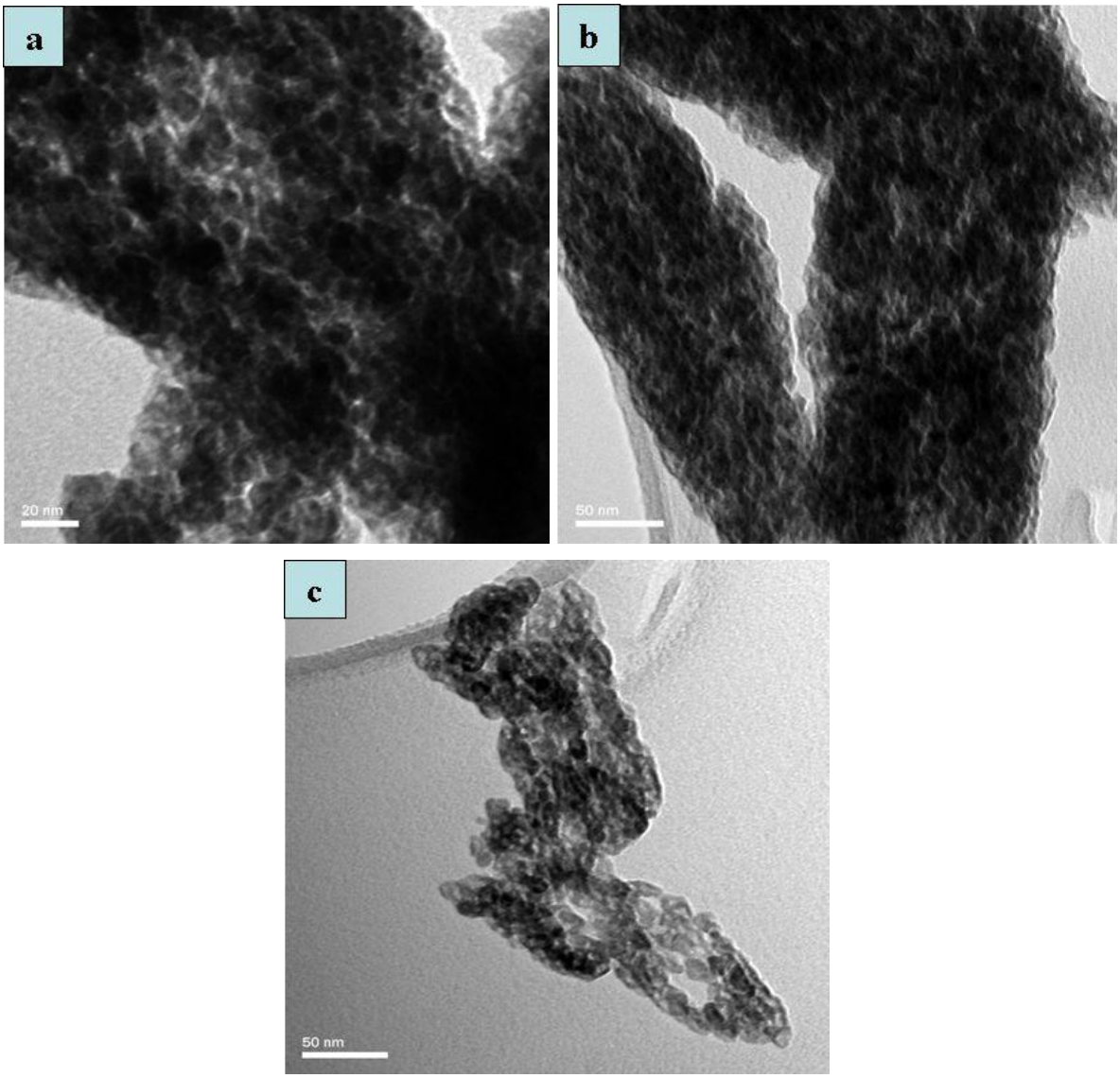

Figure 6.30: TEM images of CdS nanoparticles capped by glucuronic acid (a), glucose (b) and sucrose (c) synthesized from cadmium chloride and 1-methyl-2-thiourea.

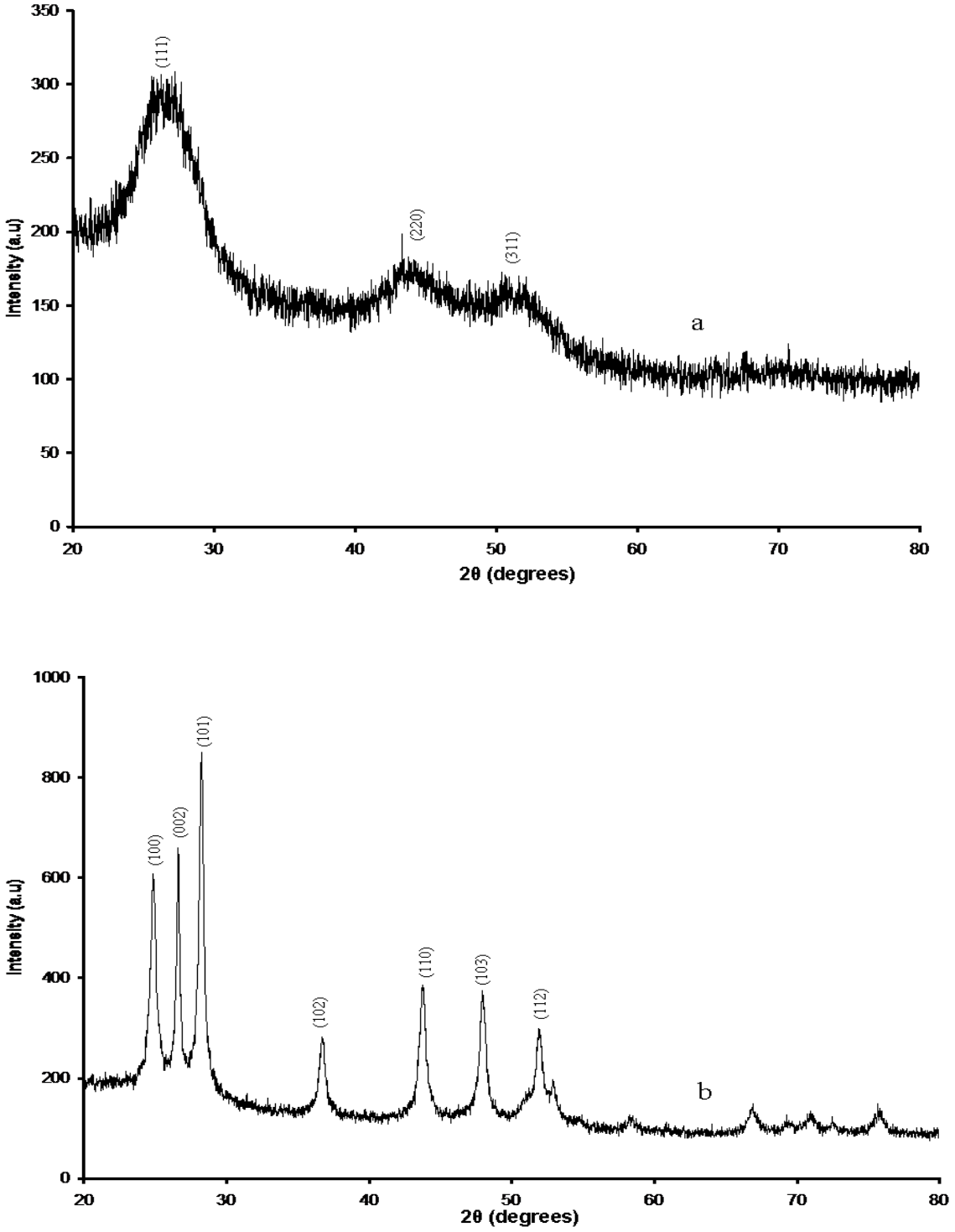

Figure 6.31: XRD patterns of CdS nanoparticles capped by glucuronic acid (a) and sucrose (b) synthesized from cadmium chloride and 1-methyl-2-thiourea.

TEM images of Co_xS_y nanoparticles capped by glucuronic acid (a), glucose (c) and sucrose (e) synthesized from cobalt chloride and 1-methyl-2-thiourea for an hour at 160 ^oC are shown in Figure 6.32. The histograms of particle size distriburion for Co_xS_y nanoparticles

capped by glucuronic acid (b), glucose (d) and sucrose (f) with an average diameter of 2.6 nm (a), 6.2 nm (b) and 3.4 nm (c), respectively, are also shown in Figure 6.32. The morphology of the particles observed when glucuronic acid, glucose and sucrose were the capping agents was spherical shaped. Figure 6.33 shows XRD pattern of Co_xS_y nanoparticles capped by glucuronic acid synthesized from cobalt chloride and 1-methyl-2-thiourea. The peaks observed on the pattern did not match any peaks of the cobalt sulphide nanoparticles phases. Those peaks are due to the impurities. The absence of the significant cobalt sulphide nanoparticles demonstrate that the material synthesized is amorphous.

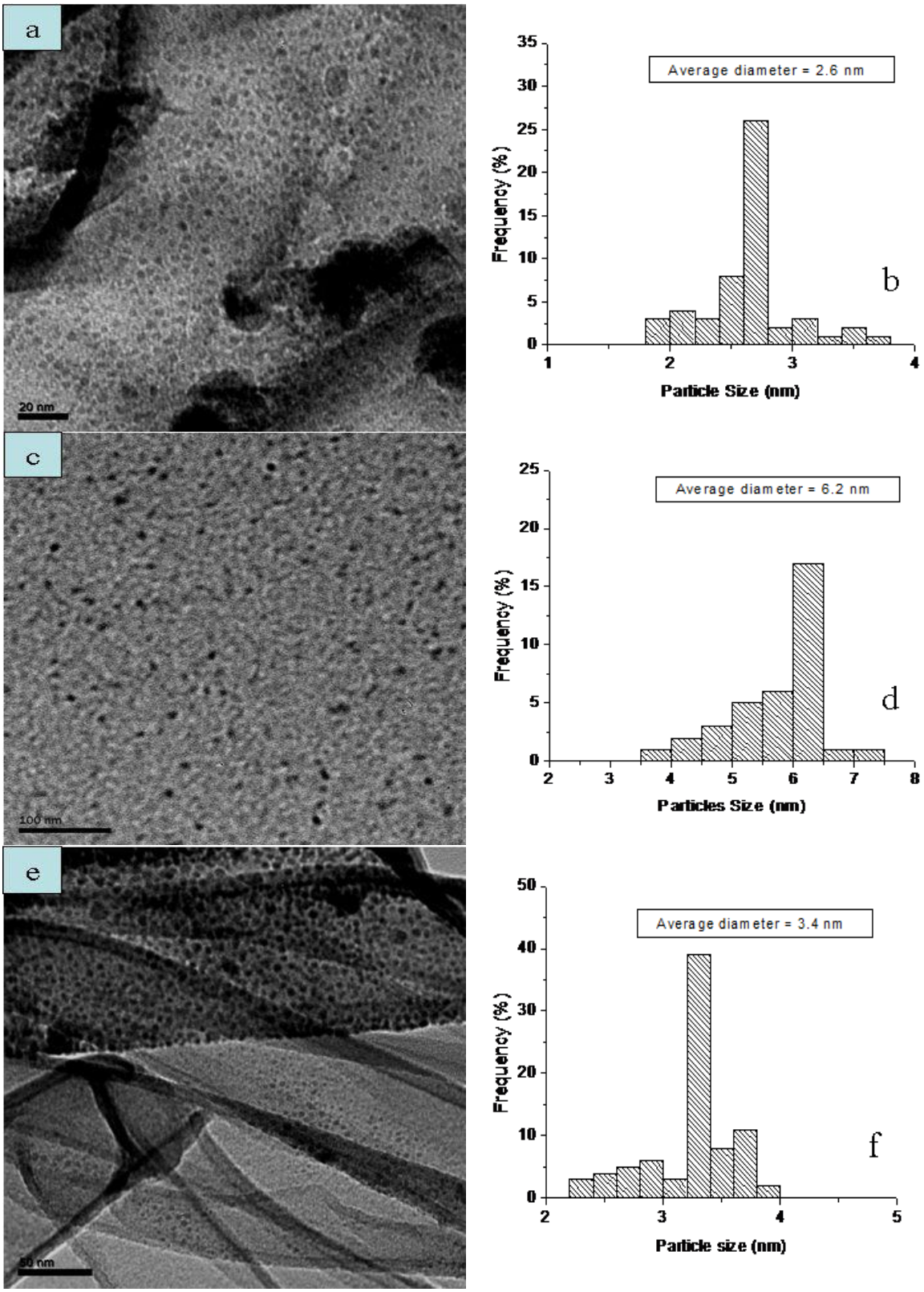

Figure 6.32: TEM images of Co_xS_y nanoparticles capped by glucuronic acid (a), glucose (c), and sucrose (e) synthesized from cobalt chloride and 1-methyl-2-thiourea, and their corresponding of particle size distriburion histograms (b, d, f).

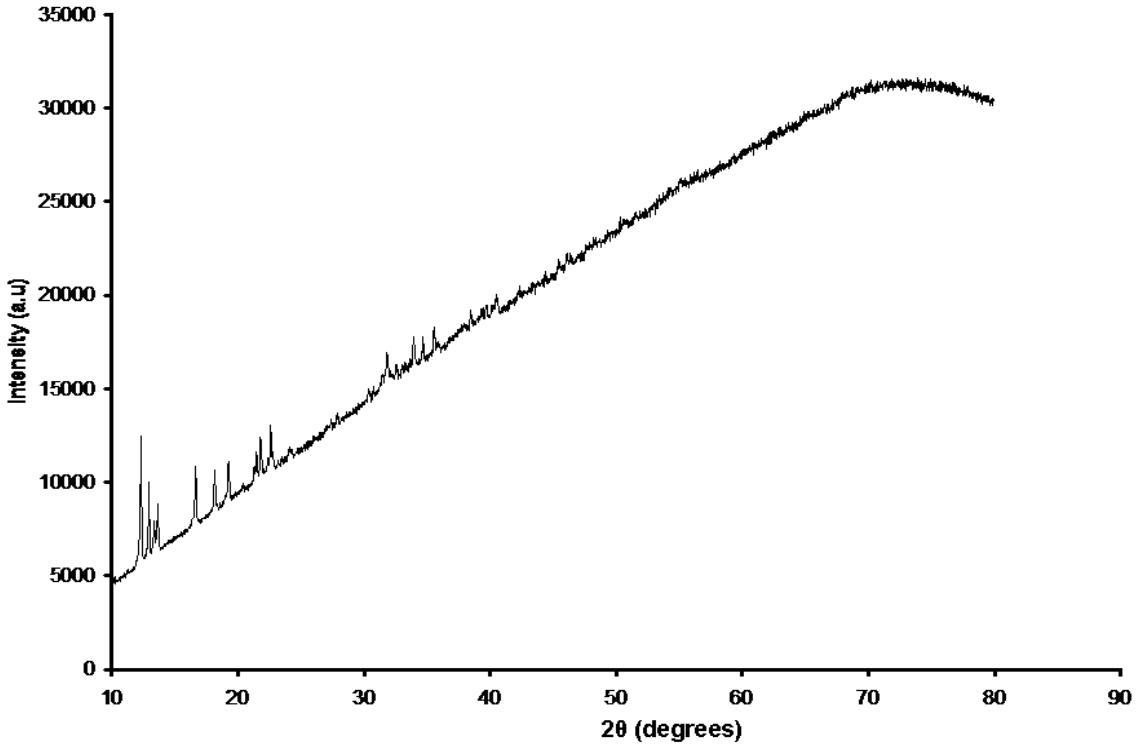

Figure 6.33: XRD pattern of Co_xS_y nanoparticles capped by glucuronic acid synthesized from cobalt chloride and 1-methyl-2-thiourea.

The TEM images of ZnS nanoparticles capped by glucuronic acid (a), glucose (c) and sucrose (e) synthesized from zinc chloride and 1-methyl-2-thiourea at 160 ^oC for an hour, together with histograms of particle size of ZnS capped by glucuronic acid (b) and glucose (d) are shown in Figure 6.34. The morphology of the particles capped by glucuronic acid depicts cubic particles with an average diameter of 24.9 nm. When particles were capped by glucose, hexagonal particles were observed. The average diameter of the particles was measured to be 24.3 nm. The sucrose-capped ZnS nanoparticles revealed some irregular-shaped particles. The XRD pattern of ZnS nanoparticles capped by sucrose synthesized from zinc chloride and 1-methyl-2-thiourea at 120 ^oC for an hour is shown in Figure 6.35. The broad peaks signifying finite size of ZnS nanoparticles can be indexed to hexagonal phase of ZnS nanoparticles, with 2θ values appearing at 28.8^o (002), 48.1^o (110), 52.1^o (103) and 56.6^o (112). The XRD patterns of ZnS nanoparticles capped by glucuronic acid and glucose were also analysed and gave hexagonal phase with broad peaks.

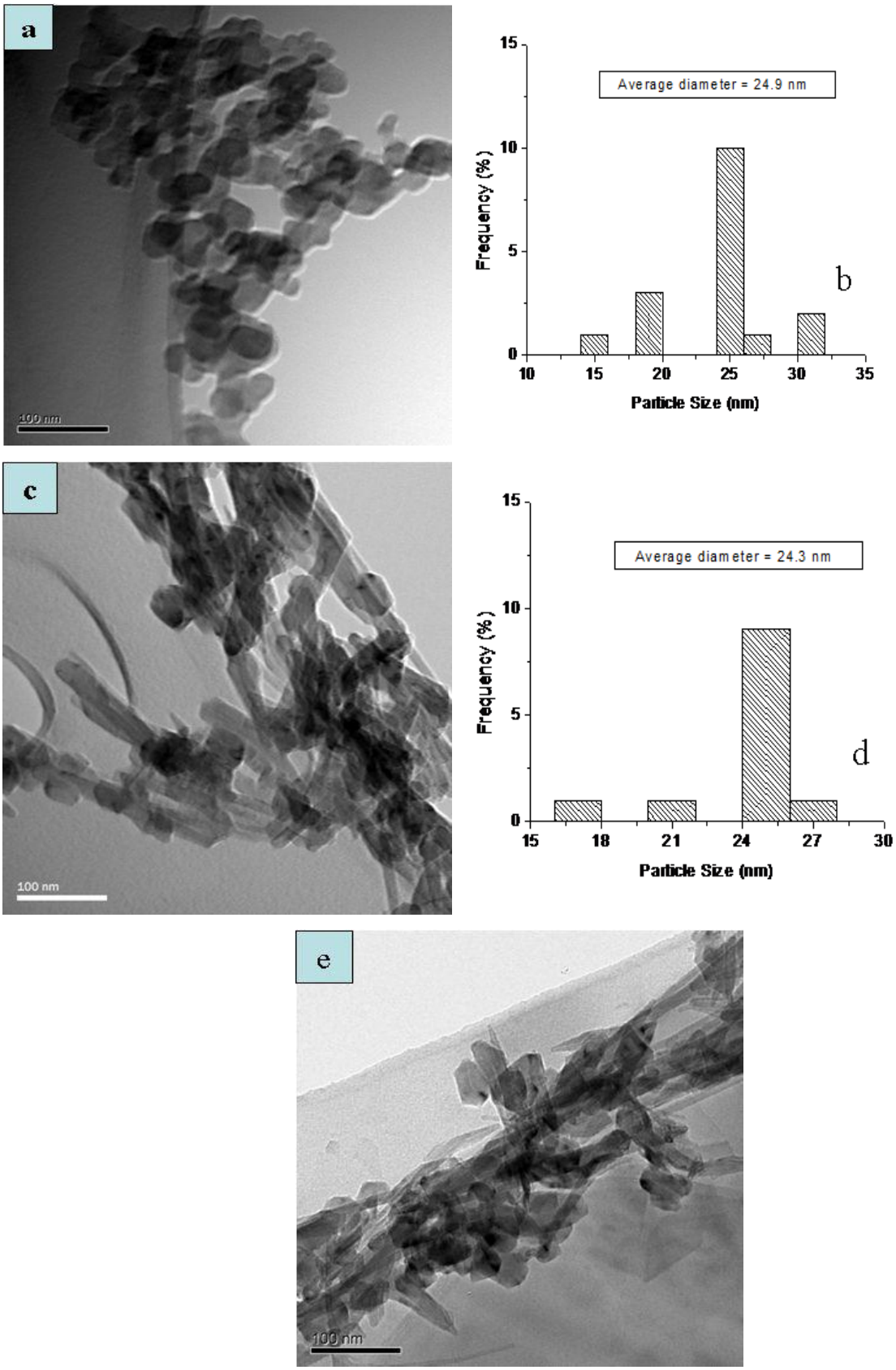

Figure 6.34: TEM images of ZnS nanoparticles capped by glucuronic acid (a), glucose (c) and sucrose (e) synthesized from $ZnCl_2$ and 1-methyl-2-thiourea, and their corresponding size distribution histograms (b, d).

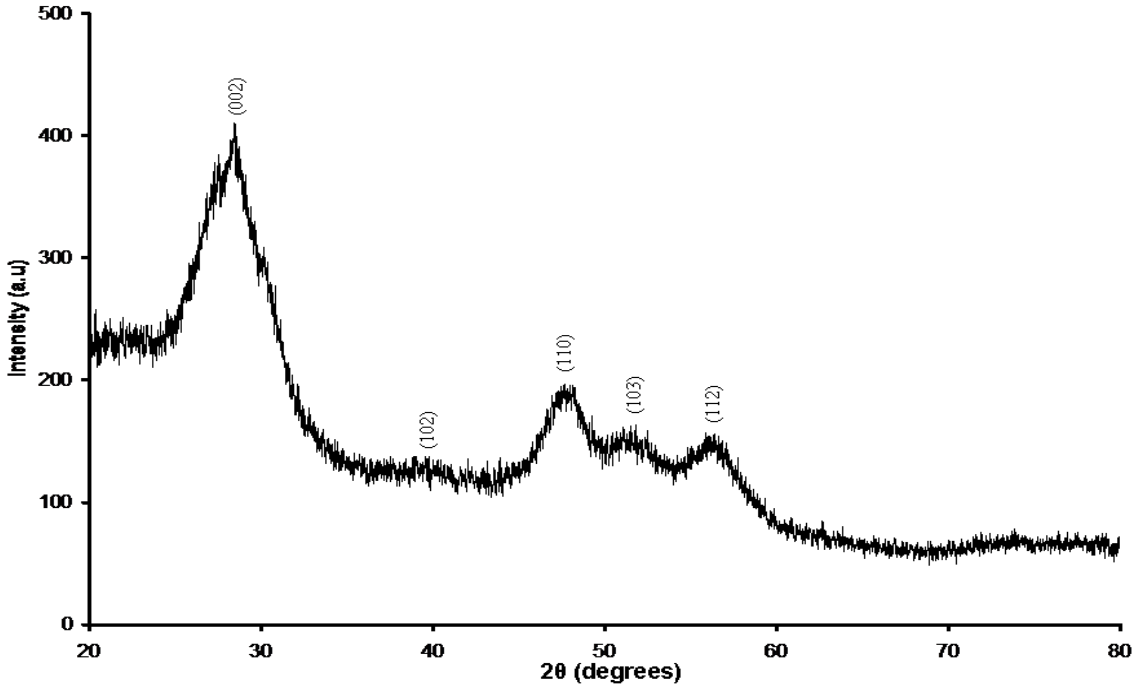

Figure 6.35: XRD pattern of ZnS nanoparticles capped by sucrose synthesized from $ZnCl_2$ and 1-methyl-2-thiourea.

6.2.1.4 Sugars-capped CdS, Co_xS_y and ZnS nanoparticles from cadmium chloride, cobalt chloride and zinc chloride and diethyldithiocarbamate

(a) Optical properties

The absorption and photoluminescence spectra of CdS nanoparticles capped by glucuronic acid (a), glucose (b) and sucrose (c) synthesized from cadmium chloride hydrate and diethyldithiocarbamate at 160 ^oC are shown in Figures 6.36 and 6.37, respectively. The absorption spectra, which are blue-shifted to bulk CdS band gap, have a band edge appearing at 461 nm (2.69 eV). The photoluminescence spectra of the as-prepared CdS nanoparticles show broad emissions, with the emission maxima in the range of 340-560 nm with an excitation wavelength of 250 nm. The emission maxima are very close to the band edges. All the spectra were analyzed using de-ionized water as a solvent.

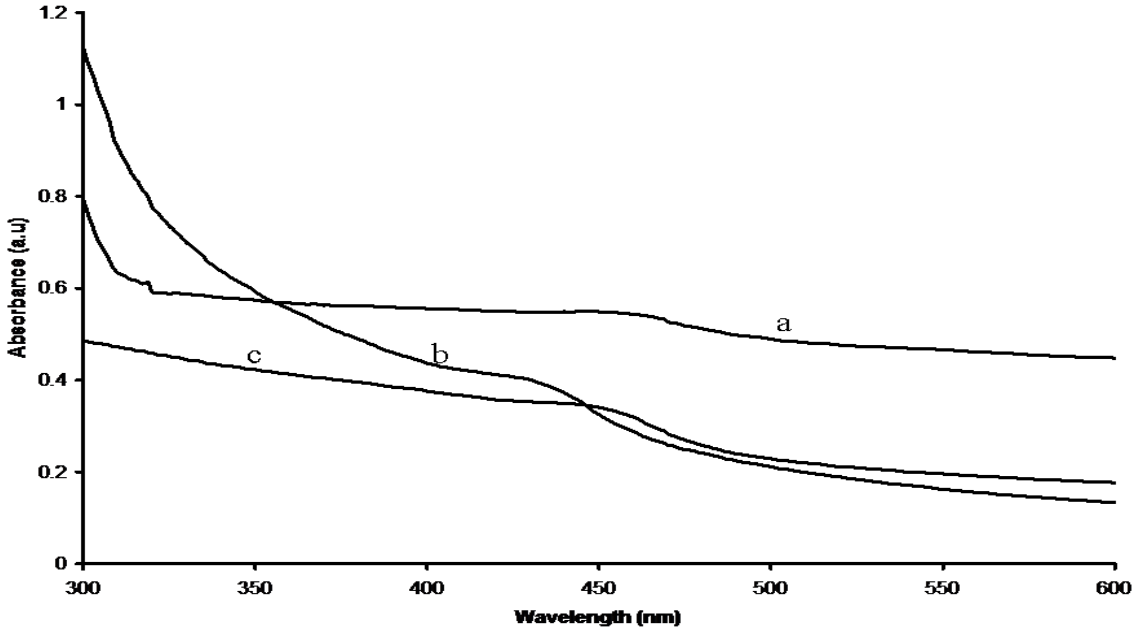

Figure 6.36: Absorption spectra of CdS nanoparticles capped by glucuronic acid (a), glucose (b) and sucrose (c) synthesized from cadmium chloride and diethyldithiocarbamate.

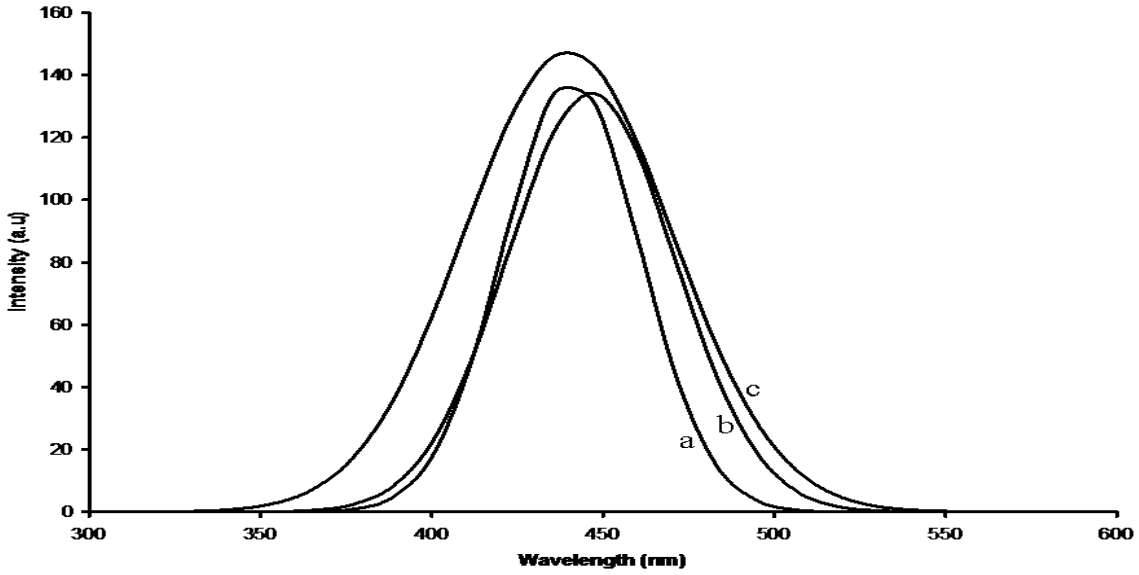

Figure 6.37: Photoluminescence spectra of CdS nanoparticles capped by glucuronic acid (a), glucose (b) and sucrose (c) synthesized from cadmium chloride and diethyldithiocarbamate.

The absorption spectra of Co_xS_y nanoparticles capped by glucuronic acid (a), glucose (b) and sucrose (c) synthesized from cobalt chloride and diethyldithiocarbamate at 160 ^oC for an hour are shown in Figure 6.38. The band edge of the spectra, which appeared at 313 nm

corresponding to 3.96 eV, is blue shifted to bulk Co_xS_y band edge. The absorption peaks, which are also strongly blue shifted, are positioned at 270 nm. Figure 6.39 shows the photoluminescence spectra of Co_xS_y nanoparticles capped by glucuronic acid (a), glucose (b) and sucrose (c). The spectra are red shifted to their as-prepared absorption spectra. The maximum emission peaks of Co_xS_y nanoparticles capped by glucose and sucrose are slightly shifted to higher wavelength as compared to glucuronic acid-capped Co_xS_y. This simply suggests that the particle sizes are different. The maximum emission peak of glucuronic acid-capped Co_xS_y nanoparticles is positioned at 327 nm (3.30 eV), while those of glucose and sucrose-capped Co_xS_y nanoparticles are positioned at approximately 334 nm (3.23 eV). All the absorption and photoluminescence spectra were characterised by dispersing a small amount of particles in de-ionized water.

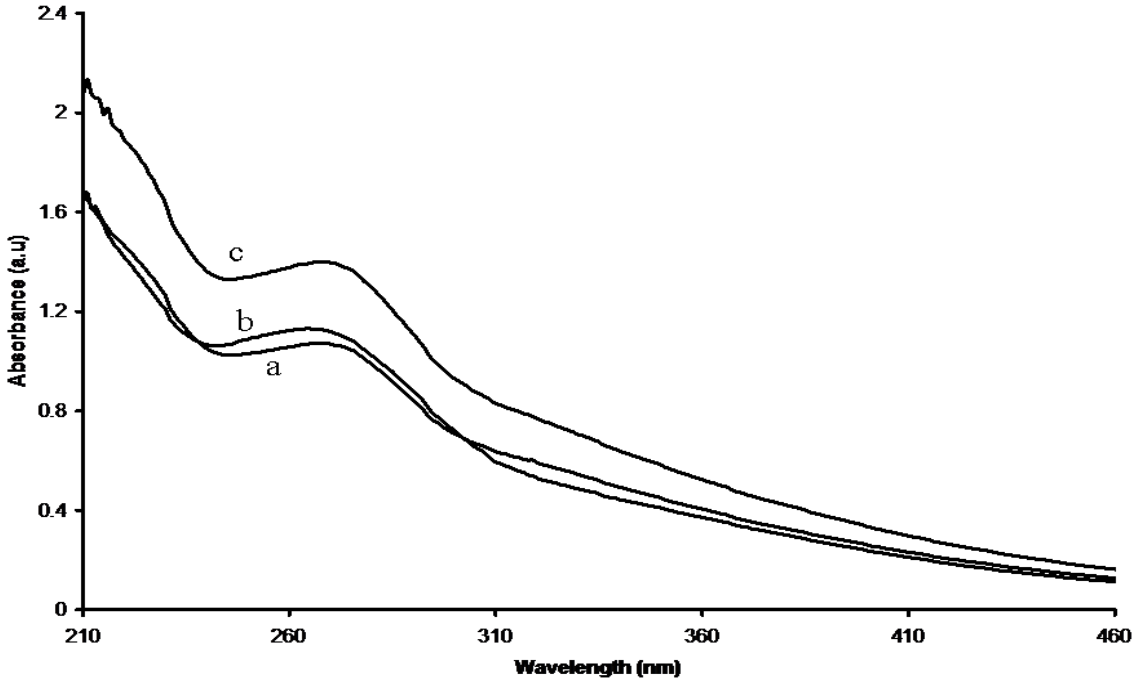

Figure 6.38: Absorption spectra of Co_xS_y nanoparticles capped by glucuronic acid (a) glucose (b) and sucrose (c) synthesized from cobalt chloride and diethyldithiocarbamate.

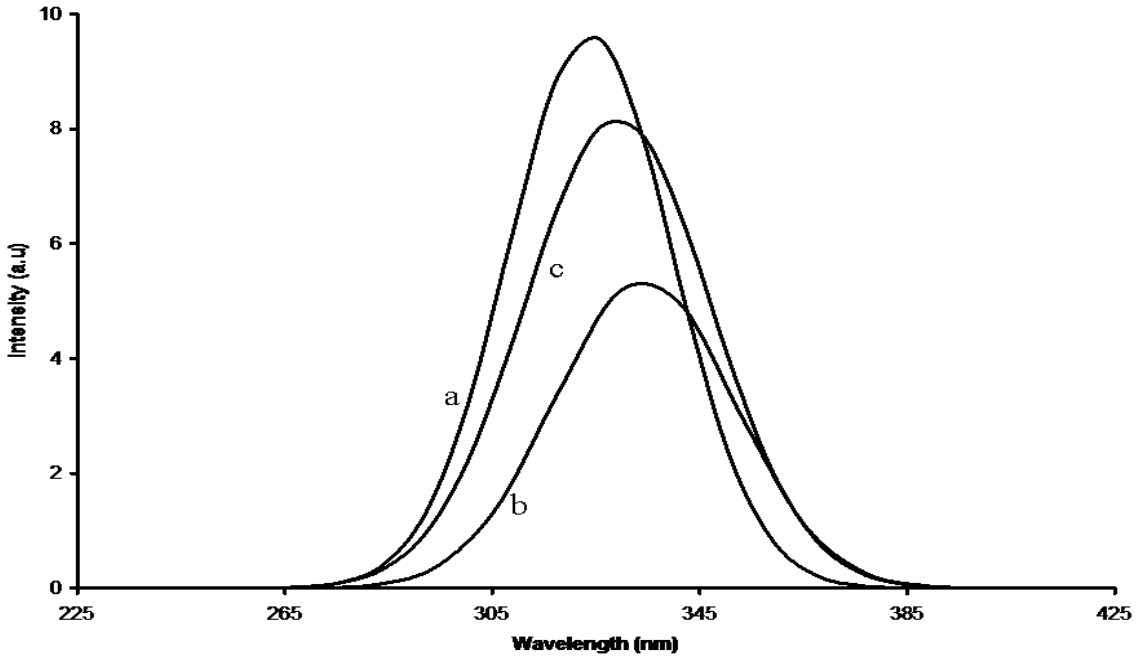

Figure 6.39: Photoluminescence spectra of Co_xS_y nanoparticles capped by glucuronic acid (a), glucose (b) and sucrose (c) synthesized from cobalt chloride and diethyldithiocarbamate.

Figure 6.40 shows the absorption spectra of ZnS nanoparticles capped by glucuronic acid (a), glucose (b) and sucrose (c) synthesized from zinc chloride and sodium diethyldithiocarbamate trihydrate at 160 ^{o}C for an hour. The blue shifted absorption spectra have maximum peaks appearing at 256 nm, 258 nm and 261 nm, respectively. However, the absorption spectra show some shoulders appearing between 340 and 400 nm (more evident in glucuronic acid-capped ZnS nanoparticles), signifying poor passivation of ZnS nanoparticles. The photoluminescence spectra (Figure 6.41) are red shifted to their as-synthesized absorption spectra, with emission maximum peaks positioned at 334 nm for ZnS nanoparticles capped by glucuronic acid and glucose, and 342 nm for sucrose-capped ZnS.

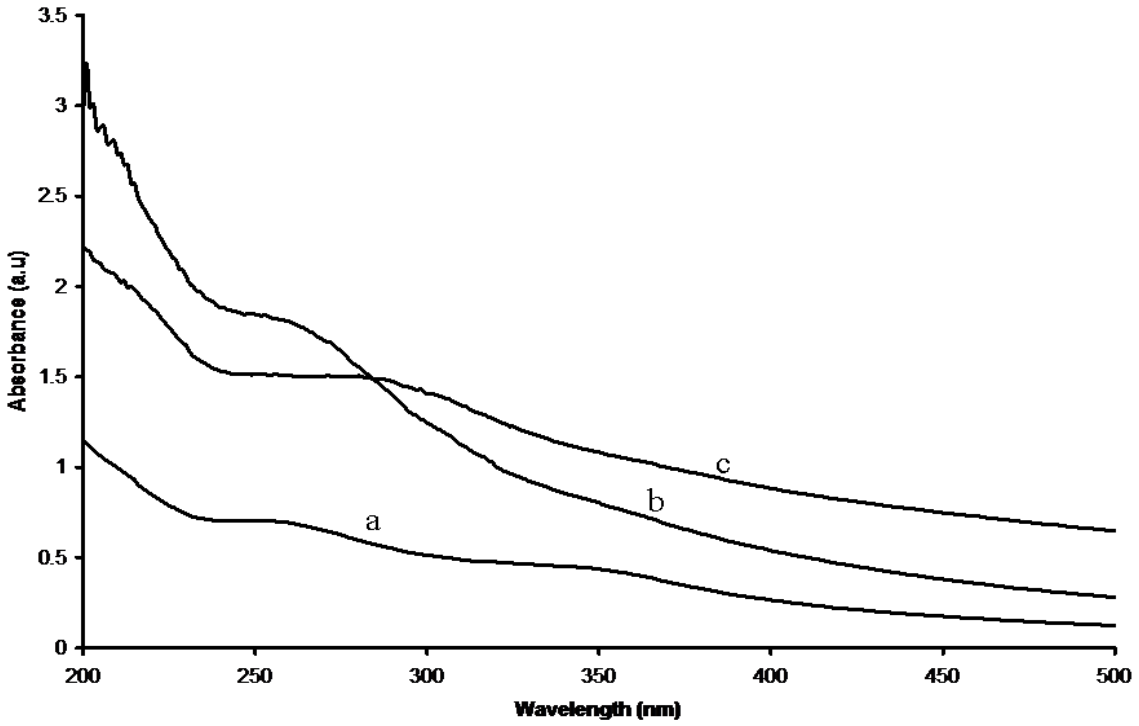

Figure 6.40: Absorption spectra of ZnS nanoparticles capped by glucuronic acid (a), glucose (b) and sucrose (c) synthesized from zinc chloride and diethyldithiocarbamate.

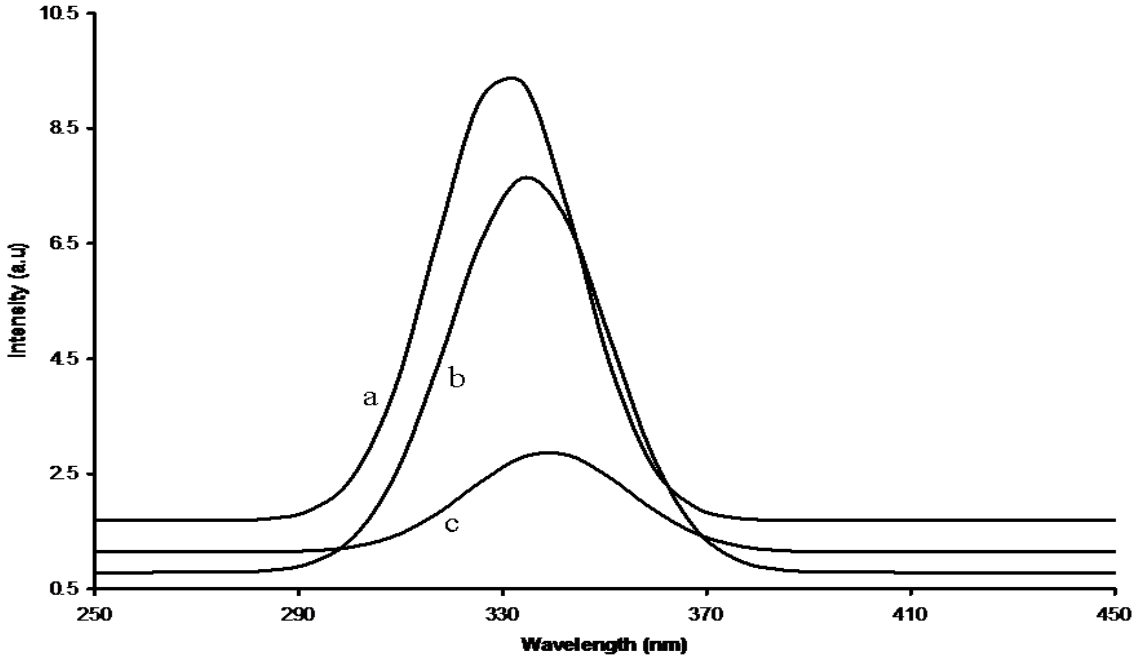

Figure 6.41: Photoluminescence spectra of ZnS nanoparticles capped by glucuronic acid (a), glucose (b) and sucrose (c) synthesized from zinc chloride and diethyldithiocarbamate.

(b) Structural properties

Figure 6.42 shows TEM images of CdS nanoparticles capped by glucuronic acid (a), glucose (b) and sucrose (d), and the histograms of particle size of ZnS capped by glucose (c) and sucrose (e) synthesized from cadmium chloride and diethyldithiocarbamte. TEM images of CdS nanoparticles capped by glucose (b) and sucrose (d) depict close-to-spherical particles with an average diameter of 3.8 nm. TEM image of CdS nanoparticles capped by glucuronic acid (Figure 6.42a) showed some particles aggregation. Figure 6.43 shows the XRD pattern of CdS nanoparticles capped by glucuronic acid. The broad peaks indicating small particles size are indexed to hexagonal phase with characteristic 28.8^{o} (002), 39.8^{o} (102), 48.1^{o} (110), 51.9^{o} (103) and 56.7^{o} (112).

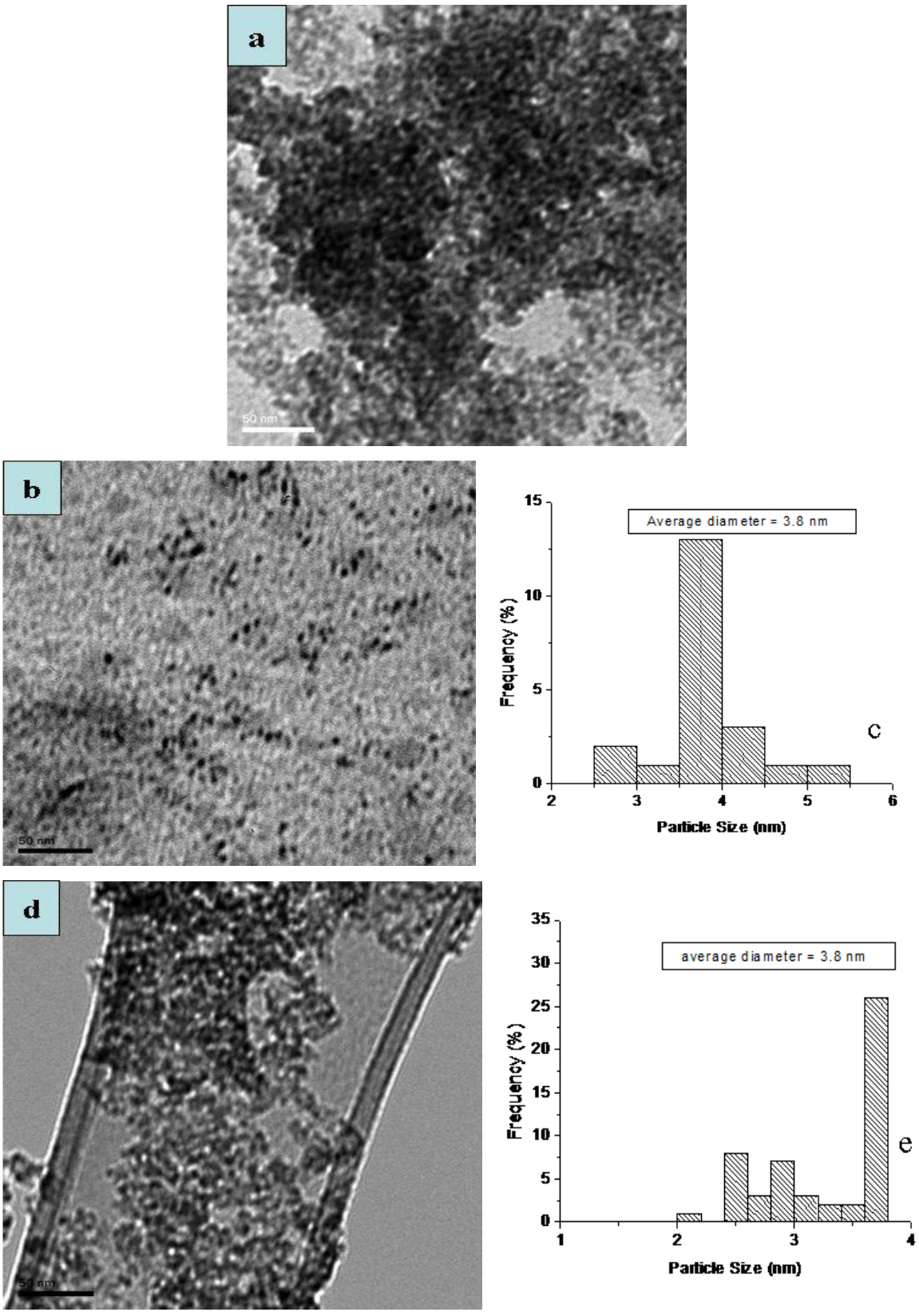

Figure 6.42: TEM images of CdS nanoparticles capped by glucuronic acid (a), glucose (b) and sucrose (d) synthesized from cadmium chloride and diethyldithiocarbamte, and their corresponding size distribution histograms (c, e).

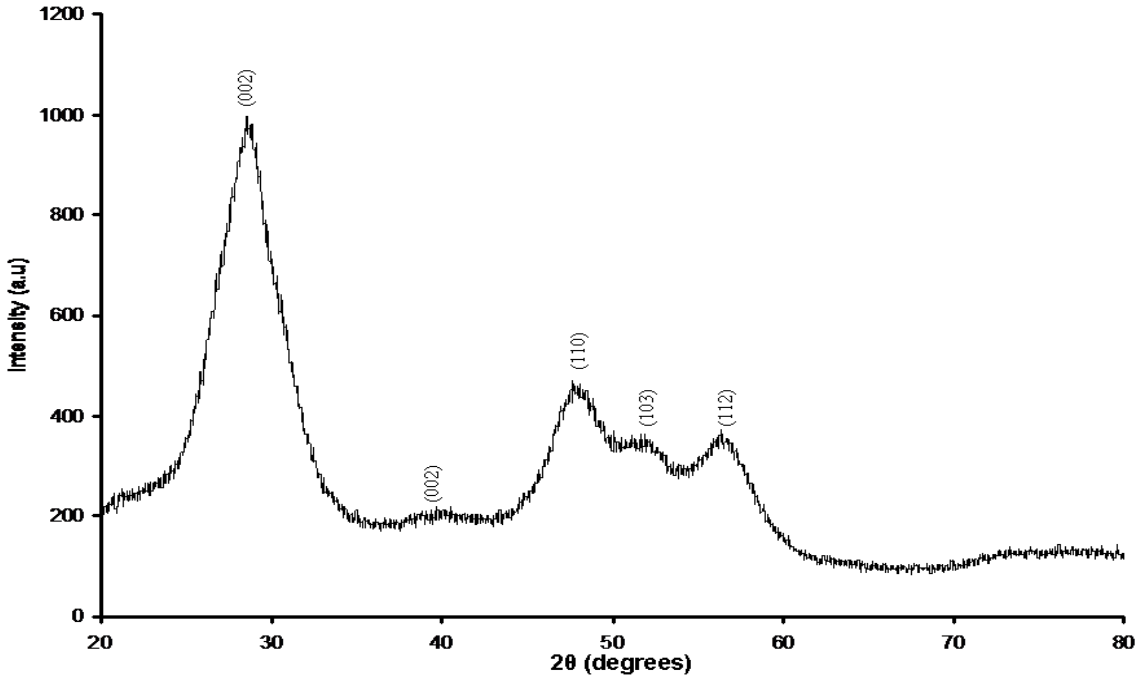

Figure 6.43: XRD pattern of CdS nanoparticles capped by glucuronic acid synthesized from cadmium chloride and diethyldithiocarbamte.

Figure 6.44 shows the TEM images of Co_xS_y nanoparticles capped by glucuronic acid (a), glucose (b) and sucrose (c) synthesized from cobalt chloride and diethyldithiocarbamte for a maximum of an hour. The morphology of all images revealed spherical-like-shaped Co_xS_y nanoparticles in other areas. However, the images are dominated by particles that are aggregated together due to their small size and surface energy. The XRD pattern of Co_xS_y nanoparticles capped by glucose synthesized from cobalt chloride and diethyldithiocarbate (not shown) revealed no obvious peaks. The pattern displayed amorphous nature of the as-prepared cobalt sulphide powder. Annealing the powder at 100 ^oC for 1 h still revealed no signs of peaks.

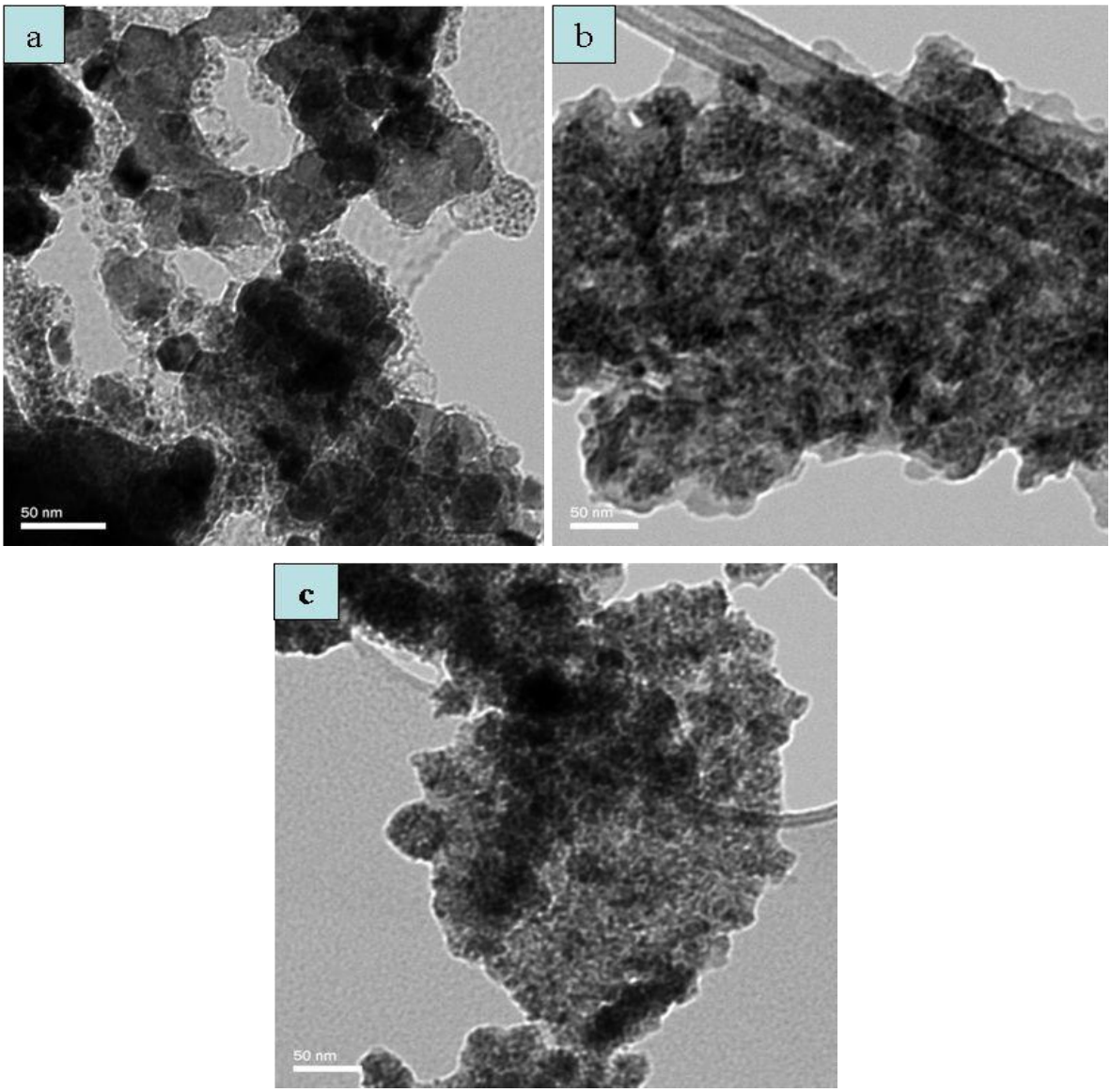

Figure 6.44: TEM images of Co_xS_y nanoparticles capped by glucuronic acid (a), glucose (b) and sucrose (c) synthesized from cobalt chloride and diethyldithiocarbate.

The TEM images of ZnS nanoparticles capped by glucuronic acid (a), glucose (b) and sucrose (c) are shown in Figure 6.45. The particles were grown from zinc chloride as a metal precursor and diethyldithiocarbamate as a sulphur precursor at 160 ^oC for an hour. The particles revealed some aggregation in other parts, which signify poor passivation of the particles. The small spherical-like-shaped particles capped by glucuronic acid, glucose and sucrose were observed with an average diameter of 2.0 nm, 2.2 nm and 2.4 nm, respectively. Figure 6.46 shows the XRD pattern of ZnS nanoparticles capped by sucrose. The pattern with broad peaks can be indexed to cubic phase with 2θ values positioned at 29.4^o (111), 48.9^o (220) and 57.5^o (311).

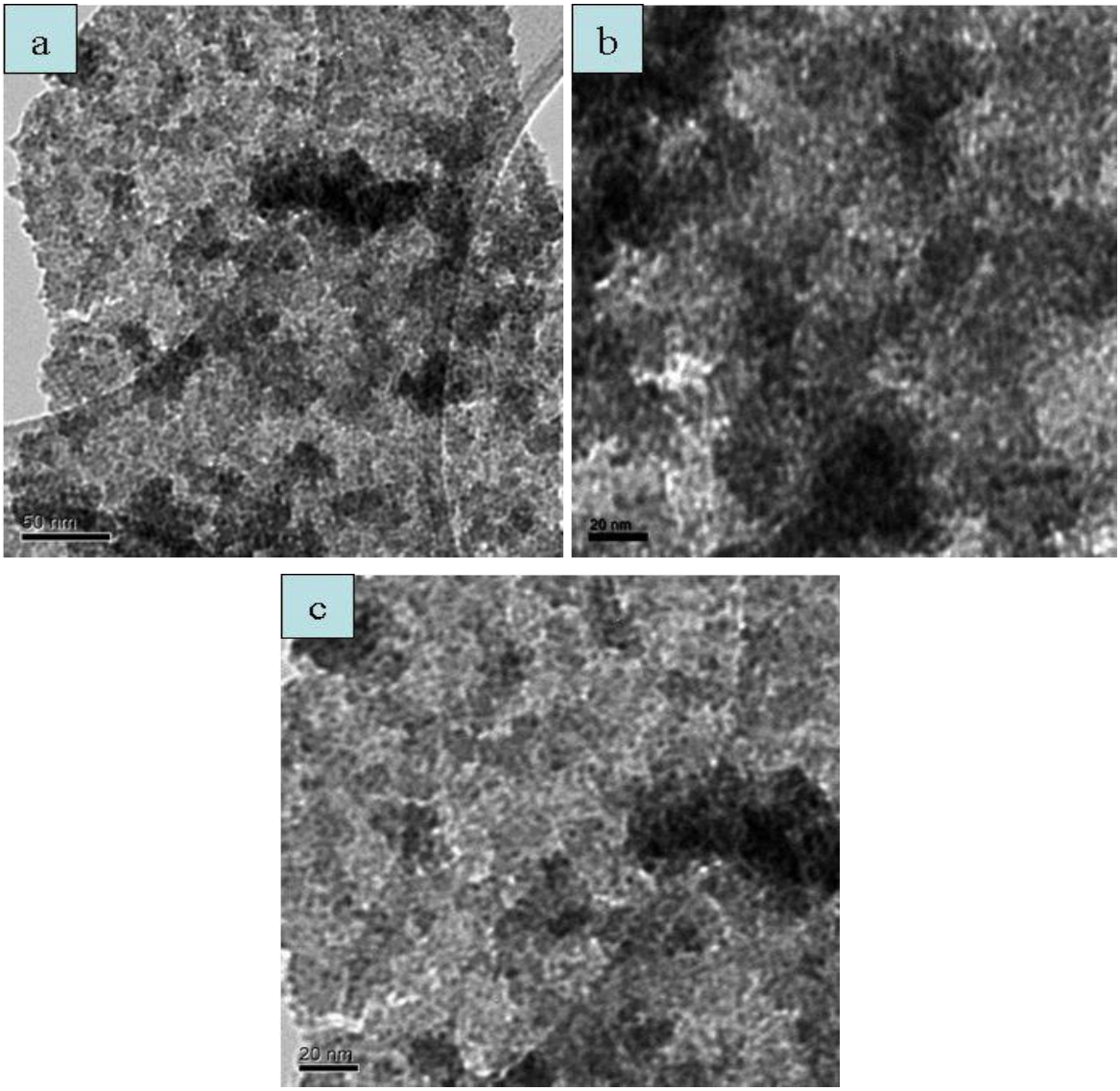

Figure 6.45: TEM images of ZnS nanoparticles capped by glucuronic acid (a), glucose (b) and sucrose (c) synthesized from zinc chloride and diethyldithiocarbamate.

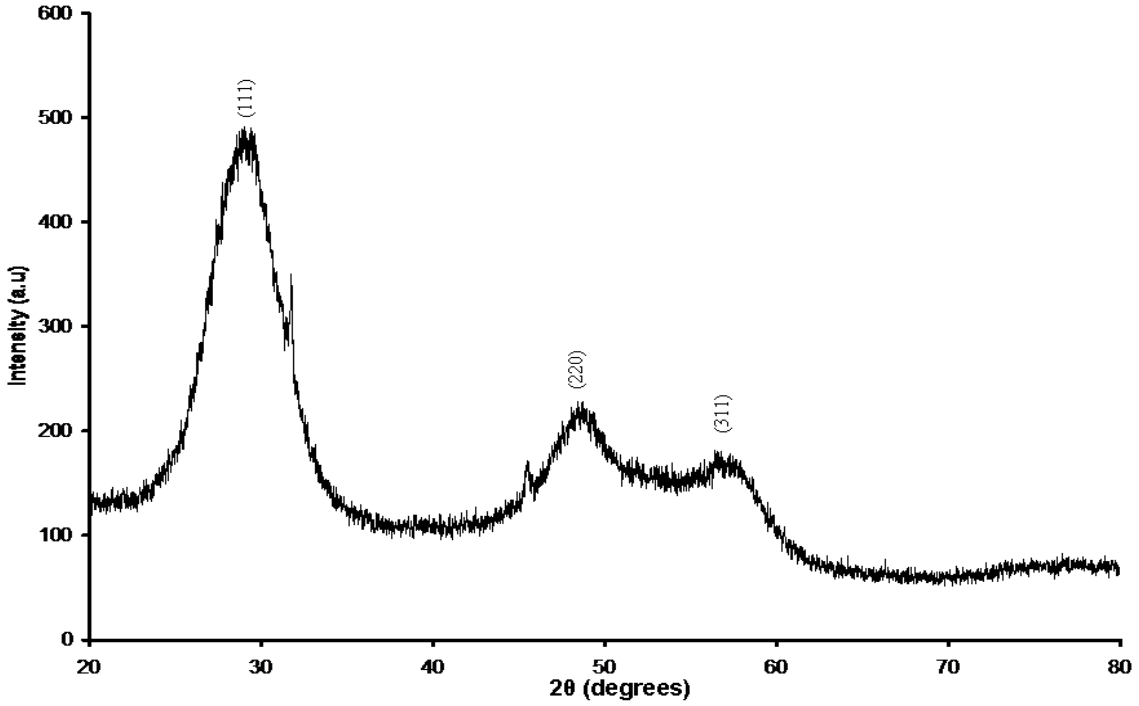

Figure 6.46: XRD pattern of ZnS nanoparticles capped by sucrose synthesized from zinc chloride and diethyldithiocarbamate.

6.3 Conclusion

The synthesis of sugars-capped semiconductor nanoparticles using direct chemical method yielded particles dominated by close-to spherical shape. Although the absorption spectra were blue shifted to their bulk materials, most of their photoluminescence spectra were very broad signifying that the particles were not well passivated. The spectra of CdS, Co_xS_y and ZnS were observed to absorb at different wavelength irrespective of particles synthesized under similar conditions, except the metal sources. This was due to the high rate of the reactions resulting from the direct chemical method, which provided high energy. It was also obsrved that the size obtained for CdS, Co_xS_y and ZnS was different in the same direct chemical method conditions. This shows that the direct chemical method could influence selectively the nucleation and growth rates of different compounds. Zhu *et al.* [26] synthesized CdS and ZnS using microwave irradiation with different absorption band edges and emission maximum peaks, together with the sizes of the particles. Mostly, work done on CdS, Co_xS_y and ZnS yielded particles that had aggregated due to their small size and high surface energy. Although different types of sugars were used as capping agents, for example; in the preparation of CdS nanoparticles from cadmium chloride and

tetramethylthiuram monosulfide, no significant difference was observed. Mostly, the absorption peaks were not as sharp as those observed in ligand exchange. It is known that sharper absorption peaks signify well dispersed particles. The temperature employed in this method was 160 ^{o}C. The sugars used as capping agents might have been affected strongly by the high temperature which made the prepared semiconductor nanoparticles to be less stable, leading to aggregation and formation of larger particles. In the case of ligand exchange (chapter 5), particles obtained were small and of almost the same size. Although these particles are soluble in water and the capping agents used being harmful, poor passivation exposes nanoparticles, and that prevents them from being used in applications such as biolabelling.

6.4 References

1. Y. J. Yang, L. Y. He, H. Xiang, *Russ. J. Electrochem.,* **42,** 954, 2006.
2. N. Kumbhojkar, V. V. Nikesh, A. Kshirsagar, S. Mahamuni, *J. Appl. Phys.,* **88,** 6260, 2000.
3. W. Chen, Z. Wang, Z. Lin, L. Lin, *J. Appl. Phys.,* **82,** 3111, 1997.
4. J. Nanda, S. Sapra, D. D. Sarma, N. Chandrasekharan, G. Hodes, *Chem. Mater.,* **12**, 1018, 2000.
5. X. D. Gao, X. M. Li, W. D. Yu, *Thin Solid Films,* **468,** 43, 2004.
6. Y. Ni, G. Yin, J. Hong, Z. Xu, *Mater. Res. Bull.,* **39,** 1067, 2004.
7. H. –Y. Lu, S. –Y. Chu, S. –S. Tan, *J. Cryst. Growth,* **269,** 385, 2004.
8. N. Goswami, P. Sen, *Solid State Commun.,* **132,** 791, 200.
9. R. Kerner, O. Palchik, A. Gedanken, *Chem. Mater.,* **13,** 1413, 2001.
10. R. Harpeness, O. Palchik, A. Gedanken, V. Palchik, S. Amiel, M. A. Slifkin, A. M. Weiss, *Chem. Mater.,* **14,** 2094, 2002.
11. G. Carotenuto, G. P. Pepe, L. Nicolais, *Eur. Phys. J. B,* **16,** 11, 2000.
12. F. Fievet, *MRS Bull.,* **14,** 29, 1989.
13. M. Bruchez Jr., M. Moronne, P. Gin, S. Weiss, A. P. Alivisatos, *Science,* **281,** 2013, 1998.
14. B. D. Butkus, *Biophotonics Int.,* **11,** 34, 2004.
15. A. M. Derfus, W. C. W. Chan, N. Bhatia, *Nano Lett.,* **4,** 11, 2004.
16. W. C. W. Chan, S. M. Nie, *Science,* **281,** 2016, 1998.

17. H. Mattoussi, J. M. mauro, E. R. Goldman, G. P. Anderson, V. C. Sundar, F. V. Mikulec, M. G. bawendi, *J. Am. Chem. Soc.*, **122** (49), 12142, 2000.
18. J. O. Winter, T. Y. Liu, B. A. Korgel, C. E. Schmidt, *Adv. Mater.*, **13** (22), 1673, 2001.
19. T. Gacoin, K. Lahlil, P. Larregaray, J. P. Boilot, *J. Phys. Chem. B.*, **105,** 10228, 2001.
20. C. J. Murphy, J. L. Coffer, *Appl. Spectrosc.*, **56,** 16A, 2002.
21. R. J. Bandaranayake, G. W. Wen, J. Y. Lin, H. X. Jiang, C. M. Sorensen, *Appl. Phys. Lett.*, **67,** 83, 1995.
22. L. Yang, Q. Shen, J. Zhou, K. Jiang, *Mater. Chem. Phys.*, **98,** 125, 2006.
23. J. S. Steckel, J. P. Zimmer, S. C. Sullivan, N. E. Scott, V. Bulovic, M. G. Bawendi, *Angew. Chem. Int. Ed.*, **43,** 2154, 2004.
24. C. Yuan, B. Gao, L. Su, L. Chen, X. Zhang, *J. Electrochem. Soc.*, **156**(3), A199, 2009.
25. P. Zhang, S. J. Naftel, T. K. Sham, *J. Appl. Phys.*, **90,** 2755, 2001.
26. J. Zhu, M. Zhou, J. Xu, X. Liao, *Mat. Lett.*, **47,** 25, 2001.

Chapter 7

Toxicity studies of CdS nanoparticles/QDs capped by sugars

7.1 Introduction

Since constituents of semiconductor nanoparticles or quantum dots such as cadmium [1] or selenium [2] are toxic to many cells, harmful effects can be expected, especially when the hydrophilic capping agent or ligand around the quantum dots is not stable and they might dissolve under the release of toxic ions. On the other hand, some cells have developed mechanisms to cope with such ions, such as assembling them to particles in a biomineralization process, which efficiently removes ions from solution. In this way, fluorescent CdS [3, 4] or PbS [5] QDs are grown in some cells. In terms of biocompartibility or toxicity, several modes on how to differentiate QDs introduction to cells must be differentiated. Certainly, the results will also strongly depend on the type of cells and on the hydrophilic ligand used to stabilize the QDs in aqueous solution.

Quantum dots dissolved in the culture medium are ingested by many cells. Concerning toxicity, some groups report as a general statement (e.g. without details about the concentration of QDs) that there are no detectable differences from unlabelled cells up to two weeks after incubation [6, 7, 8]. Derfus *et al.* [9] measured the liver specific function of hepatocyte cells incubated with QDs in terms of albumin secretion and could not determine any difference from untreated cells. In a more quantitative way Hanaki *et al.* [10] demonstrated that the viability of cells was not affected for QD concentrations of 4 g/l in the medium. Jaiswal *et al.* [11] reported that 400-600 nM QDs in the medium had no detectable effects on cell morphology or physiology. Furthermore, QDs in these concentrations did not interfere with the initiation of development of Dictyostelium discoideum cells and their response to cyclic adenosine phosphate (cAMP) [11]. Finally, Winter *et al.* [12] reported that the addition of 0.03 nM QDs (which were not ingested by the cells) did not alter the proliferation and attachment of cells within 5 days. All studies described above can at best be called quantitative and most of them are based on judging the viability of the cells by optical light microscopy. In a quantitative way, cell viability can be measured with colorimetric assays, such as the MTT reagent (3-(4,5-dimethylthiazol-

2yl)-2,5-diphenyl tetrazolium bromide). Such quantitative assays allow for measuring absolute numbers for the survival rate of cells upon incubation with toxins. With the MTT assay Mattheakis *et al.* [7] demonstrated that no toxicity of high purified polymer-coated CdSe/ZnS QDs could be observed for typical labelling concentrations of 10 nM.

In this chapter, toxicity using CdS nanoparticles/QDs was investigated. Different conditions such as concentration and time were considered.

7.2 Results and discussions

In the toxicity studies, CdS nanoparticles capped by glucose, sucrose and glucuronic acid were studied. The water soluble semiconductor nanoparticles/QDs used were synthesized using ligand exchange method, with pyridine that was used as a solvent to displace HDA or TOPO. The numbers 1, 2, 3, 4 and 5 in the x-axis (Figures 7.1, 7.2, 7.3, 7.4, 7.5, 7.6 and 7.7) represent the untreated cells and the materials used. The materials studied for toxicity are glucose-capped CdS nanoparticles (2) exchanged from HDA-capped CdS nanoparticle (120 ^{o}C) that was prepared from diphenylthiourea cadmium complex, sucrose-capped CdS (3) exchanged from HDA-capped CdS nanoparticle (120 ^{o}C) that was prepared from diethyldithiocarbamato cadmium complex, sucrose-capped CdS nanoparticles (4) exchanged from HDA-TOPO-capped CdS nanoparticle (120 ^{o}C) that was prepared from diethyldithiocarbamato cadmium complex and glucuronic acid-capped CdS nanoparticles (5) exchanged from HDA-capped CdS nanoparticle (180 ^{o}C) that was prepared from diethyldithiocarbamato cadmium complex. The control or untreated cells are represented by number 1 in the x-axis (Figures 7.1, 7.2, 7.3, 7.4, 7.5, 7.6 and 7.7).

Figures 7.1, 7.2, 7.3 and 7.4 show the bar graphs of percentage viability determined by the ATP assay of U937 cells treated with the various semiconductor nanoparticles or quantum dots in triplicate for 1, 3, 24 and 48 hour incubation periods at concentrations of 10 µg/ml, 25 µg/ml and 50 µg/ml, respectively. The basic principal of this assay was to show that cells produce ATP when they are viable, which was quantified with ATP kit. The ATP produced was proportional to the viable cells. Results from our assay show that the treatment of cells with CdS nanoparticles containing 10 µg/ml, 25 µg/ml and 50 µg/ml concentrations over 1, 3, 24 and 48 hour time period did not result in any toxicity with some few exceptions. The cell viability was greater than 90% for almost all time points

tested, except for sucrose-capped CdS (3) transferred from HDA-capped CdS nanoparticle (120 ^{o}C) when the concentration was 50 µg/ml for 48 hours, and for glucuronic acid-capped CdS nanoparticles (5) transferred from HDA-capped CdS nanoparticle (180 ^{o}C) when the concentration was 25 µg/ml and 50 µg/ml for 48 hours, showing detection of little toxicity. Toxicity was detected by comparing the treated cells (2, 3, 4 and 5) with the untreated cells (1) that have a viability of 100%. The bar graphs also revealed some signs of bars with percentage viability above 100%. This scenario usually happens when the well that the cells were treated in has more cells than that of the control wells. It is also vital to understand that even though the cells are dying the mitochondria that produce the ATP could still function and produce ATP, thus resulting in giving false representation of the true viability. However, Cd-containing compounds are highly toxic, a scenario or point that cannot be neglected. Some publications carried out on the toxicity and clearance *in vitro* and *in vivo* of Cd-containing compounds in human cancer cells showed that they are cytotoxic to human breast and prostate cancer cells [13, 14]. The toxicity effect in this chapter might have not been detected due to the time frame used. A maximum of 48 hours and the concentration used might have played a role in failing to detect toxicity. On each of the graphs the error bars are the standard deviations of the treatments performed in triplicate.

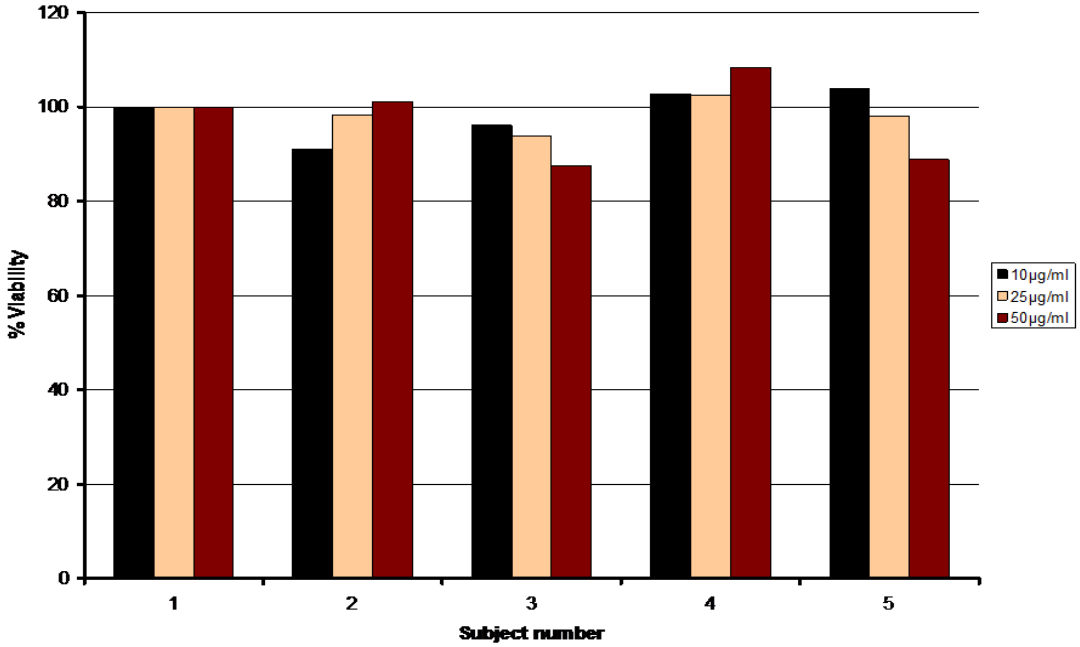

Figure 7.1: Bar graph of % Viability of U937 cells treated for 1 hour at 10, 25 and 50 µg/ml concentrations.

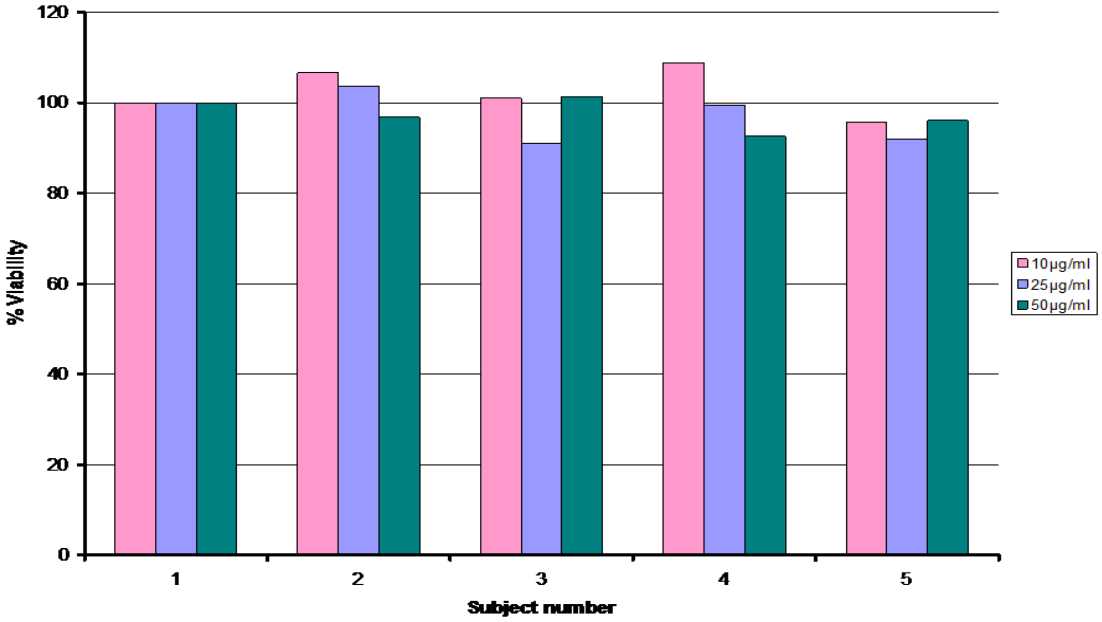

Figure 7.2: Bar graph of % Viability of U937 cells treated for 3 h at 10, 25 and 50 µg/ml concentrations.

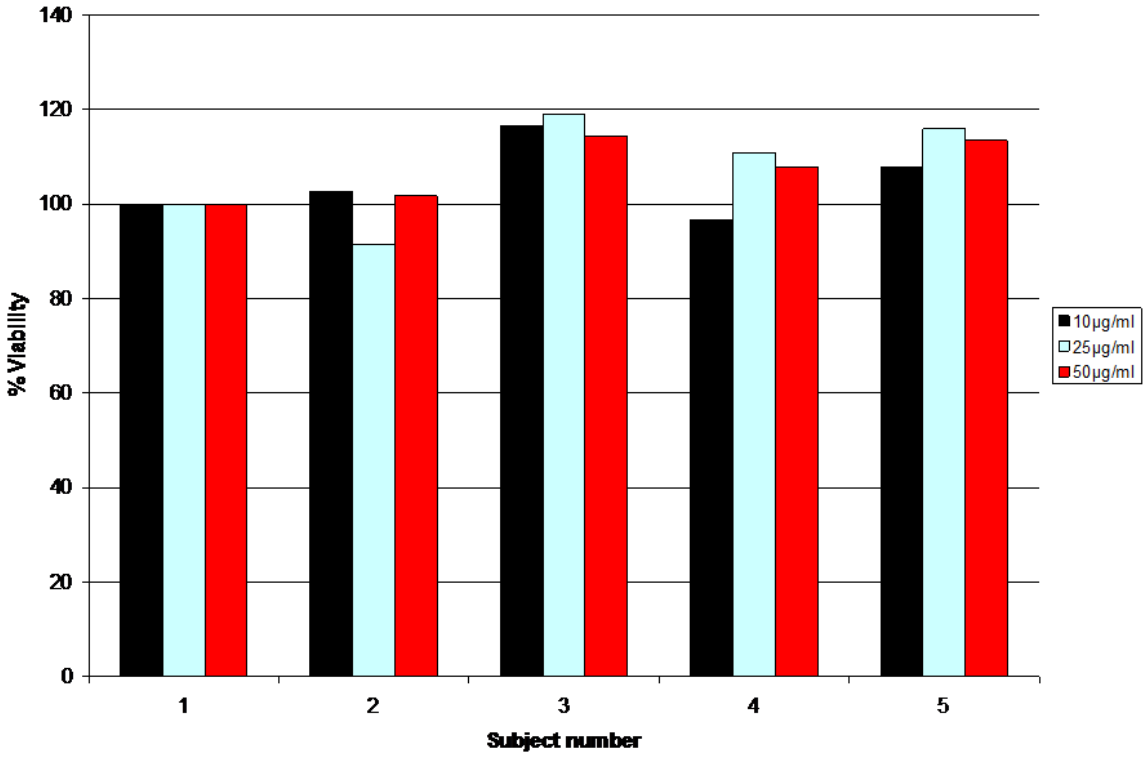

Figure 7.3: Bar graph of % Viability of U937 cells treated for 24 h at 10, 25 and 50 µg/ml concentrations.

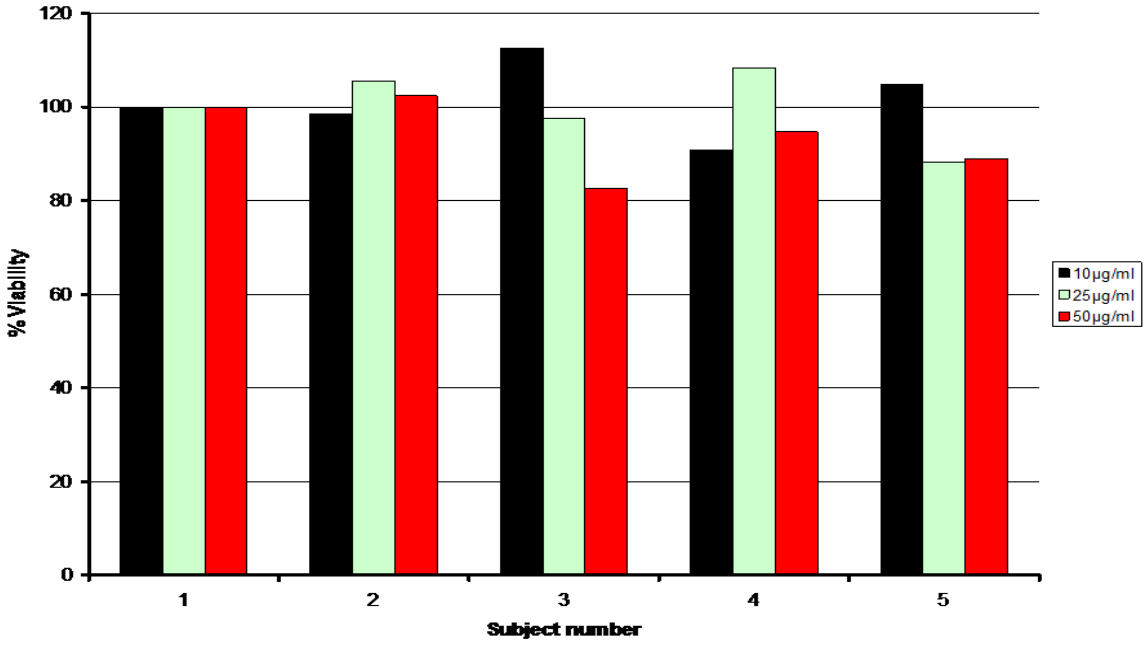

Figure 7.4: Bar graph of % Viability of U937 cells treated for 48 h at 10, 25 and 50 µg/ml concentrations.

Figures 7.5 and 7.6 show the bar graphs of percentage viability determined by the ATP assay of U937 cells treated with various quantum dots in triplicate for 1 and 24 hours incubation periods at concentrations of 50, 100 and 150 µg/ml, respectively. Although not in all materials used and concentrations, especially in Figure 7.6, it was found that increasing the concentration of most CdS materials did not have an effect on the percentage viability. There were no signs of percentage viability less than 90%, indicating that no toxicity was observed. However, in the same bar graph (Figure 7.6), when the concentration of CdS nanomaterials capped by sucrose (4) transferred from HDA-TOPO-capped CdS nanoparticles (120 ^{o}C) was increased to 150 µg/ml, a percentage viability of less than 90% was observed.The same scenarion was observed when the concentration was increased to 100 µg/ml and 150, µg/ml for glucuronic acid-capped CdS nanoparticles (5) transffered from HDA-capped CdS nanoparticle (180 ^{o}C). This is an indication of some signs of toxicity and also shows that working at higher concentration increases the chances of detecting toxicity of the quantum dots. These results agree well with published work by Zhai *et al.* [15] who reported a decrease of percentage viability showing toxicity of PAA-capped CdSe/CdS core-shell QDs by increasing the concentration from 0.007 mg/ml to 1 mg/ml after 24 hours.

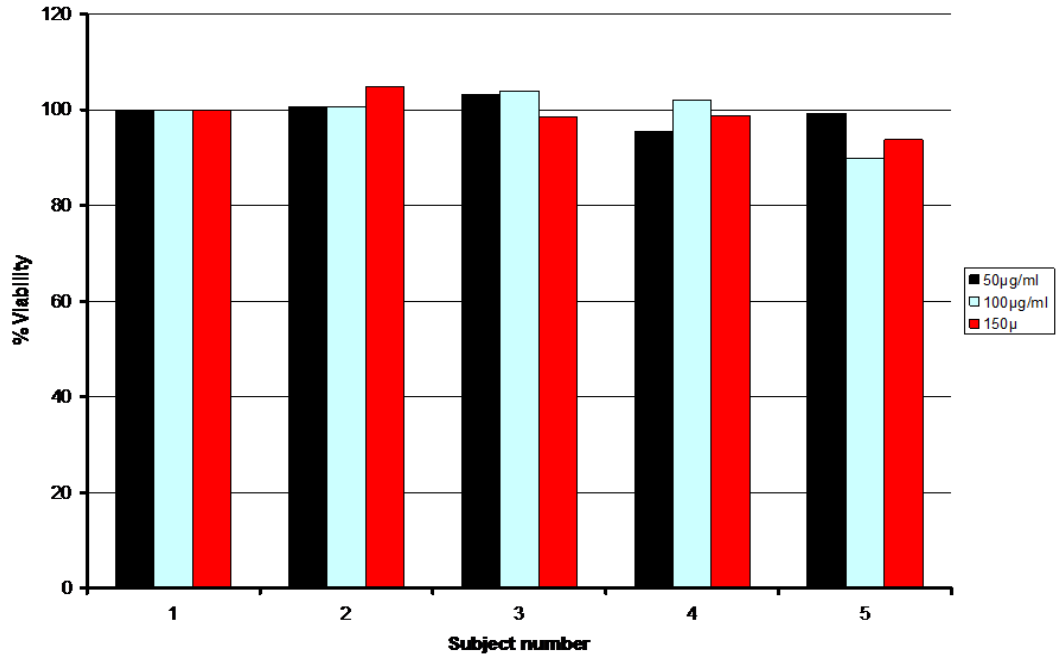

Figure 7.5: Bar graph of % Viability of U937 cells treated for 1 h at 50, 100 and 150 µg/ml concentrations.

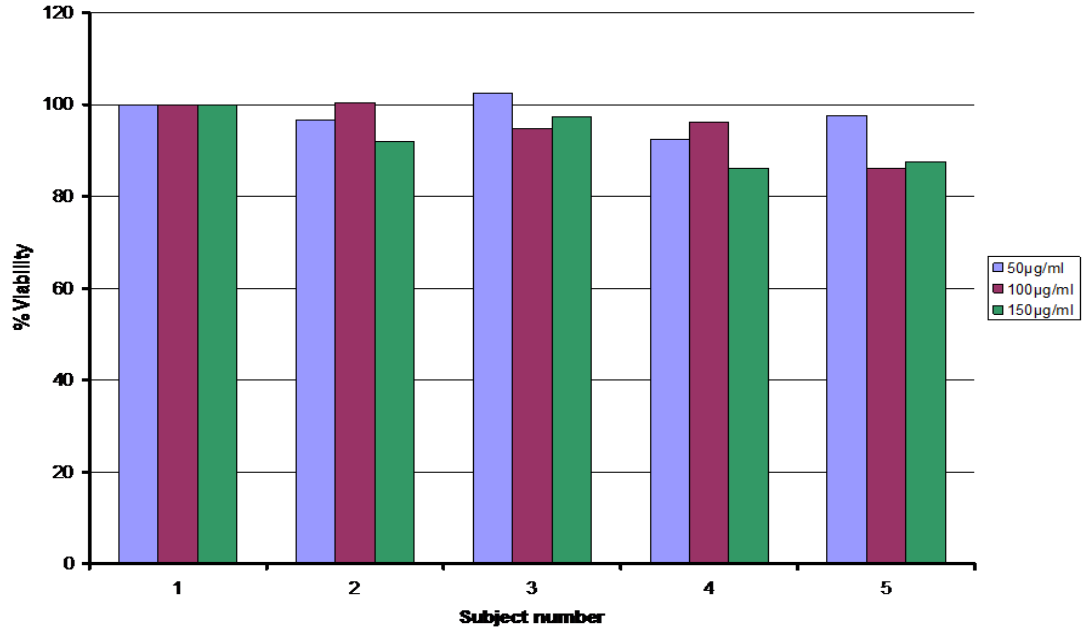

Figure 7.6: Bar graph of % Viability of U937 cells treated for 24 h at 50, 100 and 150 µg/ml concentrations.

The percentage Tail DNA of U937 cells after 1 hour treatment at concentration of 25 µg/ml is shown in Figure 7.7. This is results from the Comet assay where the % tail DNA is a

representation of the amount of DNA damage. From the graph it could be seen that there was only an increase of approximately 2% compared with the control or untreated cells. The control has tail DNA of 3% which is due to the assay procedures.

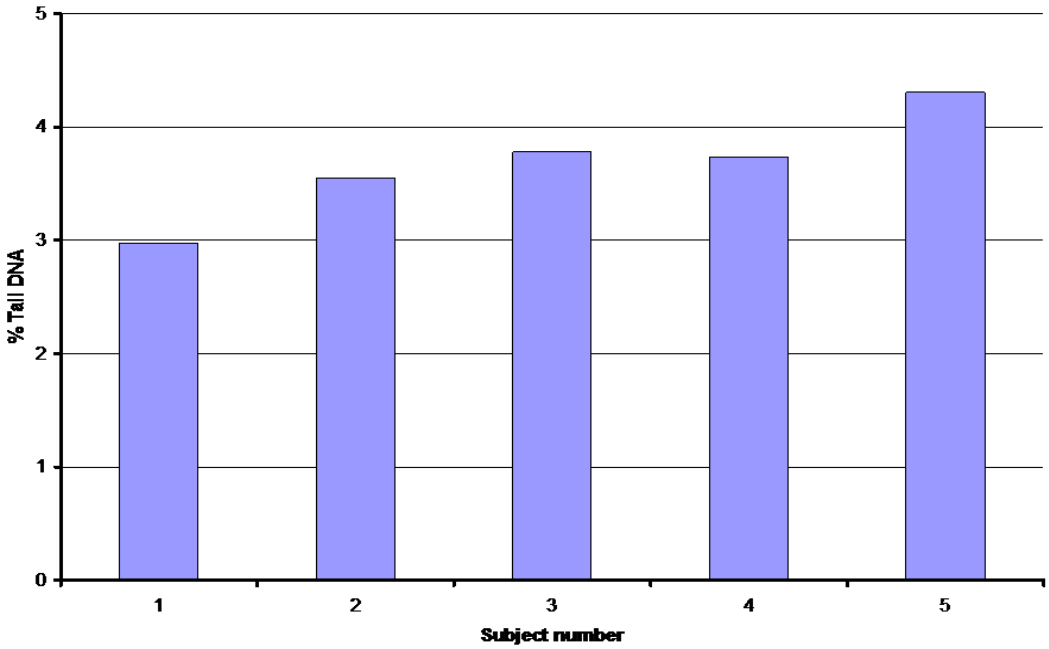

Figure 7.7: Bar graph of % Tail DNA of U937 treated for 1 hour at concentration of 25 μg/ml.

7.3 Conclusion

The work done in this chapter shows that there were no signs of toxicity detected as the % viability was high. The 90% viability was used as the mark to measure the toxicity effect of the semiconductor nanoparticles or quantum dots selected. However, since it is known that Cd-containing compounds are toxic, various points need to be investigated before looking at biolical applications. Those points include the duration or time frame of detecting the toxicity of quantum dots, and the concentration of the materials or quantum dots used. Toxicity studies on Co_xS_y and ZnS nanoparticles was not done due to unsuccessful preparation of water soluble nanomaterials using ligand exchange method. Although direct chemical method was employed as an alternative, most of the particles obtained were dominated by aggregation, which was a hindrance of looking at toxicity. Aggregation is a result of poor passivation and also very small size of the particles. Toxicity is dependent upon a number of factors including size and the capping materials. Due to the poor

passivation of the materials from direct chemical method, biological applications were out of the picture.

7.4 References

1. M. Kondoh, S. Araragi, K. Sato, M. Higashimoto, M. Takiguchi, M. Sato, *Toxicology,* **170,** 111, 2002.
2. H. M. Shen, C.F. Yang and C. N. Ong, *Int. J. Cancer,* **81** 820, 1999.
3. C. T. Dameron, R. N. Reese, R. K. Megra, A. R. Kortan, P. J. Carroll, M. L. Steigerwald, L. E. Brus, D. R. Winge, *Nature,* **338** 596, 1989.
4. P. Williams, E. Keshavarz-Moore, P. Dunnill, *Enzyme Microbiol. Technol.*, **30,** 354, 2002.
5. M. Kowshik, W. Vogel, J. Urban, S. K. Kulkami, K. M. Panknikar, *Adv. Mater.*, **14,** 815, 2002.
6. F. Pinaud, D. King, H. P. Moore, S. Weiss, *J. Am. Chem. Soc.,* **126,**6115, 2004.
7. L. C. Mattheakis, J. M. Dias, Y. J. Choi, J. Gong, M. P. Brunchez, J. Liu, E. Wang, *Anal. Biochem.,* **327,** 200, 2004.
8. M. Dahan, T. Laurence, F. Pinaud, D. S. Chemla, A. P. Alivisatos, M. Sauer, S. Weiss, *Opt. Lett.,* **26,** 825, 2001.
9. A. M. Derfus, W. C. W. Chan, S. N. Bhatia, *Nano Lett.,* **4,** 11, 2004.
10. K. I. Hanaki, A. Momo, T. Oku, A. Komoto, S. Maenosono, Y. Yamaguchi,Y. Yamamoto, *Biochem. Biophys. Res. Commun.,* **302,** 496, 2003.
11. J. K. Jaiswal, H. Mattoussi, J. M. Mauro, S. M. Simon, *Nat. Biotechnol.,* **21,** 47, 2003.
12. J. O. Winter, T. Y. Liu, B. A. Korgel, C. E. Schmidt, *Adv. Mater.,* **13,** 1673, 2001.
13. L. Liu, J. Zhang, X. Su, R. P. Mason, *J. Biomed. Nanotechnol.*, **4,** 524, 2008.
14. P. M. A. Farias, A. Fontes, A. Galembeck, R. C. B. Q. Figueiredo, B. S. Santos, *J. Braz. Chem. Soc.,* **19** (2), 352, 2008.
15. C. Zhai, H. Zhang, N. Du, B. Chen, H. Huang, Y. Wu, D. Yang, *Nanoscale Res. Lett.*, **6,** 1, 2011.

Chapter 8

General Conclusions

The complexes synthesized were very stable under normal conditions and obtained in good yields. The prepared complexes coordinate the used ligands through sulphur atom which was an advantage in the formation of metal sulphide nanoparticles. A single-source precursor method was employed for the thermolysis of the synthesized complexes to give metal sulphide nanoparticles that were dispersed in toluene. All the synthesized metal sulphide nanoparticles, irrespective of the complex used, depicted absorption spectra that were blue shifted which signify finite size of the particles. In most cases, well dispersed particles were observed when this method was used, especially for CdS nanoparticles. Analysis of CdS, Co_xS_y and ZnS nanoparticles through TEM showed various shapes such as rods, spheres and hexagonal. The particles synthesized were very small with a diameter range of 1-12 nm for all CdS, Co_xS_y and ZnS nanoparticles. Variation of capping agents (HDA and TOPO) in the synthesis of CdS provided different shapes, with HDA favouring rods while TOPO favoured spherical particles. The thermolysis of Co_xS_y nanoparticles in either HDA or TOPO resulted in three absorption features in the ultraviolet region, with the third one considered as the band edge.

No significant change was observed for water CdS nanoparticles using ligand exchange method. However, the only significant difference observed was when CdS nanoparticles capped by TOPO were transferred into water soluble. The particles were bigger because the syntheses of sugars-capped CdS nanoparticles were performed at 80 ^oC instead of room temperature. Synthesis of CdS, Co_xS_y and ZnS nanoparticles through a direct method at 160 ^oC also gave absorption spectra that were blue shifted to their bulk materials, with the photoluminescence spectra being red shifted to their as-synthesized CdS, Co_xS_y and ZnS absorption spectra, while some photoluminescence spectra had emission maximum that were close to the band edges. The diameter of the particles in this method ranged from 1-25 nm.

In this work, there are some problems that were encountered and prevented further investigation for biological applications of the as-synthesized semiconductor nanoparticles

or quantum dots. In the synthesis of water soluble semiconductor nanoparticles using ligand exchange method, only nanoparticles based on Cd-containing materials were recorded. This is because they were soluble in water and also revealed no obvious optical and structural properties changes. Cadmium metal is highly toxic and can cause damaging effects even at very low concentrations. Although work done in chapter 7 detected no toxicity, which is good for biological applications, clearance of semiconductor nanoparticles or QDs in biological systems was of concern. Some publications carried out on the toxicity and clearance *in vitro* and *in vivo* of Cd-containing compounds in human cancer cells showed that they are cytotoxic to human breast and prostate cancer cells. The ligand exchange method for cobalt sulphide and zinc sulphide nanoparticles would have been good for the biological applications due to less toxicity as compared to the cadmium-containing materials. However, unsuccessful synthesis of these materials through ligand exchange method hindered the progress or biological applications studies. Synthesis of semiconductor nanoparticles using direct chemical method yielded particles that were dominated by aggregation, indicating that particles were not well capped. Poor passivation of the particles could release the ions in the body and cause damage.

For future, a solution needs to be found on how to prepare water soluble Co_xS_y and ZnS nanoparticles using ligand exchange method since this method is controllable and does not alter the properties of the particles obtained that much as compared to those before performing ligand transfer. However, although toxicity is less compared to Cd-containing materials, toxicity on Co_xS_y and ZnS must be studied before looking at their biological applications. In order to detect the toxicity effects using the above method, it is recommended that another form of comparison other than comparing untreated and treated cells be found. For example, representing the toxicity by comparing it with uncapped QDs for a longer duration, like two weeks.